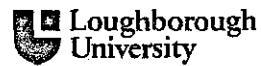


This item was submitted to Loughborough University as a PhD thesis by the author and is made available in the Institutional Repository (<https://dspace.lboro.ac.uk/>) under the following Creative Commons Licence conditions.



For the full text of this licence, please go to:  
<http://creativecommons.org/licenses/by-nc-nd/2.5/>

BLODSC no:- DX 224778



## Pilkington Library

Author/Filing Title ..... CORDINGLEY .....

Vol. No. .... Class Mark ..... T .....

**Please note that fines are charged on ALL  
overdue items.**

FOR REFERENCE ONLY

0402590082



BADMINTON PRESS  
UNIT 1, BROOK ST.  
SYSTON  
LEICESTER, LE7 1GD  
ENGLAND



---

# **ADVANCED MODELLING OF SURFACE IMPACTS FROM HOLLOW SPORTS BALLS**

**By**

**Leon Paul Cordingley. B.Eng. (Hons)**


**A Doctoral Thesis Submitted in Partial Fulfilment of the Requirements  
for the Award of Doctor of Philosophy of Loughborough University.**

**May 2002.**

**© by Leon P. Cordingley 2002.**

---



 <b>Loughborough</b> University Library
Date <i>Oct 02</i>
Class
Acc No. <i>040259008</i>

---

## ABSTRACT

Whilst tennis racket technology has progressed significantly over the last hundred years, ball design has remained essentially unchanged. Concerns over falling interest in the sport from both players and spectators require manufacturers to be able to engineer new ball products for a wider range of playing styles and surfaces. Unfortunately, little scientific knowledge exists on the effects of ball construction upon playing characteristics, particularly how the ball behaves during the impact.

Finite element analysis provides the perfect environment in which to construct complex models and interactions such as those present during a tennis ball impact. A representative set of pre-impact conditions corresponding to a range of tennis shots was selected. Various ball mesh geometries were created and a suitable set of material properties was used to develop models for uncovered rubber cores and pressurised and pressureless balls.

Post impact characteristics of velocity, angle and spin were measured experimentally using high speed digital image capture techniques, together with measurements of impact force and local deformation using laser vibrometry. These results were used to verify that the material properties used were appropriate for the strain rates present. The resulting models closely matched the experimental data.

The data input file was constructed in such a way that model parameters can be easily altered by a user, providing a powerful design tool. Furthermore, the ball model may be modified with simple manipulation so that it may be generically applied to represent any hollow sports ball.

---

## ACKNOWLEDGEMENTS

I would like to thank my supervisors Professor Roy Jones and Dr Sean Mitchell for their support throughout this project. Their knowledge and guidance was invaluable.

I am grateful to fellow members of the Sports Technology Research Group for their help, most notably Dr John Roberts and Rob Cottey for their equipment and data collection expertise. Also to Dr Steve Rothberg for his expert advice regarding laser measurement.

The school technicians are much appreciated, especially Steven Carr for frequent reliance upon his many skills.

My thanks to all at Dunlop Slazenger International Ltd. who have been involved in this project for their support and encouragement, along with the provision of equipment for experimentation. A special mention is made to Brian Machin for his enthusiasm during our many meetings.

On a personal note, I am grateful to all of my family for their continued support throughout my time at Loughborough, especially to my mother.

Finally, I should like to thank Pauline, without whom this would very likely remain a work in progress.

---

## NOMENCLATURE

$c$	speed of light
$d_c$	decay constant
$f$	frequency
$\bar{g}_i^P$	shear relaxation modulus
$m$	number of sides of a regular polygon
$n$	number of plane angles at each vertex
$n_c$	number of cycles
$p$	internal pressure
$r$	radius
$r_i$	inner radius
$r_m$	midplane radius
$r_o$	outer radius
$s$	sum of the internal angles
$t$	time
$t_h$	shell thickness
$u$	velocity
$v$	internal volume
$x$	distance
$A_I$	angle of incidence
$A_o$	outbound angle
$A_R$	angle ratio
$C_{ij}$	strain energy equation calibration constant
$C(\tau)$	viscoelastic relaxation coefficient
$E$	number of edges of a regular polygon
$E_L$	elastic modulus
$F$	number of faces of a regular polygon
$G^*$	complex shear modulus
$G'$	elastic shear modulus

---

---

$G''$	viscous shear modulus
$I_1$	strain invariant
$\bar{I}_1$	revised strain invariant
$N$	series expansion order
$O$	coordinate system origin
$R$	radius in a spherical coordinate system
$U$	strain energy density
$V$	number of vertices of a regular polygon
$V_N$	normal velocity component
$V_T$	tangential velocity component
$X$	Cartesian coordinate direction
$Y$	Cartesian coordinate direction
$Z$	Cartesian coordinate direction
$\alpha_i$	Ogden model calibration constant
$\alpha_R$	mass proportional Rayleigh damping coefficient
$\beta_R$	stiffness proportional Rayleigh damping coefficient
$\delta$	loss angle
$\theta$	azimuth in a spherical coordinate system
$\phi$	zenith in a spherical coordinate system
$\sigma$	stress
$\varepsilon$	strain
$\dot{\varepsilon}$	strain rate
$\lambda$	wavelength
$\lambda_i$	principal stretch
$\bar{\lambda}_i$	deviatoric stretch
$\eta$	viscosity modulus
$\omega$	circular frequency
$\mu_i$	Ogden model calibration constant
$\mu_k$	kinetic friction coefficient
$\mu_s$	static friction coefficient
$\mu(\tau)$	viscoelastic relaxation coefficient

---

---

$\nu_i$	Poisson's ratio
$\gamma^q$	equivalent slip rate
$\tau$	relaxation time
$\xi$	fraction of critical damping

---

<b>ABSTRACT .....</b>	<b>I</b>
<b>ACKNOWLEDGEMENTS .....</b>	<b>III</b>
<b>NOMENCLATURE .....</b>	<b>IV</b>
<b>1 A REVIEW OF LITERATURE CONCERNING SPORTS BALL IMPACTS.....</b>	<b>1</b>
1.1 BASIC THEORY OF BALL AND SURFACE INTERACTION.....	1
1.1.1 Impacts in One Dimension.....	1
1.1.2 Multi-Dimensional Impacts .....	3
1.2 A BRIEF HISTORY OF BALL GAMES .....	4
1.3 FORMATION OF THE GOVERNING BODIES.....	9
1.4 THE LAWS OF BALL SPORTS.....	10
1.5 APPROVAL FOR USE IN COMPETITION.....	13
1.6 EARLY RESEARCH CONCERNING IMPACT.....	16
1.7 THE EARLY SPORTS SCIENTISTS.....	17
1.8 SPORTS ENGINEERING AND BALL IMPACTS .....	18
1.8.1 Normal Impacts.....	18
1.8.1.1 Coefficient of Restitution.....	19
1.8.1.2 Energy Loss .....	21
1.8.1.3 Impact Duration.....	22
1.8.1.4 Contact Area .....	23
1.8.1.5 Deformation.....	24
1.8.1.6 Surface Waves.....	26
1.8.2 Oblique Impacts .....	27
1.8.2.1 Friction – Rolling and Sliding .....	28
1.8.2.2 Impact Characteristics.....	29
1.8.2.3 Models of Oblique Impacts.....	31
1.9 SPORTS BALL AERODYNAMICS .....	32
1.10 SUGGESTED RESEARCH DIRECTIONS .....	34
<b>2 RESEARCH HYPOTHESIS .....</b>	<b>35</b>
<b>3 CREATING A SPHERICAL MODEL FOR FINITE ELEMENT ANALYSIS.....</b>	<b>36</b>
3.1 INTRODUCTION.....	36
3.1.1 Discretising the Sphere.....	36
3.1.2 Spherical Meshes.....	42
3.1.3 Element Selection.....	43
3.1.4 Initial Model Definition.....	47

---

---

3.2	COMPARATORS.....	49
3.2.1	Mesh Geometry.....	49
3.2.2	Mesh Density.....	51
3.3	VARIABLES.....	53
3.3.1	Model Deformation, Impact Duration and Restitution.....	53
3.3.2	Computation Cost.....	53
3.4	IMPACT TEST PROCEDURE.....	54
3.4.1	Model Orientation.....	54
3.4.2	Initial Conditions.....	56
3.5	RESULTS.....	57
3.6	DISCUSSION.....	69
3.7	CONCLUSIONS.....	70
<b>4</b>	<b>MODELLING PRESSURISED HOLLOW BALLS IN SPHERICAL SPACE.....</b>	<b>71</b>
4.1	THE CO-ORDINATE SYSTEM.....	71
4.1.1	Cartesian to Spherical Geometry Conversion – a Practical Example.....	73
4.2	PRESSURISING THE HOLLOW SPHERE IN A FINITE ELEMENT MODEL.....	74
4.2.1	Creating Initial Equilibrium in Practice.....	77
<b>5</b>	<b>NORMAL IMPACTS OF HOLLOW RUBBER CORES.....</b>	<b>78</b>
5.1	INTRODUCTION.....	78
5.2	EQUIPMENT.....	80
5.2.1	Ball Cannon.....	80
5.2.1.1	High Speed Video System.....	82
5.2.2	Laser Vibrometer.....	85
5.3	EXPERIMENTAL PROCEDURE.....	90
5.3.1	High Speed Video Analysis of Normal Core Impacts.....	90
5.3.2	Impact Deformation Measurement.....	91
5.3.3	Laser Vibrometry Analysis of Local Deformation.....	93
5.4	RESULTS.....	97
5.5	DISCUSSION.....	102
5.6	CONCLUSIONS.....	110
<b>6</b>	<b>A HIGH STAIN RATE FINITE ELEMENT RUBBER MODEL.....</b>	<b>111</b>
6.1	INTRODUCTION.....	111
6.1.1	The Development of Modern Rubber.....	111
6.1.2	Mechanical Properties of Vulcanised Rubber.....	113
6.1.2.1	Strain Rate Effects.....	120
6.1.3	Developing Constitutive Rubber Models.....	122
6.1.3.1	Rubber Models in ABAQUS/Explicit.....	124

---



---

6.1.3.2	Adding Viscoelastic Effects .....	125
6.1.4	Tennis Ball Core Construction Method .....	128
6.2	METHODOLOGY .....	129
6.3	RESULTS .....	131
6.3.1	Low Strain Rate Tensile Testing and Subsequent Model Development .....	131
6.3.2	Increasing Strain Rate Within the Model .....	135
6.3.3	Material Damping .....	137
6.3.4	Developing the Finished Pressurised Core Model .....	139
6.3.5	Developing the Finished Pressureless Core Model .....	142
6.4	DISCUSSION .....	145
6.4.1	Low Rate Tensile Testing and Subsequent Model Development .....	145
6.4.2	Increased Strain Rate in the Model and Comparison to Experimental Data .....	147
6.4.3	Material Damping .....	147
6.4.4	The Finished Core Models .....	148
6.4.5	Bending Waves .....	149
6.5	CONCLUSIONS .....	155
<b>7</b>	<b>DYNAMIC MEASUREMENT OF FRICTION .....</b>	<b>156</b>
7.1	INTRODUCTION .....	156
7.1.1	Variables .....	161
7.2	EQUIPMENT .....	162
7.2.1	Sensicam .....	162
7.2.2	Load Cell .....	165
7.3	EXPERIMENTAL PROCEDURE .....	167
7.4	RESULTS .....	168
7.4.1	Post Impact Characteristics .....	168
7.4.1.1	Velocity and Restitution Coefficient .....	168
7.4.1.2	Rebound Angle .....	171
7.4.1.3	Spin .....	175
7.4.2	Impact Forces .....	178
7.4.2.1	Forces Normal to the Impact Direction .....	178
7.4.2.2	Forces Tangential to the Impact Direction .....	181
7.5	DISCUSSION .....	184
7.5.1	Velocity and Restitution Coefficient .....	184
7.5.2	Rebound Angle .....	186
7.5.3	Spin .....	187
7.6	CONCLUSIONS .....	188
<b>8</b>	<b>MECHANICAL PROPERTIES OF FABRICS .....</b>	<b>189</b>
8.1	INTRODUCTION .....	189

---

---

8.1.1	Fabric Construction .....	189
8.1.2	Mechanical Properties .....	191
8.1.3	Dumbbells.....	192
8.2	MATERIAL TESTING.....	193
8.2.1	Equipment.....	193
8.2.2	Experimental Procedure.....	194
8.2.3	Experimental Results.....	195
8.3	DEVELOPING THE CLOTH MATERIAL MODEL THROUGH NORMAL IMPACT ANALYSIS.....	196
8.3.1	Directional Material Properties .....	196
8.3.2	Appropriate Test Data.....	196
8.3.3	Developing the Hyperfoam Material Model .....	199
8.3.4	Strain Rate Effects.....	201
8.4	DEVELOPING THE CLOTH FRICTION MODEL THROUGH OBLIQUE IMPACT ANALYSIS .....	202
8.4.1	Experimental Determination of COR .....	202
8.4.1.1	Dynamic Friction.....	202
8.4.1.2	Static Friction.....	205
8.4.2	Friction Models in ABAQUS.....	206
8.5	RESULTS .....	208
8.5.1	Normal Impacts.....	208
8.5.2	Oblique Impacts .....	211
8.6	DISCUSSION.....	216
8.7	CONCLUSIONS .....	225
9	FINAL CONCLUSIONS .....	226
10	RECOMMENDATIONS FOR FURTHER WORK.....	228
11	BIBLIOGRAPHY .....	230

---

---

## 1 A Review of Literature Concerning Sports Ball Impacts

### 1.1 Basic Theory of Ball and Surface Interaction

#### 1.1.1 Impacts in One Dimension

In almost all ball games, the ball will be subject to an impact, either being bounced on a surface or struck by an implement such as a bat, racket, hand or foot. The motion of each object may be complex in that it possesses a three-dimensional velocity component with a compound rotation about some point or axis. Whilst in many sports both the ball and impacting object (bat, foot etc) may both display independent motion prior to the impact, for analysis it is often convenient to consider only the relative motion between the two. The simplest of such impacts is that of a ball dropped from a height onto a solid surface with little or no spin. This may be considered a one-dimensional impact, with motion confined to a single Cartesian direction only. (During impact the ball will deform uniformly, meaning that there will be deformation in three dimensions, but since the principal ball movement is in one plane then the motion is assumed to be uni-dimensional). In such a case, Daish (1972) tells us that the ball will rebound but not to the same height, as some energy will be lost during the impact itself. The result is that the velocity with which the ball rebounds from the surface is less than was possessed initially, and division of the rebound velocity by the initial velocity gives us the *Coefficient of Restitution* (COR). Clearly, if the ball were truly elastic then it would have a COR of one and were it completely plastic then its COR would be zero. Hence, this coefficient is an indicator of ball elasticity or 'bounce' and is commonly used to define the rebound characteristics of sports balls. Through simple manipulation it can be shown that the ratio of rebound height to original drop height is equal to the square of the COR and this is often a more convenient way to measure the characteristic.

---

For any impact, the ball will be in contact with the surface for a finite duration, which is dependent upon factors such as ball and surface material and their relative velocities. The general case of such an impact is one where the relative velocity is initially negative and the reactive force increases to some maximum value, at which time the relative velocity is zero. The force then falls to zero itself at which time the relative velocity reaches its maximum positive value and the impact ends. Daish states that the higher the velocity, the greater the ball compression and thus the higher the energy lost during impact and hence increasing impact velocity will reduce the measured COR for a given ball type.

---

### 1.1.2 Multi-Dimensional Impacts

The simple case of a dropped ball is a one-dimensional problem, with a zero velocity component in the plane of the impacting surface. However as was initially noted, most impacts that occur in ball sports are at least two-dimensional, they may also possess spin prior to impact and almost certainly will upon rebound. If the ball has a component of velocity in the plane of the surface then during impact a resistive frictional force will act upon the ball, retarding its motion. Further, as this force does not act through the centre of mass of the ball then the initial spin of the ball will be effected. It has already been shown that the impact force is proportional to ball compression, which is itself dependant upon impact velocity, or its normal component in this case. It is also known that the tangential friction force is related to the normal force by a *coefficient of friction* (COF), which is a product of the surface properties of the materials in contact. It should be clear that both restitution and friction coefficients have an effect on the rebound velocity and angle of balls in oblique impacts. Daish also states that the spin a ball possesses prior to impact can have a marked effect on its rebound. A ball that has heavy topspin, i.e. one that rotates clockwise whilst moving from left to right, will promote a frictional force toward the direction of motion.

To further complicate oblique impacts, a ball may possess spin about an axis along its direction of travel, such that a friction force develops with a component at right angles to the tangential velocity vector. In this case a compound friction force will act at an angle proportional to the ratio of tangential velocity to rotational velocity and will cause the ball to rebound in a direction at some angle to the initial velocity vector. This is the basis for spin bowling in cricket and contributes to the swerve shot in snooker. A ball may also spin about an axis perpendicular to the impact surface, but having a net zero velocity component parallel to the surface this has little effect on the rebound. Rather this type of spin, known as *hook* and *slice* in golf, effects the flight of the ball prior to impact due to the Magnus effect. This is discussed in section 1.9.

---

## 1.2 A Brief History of Ball Games

Whilst most current ball sports are relatively modern 'inventions' developed over the last few hundred years, games involving the use of balls have been in existence for as long as historical records exist. Decker (1992) presents a detailed account of ancient Egyptian pastimes, of which ball games were a part; even thousands of years ago it appears that the effect of material properties on ball characteristics was appreciated. Most were made of a number of leather strips, sewn together and stuffed with material such as straw, reeds, hair or yarn. Balls of solid stone, wood or clay also existed and the range of sizes suggests that many different games were played. Sport as we now know it did not exist at this time and it appears that ball games were merely a distraction, played mostly by women. Their games used either the hand or an implement of some sort to propel the ball, although bat and ball games appear to have been less popular. Of the 'handball' games, Decker describes them as either catching or juggling types, where the object appears to have been to keep the ball in the air. However, as much of the evidence is drawn from a limited source then even this basic 'rule' is open to question. Relating to the bat and ball games, Decker suggests that these may have a ritual origin, taking evidence from a temple drawing which shows King Tuthmosis III holding a stick and ball and standing before the god Hathor.

At a similar time in the continent of South America, the Aztecs and Mayas had constructed playballs from the dried sap of the tree *Hevea brasiliensis*, which would later become known to Europeans as the 'rubber' tree (Ciesielski, 1999). In contrast to those of the Egyptians, the properties of the latex made these South American balls very 'bouncy'.

The era of Greek and Roman dominance in cultural development shows evidence for what would now be called sport and by far the most dominant pastimes were those which combined to form athletics. It is known that the ancient Olympics were held in Greece from 776BC and consisted of events in running, throwing, jumping, wrestling and boxing. However, at this time there appeared little interest in any game that would

---

---

require a ball. Harris (1972) states that, in the times of Greek and Roman dominance, ball games were initially the pastime of children. He also refers to a medical writer Galen, who describes a ball made by Greek children from the inflated bladder of a pig, which was warmed in the ashes of a fire and rubbed to improve its shape. This would appear to be the origin of the inflated ball that is now used in many modern sports. There is a reference to a small ball made of panels and stuffed with feathers in a similar manner to the Egyptian ball and also to a large stuffed ball weighing over two pounds, although for what use it was intended appears to have been lost. According to Harris, the Romans had names for at least five different types of ball.

Whilst competition was the basis of Greek athletics there was by contrast little emphasis on the outcome of ball games. Few would stop to observe a ball game and those who did would be more interested in the skill of the players. Throwing and catching would seem to be the basis of these games, as it was for the Egyptians, although references describe a 'rhythmical' passing of the ball, in keeping with the appreciation of the skill of the players. Later Greek literature talks of a *sphairisterion*, the first reference to an area specifically created for ball-play, which was attached to the complex of athletics buildings.

As the Roman empire fell and Europe moved into medieval times, references to ball games diminish. Carter (1992) describes a feudal society where war dominated and emphasis shifted to martial skills used by the nobility to train for combat, such as archery and jousting. This led to the creation of the knights tournament, which consisted of a mounted skirmish, a joust and the passage of arms. Gillmeister (1997) suggests that the final event, which represented the attack or defence of the castle gates, was the inspiration for the 'inventors' of medieval ball games. He further suggests that the peasants engaged in ball games as their own form of tournament and that these games were physical affairs that mirrored the contests of the knights. Around 1175, Titley and McWhirter (1970) refer to 'the well known game of ball' and this peasant ball game is commonly accepted as the origin of football, although it is hardly recognisable in its modern form. Gillmeister further suggests that tennis was originally an offshoot of football, giving reference to a game played in Sweden where the ball is both hit with the

---

---

hand and kicked. Carter suggests that writing was expensive in medieval times and most records were written by lawyers or monks, there is therefore little evidence on how games that were known by the nineteenth century had developed. Some legal records make reference to ball games being outlawed due to their violent nature and the amount of wagering that had become associated with them.

It is clear from the records available that by the end of the medieval period many different ball games had developed. Most seemed to involve propelling the ball at some target and as balls were still usually made from stuffed leather then the lack of bounce meant that the ball was most often kept in the air. Some games involved the use of a striking implement to propel the ball, such as a bat or club, whilst in others the ball was played with the bare hand. The 'handball' games were the origin of tennis and the French name for tennis, *Jeu de Paume* meaning the hand game, betrays its heritage. Much has been written on the history of tennis, which developed into what is known today as Real or Royal tennis, by authors such as Morgan (1995) and Gillmeister (1997) and it appears there are many conflicting stories of its origin. Gillmeister suggests, as do many others, that tennis developed in the French monasteries and was commonly played in churches. However, Harris (1972) provides evidence to show that tennis evolved as a street game, played originally by commoners. What is known is that the balls used to play the game were at first hard and with little bounce and this determined how the game developed. The ball was most often struck on the volley with the speed dependant upon the skill of the player and as the ball often landed and rolled, so the chase rule was introduced.

In the fifteenth century (Morgan, 1995) balls were made with heavier filling material as this was known to improve their playing characteristics. Even today, balls used for traditional Basque games have a pellet of lead at their core for the same reason. Inflated balls were then also made of leather to protect the inner animal bladder from bursting and used for the game of football. The name would suggest that the ball was kicked although descriptions of the original game would liken it more to rugby, where the ball is carried amongst a large group of players. The shape of the ball was determined by the bladder and so not being round it would have been difficult to do much more than punt it

---



---

in some general direction. It is of interest that before this time, games where the ball was kicked were not documented. This does not mean that they did not exist, but it is possible that the achievable characteristics of balls of the time did not lend themselves to a game of this type.

The earliest reference to golf is found in Scottish Parliamentary records from 1456 and by the sixteenth century the game was well developed, played with balls of the stuffed variety. Hockey developed a short time later and the original rules, which called for the ball to be an ordinary sized cricket ball painted white, may point to hockey being developed from cricket.

Without a doubt, the single most important development in ball games came from the introduction of rubber into Europe and the subsequent discovery of vulcanisation by Charles Goodyear in the late nineteenth century. Suddenly balls could be constructed that would rebound when dropped to the ground and travelled much faster than the stuffed balls when struck with a similar force. The opportunity to develop ball games to take advantage of this new material was seized by many people and a number of new sports were invented, such as basketball, netball, volleyball and indeed lawn tennis. However, to say these games were true inventions is somewhat misleading, rather they were adaptations of a number of games, often created to suit the fitness needs of specific groups. Rubber was exploited in its use to replace animal bladders in inflated balls, although they initially retained the non-round shape. Over time footballs became more rounded whilst rugby balls were made more oval, to suit the styles of play that had developed. Similar balls were used for sports such as basketball and volleyball. Interestingly, rubber was not widely adopted for use in solid balls of the type used in club and bat sports. The object of many of these games, such as golf, is to hit the ball a great distance and so they require high ball speed. A hard ball of solid wood or even tightly packed feathers could be made to travel a much greater distance than one of rubber and so these stuffed or solid balls were retained. However, with the later invention of polymers many balls came to be made from some form of polymeric material, such as modern golf balls.

---

Lawn tennis was invented by Major Walter Wingfield who took advantage of rubber balls to devise a simplified version of real tennis that could be played on the Victorian lawns, which laid empty after a brief public interest in croquet. He originally patented the game under the name of *Sphairistike*, from the Greek word meaning ball game, however this did not prove popular and it soon became more commonly known by its current name. Initially the balls were made from sheet rubber which was cut out and stitched together, but being only approximately round and uncovered they were difficult to control. Eventually, tennis balls were made from moulded rubber shells and covered with cloth to improve their playing characteristics. A similar ball was also used in early forms of table tennis.

---

### 1.3 Formation of the Governing Bodies

Around the same time as rubber began to find favour in ball construction, governing bodies were formed for many of the sports which were fast developing. At first, most games were played to a number of different 'local' rules and as their popularity grew, so people sought to bring some kind of order to their sports. By the eighteenth century the game of bat and ball had evolved to become cricket and was well established. The Marylebone Cricket Club was founded in 1787 and played their sport at Lords, which was to become the 'home' of cricket. It is interesting that it was also this club, nearly a hundred years later that drew up the first set of rules for lawn tennis. The late Eighteenth century also saw the formation of the Football Association and the Rugby Union, both producing a set of rules for their respective sports.

The Honourable Company of Edinburgh Golfers (now resident in Muirfield) was formed in 1744 and defined the first set of thirteen rules for golf. Subsequently the Royal and Ancient Golf Club took over the administration of golf rules and it now shares these responsibilities with the United States Golf Association. The R&A administer the rules for the world with the exception of the USA and Mexico who come under USGA jurisdiction. This situation has led to a number of occasions when there have been different specifications for balls and equipment.

With rules in place for most of the major sports, competitions became commonplace and the first sporting celebrities appeared. Whilst most of the top events were still amateur competitions, their popularity attracted money and sponsorship and Viney (1978) tells us that many of the top players were known as 'shamateurs' as a result. 'Open' competition was adopted by many sports where professionals and amateurs could compete together, although the International Lawn Tennis Federation (founded in 1913 and later to become the ITF) resisted the temptation at first. Eventually, after Wimbledon became an 'open' competition in 1968, nearly one hundred years after its inception in 1877, the ILTF realised that this was an inevitable step.

---

---

## 1.4 The Laws of Ball Sports

As sport became a profession and large sums of money were involved, so the need to provide a 'level playing field' and to prevent cheating was ever greater. The rules, laid down by respective governing bodies, were an important part of the sport and often these rules included reference to the ball. However even today, these rules are often brief and rarely require the balls to have a specific set of playing characteristics. Most governing bodies would appear to recognise the importance equipment plays in the character of their sports as the laws governing these items are stated early in any rulebook. However, in most sports the sparse content of these rules highlights a lack of understanding that specific ball characteristics have on the games themselves.

Considering the rules as given by the international governing bodies, some sports such as cricket (MCC, 2000), netball (IFNA, 2001) and table tennis (ITTF, 2001) only have requirements for ball size and weight. Others such as football (FIFA, 2001), rugby (IRB, 2001) and volleyball (FIVB, 2001) also specify an acceptable range for the internal pressure. Whilst size and weight are good starting points, it is clear that two balls meeting the same requirements could easily be produced to have very different playing characteristics such as 'bounce' or 'spin'. In the case of cricket, the material for construction is not even given and many sports require that 'synthetic' or 'suitable' materials should be used, which is hardly specific. It is clear that some governing bodies have begun to recognise the importance of the physical characteristics of the balls used for their sports, with attempts to define simple rebound characteristics. Most use some form of drop test as their standard, whereby the ball is released from a specified distance above an impacting surface and must rebound within a given range of height. This is often expressed within the laws as a Coefficient of Restitution and such rules exist for tennis (ITF, 2000), basketball (FIBA, 1998), squash (WSF, 2001) and association croquet (CAEC, 1989). However, the impacting velocity of the dropped ball is often far removed from that experienced in play or appears to be an arbitrary value. For example, tennis rules require that the ball be dropped from a height of 100 inches, which provides an impact velocity of around 15mph, yet service speeds for the top professionals have

---

been recorded at up to 150mph. Also, whilst ball behaviour will be significantly different over a range of impact velocities experienced in play, nearly all specifications require testing at only a single value. In addition, ball spin is now a significant component of play and yet no games have regulations to cover this.

Tennis and squash have further requirements that the ball exhibit a defined stiffness when compressed under a specified loading condition, with the tennis rule also requiring a specific energy to be returned during the subsequent relaxation. This test, conducted using a 'Stevens' machine (ITF rules, Appendix I), is intended to provide a measure of how 'hard' the ball is and how much energy is lost during impact. However, it is again unclear how this test relates to conditions experienced in play. By far the most developed rules governing ball characteristics are seen in golf. Here balls are impacted under a given set of test conditions and limits are set on the initial velocity and overall distance the ball travels. As the test conditions are typical of those experienced during play then these rules appear the most suitable of all the ball sports.

With respect to ball construction, the rules of most sports are even more vague. The ball is often required to be 'spherical' or made of a 'suitable' material, yet these descriptions are not defined in terms that would be measurable in a laboratory. More often it appears that the manufacturer can choose the material, with national governing bodies having the final say on whether equipment is to be 'approved' under their own rules, as discussed later in the chapter. Some rules give more detail regarding ball construction, with rugby specifying four panels and basketball requiring eight 'traditionally shaped' panels with a seam of a maximum width. Volleyball rules demand a flexible leather or synthetic outer case with a rubber or similar bladder, whilst squash rules call for high quality rubber to be used and that it is free from defects.

Ball colour is specified in many sports although most governing bodies are more concerned with the details of printed advertising and manufacturers logos on equipment. Also related to manufacturing is a rule in squash that specifies the minimum failure stress of the seam joining the two rubber hemispheres, which appears to be the only ball

---

---

rule requiring an experimentally determinate construction characteristic. By far the most specific rule on ball construction belongs to baseball:

“The ball shall be a sphere formed by yarn wound around a small core of cork, rubber or similar material, covered with two stripes of white horsehide or cowhide, tightly stitched together.”

This rule defines the shape, materials and construction method for the ball and yet is still rather vague. The descriptors *sphere*, *small*, *similar* and *tightly* are all used and yet none of these are specified in a manner that may be measured experimentally.

---

## 1.5 Approval for Use in Competition

In recent years, national organisations and 'leagues' have taken it upon themselves to specify more stringent requirements for balls to be used in their own competitions. These specifications most often take the form of a 'technical document' that is issued to all ball manufacturers, although why these specifications are not found within the laws themselves is somewhat puzzling. In the United States, the governing body of college sports, the National Collegiate Athletic Association (NCAA) has requirements for baseballs that are supplemental to those of the international rules IBAF (1999). This is due to the concern of the NCAA for the safety of its athletes, specifically if struck by a batted ball. Having worked closely with the National Institute for Sports Science and Safety to determine the risk involved to their athletes, they specify an acceptable COR based on the results of their investigation. Whilst this is a reasonable step to take, the requirement may still be considered unrealistic as the impact velocity is specified as 60mph for the test, whilst in play the relative speed between bat and ball approaches 150mph.

It has become common practice for sports balls to be regulated by national and international governing bodies through 'approval' schemes, whereby balls must meet certain requirements in order to be approved for use by the respective bodies. Whilst the criteria for acceptance are included within the rules for tennis and golf, most sports have separate technical documents which cover both the mechanical properties of the ball and the construction methods and materials used. FIFA has two levels of testing resulting in the award of either 'FIFA approved' or 'FIFA inspected' quality marks. Both balls undergo the same testing procedure with the balls seeking approved status being subject to an additional durability test and having requirements that are more stringent. Criteria such as COR, pressure loss, water absorption and sphericity are all measured. Similar 'approval' schemes exist for table tennis (ITTF, 1994), bowling (ABC, 1993) and cricket, although cricket appears unique in that balls for use in English county competition must conform to a British Standard, BS5993 (BSI, 1995). Here such things as seam geometry, stitching quality and cover finish are specified, although interestingly

---

---

the material and construction method used for the core are not included in the standard. The same standard also governs balls used for league and club competition, with the requirements for each being more relaxed, in a similar manner to the FIFA specifications.

As has been noted previously, the criteria for approval of tennis balls are specified within the rules. A recent addition to the rules allows the use of different ball types, classified as *fast*, *medium* and *slow*, on appropriate court surfaces as specified by the ITF *pace* test (ITF, 1998). All balls must meet the same specifications regarding weight and COR, but the *fast* ball must have smaller forward and return deformations whilst the *slow* ball must be of a greater diameter. These new rules are an attempt by the ITF to match ball type to court surface in a manner that would result in play being similar over the range of available court surfaces. Games played on traditionally fast courts such as grass would be slowed down, reducing the emphasis on the 'big serve', whilst play on slow courts such as clay would be made faster, reducing the length of baseline rallies. This represents a concerted effort by the ITF to increase the appeal of its sport to the viewing public by making games more 'exciting'. Unfortunately players have not been keen to accept this idea as it would result in them losing the advantage they traditionally had on their 'home' surface and particular styles of play would no longer be so effective. Whilst this new idea has been unsuccessful thus far, it serves to highlight the concern of a governing body for the popularity of their sport in a very competitive market.



The rule specifications of weight, diameter and restitution coefficient are given in Table 1.1 below. It can be seen that COR varies considerably depending on the game, from a maximum of 0.91 for table tennis to 0.53 for cricket.

	SPORT	Weight (g)		Diameter (cm)		COR	
		Min.	Max.	Min.	Max.	Min.	Max.
HOLLOW BALLS	Tennis	56.0	59.4	6.541	6.858	0.73	0.76
	Soccer	420	445	68.5#	69.5#	0.77	0.91
	Basketball	567	650	74.9#	78.0#	0.82	0.88
	Squash	23	25	3.95	4.05	0.51	0.57
	Table Tennis	2.40	2.53	3.73	3.81	0.88	0.91
	Volleyball	260	280	65#	67#	n/a	n/a
	Netball	400	450	69#	71#	n/a	n/a
SOLID BALLS	Golf	n/a	45.97	4.267	n/a	n/a	n/a
	Cricket	156	163	22.4#	22.9#	0.53	0.62
	Field Hockey	156	163	22.4#	22.9#	n/a	n/a
	Baseball	142*	149*	22.86*#	24.13*#	n/a	0.555
	Tenpin Bowling	n/a	7257*	21.59*	21.83*	0.65	0.78
	Croquet	439*	468*	9.128*	9.287*	0.72	0.79

\* - converted from imperial values

# - calculated from specified circumference

**Table 1.1 – Selected Sports Ball Characteristics as Specified in Either the International Rules or Under ‘Approval for Play’ Regulations.**

---

## 1.6 Early Research Concerning Impact

In his book on the subject, Stronge (2000) gives an account of the development of impact mechanics, starting in the sixteenth century with the early work of Galileo on the ballistics of musket balls. He states that John Wallis appeared to be the first to appreciate restitution in partly elastic collisions, but like many of the great minds of the time he concerned himself with the fully elastic collision of rigid bodies. In Newton's famous *Principia* (Newton, 1687), we see the first reference to restitution being material dependent. He describes a simple pendulum experiment using balls of wool, steel, cork and glass that are allowed to collide and the rebound velocity calculated. He noted that the velocity after impact was some fraction of that prior to impact and that the ratio was different for each material, being around  $5/9$  for wool and about  $15/16$  for glass. However, limited by the size of his pendulums he incorrectly assumed that this proportionality was independent of velocity.

Hertz (1882) developed what is now considered the classical theory for contact between solid bodies with spherical contact surfaces, relating contact force to the elastic deformation through an elliptical pressure distribution. Whilst the theory was originally developed for quasistatic contact, it provides very good approximation for dynamic impacts assuming the contact region is small in relation to the size of the bodies. However, the theory does not hold where either body exhibits large strains under loading.

---

## 1.7 The Early Sports Scientists

Whilst much of the early literature concerning impact used balls or spheres as their colliding objects, work concerning sports balls was limited. One of the first papers to reference sports balls specifically was written by Lord Rayleigh (1877) and discussed not impact, but rather the aerodynamic 'Magnus' effect and its influence on tennis ball flight. Whilst his explanation of the phenomenon, likened to a ball with projecting blades, is somewhat limited he does provide a mathematical solution for the simplified case of a cylinder rotating in a 'perfect' fluid. The same effect is presented by Thomson (1910) with reference to a spinning golf ball. Here a simple explanation is given as to the generation of the force and an interesting electromagnetic arrangement is used to demonstrate the effect.

Whilst early work concerning sports balls is limited, from the early 1970s interest in the area grew quickly. Daish published his book 'The Physics of Ball Games' in 1972 and technical papers began appearing in a variety of physics, engineering and biomechanics journals.

---

## 1.8 Sports Engineering and Ball Impacts

### 1.8.1 Normal Impacts

Research undertaken on rebound characteristics of sports balls may be split into two areas – normal and oblique impacts. A normal impact is the simplest case, as general motion may be considered one-dimensional. If there is no initial spin component then there is theoretically no friction effect during the impact and so there will be no spin after the bounce either. In the work concerning normal impacts, the ball is nearly always allowed to fall from rest at a certain height, providing an impact situation similar to the standard drop test used by most governing bodies to approve balls for play. The Rules of Tennis require a ball to be dropped from a height of 100 inches which, neglecting air resistance, will attain a velocity of 7.1m/s upon impact. Haake and Goodwill (1998) found from video analysis that a medium paced forehand would impact the ground at 16m/s with an angle of 22 degrees, giving a vertical component of 6m/s. Brody (1984) states that a well hit shot has a vertical component of about 5m/s, although no source is given for the data. This is of the same order as the bounce tests and so these tests would seem a reasonable representation of actual impacts. However, it is the service aspect of the game that is currently causing much concern. During a serve the ball is projected downwards at the court. The ball can leave the racket at a velocity of up to about 65m/s (140mph). Data published by NASA (1997) shows that ball velocity prior to impact is around 90mph, which at an inbound angle of about 25 degrees results in a vertical component of 17m/s. This is almost three times the impact speed of the drop test and at these greater strain rates the balls characteristics may well be considerably different.

---

### 1.8.1.1 Coefficient of Restitution

Most work on normal impacts concerns the coefficient of restitution of the ball. The rules of tennis imply that the COR for a ball must lie between 0.73 and 0.76 when dropped from a height of 100 inches. However, it is found that COR for sports balls is not constant, rather it is proportional to impact velocity. Daish states that the harder (and hence faster) a ball is hit, the more it is compressed and so the greater the energy loss. Casolo (1997) describes a linear relationship between COR and pre-impact velocity between 10 and 40 m/s, based on a mass spring damper model. The results fit the experimental data well although at the higher speeds the data is about 4% greater than the theory suggests. This is further developed by Casolo, Vallatta et al. (1997) where impacts against steel plates produced results which are best represented by a second order quadratic approximation. Both papers suggest that the difference in COR between new balls and 'old' balls (having lost some internal pressure) is about 0.06 or 10% over most of the velocity range. Caffi and Casolo (1993) looked at the CORs for pressureless, 'new' pressurised and 'old' pressurised balls at different velocities and compared them to deformations of the same balls under a load of 40N, after both one second and one minute. They found no correlation between the two sets of data and so concluded that ball stiffness cannot be directly compared to the rebound speed. Rather it must take into account the elastic constant, damping coefficient, internal pressure and mass of the ball. They also describe a mass spring damper model using constants suggested by Leigh (1992). Rose (1999) presents impact data for tennis balls of varying stiffness, as measured by the ITF forward and return deformation test defined in the rules of tennis. Ball stiffness appears to have little effect on COR over a large impact range, although as all balls may well have been constructed to conform to ITF rules then this is not necessarily unexpected. The pressureless ball type tested did have a significantly lower COR at higher impact velocities. It appears that stiffer balls give a higher 'pace' value, which is related to the COF of the impact, probably due to the smaller contact area.

---

Cross (2000) presents a mathematical model of the COR for collision between two balls, where energy loss is a function of the stiffness modulus of each ball, defined as an elastic spring constant. A ball bouncing upon a rigid surface is shown to be the case where the stiffness and radius of the second ball approach infinity. Using this theory, he presents an experimental analysis of a ball and racket impact which suggests that the use of a ball with zero COR (in impact with a solid surface) would only reduce service speeds by 19%. Guban (2000) notes that the COR of a croquet ball impacting a steel surface is lower than when subject to a similar collision with a wooden mallet. As the relative stiffness between the wood and ball is less, then ball deformation is lower and so the energy loss is reduced. Cross notes that, whilst ball CORs are strictly limited by the rules, the bat and ball interaction is seldom restricted and attempts have been made to exploit this fact by sports equipment manufacturers. This has led to the introduction of a new rule in golf which states that 'the club face shall not have the effect of a spring', however no such rule exists in other sports.

There are two methods by which the COR is usually ascertained. Firstly, using a video recorder focused at the highest point of the rebound, with some markings behind to allow height to be measured, the bounce height may be directly determined. However, as the ball must bounce in a different plane to that of the measuring apparatus then if the bounce height is slightly more or less than the height of the focal plane, some parallax could be involved. Brody (1990) suggests that over the range of rebounds allowed by the ITF, parallax error can be up to 1cm, but for a set of data recorded the average bounce height with correction for parallax only changed by 1mm.

Bernstein (1977) and Brody both describe a method whereby COR may be determined indirectly from the sound made by the bouncing ball. A recording is made over several bounces after the initial drop, although only the first two impacts are needed, between which the ball will spend equal amounts of time rising and falling. If the bounce time is denoted as  $t$ , then the maximum height to which the ball will rise is equal to the distance that it falls under gravity in the time  $t/2$ . If the initial drop height is known then the COR can easily be calculated. This method calculates COR from the time between the ball leaving the surface and approaching the next bounce, whereas the recording gives the

---

---

time between similar impact positions. This requires the contact time to be included in the calculations and it was found that 5.3 milliseconds gave good agreement with the data from video. Stensgaard and Laegsgaard (2001) present a revision of this method using a standard PC soundcard and custom written software to analyse the sound file, although here experimental analysis is conducted using steel balls dropped from a few centimetres.

### **1.8.1.2 Energy Loss**

The fact that a tennis ball only rebounds to about a half of its original height indicates that a large energy loss occurs during impact and Daish suggests that it is dissipated as heat. As the ball warms up during play it becomes noticeably faster. He suggests that as the air inside the ball heats up its pressure increases and so the ball is able to compress less during impact, increasing the COR. The properties of the rubber may also change through heating, although having a low thermal conductivity it would take some time to become warm. Cross (1998) suggests there are other methods of energy loss during impact, such as dissipation in the ball during the collision through internal friction, or permanent deformation of the ball or the surface. Alternatively, energy may be stored in the ball as a result of its compression and subsequently dissipated after the rebound either in internal modes of oscillation or by a slow recovery of the ball to its original shape. He suggests that the energy loss may be predicted from static hysteresis curves, but that these predictions do not account for the difference between the dynamic and static properties of a ball. A method is presented to experimentally determine dynamic hysteresis curves for a number of different balls and both force and displacement traces against time are shown to approximate a half sine wave. Although the peak force occurs at half of the total impact time, the impulse during the compression phase is larger than during expansion and so it follows that the ball will rebound with a lower velocity. It is also shown that the ball rebounds in a compressed state, with the vertical displacement being finite at the end of impact. A static hysteresis curve for a tennis ball predicts only 50% of the energy actually lost during impact, whilst the dynamic hysteresis curve

---

accounts for 100% of the energy loss. Suggested reasons for the difference between static and dynamic results are that firstly, during compression the rubber is initially much stiffer than throughout the remainder of the impact. This increased stiffness occurs during approximately the first 200 microseconds of impact and ends with the transition from a compressive to a bending mode of deformation. Secondly, it is known that the cloth cover contributes significantly to the energy loss, since tests on cores show much higher rebound speeds. During the static tests, the cloth is allowed to recover elastically and so will not retain the same energy as in the dynamic tests. Finally, it is suggested that more stored energy is lost after the rebound in the form of vibrations travelling around the ball. A small piezo element glued to the top of the ball showed a small amplitude oscillation of around 700Hz. This persists for 2 ms after the ball rebounds, giving a period of oscillation of 1.5 ms. There is a delay in the initial propagation of around 0.4ms, which is consistent with the transition from high to low stiffness already noted. Ujihashi (1994) measured golf ball deformation using high speed video and combined this with force measurements taken using an accelerometer to calculate energy losses. A mass spring damper model showing good first order approximation of the experimental results is suggested for use in finite element code to represent the ball to club impact.

### **1.8.1.3 Impact Duration**

Cross (1998) tested several solid ball types and calculated that contact times were proportional to impact speed, but the contact time of the tennis ball was found to be independent of velocity. A value of 5ms is suggested, which is generally agreed by most authors, although in his analysis Cross limited ball velocities to a maximum of 8m/s which is not representative of game velocities. Guban (2000) measured impact duration for croquet balls by breaking a laser beam and found it to be proportional to velocity, with close approximation to Hertz theory seen. It is suggested that contact time is increased due to lower recoil speed but decreased by a residual compression of the ball at separation. Impact velocities are again low, being less than 6m/s.



---

Roberts, Jones et al. (2001) presents a method of determining impact duration to a high degree of accuracy using a conductive coating on the ball to create an electrical switch, preceded by a review of previous work. Duration was measured for impacts between both two and three piece golf balls and various clubheads with two piece balls having a shorter duration in all cases, being around 0.460ms compared to around 0.475ms for the three piece balls. Ball compression was also shown to affect contact duration which decreased from around 0.490ms at 80 compression to 0.444ms at 100 compression. Increasing clubhead speed also reduced impact duration and results show good agreement with theoretical values derived from Hertz law.

#### **1.8.1.4 Contact Area**

Some work has attempted to measure impact forces to assess the injury potential of different sports balls. Dowell, Snowden et al. (1991) dropped several different balls onto a force plate, which was used to calculate only the mean impact load. A sheet of paper was placed over carbon paper on top of the force plate to produce 'footprints' of each ball, allowing the compression areas to be calculated. Bridge (1998[a]) describes a similar method of measuring the contact area by placing a sheet of thin paper over sandpaper. However it is not known whether either measuring method will affect the bounce of the ball significantly. By examination of the different impact areas, it was concluded that the impact force depended on the ball's compressibility, weight and impact velocity. Contact force per unit area did vary by around 10% over the small velocity range investigated (4.88-8.4 m/s) but there was no clear pattern due to insufficient data. Carbon paper was also used by Guban (2000) to measure the contact area of croquet balls at various impact velocities. The results show good agreement with Hertz theory of elastic impact, despite the significant energy loss. The author suggests that contact area is dependent only upon the compression phase and that no energy is lost during this time.

---

#### 1.8.1.5 Deformation

Snowden, Dowell et al. (1989) measured the 'stopping distance', defined as the maximum compression of various ball types. The compression area is seen to increase with velocity, although the rate of increase is lower at greater velocities and is said to approach a maximum compression value. The relationship between velocity and stopping distance is described as linear, up to some maximum value, however the limited velocity range prevents meaningful conclusions being drawn. It is also suggested that the force during impact will be concentrated at the centre of the contact area and so this method may not be accurate in predicting injury. Cross (1998) suggests the construction of a piezo array to measure the impact force over the contact area.

Levendusky, Armstrong et al. (1987) investigated force profiles for moulded and stitched soccer balls to determine injury potential from heading the ball. Balls were dropped onto a force plate from a height of over 18 meters to achieve realistic velocities, but ball asymmetry and aerodynamic effects required around 75 drops to record five useful impacts. The lack of published data relating injury to the parameters measured restricts the usefulness of the work. In a further paper Armstrong, Levendusky et al. (1987) describes the effect of increasing the internal pressure and the mass, through water retention, of the balls. As would be expected, raising the pressure increases the stiffness of the ball resulting in greater impact loads and a reduced impact duration, whilst increasing ball mass similarly raised the impact force but had little effect on the duration.

Crisco, Hendee et al. (1997) present mathematical models of baseball impacts with the head and chest in an attempt to assess injury potential of various baseballs. Ball stiffness and mass both affect impact force in the mass spring damper systems. In a later paper, Hendee, Greenwald et al. (1998) statically compressed baseballs, including those which had been modified in an attempt to reduce injury, to investigate any relationship between static and dynamic properties. They found that peak impact force was proportional to ball stiffness and impulse was related to the mass of the ball. COR appeared independent

---

---

of both mass and stiffness and so it was suggested that, through careful material selection, balls may be constructed that display similar rebound characteristics yet impart substantially reduced forces during impact. Johnson, Reid et al. (1973) use three increasingly complex models to predict the rebound of an association football and compare their results to experimental data. The theory fits the experimental data well, especially the third order approximation, but there is a small and constant difference due to the model not including all energy losses. The increasing internal pressure during contact is suggested to be the main factor in impact behaviour of hollow balls. Dowell and Krebs (1991) investigated the compression of various balls at different velocities and found the relationship to be linear. They define coefficients of compressibility, which are simply the gradients of the plots of velocity against compression.

Hocknell, Jones et al. (1996) present a method whereby large elastic deformations may be measured during impact, in this case a golf shot, using laser vibrometry. Values of lateral ball deformation as well as ball and clubhead velocity are measured and ball compression may be calculated, allowing an estimation of the contact area to be made. In a later paper, Hocknell, Jones et al. (1998) use this data to verify a finite element model of a golf ball and clubhead impact. Close agreement is seen between ball lateral deformation and rotational velocity.

Pauchard and Rica (1998) present a discussion of the compression of spherical shells, based on Hertz law. By statically compressing half table tennis balls a transition deformation is identified at which point the shell buckles and the contact area inverts. It is suggested that once this occurs, then the dissipated energy is a function of the friction coefficient. Finally, the effect of a localised load on a table tennis ball is presented and is seen to promote polygonal buckling patterns within the contact area. However, it is doubtful that the ball would be subject to such a loading condition during play.

---

#### 1.8.1.6 Surface Waves

Bridge (1998[b]) presents an improvement to his earlier model for the impact of a hollow pressurised ball with a rigid surface. Surface waves are again described, travelling at 30m/s around the ball and it is these waves which are suggested to be responsible for the transfer of momentum during impact. He also suggests that the rebound is due to an upward pull from the rest of the ball, which accounts for some loss of energy. However, it is the strongly damped surface waves which are indicated as the major cause of energy loss. A computer model is described, which has been generated using finite element techniques to investigate impact conditions. The model takes into account internal pressure, elasticity, surface waves and damping. It is interesting to note that during the initial stage of impact the cross section of the ball is simply a circle intersecting a plane, with the edges of the contact area not developing curvature immediately. This corresponds to the initial high stiffness suggested by Cross. It is also noted that the model includes no hysteresis effect. Unfortunately there is no experimental evidence to support these suggestions.

---

### 1.8.2 Oblique Impacts

Oblique impacts are significantly more complicated as they involve both horizontal and vertical components of velocity, as well as friction effects between the ball and the surface in the horizontal direction. The ball may also possess spin before the impact and will generally always be spinning after the impact. Daish provides a basic model for oblique impacts but assumes that both the ball and the surface are perfectly rigid. He suggests that the spin of a ball will determine the speed and angle of rebound, with a topspin ball rebounding lower and faster and a backspin ball rebounding higher and slower. It is also suggested that with enough topspin, a ball may have a higher rebound speed than the incident speed and that if there is enough backspin, the ball will change its horizontal direction and bounce backwards. Finally, it is suggested that a ball with no spin will rebound at the same angle as it was incident. Whilst this case is possible, it is highly unlikely as the rebound angle is a function of not only spin but also of the coefficients of restitution and friction between the surface and ball. Brancazio (1981) uses simple energy equations to show how a basketball shot with backspin is more likely to go in due to losing more energy on impact compared to shots with topspin or no spin at all. However, he makes many assumptions such as perfect elasticity in the normal direction and zero deformation of the ball or surface during impact. Andrews (1983) develops a mathematical model for the collision of a rough elastic ball with an inertial surface using a torsional coefficient of restitution. This model is applied to the handball hop serve and shows that the ball must be served with a component of spin about a horizontal axis in line with the service direction to produce greatest hop.

In order to investigate oblique impacts experimentally, the ball must be projected at the surface at some angle of incidence either with or without spin. Most researchers have used either a ball cannon or bowling machine, although Dunlop, Milner et al. (1992) describe a method by which the incident and rebound velocities are more easily measured. The ball is dropped vertically onto a rotating drum, which is covered with a sample of playing surface. The horizontal point of impact on the drum is varied until the ball rebounds vertically along the same line, so that the ball bounces at some angle

---

relative to the drum, given as the tangent to the drum at the impact point. The initial and rebound heights can be measured and converted to velocities, which together with the tangent angle give the equivalent incident and rebound angles. Unfortunately it is not possible to investigate angle and velocity independently using this method. Brody (1990) also notes that gravity is acting upon the ball but even at low speeds, around 4m/s, the acceleration due to impact is 150 times as large as gravitational acceleration and so this may be neglected. Assuming a non-deforming ball it is shown that the fractional change in the horizontal velocity is proportional to the COF and decreases as the angle of incidence decreases, assuming sliding throughout. However, as the incidence angle increases, the ball is more likely to enter a rolling mode during the impact, occurring at some minimum value of COF which is a function of incident angle and COR. Finally Brody describes a method of measuring the COF of a surface by cutting a tennis ball in half, adding weights to the inside and measuring the force needed to keep the hemisphere sliding at a constant velocity. It was noted that the contact area of the ball did not influence the COF, but the sliding velocity was not stated and the effect this has on the COF is unknown. Haake (1999) shows that the effect of increasing the diameter of a tennis ball is to increase the rebound angle, due to the increased friction of the larger contact area. The larger ball is constructed to conform to ITF rules (Type 3) and so has a similar COR to that of a standard tennis ball (Type 2). Unfortunately, the data relating to rebound angle is highly scattered such that no meaningful conclusion may be drawn. The limited number of impacts also prevents any useful statistical analysis.

#### **1.8.2.1 Friction – Rolling and Sliding**

Maw, Barber et al. (1976) investigated the impact of solid steel and rubber spheres with surfaces of the same material and using some basic assumptions attempted to model the impacts. They suggest that during impact the contact region may be divided into several annuli, each of which may or may not be slipping instantaneously. It is seen that for impacts at high incidence angles the surfaces stick until just before maximum compression. Microslip commences and the elastic strain energy dissipates in microslip.

---

---

The annulus of slip spreads inwards until gross-slip is established. At intermediate incident angles the impact commences in gross-slip and the conditions over the whole region change instantaneously from gross-slip to complete stick. The rebound phase of the impact is as above. Finally, for very shallow angles the entire impact takes place in gross-slip. Witters and Duymelinck (1986) present a simple theory of rolling resistance assuming a rigid ball and deformable surface, comparing results with experimental values taken for billiard balls. A test rig is used which comprises a ball attached to a motor to generate a constant angular velocity, being allowed to 'roll' over a surface under its own weight. The ball is kept in position by a lateral force applied through two roller bearings suspended from a frame and this force can easily be determined and converted into a coefficient of sliding friction. Gobush (1990) presents a method to determine friction forces by projecting golf balls at a three component force transducer, with strobe lights used to measure velocity and spin. Results are compared to those of a finite element model in a later paper by Chou, Liang et al. (1994) and good agreement is achieved. However the ball is modelled as a two-dimensional plain strain cylinder and model parameters, rather than being measured experimentally, are selected to best fit the data.

#### **1.8.2.2 Impact Characteristics**

Dowell, Smith et al. (1987) describe the effect of angle of incidence on rebound angle. A variable 'angle of deviation' is defined as the difference between the angles of rebound and incidence. Over the range of  $10^{\circ}$ - $70^{\circ}$  it was found that for impacts with no initial spin, the angle of rebound was always greater than that of incidence. The angle of deviation increased with angles of incidence from  $0^{\circ}$ - $35^{\circ}$  to a peak value of  $11^{\circ}$  and then decreased for angles greater than  $35^{\circ}$ . Theoretically the angle of deviation would be zero at  $0^{\circ}$  and  $90^{\circ}$  incidence. Smith (1990) performed a statistical analysis on his theory that  $AD = AI + VI + RI$ , where AD is again the angle of deviation and AI, VI and RI are angle, velocity and rotation of incidence respectively. It was found that whilst AI and RI were significant, VI was not and so he presents his final model as  $AD = 20.7065 -$

---

$(0.2525*AI) - (0.3310*RI)$ . However, this model can only account for 80% of the variation in AD.

Haake (1995) developed a finite element model to investigate ball and turf impacts in golf. Whilst the model agrees well with experimental data for impacts with a steel plate, the turf impacts show a 10% difference in velocity. It is not known if this is constant as only a small range of impact angles are investigated, these being  $60^{\circ}$ ,  $65^{\circ}$  and  $70^{\circ}$ . It is suggested that the error is due to an underestimated friction coefficient, as the values were simply taken from literature. Also, whilst spin during impact was modelled, it was not compared to experimental data and so should be viewed with caution.

Hope, Dowell et al. (1988) introduce the term 'velocity deviation' as the difference between rebound and incident velocity and generally having a negative value. The effect of changing angle of incidence on velocity deviation is investigated for three incident velocities of 50, 70 and 100 ft/s. It was found that the peak velocity deviation occurs at two incident angles, one greater than  $45^{\circ}$  and one less than  $45^{\circ}$ . As the incident velocity increases these angles approach  $45^{\circ}$  and so it is suggested that for a theoretical impact of infinite speed, there will only be one maximum velocity deviation, occurring at  $45^{\circ}$  incidence.

Little is written on the effects of spin, although coaching books by Groppe (1992) and Anderson (1982) both briefly describe similar effects to those already covered by Daish. That is, topspin will tend to cause the ball to bounce lower and quicker than with no spin and backspin will tend make the ball bounce slower and sit up. However if the angle of impact is sufficiently shallow that the ball slides, then it has been observed to rebound lower than it was incident. During play, balls that have heavy topspin may appear to bounce high, as the aerodynamic effect of topspin is to increase the impact angle. This will increase the vertical rebound velocity and although the horizontal velocity is also greater than for a shot with no spin, the ball will approach the player more quickly and with a higher overall trajectory. Conversely, balls with backspin will generally impact the court at shallower angles.



---

### 1.8.2.3 Models of Oblique Impacts

Johnson and Lieberman (1994) present a torque based parametric model for oblique impacts. Normal forces are calculated from multi-component mass spring damper models described in a previous paper (Lieberman and Johnson, 1994) and related via a COF. However, the parameters in the torque model may only be estimated so as to match previous data. Duery (1994) presents a model developed to predict the trajectory and bounce of table tennis balls. Of particular interest is his 'spin parameter' which is defined as the ratio of the velocity of a peripheral point on the ball to the velocity of the centre of gravity of the ball. It follows then that spin parameter is positive for topspin, zero for no spin and negative for backspin. A plot is given of spin parameter against impact angle which shows regions of sliding and rolling. Haake and Goodwill (1998) investigated the rebound of pressureless, low pressure and high pressure balls, although no indication is given as to the difference between low and high pressure balls. Ground strokes were analysed to find pre-impact conditions comparable to those in play. Tests were carried out at 20m/s and 25m/s at both 20° and 25°. It was found that the rebound conditions were almost the same for the high and low pressure balls but that the pressureless balls rebounded lower and faster in all cases. This is caused by the pressureless ball deforming less during the impact so the frictional force is lower throughout, giving a higher horizontal velocity. In a similar paper by Goodwill (1997) again using three ball types, it is noted that the lower deformation of the pressureless ball is responsible for less spin being generated during the impact than for the other two balls.

---

## 1.9 Sports Ball Aerodynamics

Whilst the flight of the ball is not the concern of this work, the subsequent effect of rebound characteristics upon ball behaviour should be appreciated. For this reason, a brief discussion of the forces exerted on a ball due to relative motion through a viscous medium is presented.

There are two component forces that may act on a ball as it travels through the air; these being lift and drag. Drag acts against the direction of relative motion and is proportional to the velocity and radius of the ball. Its effect is generally seen in a reduction in the distance that the ball travels through the air as it falls under gravity. Lift force acts perpendicular to the direction of travel and occurs due to the spinning of the ball as noted by Rayleigh. However the mechanism by which both these forces act was not fully understood at the time. It has since been shown Metha (1985) that the spinning ball results in asymmetrical boundary layer separation points and a pressure differential across the ball, resulting in a lateral force. Stepanek (1988) showed that the drag and lift coefficients of a tennis ball both increased with spin rate, whilst Metha showed similar effects for golf balls, although interestingly drag coefficient reduced with spin for velocities below 30m/s at spin rates of less than 4000rpm.

Metha states that Prandtl introduced the 'boundary-layer' concept in 1904, whereby a velocity gradient exists within a thin layer of fluid adjacent to the surface of the ball. This layer may be either laminar, where the velocity gradient is smooth and the resulting layer is thin, or turbulent, where the layer is much thicker and contains vortices. Whilst the laminar layer is much smaller and more uniform, it easily becomes separated from the ball as it travels around its surface. The turbulent layer is much less sensitive to pressure gradients and so remains attached over a much greater proportion of its surface. A trailing 'wake' develops from the separation points and is primarily responsible for the drag on sports balls. As the turbulent boundary layer separates further round the ball its associated wake is narrower and hence the drag force is lower.

---

---

Transition between these two states occurs at what is termed the critical Reynolds number, which is a function of flow velocity and ball radius, or may be tripped by a discontinuity in the surface of the ball. Achenbach (1972) identified four regimes of flow as subcritical, critical, supercritical and transcritical based on their Reynolds number and noted that the drag coefficient falls sharply within the critical regime. Metha (2001) showed that the flow around a tennis ball was within the transcritical regime with the cloth cover causing early transition and thickening of the boundary layer. However, Metha also found that the drag coefficient increased with decreasing Reynolds number, contrary to the theory of turbulent flow. Through close inspection of various tennis balls in a wind tunnel, it was proposed that the increased drag was due to the fuzzy nature of the cloth cover. At lower flow speeds, the fuzz lifted from the surface of the ball, effectively projecting hundreds of small cylindrical elements into the flow, each of which had its own drag component. At higher flow speeds the fuzz was flattened against the ball and hence the drag coefficient was reduced.

It was noticed by early golfers that a scored or marked ball flew further than a smoother new ball, which generally only carried around 100 yards. This led to the development of the modern balls, which are covered in a number of dimples and can carry over 250 yards. The dimples cause turbulent mixing within the boundary layer causing it to speed up, effectively lowering the critical Reynolds number and resulting in later separation of the boundary layer. The dimples also increase the lift generated by the Magnus effect, with dimple width and depth further affecting trajectory. Modern dimple patterns are based on the regular polyhedrons, discussed in chapter 3, providing greater symmetry and thereby increasing accuracy, although some allowance must be made for a seam line to allow the ball to be constructed DSI (1988).

Metha notes that tripping the flow is a means of inducing a curving ball flight in cricket and baseball where the seam of the ball, positioned non-symmetrically to the flow, promotes premature boundary layer transition at sub-critical Reynolds numbers. One side of the ball possesses a laminar boundary layer whilst the other side has a turbulent layer and so their respective separation points are asymmetrical. This results in a similar pressure gradient and hence lateral force as occurs for the Magnus effect.

---

---

### **1.10 Suggested Research Directions**

Clearly there is considerable merit for a model that accurately predicts rebound characteristics for hollow sports balls from a given set of initial conditions. However, previous work has presented models that are capable of resolving only one or two individual characteristics. Furthermore those that are not under consideration are often subject to assumptions that reduce the usefulness of the results. The range of conditions examined is often limited and more importantly much of the modelling work has lacked experimental data to verify the accuracy of predicted values. Ideally any model should be capable of predicting the rebound characteristics from known initial conditions and should have been subject to comprehensive experimental verification.

The more promising work has attempted to apply finite element methods to model the ball-surface interaction and with the continuous advances in computer technology, this method is becoming increasingly powerful. Any number of impact characteristics may be extracted from analyses and model parameters such as mass and length are easily changed, allowing 'prototype' models to be developed quickly.

---

## 2 Research Hypothesis

From the review of previous work in chapter 1, it is clear that the need to advance knowledge in the area of sports ball impacts is best met by the design of a detailed model that will predict characteristics both after impact and during the contact phase itself. It is suggested that Finite Element Analysis will provide the most appropriate means of producing such a model. It is also seen that extensive experimental verification is necessary in order for the model to be used confidently as a predictive tool and to investigate the processes during impact that lead to the post-impact characteristics.

It is hypothesised that a detailed finite element model of the ball/surface impact will prove successful in accurately predicting post-impact rebound characteristics from any known incident condition.

Furthermore, it is expected that an accurate model will provide insight into the complex mechanisms by which balls exhibit rebound characteristics such as the coefficient of restitution and post impact spin.

It is therefore proposed that a detailed finite element model be developed for a ball and surface interaction, which will allow any type of hollow sports ball to be replicated through simple modification of the input parameters. In order to assess the ability of the model to predict impact characteristics of real balls, a complimentary program of experimental testing will be developed to verify the model, with the tennis ball used as a practical example. This ball type has a layered construction of differing materials and is probably the most complex of all hollow balls, any generic model should therefore be able to predict the behaviour of a tennis ball.

---

### 3 Creating a Spherical Model for Finite Element Analysis

#### 3.1 Introduction

##### 3.1.1 Discretising the Sphere

The surface of a sphere is a special case in that it is continuous; having no vertices and every point on it is at the same fixed distance from its centre, being the radius. Unfortunately, this provides no obvious means of discretising the surface into finite elements and it is necessary to use spherical trigonometry to provide a solution.

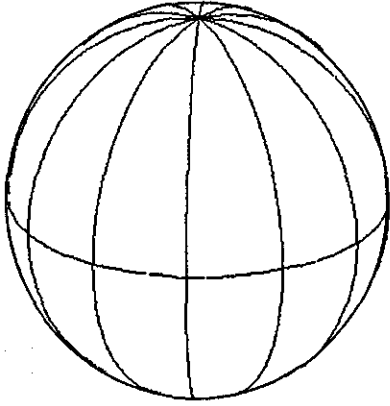
A plane may be drawn through any two points on the surface of a sphere such that the resulting section will always define a circle. Should the plane also pass through the centre of the sphere then the circle will have a radius equal to that of the sphere and is known as a *great circle* otherwise the radius will be less than that of the sphere and this is called a *small circle*. The shortest distance between two points on the surface of a sphere is the arc of a great circle, known as a *geodesic*. So long as the points are not the extremities of a diameter then there is only one great circle that can pass through them. Should the two points be diametrically opposite then it is possible to define an infinite number of great circles between them. The projection of the centre of any spherical circle perpendicularly onto the sphere in both directions provides the *poles* of that circle.

Armed with these basic definitions, it is possible to construct the first basic discrete spherical model. By defining any great circle and its poles, it is then possible to create any number of further great circles through these poles, dividing the original circle into a number of arcs of equal length, as shown in Figure 3.1a. By further dividing the hemispheres created by the original circle, using small circles with the same poles, then we arrive at our first discretised sphere, Figure 3.1b. This model is often referred to as a swept or revolved model as in reality it is commonly created by revolving a two

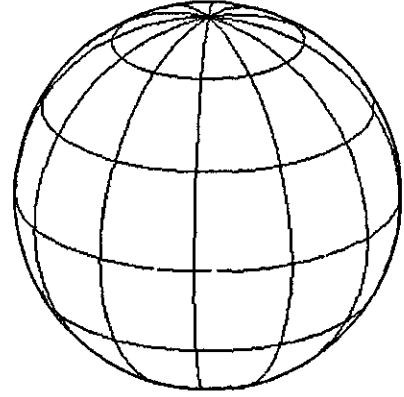
---

---

dimensional discretised semicircle through 360 degrees about its endpoints, in a number of finite steps.



**Figure 3.1 a –Great Circle Discretisation.**



**Figure 3.1 b – Addition of Small Circles.**

All further discrete models are defined using great circles only and are based on polyhedrons. A polyhedron is a solid bounded by any number of plane rectilinear faces. If all of these faces are similar and equal polygons and all solid angles are equal then the polyhedron is regular. As it is desirable to have a model that is symmetrical in rotation then we shall restrict our interest to these regular polyhedrons.

Any regular polyhedron is composed of a number of vertices  $V$ , faces  $F$  and edges  $E$ . Suppose we create a sphere of radius  $r$  with its centre anywhere within the polyhedron and draw lines from this centre through the vertices of the polyhedron to the surface of the sphere. If these points on the sphere are joined by great circles then the surface of the sphere is divided into as many polygons as the polyhedron has faces. Let  $s$  denote the sum of the angles of any one of these polygons,  $m$  the number of its sides, then the area of the polygon can be shown to be  $r^2\{s-(m-2)\pi\}$ . The sum of the areas of all polygons is the surface area of the sphere, i.e.  $4\pi r^2$ .

---

---

Hence, since the number of polygons is  $F$ , then:

$$4\pi = \sum s - \pi \sum m + 2F\pi$$

Equation 3.1

$\sum s$  denotes the sum of all the angles of the polygons, and is therefore equal to  $2\pi$  times the number of vertices, i.e.  $2\pi V$ .  $\sum m$  is equal to the number of all the edges of all polygons, i.e.  $2E$ , since every edge gives rise to an arc common to two polygons. Substitution into Equation 3.1 gives us:

$$\begin{aligned} 4\pi &= 2\pi V - 2\pi E + 2F\pi \\ \therefore V + F &= E + 2 \end{aligned}$$

Equation 3.2

Also, if  $n$  is the number of plane angles at each vertex then the number of plane angles in the polygon is  $mF = nV = 2E$ . Substitution into Equation 3.2 then leads to:

$$V = \frac{4m}{2(m+n) - mn} \quad E = \frac{2mn}{2(m+n) - mn} \quad F = \frac{4n}{2(m+n) - mn}$$

These expressions must be positive integers and so  $2(m+n) > mn$ .

$$\therefore \frac{1}{m} + \frac{1}{n} > \frac{1}{2}$$

Equation 3.3

As  $n$  cannot be less than 3, then from Equation 3.3 we see that  $\frac{1}{n} < \frac{1}{3}$  and hence  $\frac{1}{m} > \frac{1}{6}$ .

Also,  $m$  must be an integer and cannot be less than 3 either, so that the only possible values of  $m$  are 3, 4, and 5. Further, it can be shown that the only values of  $m$  and  $n$  that

---



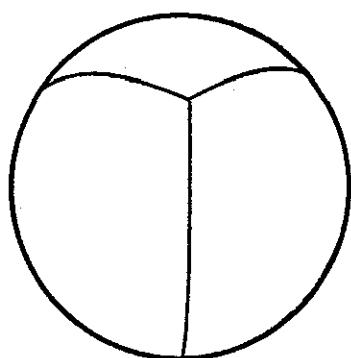
satisfy all conditions are those given in Table 3.1. The name of each regular polyhedron is derived from its number of plane faces.

<i>m</i>	<i>n</i>	V	E	F	Name of Regular Polyhedron
3	3	4	6	4	Tetrahedron (regular pyramid)
4	3	8	12	6	Hexahedron (cube)
3	4	6	12	8	Octahedron
5	3	20	30	12	Dodecahedron
3	5	12	30	20	Icosahedron

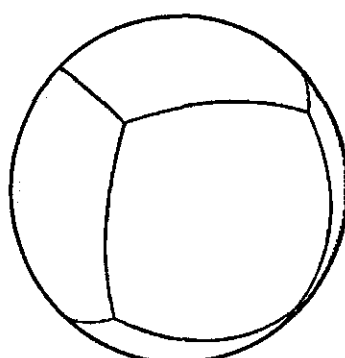
**Table 3.1 – Construction Values for the Five Regular Polyhedrons.**

Having determined this list of five regular polyhedrons, it is now necessary to consider their construction on the surface of a sphere. It is possible to define a sphere such that all vertices of a regular polyhedron are points on its surface. The shortest path between each pair of vertices is then the arc of a great circle. If these arcs replace all edges then we have created a spherical polyhedron. Another way to visualise this transformation is as a central (gnomonic) projection of the edges of the polyhedron onto its circumscribing sphere. The five basic spherical polyhedrons are shown in Figure 3.2 overleaf.

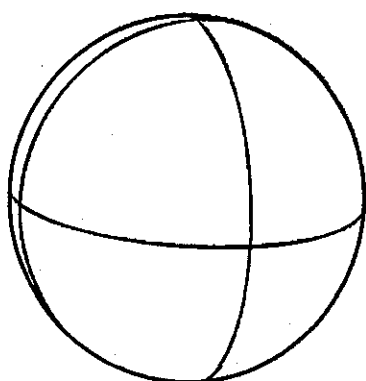
By joining the face in-centres of each polyhedron using great circle arcs then we describe its *dual* as shown in Figure 3.3. It is clear that the dual of a hexahedron is in fact an octahedron, and vice versa. Also, the dual of a dodecahedron is an icosahedron, whilst the dual of a tetrahedron is simply another tetrahedron.



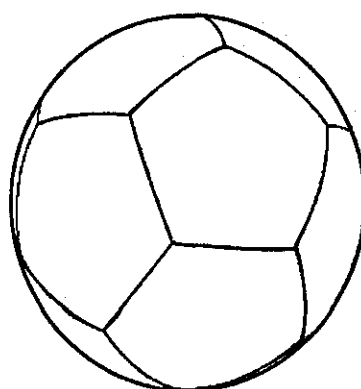
**a – Tetrahedron**



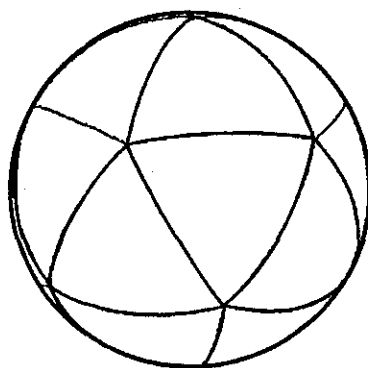
**b - Hexahedron**



**c – Octahedron**

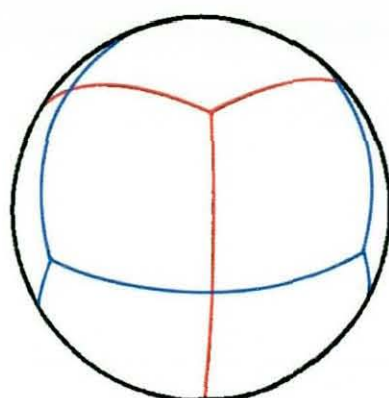


**d - Dodecahedron**



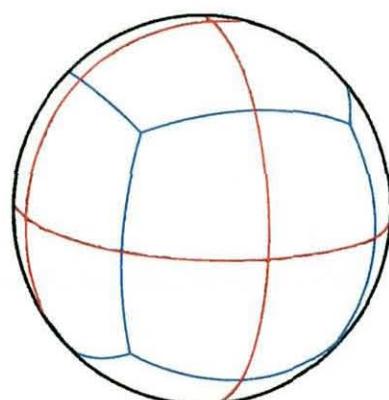
**e - Icosahedron**

**Figure 3.2 – Regular Spherical Polyhedrons.**



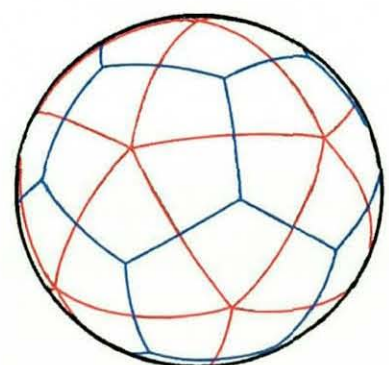
- Tetrahedron

- Tetrahedron



- Hexahedron

- Octahedron



- Dodecahedron

- Icosahedron

**Figure 3.3 – Duals of Regular Polyhedrons.**

---

### 3.1.2 Spherical Meshes

If we first consider the tetrahedron, it is clear that with only four faces, each would have to be divided much further still in order to construct a viable mesh. In addition, with only four vertices, it is limited in its rotational symmetry which makes the tetrahedron undesirable.

The hexahedron with six faces provides a more refined model. It is simple to visualise and construct, and as a result has been used in research varying from golf ball impact analysis (Haake, 1995) to weather forecasting (Ronchi, Iacono et al., 1996). It also needs further refinement to be used as a model. By dividing the faces along the lines of symmetry through their edges we arrive at its dual, the octahedron and so it is only necessary to use a single model to represent both spherical polyhedrons. It may also be shown that the octahedron can be further subdivided to produce the revolved model previously defined (Figure 3.1b).

The icosahedron with twenty faces is the most complex geometry. Subdivision by symmetry provides its dual, the dodecahedron. However, these two models are not interchangeable as are the hexahedron and octahedron. Whilst the dodecahedron provides better rotational symmetry with its twenty vertices, the triangular faces of the icosahedron provide a simpler model definition that is more suited to finite element analysis. This geometry has also found use in weather forecasting (Sahr and White, 1998) and golf impacts (Hocknell, Jones et al., 1998).

Through elimination by symmetry (duals) and complexity, it is seen that there are in fact only three individual constructions that need to be considered for a discretised spherical model.

---

### 3.1.3 Element Selection

Having discretised the sphere, element selection must now be considered and it is necessary to decide whether to use shell or solid elements.

Shell elements are desirable as they are computationally efficient and provide a good representation of a thin hollow sphere. They are defined as either 3 node triangles or 4 node quadrilaterals, using a specified thickness parameter as the third dimension, seen in Figure 3.4.

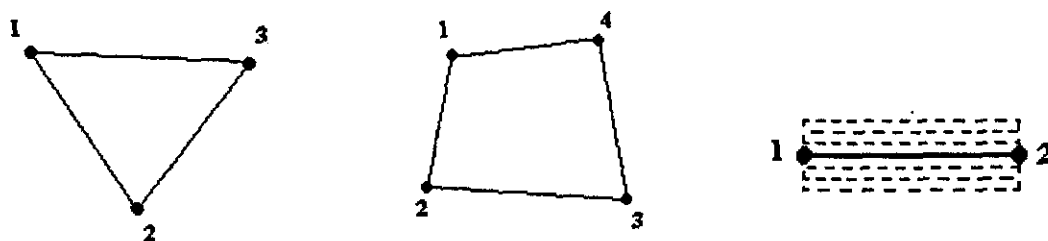
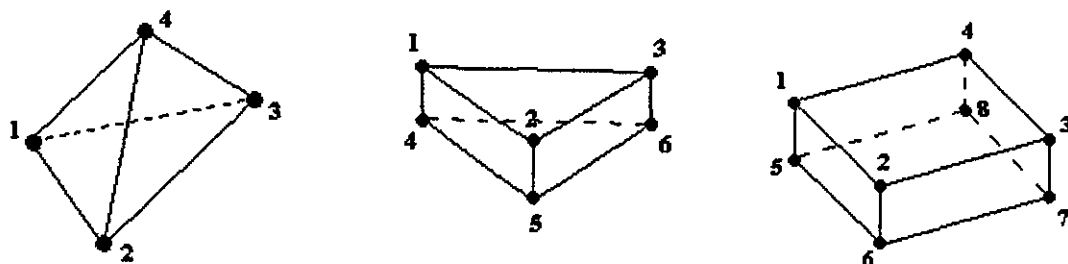


Figure 3.4 – Two Dimensional Shell Elements and their Computational ‘Thickness’ Layers.

Shell elements are of use when the thickness is small compared to the other dimensions. For example, Baran (1988) suggests that shell elements be used to model pressure vessels where the ratio of outer radius to thickness,  $r_o/t_h > 10$ . In general, shell elements are suitable when the thickness is no more than 10% of the other dimensions and this condition is only met by a very coarse mesh. As it is refined, the thickness ratio drops considerably and so shells become no longer suitable.

Solid elements may be either two or three dimensional. 2-D elements are desirable as they are computationally efficient, however they may only be used where loading is limited to the defining X-Y plane. This rules out their use in bending problems.

3D solid elements are not so limited in their application. The section thickness is represented physically and so the elements become building blocks. These elements can be hexahedra (bricks) with 8 nodes, 6 node triangular prisms (wedges) or 4 node tetrahedra, seen in Figure 3.5. These elements are most suited to the situation where all edge lengths are similar and so are more appropriate to higher density meshes than shell elements.



**Figure 3.5 – Three Dimensional Solid Elements.**

As the application in this instance is concerned with a high speed impact analysis, first order reduced integration elements must be used. These elements have a single integration point, the point at which stresses are calculated within the element, situated at the geometric centre. First order full integration hexahedral elements have eight integration points, located near to the element corners, equidistant from the three nearest faces. The location of four of these points, nearest to the front face of the hexahedral element in Figure 3.5, is shown in Figure 3.6.



**Figure 3.6 – Integration Points for a Fully Integrated First Order Brick Element (front view) and the Associated Shear Locking Phenomenon.**

These elements are not available within explicit analyses as they can display a phenomenon known as 'shear locking' whereby the element is constrained in the bending mode and hence is subject to artificial shear stress at the integration points (Figure 3.6). This causes the element to behave much stiffer than it should, giving inaccurate results. Second order accuracy elements can be used to overcome this problem, as shown in Figure 3.7, but the increased number of nodes per element greatly increases computation cost.



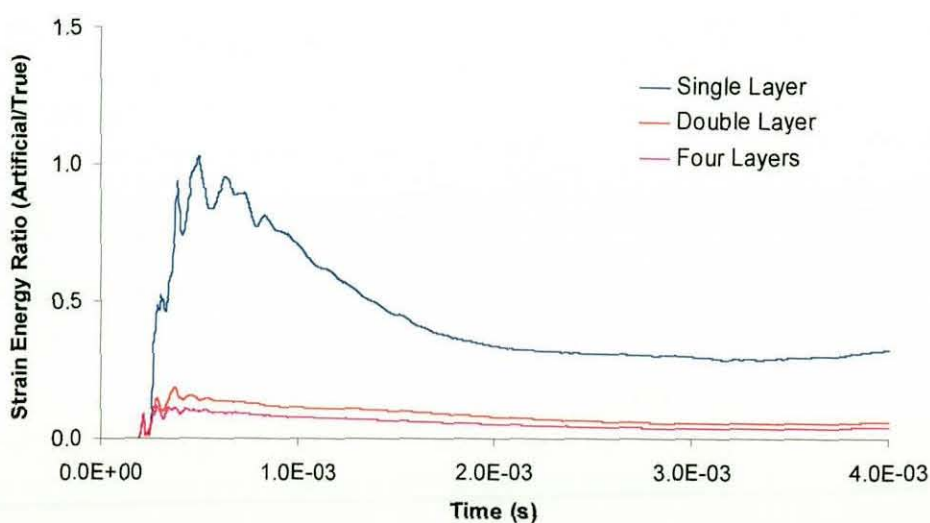
Figure 3.7 – Second Order Brick Element Definition and the Resolved Bending Problem.

Using a single layer of first order reduced integration solid elements to model the ball can introduce a new problem, known as *hourglassing*. For a single element in bending, it is possible that the tensile load in the outer surface can be equal to the compressive load on the inner surface and so the neutral axis will be located through the integration point, giving zero strain (Figure 3.8 overleaf). Hence for this bending case the software will predict zero stress. This leaves out of balance loading in the system which must be countered by the addition of some value of artificial strain energy. Furthermore, as each element is susceptible to this mode of deformation, it can quickly propagate throughout the model, raising the levels of artificial strain energy unacceptably. Even well designed analyses are subject to some degree of hourglassing and in general it is considered insignificant if the artificial strain energy is less than 1% of the value of other typical energies, such as the true or recoverable strain energy. For a basic single layered sphere model, the ratio is nearer 30%, which is unacceptable.



**Figure 3.8 - 'Hourglassing' Associated with Reduced Integration Elements, and the Same Problem Using Two Element Layers.**

The problem can be reduced greatly by introducing a second layer of elements, also shown in Figure 3.8. In this case it can be seen that the outer layer captures the majority of the tensile loading whilst the inner layer is subject mostly to compression, depending on the instantaneous location of the neutral axis. This reduces the strain ratio to below 5% for much of the impact, which whilst still high is acceptable. It is seen in Figure 3.9 that using four elements through the thickness fails to provide much improvement and doubling the number of elements in the model is severely detrimental to the computation cost.



**Figure 3.9 – Strain Energy Ratio for Balls Modelled with an Increasing Number of Element Layers.**



---

### 3.1.4 Initial Model Definition

Section 3.1.3 highlights the need to use a double layer of elements through the ball thickness to enable the software to accurately predict impact characteristics. However, the concern of this chapter is to assess the effect of mesh geometry and density on analysis results. As the model will still be incomplete with regards to material properties and internal pressurisation, the accuracy of the results compared to experimental data is not of importance at this stage. It is the comparison of results from the different models that is of interest and providing initial conditions are held constant, this is possible. Using two layers of elements in each model would greatly increase the computation cost for each analysis and with 80 of these to be run (section 3.4.1) this is undesirable. Hence all the models will be constructed initially from a single layer of elements.

Whilst internal pressurisation is not of interest initially, it is noted that the software does not provide an atmosphere in which to conduct the analysis, unless one is specified. This causes the enclosed volume within the sphere to be treated as a vacuum and the lack of increasing internal pressure during impact prevents the ball from rebounding correctly and returning to its original shape. For this reason it is necessary to specify an atmosphere within the analysis and to internally pressurise the ball to atmospheric pressure. This is accomplished by lining the internal surface of the ball with two dimensional fluid elements, sharing nodes with the solid elements. These elements act as a membrane, onto which a uniformly distributed pressure load is defined. As the internal and external pressures acting on the ball are equal at one atmosphere, initial equilibrium is maintained and no further loading of the ball is necessary. The full internal pressurisation process is described in chapter 4. At this stage, the model simply represents the case of a 'pressureless' or constant pressure ball.

---

As previously noted, the rubber material properties at this stage of the modelling process are not representational of those in a real ball, but in order to allow this analysis to be carried out, a set of material parameters is needed. The determination of rubber properties at the high strain rates experienced in these analyses is discussed in chapter 5. For this stage of the model, rubber properties taken from low strain rate tensile test data are used as an approximate starting point and this data is also available in chapter 5.

---

## 3.2 Comparators

### 3.2.1 Mesh Geometry

Section 3.1.2 defines the three models of interest. From previous work, it is seen that the most common model used to represent a sphere is based on either the cube, or a revolved semicircle. Both these models are straightforward to implement within a F.E. package and are easy to visualise. However, both these models have limitations in that they are clearly non-isotropic.

The cubic model as its name suggests is based on the cube and elements near the vertices are smaller and more skewed than those near the face centres. This model is shown in Figure 3.10a and can be seen to be composed entirely of hexahedral elements.

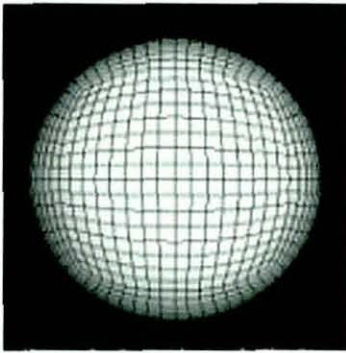
The revolved mesh has two poles from which its elements radiate, and at these points the elements are much smaller than those around the equator and are of a different type altogether. This model has only two possible similar orientations of the poles, although rotation about these poles is limited only by the number of elements around the equator. Clearly, the orientation of the model at impact will have an effect on the results obtained. This model can be seen in Figure 3.10b and is composed mainly of hexahedral elements except at the poles where each element sharing this node is a triangular prism.

In comparison, the model based on an icosahedron, as described previously, has seen less use in modelling work. It may be that the relative complexity in generating this model compared to the cubic and revolved meshes has kept it from being considered appropriate. However, it can be seen that this model appears far more applicable than both the cubic and revolved meshes. It is made up entirely of 6 node wedge elements as can be seen in Figure 3.10c.

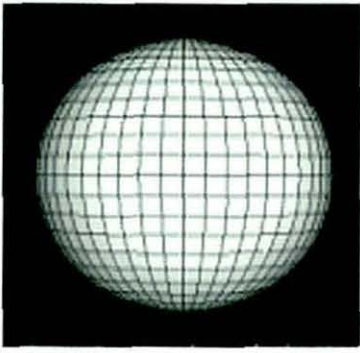


---

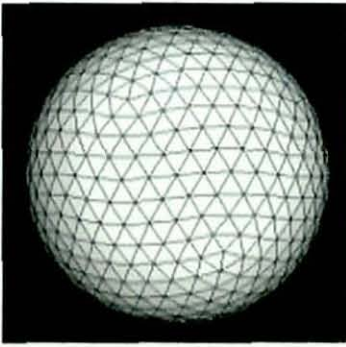
It is also of interest to know if the geometry of the cloth ‘dumbbells’ which make up the outer layer of a tennis ball can be represented. For this purpose, the basic revolved mesh can be adapted by simply rotating one half of the mesh through 90 degrees about an axis through the equator. This last model is shown in Figure 3.10d and being based on the revolved model it is also comprised mainly of hexahedral elements with wedges located at the poles.



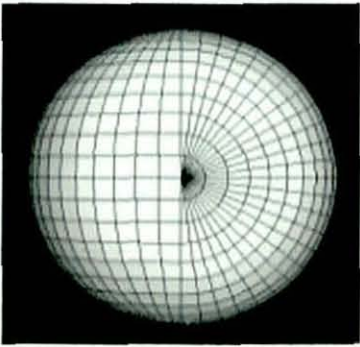
**a – Cubic Model**



**b – Revolved Model**



**c – Icosahedral Model**



**d – ‘Dumbbell’ Model**

**Figure 3.10 – Finite Element Ball Models Based on the Previously Defined Geometry.**

---

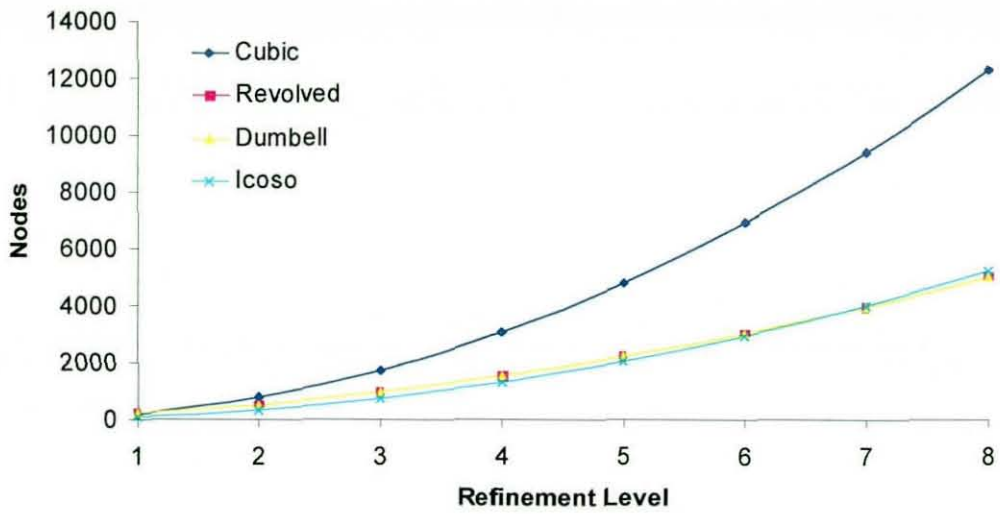
### 3.2.2 Mesh Density

With the model geometry selected, it is necessary to consider the effects of mesh density. By increasing the number of nodes along a given edge, the number of elements within the model is increased uniformly. This has the effect of increasing the accuracy of the solution, but at a cost of greater computation time. It is also seen that an increase in mesh density causes softer model behaviour, whilst in reality the material properties remain unchanged.

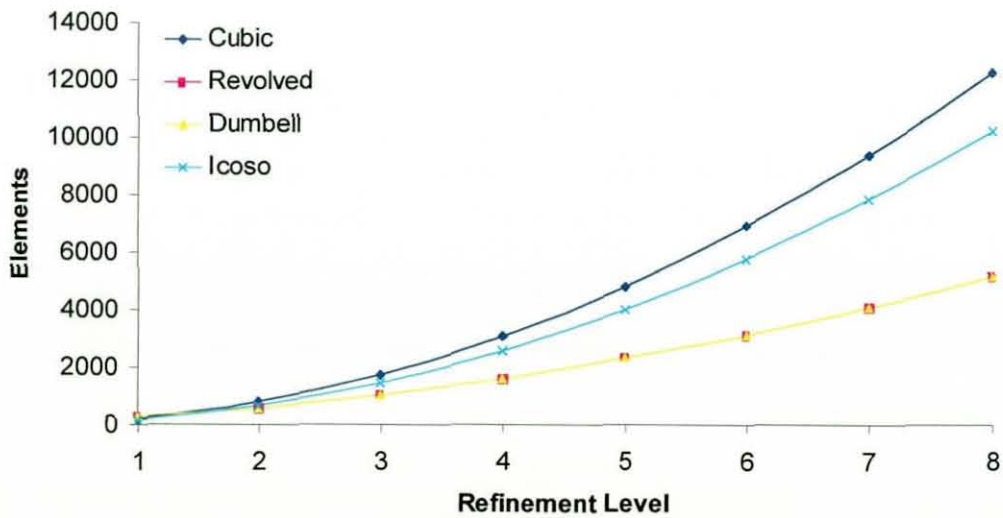
In order to assess the effects of increasing mesh density, the four models will be analysed at eight different, increasing levels of refinement, such that the average element edge length at each density level is comparable across the different geometry types. The resulting number of nodes and elements can be seen in Table 3.2, shown graphically in Figure 3.11a and Figure 3.11b overleaf.

Refinement Level	Cubic Mesh		Revolved Mesh		Icosahedral Mesh		Dumbell Mesh	
	N	E	N	E	N	E	N	E
1	196	192	228	256	84	160	228	256
2	772	768	532	576	324	640	532	576
3	1732	1728	964	1024	731	1440	964	1024
4	3076	3072	1524	1600	1299	2560	1524	1600
5	4804	4800	2212	2304	2031	4000	2212	2304
6	6916	6916	3028	3136	2926	5760	3028	3136
7	9412	9408	3972	4096	3989	7840	3972	4096
8	12292	12288	5044	5184	5212	10240	5044	5184

Table 3.2 – Nodes and Elements in Each Model.



**Figure 3.11a – Number of Nodes in Each Model.**



**Figure 3.11b –Number of Elements in Each Model.**

---

### **3.3 Variables**

#### **3.3.1 Model Deformation, Impact Duration and Restitution**

In order to assess the effects of the differing mesh types and densities on the analysis results, the models will be analysed to give results of COR, impact duration and local deformation. As previous work has reported the possibility that the whole of the footprint does not remain in contact throughout the impact then the position of the initial impact node was monitored. If contact were complete through the whole of the impact then this point would be used to instead look for possible “chattering” that can occur in contact problems.

#### **3.3.2 Computation Cost**

Of secondary interest is the computation cost for each of the models, which will be monitored, to determine the most efficient geometry. This will be measured as the true (wall clock) time taken for each analysis to run.



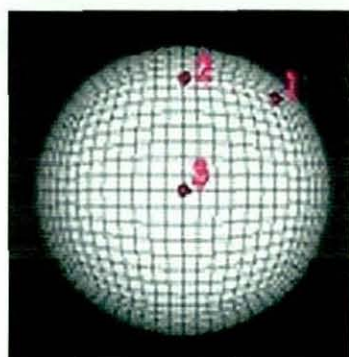
---

### 3.4 Impact Test Procedure

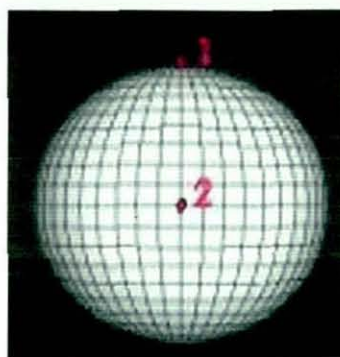
#### 3.4.1 Model Orientation

The purpose of these analyses is to determine the suitability of each of the mesh patterns for modelling an isotropic hollow sphere (tennis ball core). Consequently, it is necessary to analyse each model over a range of orientations such that all possible loci of initial impact are seen. However, if each model was to be run so that every node in turn became the initial impact point, for the most detailed mesh (level 8 cubic) with 6146 exterior nodes this would be impractical. Instead, each model is subjected to impacts such that the extremes of the mesh are used as the initial point of contact. For the cubic model, analyses are run using the vertex, edge centre and face centre in turn as the initial impact point, shown in Figure 3.12a as points 1, 2 and 3 respectively. This covers the range of possible impacts and uses the mesh symmetry to extrapolate for the whole model. For the revolved model it is only necessary to run two analyses, where the impact occurs at a pole or a point on the equator, points 1 and 2 in Figure 3.12b. Model symmetry allows extrapolation to the whole mesh. Similarly, for the 'dumbbell' pattern model, it is only necessary to run two analyses at a pole and the equator, shown as points 1 and 2 in Figure 3.12c, as these are the extreme points and all others fall within this range. Finally, for the icosahedral model, it is necessary to run analyses whereby the initial impact occurs at a corner, edge centre and face centre of one of the constructing triangles, points 1, 2 and 3 in Figure 3.12d. This equates to ten analyses at each refinement level and with eight levels there are a total of eighty individual analyses to be run.

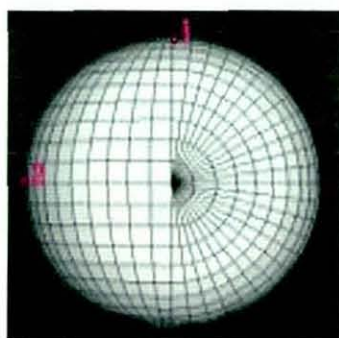




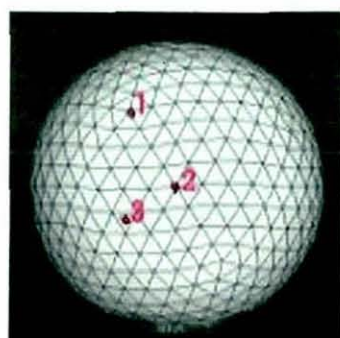
**a – Cubic Model**



**b – Revolved Model**



**c – Dumbell Model**



**d – Icosahedral Model**

**Figure 3.12 – Initial Impact Points for Each Mesh Geometry.**

---

### 3.4.2 Initial Conditions

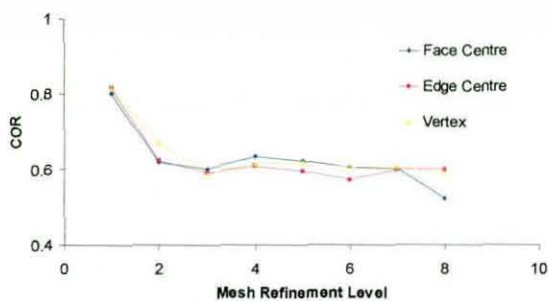
Whilst any arbitrary initial impact conditions could have been chosen, it was decided to use those specified by the ITF for their standard drop test. The ball is dropped from rest at 100 inches and allowed to rebound from a concrete surface, allowing the ball to achieve a velocity of 7.06m/s immediately prior to impact and this was used as the initial velocity in the model. As the stiffness of concrete is several orders of magnitude greater than that of rubber then it is reasonable to assume the impact surface is rigid relative to the ball, i.e. there is no deformation of the concrete. This allows us to simplify the model considerably, as no calculations are necessary for the impact surface other than to ensure the ball does not penetrate its geometry. It is simply modelled as an infinitely long surface extruded from a specified curve, in this case a single straight line.

---

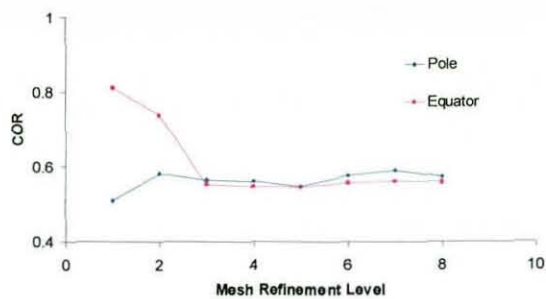
### 3.5 Results

In order to extract useful data from each model, reference points were defined at six points on the sphere, each being equidistant from four others and diametrically opposite the last. These points can be considered equivalent to the face centres of the cubic model, or the poles and quadrant intersections of the polar model. The points were moved for each impact orientation such that they always defined the vertical and horizontal extremities of the model. For simplicity, these points were named top, bottom, front, back, left and right for obvious reasons. It is then possible to request data output for mechanical and spatial variables such as strain and velocity at each point, throughout the time history of the impact.

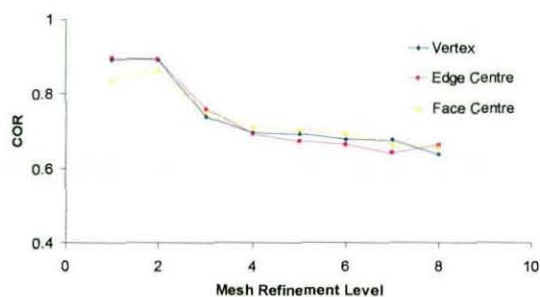
Whilst extraction of whole body velocity data from the model using the reference points is difficult due to large local variations, it is possible to determine a value using the model energy data. Whilst the kinetic energy term will initially contain a contribution due to post impact vibrations within the ball, this contribution, seen as an oscillation about some constant value in the kinetic energy history, it is acceptably small. As gravitational acceleration is not included in the definition, then following impact the model will possess a constant velocity for the remainder of its duration and correspondingly a constant kinetic energy. From the change in kinetic energy it is possible to calculate the restitution coefficient for each model. Figure 3.13 overleaf shows the CORs for the each model geometry in turn over the range of mesh refinement levels. All models show little effect due to orientation at impact from refinement level three upwards.



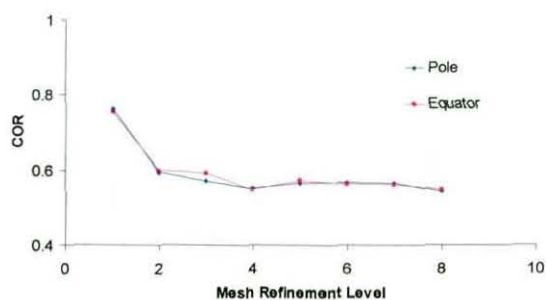
**a - Cubic Model**



**b - Revolved Model**



**c - Icosahedral Model**



**d - Dumbell Model**

**Figure 3.13 – Coefficient of Restitution for Each Model Type.**

By averaging the values for all orientations at each level, it is possible to compare the different models, as seen in Figure 3.14. It is apparent that the icosahedral model exhibits a higher COR than the others, as would be expected due to its wedge elements defining a stiffer model for the same material definition. The other models all display comparable values over the range. All models have a fall in COR as the mesh density is initially increased, although from level four upwards it appears that the change in COR for all models is low enough for it to be considered constant.

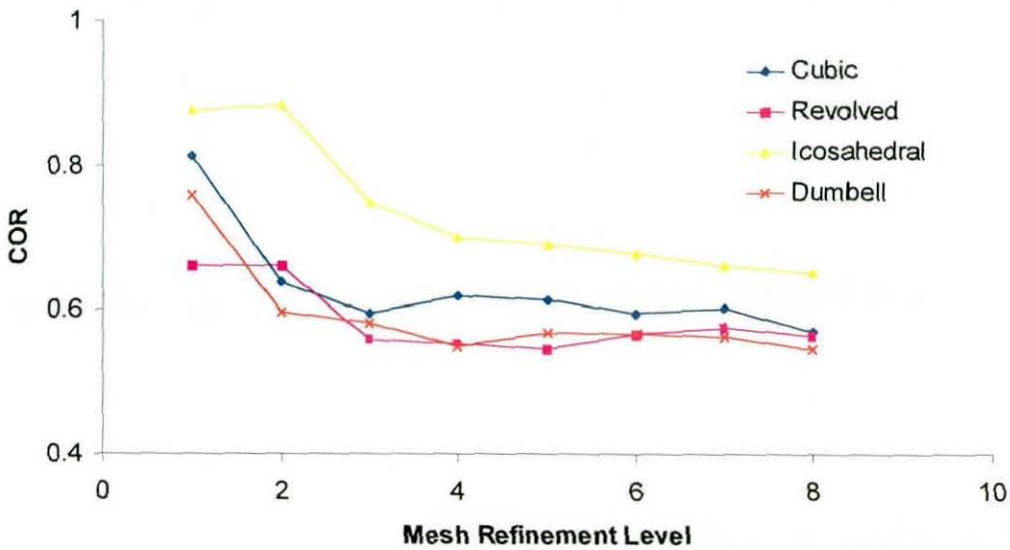


Figure 3.14 – Average COR for Each Model Type at Increasing Refinement Level.



Considering the motion of the 'bottom' reference point in each case, it is possible to determine the start and end of impact and hence the duration. This is shown in Figure 3.15 for each model and again little effect from orientation is seen at the higher refinement levels. The impact duration averaged over all orientations for each model is shown in Figure 3.16 overleaf. There is an initial rise over lower levels again indicating the tendency for apparent softening of the model with increasing mesh density. In contrast, the difference between consecutive higher refinement levels is much less.

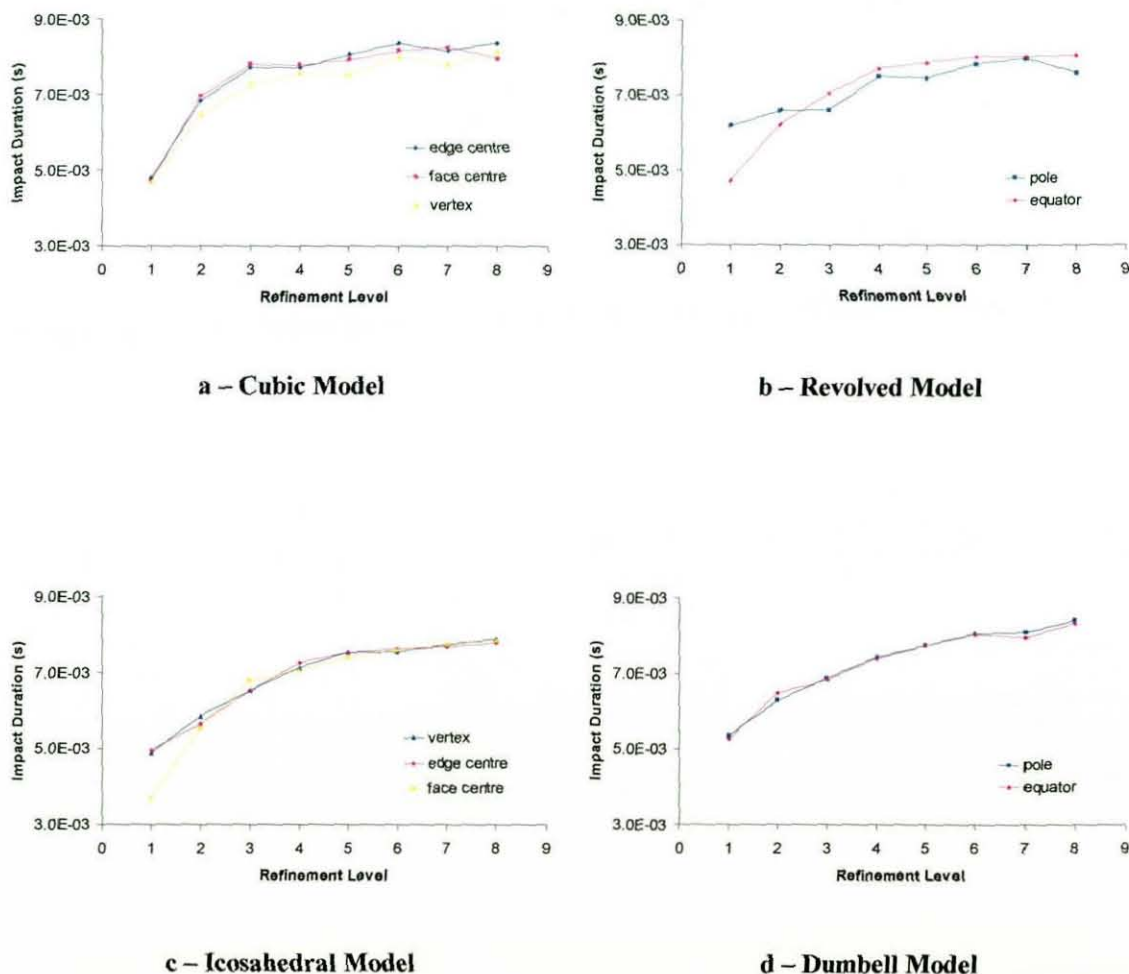


Figure 3.15 – Impact Duration for Each Model Type at Increasing Refinement Level.

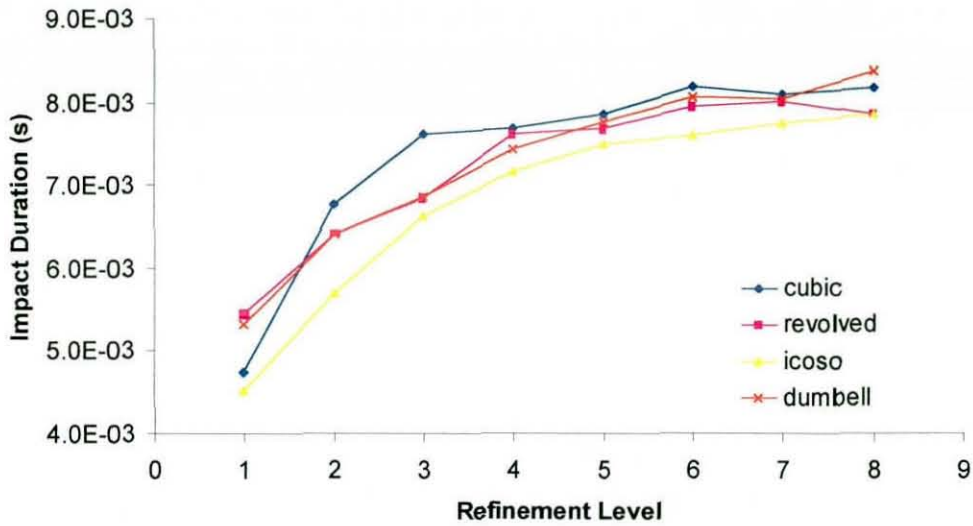
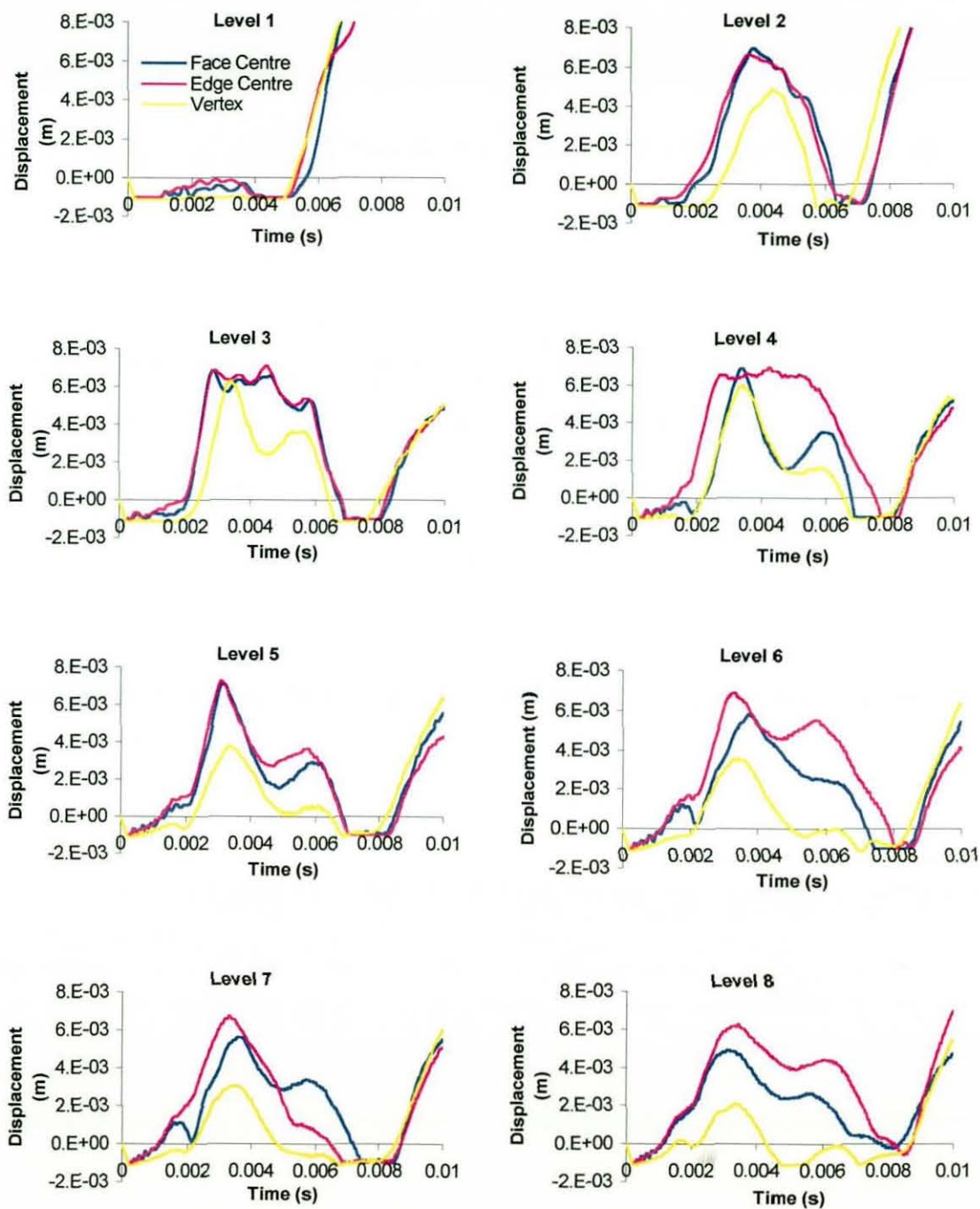


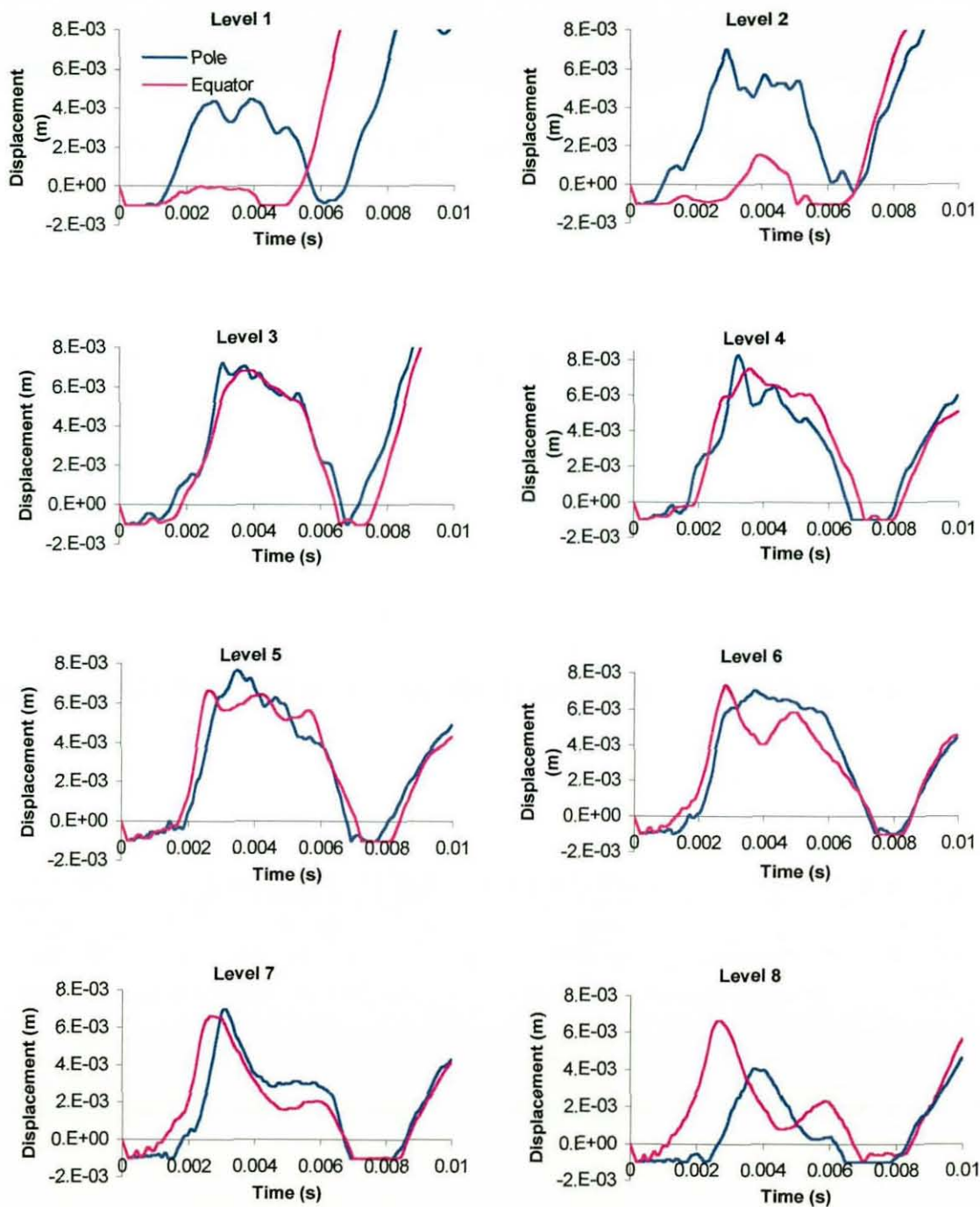
Figure 3.16 – Impact Duration for Each Model Type Averaged over All Orientations.

Figure 3.17 to Figure 3.20 on the following pages show the position of the ‘bottom’ reference point over the period of interest. All models exhibit little deformation at the coarsest mesh level, further highlighting the effect of mesh density related softening. At higher refinement levels then the maximum value of deformation for any geometry type appears similar at each level. However, the form the deformation takes differs between levels and between orientations within the same level. Whilst these differences due to orientation would limit the validity of comparing average values for different geometries, it is possible to use average displacements within a geometry type to assess the effect of mesh density. These average values for meshes from refinement levels four to eight are shown in Figure 3.21 for each mesh type in turn. It is clearly seen that the deformation pattern varies greatly for both the cubic and revolved mesh geometries whilst the icosahedral and dumbbell models exhibit similar deformations in pattern, magnitude and timescale, over the range of refinement level. It may also be suggested that the change is small enough from level six onwards that the models may be considered the same.

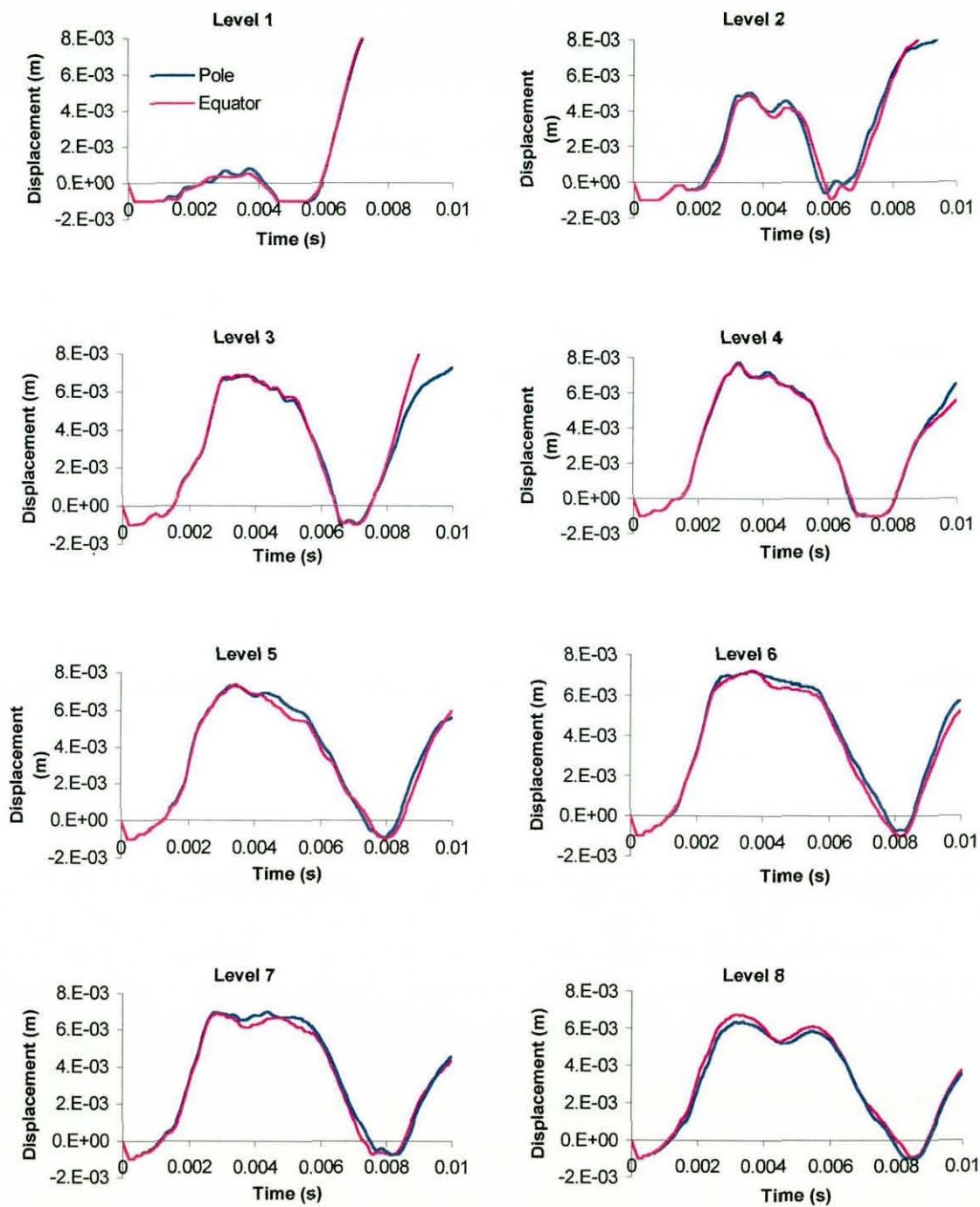


**Figure 3.17 – Displacement of Initial Contact Node During Impact for Cubic Models at Increasing Refinement Level (legend shown for level 1 only).**

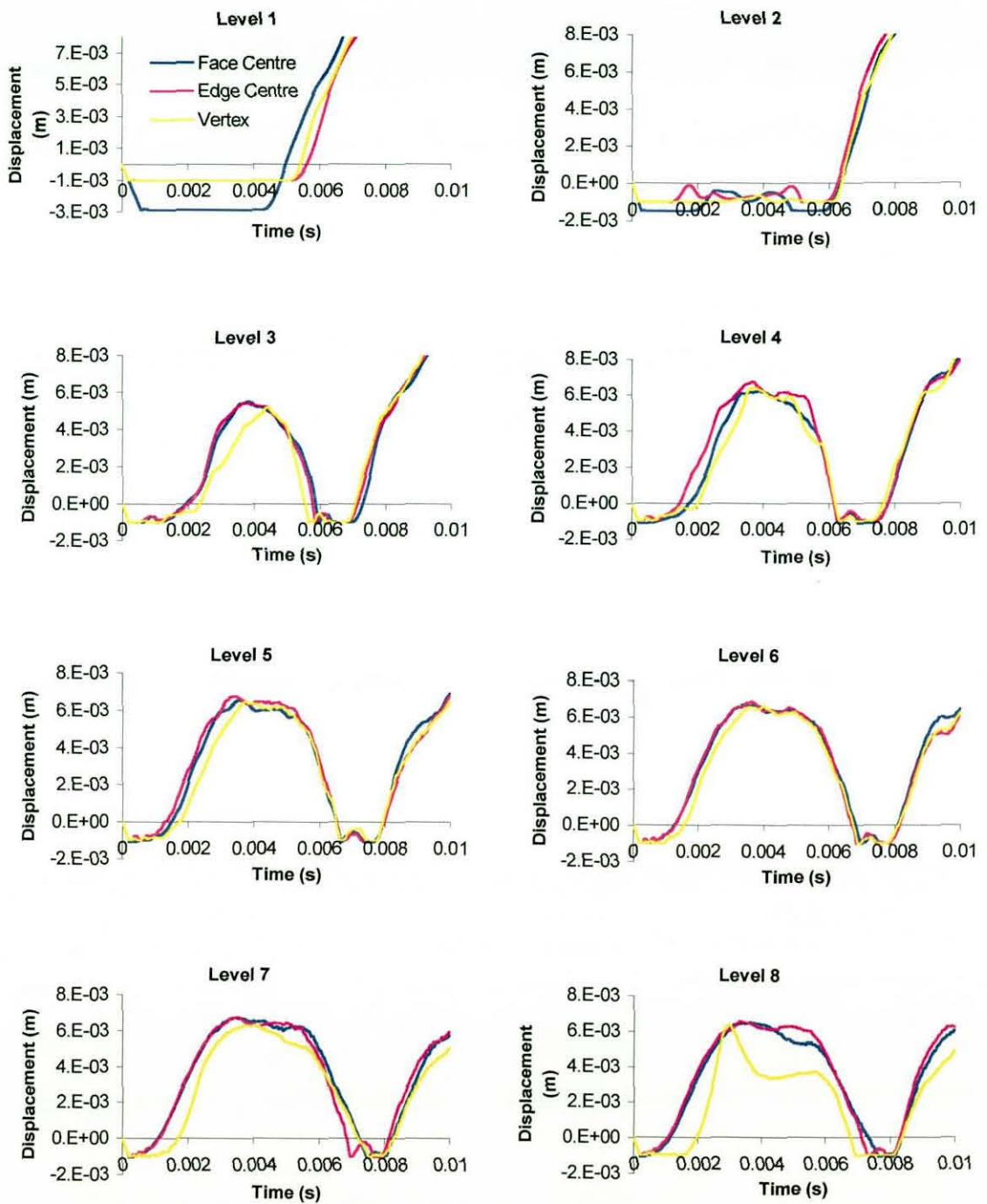




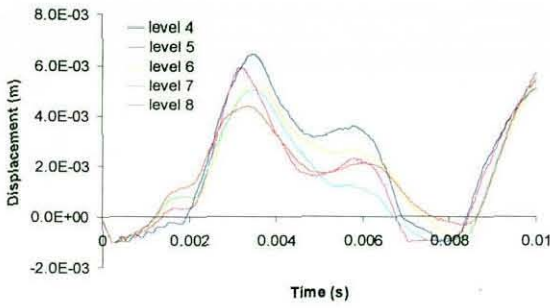
**Figure 3.18 - Displacement of Initial Contact Node During Impact for Revolved Models at Increasing Refinement Level (legend shown for level 1 only).**



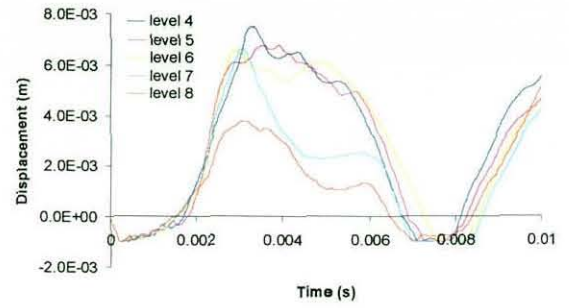
**Figure 3.19 - Displacement of Initial Contact Node During Impact for Dumbbell Models at Increasing Refinement Level (legend shown for level 1 only).**



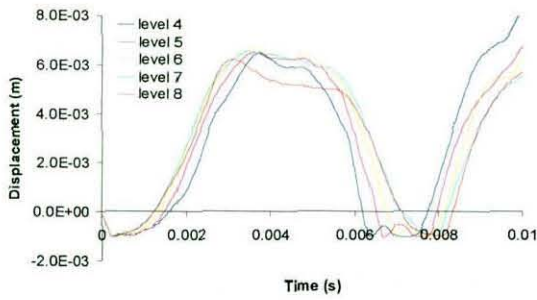
**Figure 3.20 - Displacement of Initial Contact Node During Impact for Icosahedral Models at Increasing Refinement Level (legend shown for level 1 only).**



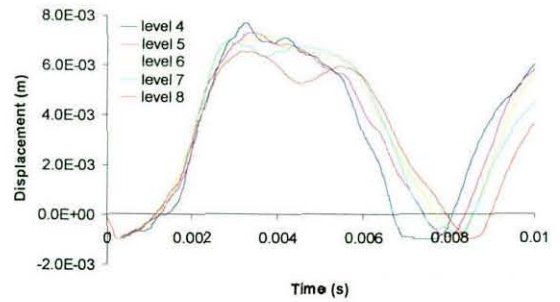
**a – Cubic Model**



**b – Revolved Model**



**c – Icosahedral Model**



**d – Dumbbell Model**

**Figure 3.21 – Impact Duration for Each Mesh Type Averaged Over All Orientations.**



Finally, in order to assess the efficiency of each geometry it is necessary to compare the computation cost of each model. The wall clock time taken for each model to complete an analysis is useful in that it is an indicator of the model complexity, but unlike other possible comparators, such as file size, it is easily visualised. The run times are shown in Figure 3.22 and each model shows an exponential increase with mesh density. Again there appears little effect due to orientation with the exception of the revolved mesh, where the difference increases with refinement level up to a maximum of over 200 seconds difference, or around 20 percent, at level eight.

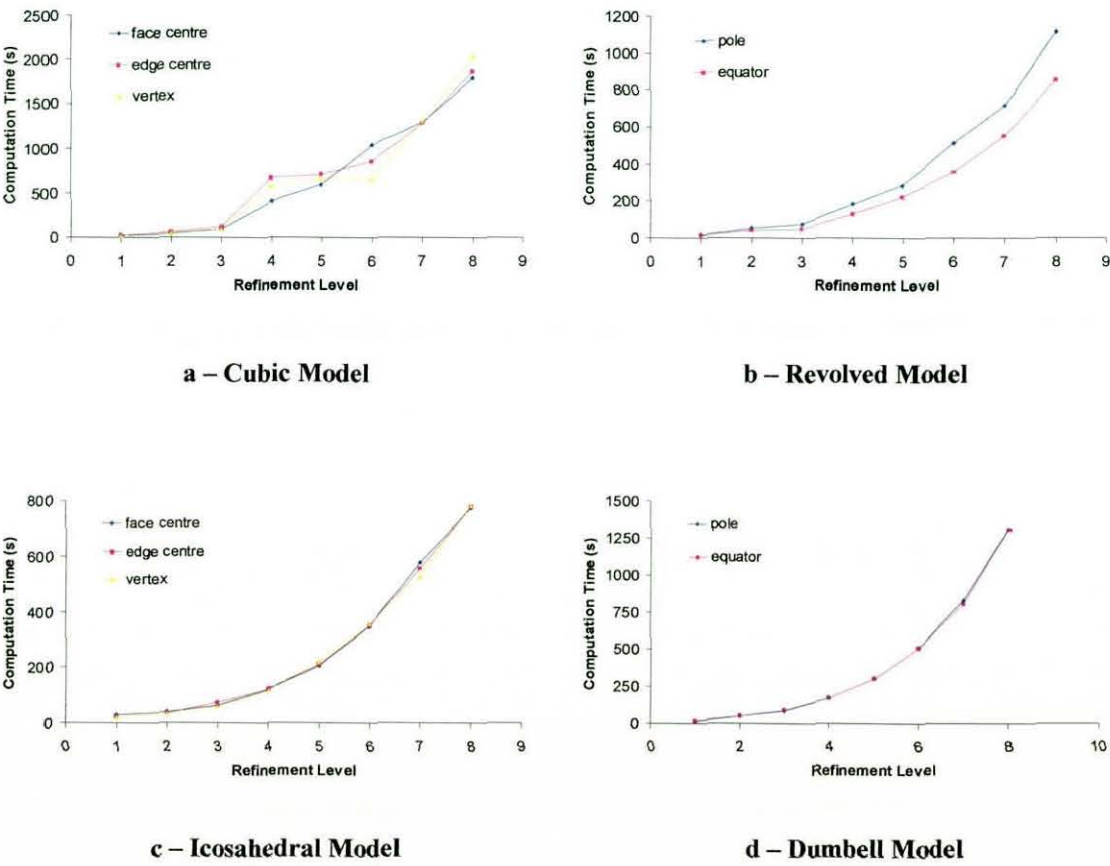
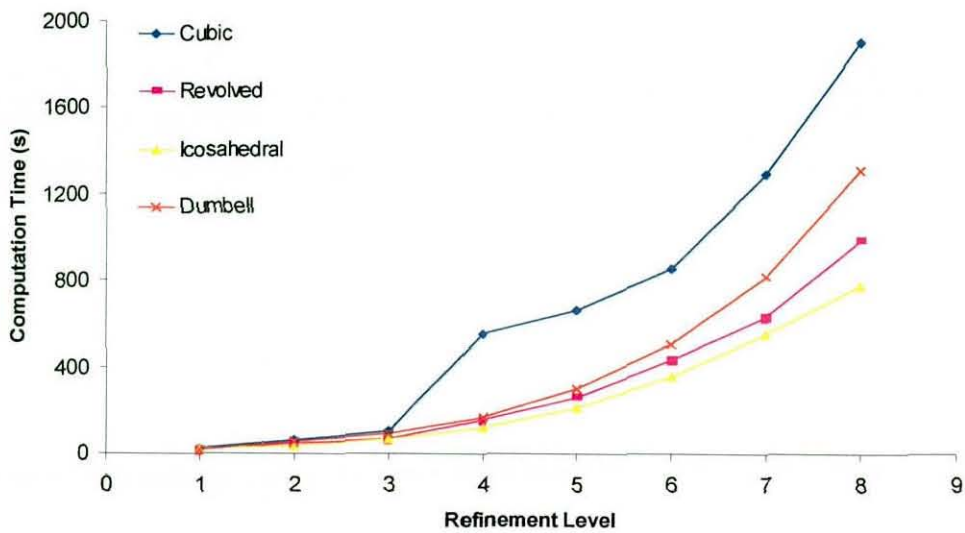


Figure 3.22 – Computation Times for Each Model Type.

Comparing the average values in Figure 3.23 it is seen that all models run in comparable times at lower levels. With increasing mesh density and hence model complexity, the curves diverge revealing the icosahedral model to be most efficient by this definition and the cubic model the least. At the highest level of refinement considered here, the analysis time for the cubic model would be more than double that of the icosahedron.



**Figure 3.23 – Computation Time For Each Model Type Averaged over All Orientations.**

---

### 3.6 Discussion

The results from these tests show a number of characteristics that enable the choice of suitable mesh geometry and density to be selected, from which the more detailed model will be developed. Regarding the COR, whilst the actual value is of little consequence to the final choice, it is reassuring that all models provide an essentially constant value at higher densities. This allows any geometry to be chosen providing the mesh density is taken from at least level four. Above this the effect of impact orientation is also negligible. If we then look at impact duration, again noting that the actual value is of little interest, we see that orientation has little effect above level four. Whilst the increase in value appears to diminish at higher level, it never truly reaches a plateau over the range of interest and so this has little bearing on the choice of a final geometry type.

It is the displacement patterns which are of greatest significance in the choice of mesh geometry, as all models show effects of orientation and refinement level to some degree. Above level four then it is clear that the dumbbell and icosahedral models are far superior to those based on the revolved and cubic meshes. The first two show little effect of geometry at the higher levels and from levels six to eight the displacements are quite similar, although for the level eight icosahedral vertex impact there is a distinct anomaly. As the displacement pattern exhibits two distinct phases during the impact it is possible that this position corresponds to a vibration node within this particular model and the deformation pattern seen is excited only under these specific conditions.

So it would appear that the model should be based on either the icosahedral or the dumbbell geometry, with a refinement level of 6. Consideration of the computation cost of each eliminates the dumbbell model as its cost at the higher levels is around 50 percent higher than that of the icosahedral model. Whilst the true time difference is only slight at around six minutes this will only increase as the model becomes more complex.

---

### 3.7 Conclusions

The geometry used to discretise a sphere for use within a large deformation finite element impact simulation has a significant effect on analysis results. Orientation of the mesh at impact has little effect on impact duration or COR providing a sufficiently fine mesh is used. However the orientation may affect local displacements if the mesh geometry is inappropriate. By increasing mesh density the solution will converge whereby at some point, further increasing density adds little more than computation cost to the model. Wedge elements create a stiffer overall model but the resulting computation cost is less.

In order to successfully model a hollow sphere subject to large scale deformations during a short duration impact, the most appropriate mesh geometry is one based on an icosahedron with two layers of elements at refinement level 6.



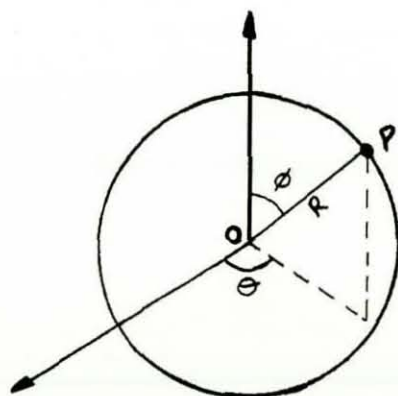
---

## 4 Modelling Pressurised Hollow Balls in Spherical Space

Within most commercial finite element pre-processors, it is possible to generate model geometry in a number of different co-ordinate frameworks, the most common being cartesian, cylindrical and spherical. Each of these co-ordinate systems offers different advantages in creating objects dependant upon the component shape and dimensions being defined. As might be expected, the simplest definition of a sphere is possible within a spherical co-ordinate system. It will be shown that this system allows easy user modification and facilitates model pressurisation.

### 4.1 The Co-ordinate System

In order to define any point in spherical space, it is necessary to construct a polar axis which is projected both positively and negatively from an origin  $O$ . The equatorial plane is then normal to the polar axis and passing through the origin. Upon this plane, an initial vector is projected, again from the origin. It is then possible to describe a point  $P(R, \theta, \phi)$  as shown in Figure 4.1.



$R$  is the length of line  $O-P$

$\theta$  (azimuth) is the angle between the initial vector and the projection of  $OP$  onto the equatorial plane

$\phi$  (zenith) is the angle between  $OP$  and the positive polar axis

Figure 4.1 – Spherical Co-ordinate System.

---

It can be seen that if the reference axes are tied to the axes of a cartesian co-ordinate system, as shown in Figure 4.2, then it is possible to convert geometry defined in one system to that of the other by a simple set of equations, given below.

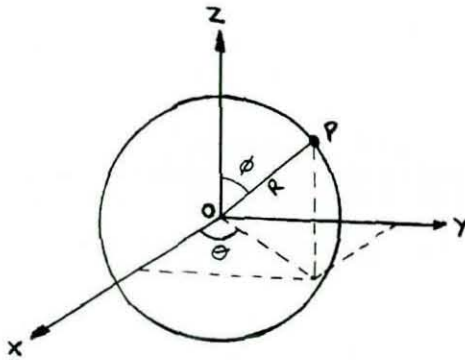


Figure 4.2– Spherical & Cartesian Systems.

**Spherical → Cartesian**

$$X = R \cos \theta \sin \phi$$

$$Y = R \sin \theta \sin \phi$$

$$Z = R \cos \phi$$

**Cartesian → Spherical**

$$R = \sqrt{X^2 + Y^2 + Z^2}$$

$$\theta = \arctan \frac{Y}{X}$$

$$\phi = \arctan \frac{\sqrt{X^2 + Y^2}}{Z}$$

The main advantage of defining the sphere within a spherical co-ordinate system is that the same value of  $R$ , being equal to the radius, defines all points on the surface. This allows changes to be made easily to the overall size of the model whilst maintaining the same mesh geometry throughout. It also allows easy identification of nodes corresponding to individual layers within a 3-dimensional, multi-layered model. With these similar nodes grouped into sets it is possible to effect changes in thickness to individual layers by simply scaling one co-ordinate within the node set. In this manner, we may construct a multi-layered spherical model which has complex geometry yet is relatively simple to modify on both local and global levels.

---

#### **4.1.1 Cartesian to Spherical Geometry Conversion – a Practical Example.**

We have seen that the conversion between the two co-ordinate systems is relatively simple, involving the application of basic trigonometric equations. However, with 5886 nodes in the model concerned, it is not trivial. In addition, it should be noted that this is made necessary due to the way in which the FE pre-processor interprets mesh data.

Whilst many different co-ordinate systems are available within the pre-processor, in order to perform the numerical calculations during FE analysis, the pre-processor converts all geometry definitions to the cartesian system before producing the solver input file. This file is the primary means of communicating with the solver and is essential for making small changes between analyses. Without this facility a new pre-processing session would have to be run each time. Hence it is necessary to transform the cartesian geometry definition created by the pre-processor to the relative spherical co-ordinates, to facilitate easy model manipulation between analyses.

In practice, this is accomplished by transferring the cartesian co-ordinates from the solver input file defined by the pre-processor to a PC based spreadsheet program as a text file. The data is then manipulated using the previously defined equations resulting in a set of spherical co-ordinates. This new data is then transferred back to the workstation as a text file where it is edited once more to match the solver input file format.



---

## 4.2 Pressurising the Hollow Sphere in a Finite Element Model

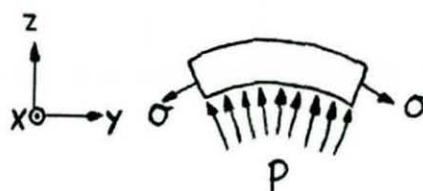
In order to complete the core model development, it is necessary to define an internal pressure within the model to replicate a pressurised tennis ball core. As previously noted in chapter 3, even a 'pressureless' core must be modelled with internal pressure, equal to atmospheric, as without this the software would interpret the hollow to be a vacuum, which would cause modelling inaccuracies. The model deformation during impact would be exaggerated and also the ball would not return to its original shape, but rather the impact surface of the sphere would invert, causing the core to rebound with the lower surface 'inside out'. Inclusion of balanced internal and external atmospheric pressures cures all these associated problems. This is accomplished within the model by creating a set of 2-dimensional fluid elements on the internal surface of the hollow sphere. These elements are given an initial reference pressure, which is then applied outwards at the corresponding internal nodes. As the internal and external pressures are balanced, the model is initially in equilibrium.

However, the internal pressure of a pressurised core is significantly greater than atmospheric, being almost double. Simply increasing the core model internal pressure accordingly would cause the force exerted on the inside surface of the core to be much greater to that on the outside. The model would no longer be in initial equilibrium and if unconstrained, the wall of the core would begin to move outwards, in the direction of net force. If the equivalent gas volume were free to expand then it would follow the ideal gas law where, at constant temperature for a specific gas the pressure  $p$  is related to volume  $v$  by the equation:  $pv = c$ , where  $c$  is a constant. Hence, the gas would expand freely until the pressure differential reduced to zero.

We can see that the gas is not free to expand as it is enclosed within a shell of finite thickness. Any expansion would result in the generation of a proportional stress within the core wall. The geometry of a sphere means that this stress would be equal at all points around the core and in all directions within the plane of the wall.

---

Left to its own devices the core would expand and contract over time until the internal pressure was balanced by stresses within the core created by the expansion. Unfortunately, as the model has previously been shown to be non-isotropic due to the mesh geometry, the core would no longer be spherical and the resulting stresses would vary throughout the model. Were the impact simulation to be run with the internal pressure and membrane stress initially out of balance then the core would still be equalising during the impact itself. The resulting high frequency oscillations would severely reduce the stable time increment. If the simulation was started after the forces had been allowed to equalise, then the core would be larger, less spherical and non-uniformly pre-stressed. Either of these positions is undesirable for the start of an analysis as the computation time and results would be adversely affected, so it is necessary to balance the internal pressure with initial stresses in the model.



**Figure 4.3 – Resultant Pressurisation Stresses.**

It follows that the pressurisation of a core would cause tension in the local X and Y axes and compression in the local Z axis, as shown in Figure 4.3, for any element. As the normal vector to each element differs throughout the model, so the local cartesian axes also change and can not be easily defined. Hence it is not possible to simply define these initial stresses within a cartesian system. It is possible to define the local co-ordinates for each element within a global spherical geometry, as has been shown previously. Each element normal is coincident with the R axis, with tensile stresses then present in the  $\theta$  and  $\phi$  directions, as seen in Figure 4.4 overleaf.

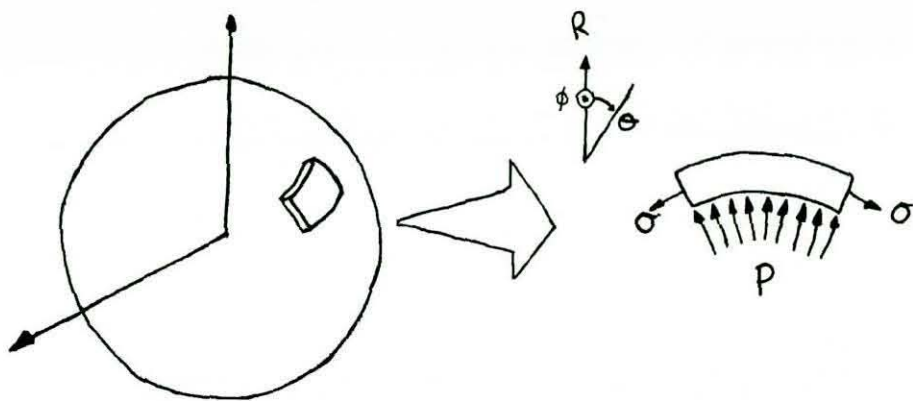
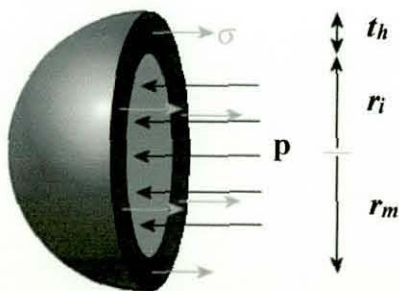


Figure 4.4 – Element Stresses in the Spherical Co-ordinate System

This allows the application of initial stresses relative to individual elements, being purely tensile or compressive, resulting in overall membrane stresses that balance with the internal pressure. To calculate initial membrane stresses then consider a pressurised sphere dissected by a great circle (Figure 4.5). The pressure acting on the apparent internal area must be equivalent to the stress through the section for equilibrium.



$$p\pi r_i^2 = 2\pi r_m \sigma t_h \text{ where } r_m \text{ is the midplane radius}$$

$$\text{for thin shells } \left( \frac{r_i}{t_h} \geq 5 \right) \text{ then: } r_i \approx r_m$$

$$\therefore \sigma = \frac{pr_i}{2t_h}$$

Figure 4.5– Deriving Initial Element Stress.



---

#### 4.2.1 Creating Initial Equilibrium in Practice

While the internal pressure and wall stresses now balance mathematically, creating equilibrium within the model is not so simple. The assumption made by equating the radii means that there is a slight out of balance force initially. Furthermore, whilst all nodes defining the internal surface of the core are at an equal radius, the elements they define are planar and hence their integration points are at a slightly reduced diameter.

If the model is allowed to move freely in space, there is an immediate oscillation present whereby the sphere expands and contracts between radii of 28.27mm and 28.91mm at a frequency of just less than 1.5kHz. Whilst the change in radius is only 0.64mm, only just over 2% of the average radius during this time, it slightly reduces the stable time increment of the analysis. It is also seen that this oscillation is still present over 5 seconds after its initial appearance, 1000 times longer than the average impact time, if no damping coefficient is used to define the rubber material. In order to reduce this vibration, additional damping must be added to the model using one of the analysis software damping options. As damping is used to define the material properties in chapter 6 then this is not a problem and the diametric oscillation due to pressurisation is considerably reduced, with the ball stabilising in around 0.1ms. The resulting pressurised ball has deformed less than 0.5mm at its maximum and so may still be considered spherical and it is this pressurised model that will be used in all subsequent analyses.

---

## 5 Normal Impacts of Hollow Rubber Cores

### 5.1 Introduction

In order to verify that the discretised model accurately simulates the impact of a tennis ball rubber core, it is necessary to develop an experimental program such that the impact characteristics of the core can be determined. A tennis ball impact in play is complex in that linear motion may be present in three dimensions with a compound rotation also possible. However, it can be simplified by considering the normal impact situation. In this case there is zero spin throughout impact and linear motion is mainly confined to the direction of impact only, although the ball will deform locally in three dimensions. Using this simple impact case it is possible to ensure that the core model represents actual impacts, before developing a cloth covered ball model.

Within the normal impact, many characteristics can be examined to determine the behaviour of the core. The most obvious is 'whole ball' velocity, which can easily be measured before and after impact. It is more common to represent normal velocities as the coefficient of restitution, defined in section 1.1, as this is a standard ball rebound characteristic specified within many rules of sports.

In order to determine changes in ball characteristics during impact there are two solutions that present themselves. Firstly, it is possible to measure post-impact characteristics such as velocity and spin, then use these results along with initial conditions to develop a mathematical model describing how the characteristic of interest varies. This method is relatively simple, however it generally requires assumptions to be made and so accuracy is questionable. It is much more desirable to physically measure the core properties throughout the impact itself. Because of the difficulties in taking accurate measurements during short duration impacts (typically less than five milliseconds in tennis), very little experimental evidence exists in this area. Whilst it is a non-trivial task to conduct such measurements, the current availability of high speed,

---



---

non-contacting measurement systems provides a solution. It is possible to achieve reasonable measurement of ball deformation during impact using a high-speed video system, or more accurate measurement using a laser vibrometer. Previous work (Hocknell, Jones et al., 1996), (Roberts, Jones et al., 2001) in golf has shown that deformation and time measurements can be made although golf has the advantage that the ball velocity is zero initially. However in tennis, it would be difficult to take accurate measurements in the moving ball moving racket situation. A representative ball impact situation has therefore been developed where balls are fired onto stationary surfaces and the appropriate measurements made.

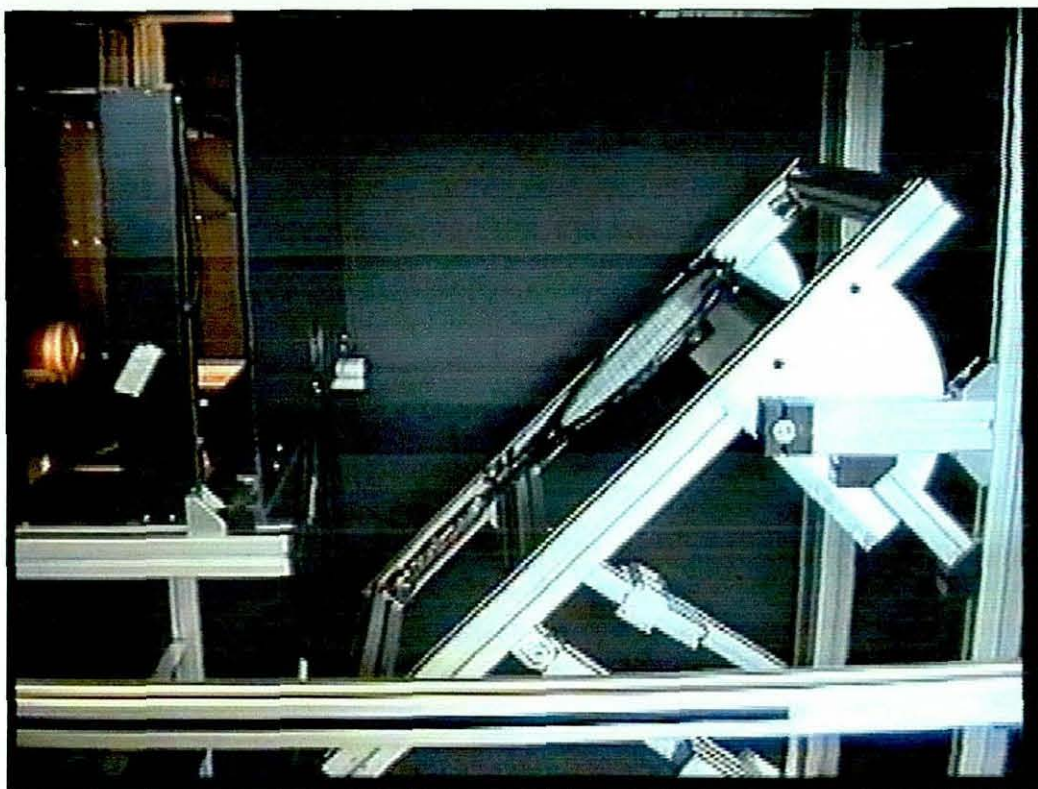
A tennis ball core is constructed from two hemispheres of rubber bonded together to form a uniform spherical shell. This results in its impact being characterised by large-scale deformation ( $\epsilon \approx 50\%$ ) at high nominal strain rates ( $\dot{\epsilon} \approx 300/\text{s}$ ). Thus, it is expected that the behaviour of the rubber material during impact is the overriding influence on core rebound characteristics. It is necessary to ensure that the model accurately captures large deformations over the appropriate timescale and so it is these characteristics that must be measured.

---

## 5.2 Equipment

### 5.2.1 Ball Cannon

In order to project tennis balls and cores at an impacting surface, a pneumatic ball cannon was used. Air is supplied from the main compressor to a reservoir at 80 PSI, which is connected to a pressure amplifier allowing air pressure up to 160 PSI to be generated. The air is released via a manually triggered valve through the breach, projecting the ball along a horizontal barrel. Barrels are interchangeable and numerous breach inserts allow a range of ball sizes to be tested, from 41mm dia. (e.g. squash balls) up to 63mm dia. (the ITF 'Type 3' tennis ball). Balls are projected into the enclosure through a set of ballistic light gates which enable the incident ball velocity to be measured in an electronic context. The photocells are spaced 200mm apart and provide a measurement accuracy of  $\pm 0.5\text{m/s}$ . A signal from one of the gates also acts as an electronic trigger for other measurement systems. At the end of the enclosure is mounted a rigid frame which is adjustable in height and angle, allowing a range of impact conditions to be created (Figure 5.1). The frame is able to support rackets, both rigidly clamped or held by the handle, sports surface samples, or instrumentation such as load cells. The exterior of the enclosure provides mount points for camera systems allowing pre and post impact measurements to be made.



**Figure 5.1 – Ball cannon test cell showing adjustable frame.**

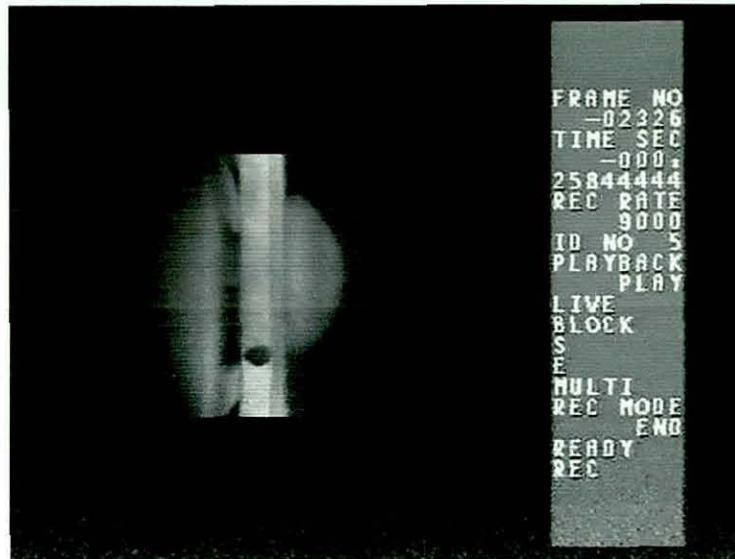


---

#### 5.2.1.1 High Speed Video System

In order to measure contact time and local deformation during impact, a high-speed video system (HSV) was used. The Kodak HS4540 HSV camera is part of a digital system where frames are stored as individual images directly to solid state memory in a continuous loop until the unit is triggered. The trigger can be set to act at the start, during or end of the time span of interest depending on application. In start mode the camera records from the trigger point until the memory is full, whereas recording stops immediately the trigger is activated in end mode. Here, images are captured prior to triggering for as much time as is available within memory. Trigger mode selection is controlled from a hand held cable remote unit, along with other options such as frame rate and image playback. The trigger itself may be either an electrically generated pulse, from a piece of analysis equipment for example, or simply a manually operated push button circuit maker.

The system is capable of recording up to 3072 full frames at rates up to 4500 frames per seconds (fps) and provides a resolution of 256x256 pixels at this rate. The system can operate at up to 40,500 fps but the field of view is displayed on a reduced screen size, typically 40mm x 40mm on a 625 x 625 pixel monitor. At higher rates (above 4500 fps) memory restraints require the resolution to be reduced such that a rate of 9000fps gives a half screen display with a resolution of 256x128 pixels and so on. A sample image at 9000fps is shown in Figure 5.2.



**Figure 5.2 – Sample image from HSV capture.**

The data storage unit has a number of in-built input and output channels. Data can be output in either digital or video format. A built-in PC interface port enables captured frames to be exported in a series of .GIF files. This allows individual images to be studied, or the video to be reconstructed using image editing software. A video output channel enables images to be stored to videotape, with a second channel allowing concurrent viewing on a portable monitor. A third output channel allows individual images to be printed out via a black and white printer, although image quality is generally poor.

The on-screen image may be accompanied by a status block, with this option controlled by the remote unit. Inclusion of a status block as seen in Figure 5.2 necessitates the reduction in size of the available viewing area on screen. The status block includes all relevant information concerning the currently viewed frame. The image ID can be sequenced manually via the remote unit and remains constant for all images in the sequence, allowing each video sequence to be identified. Each frame is then individually identified further. The main identifiers are the frame number and time from trigger, each

---

of which is unique to that particular image and is calculated from the last frame captured before trigger, in end mode. This allows direct calculation of timing between events that may be separated by several frames. Image resolution is sufficient to allow events to be determined to within  $\pm 1$  frame. Accuracy is then dependent upon the frame rate and event duration. For example, a typical impact of 4ms duration captured at 9000fps provides one frame every 0.11ms, or 36 frames in total, giving a duration measurement accuracy of 5.5%. Other information displayed includes the frame rate and the recording and playback modes in use at that time.

In order to measure distances such as deformation within an individual frame, it is first necessary to calibrate the video system. This involves setting up the camera in position to record the event of interest. A calibration grid is then set up within the anticipated field of view and an image is captured using the HSV. It is then possible to measure the distance between the grid lines, either directly from the screen or more accurately using the digital image on a PC to obtain a value in pixels. These distances are compared to the actual spacing of the grid (20mm in this case) to determine horizontal and vertical conversion factors. Measurements can be taken from the screen at an accuracy of  $\pm 1$ mm or from a digital image at  $\pm 1$ pixels. Over a grid size of 300x200mm, captured at 256x256 pixels, this equates to an accuracy of the calibration of either 1% or 0.8% respectively. However, the accuracy of measurements taken from recorded events is dependent upon the dimensions measured as a percentage of a characteristic dimension (e.g. ball diameter).

---

### 5.2.2 Laser Vibrometer

The Laser Doppler Vibrometer (LDV) is a non-contacting sensor capable of resolving projectile velocity over small timeframes and to a high degree of accuracy. It makes use of the Doppler effect, this being the change in frequency of a measured wave due to relative motion between the source and observer.

A wave projected from a source at  $D$  having some frequency  $f$  with a wavelength  $\lambda$  is shown in Figure 5.3a. At time  $t_0$  wavepoint  $A$  is emitted such that it is seen by the observer at a time  $t_A$  after having left the source. The distance  $AD$  is equal to  $ct_A$  with  $c$  being the speed of light. The number of cycles between  $A$  and  $D$  is  $n_c$ , such that;

$$n_c \lambda = ct_A$$

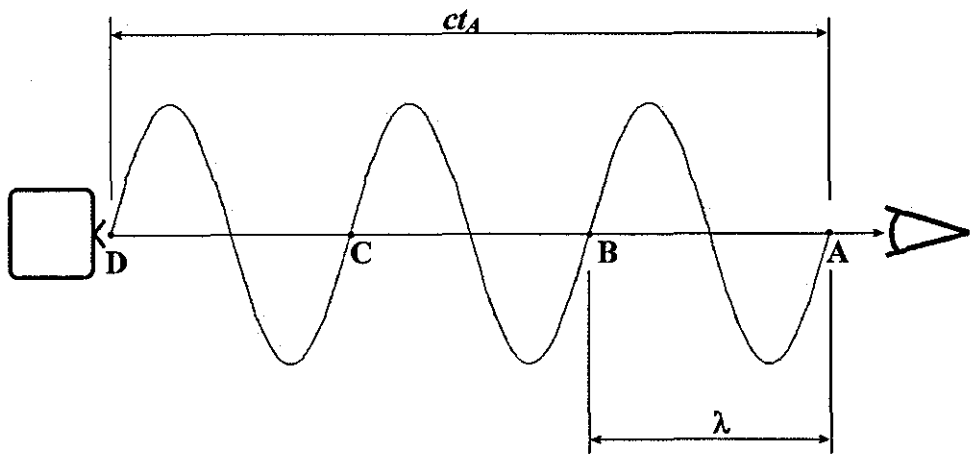
$$\text{but } f = \frac{c}{\lambda}$$

$$\therefore n_c = \frac{ct_A}{\lambda} = ft_A$$

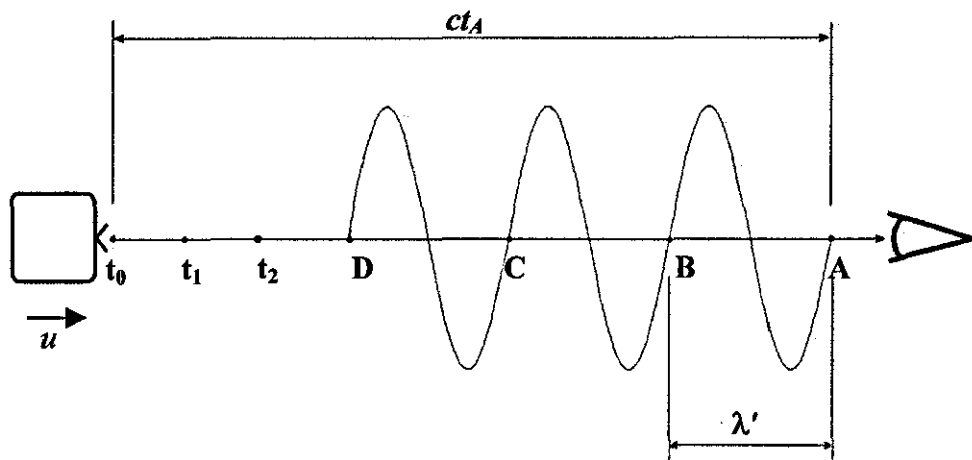
Equation 5.1

Suppose that the source is moving to the right with a constant velocity  $u$ . Wavepoint  $A$  will still leave the source at time  $t_0$ ,  $B$  will still leave the source at  $t_1=1/3t_A$ ,  $C$  will leave the source at  $t_2=2/3t_A$  and wavepoint point  $D$  will just be leaving at time  $t_A$ . Throughout this time the source will have been moving such that at  $t_A$  the space diagram will be as seen in Figure 5.3b. As all three cycles must now fit within a shorter space then the new wavelength  $\lambda'$  must be lower. Therefore the frequency  $f'$  measured by a fixed observer must increase as  $f' = \frac{c}{\lambda'}$ .

---



**a - Wave Projected from a Fixed Source.**



**b - Wave Projected from a Moving Source.**

**Figure 5.3 – Spatial Diagram Showing the Doppler Effect.**



---

The number of cycles emitted within the time  $t_A$  is the same as for the fixed source case and so we can write:

$$n_c \lambda' = ct_A - ut_A$$

$$n_c = \frac{(c-u)t_A}{\lambda'} = \left( \frac{f'}{c} \right) (c-u)t_A$$

$$\therefore n_c = f' \left( 1 - \frac{u}{c} \right) t_A$$

**Equation 5.2**

As  $n_c$  is independent of source movement, then we may equate Equation 5.1 and Equation 5.2 to give:

$$f' \left( 1 - \frac{u}{c} \right) t_A = ft_A$$

$$\therefore f' = \frac{f}{1 - u/c}$$

**Equation 5.3**

In the case where the source moves away from the observer, then the sign of the velocity is simply reversed and Equation 5.3 becomes:

$$f' = \frac{f}{1 + u/c}$$

**Equation 5.4**

Assuming the source frequency is known, then by monitoring the observed frequency it is possible to determine the velocity of the source relative to the observer.

---

---

This is the basic principle on which the laser vibrometer operates, however the actual equipment itself is much more complex as there are many inherent problems. Figure 5.4 overleaf shows schematically the design of a typical LDV and it can be seen that the light source and photodetector are within the same unit. Because of this, the light is not emitted from a moving source towards the photodetector but rather is projected from a stationary source toward a moving object from which it reflects back to the photodetector. Hence, for a target object that moves a distance  $dx$  then the distance travelled by the light from source to the photodetector is changed by  $2dx$ . If the velocity of the object is  $u_0 = \frac{\partial x}{\partial t}$ , then the apparent velocity measured by the photodetector will be  $2u_0$ . Also, the photodetector is unable to directly demodulate the scattered light, which has a frequency of the order of  $10^{15}$  Hz. Instead, the doppler shift is measured by mixing the scattered light with a reference beam derived from the same coherent source. The intensity of this combined light produces a heterodyne or beat in the output whose frequency is equal to the difference in frequency of the two beams. However, this results in the setup being unable to determine direction of motion as the photodetector output disappears when the measured velocity is zero. This requires the reference beam to be pre-shifted, often accomplished through Bragg cells, such that for zero velocity the photodetector output registers a constant frequency equal to the shift frequency. Positive or negative object velocities then result in an increase or decrease in frequency respectively.

As the light is incident on a surface which can be considered rough on the scale of the optical wavelength, each surface element within the laser spot scatters the light, acting as individual point sources for coherent light. At any point in space the individually scattered wavelets interfere either constructively or destructively producing a bright or dark speckle respectively. For any plane within the scattered light, such as the screen of the photodetector, a speckle pattern is produced. The speckle pattern is a continuous random distribution of light amplitude and phase and the geometry of the detector is such that it samples several speckles with the output being proportional to the instantaneous mean of the intensity distribution.

---

For motion parallel to the incident beam, the Doppler effect produces a uniform rate of change of phase and so the signal can be demodulated extremely accurately to less than  $1\mu\text{m/s}$ . However, if the target tilts or moves other than normal to the surface, the speckle pattern may change spatially and temporally. This produces phase modulation which the detector is unable to distinguish from the Doppler shift. This 'pseudo-vibration' is a major source of noise within laser vibrometry.

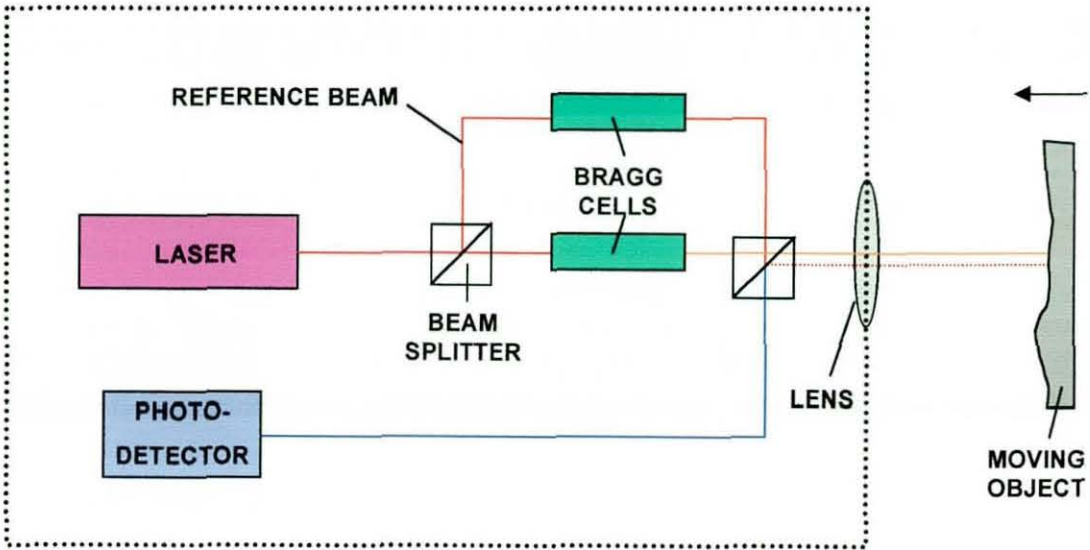


Figure 5.4 – Laser Doppler Vibrometer Schematic.

---

## **5.3 Experimental Procedure**

### **5.3.1 High Speed Video Analysis of Normal Core Impacts**

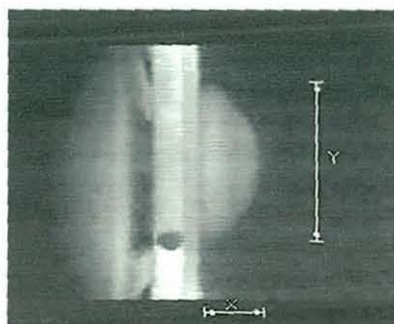
Tennis ball rubber cores and cloth covered balls were subject to normal impacts with a solid surface in order to determine their impact characteristics, as discussed previously. Both pressurised and pressureless cores and balls were used for comparison and as a means of verifying that the model pressurisation process detailed in chapter 4 is valid. All balls and cores were stored under atmospheric conditions specified by the ITF rules of tennis Appendix I and pre-compressed accordingly before testing.

The balls were fired from the barrel of the pneumatic cannon at velocities in the range of 15-35m/s, verified by the ballistic light gates. There was nominally zero spin on the balls (less than 70rpm) which is consistent with ITF testing procedures. The balls were projected 'normally', that is at ninety degrees to the impact surface, onto a rigid aluminium plate such that following impact the ball will return nominally along the same path that it approached the surface. This allowed rebound velocity to be measured by the light gates as well as approach velocity and has proved to be an efficient method of measuring the COR. Although it was not necessary to use aluminium as the impact surface for this specific test, the laser vibrometry analysis detailed in section 5.3.3 required the use of a specially designed aluminium plate. To eliminate surface friction differences between the tests as a possible cause of error the same surface was used throughout. The structure of the plate was such that any deformation would have been small and could be neglected. In addition, laser vibrometry has shown the plate holding structure to move less than one millimetre in the direction of impact for a 35m/s tennis ball impact, allowing the surface to be considered fully rigid. The impact itself was captured using the Ektapro HSV camera described previously. A digital sequence was recorded at 9000fps using the end-mode trigger, set manually using the impact sound as a guide. These video sequences were then analysed during playback in order to determine impact duration and gross deformation for each impact.

---

### 5.3.2 Impact Deformation Measurement

As previously discussed, the measurement accuracy from HSV images is dependant upon the measured dimension and so it is desirable to measure as large a dimension as possible. For this reason, measurements of the maximum normal and tangential deformations were taken for each impact, as shown in Figure 5.5. It has been seen that at maximum deformation, the ball may compress to less than half its original diameter in the normal direction to flight. This gives a potential measurement error of up to 8.7%. As the plate is considered fully rigid in space then all measurements made relative to the plate are also absolute at all times during impact. Also, it was noted that maximum normal and tangential deformation occur within the same HSV frame during the impact, that is within 0.11ms and so may be considered simultaneous.



X – Maximum Normal Deformation

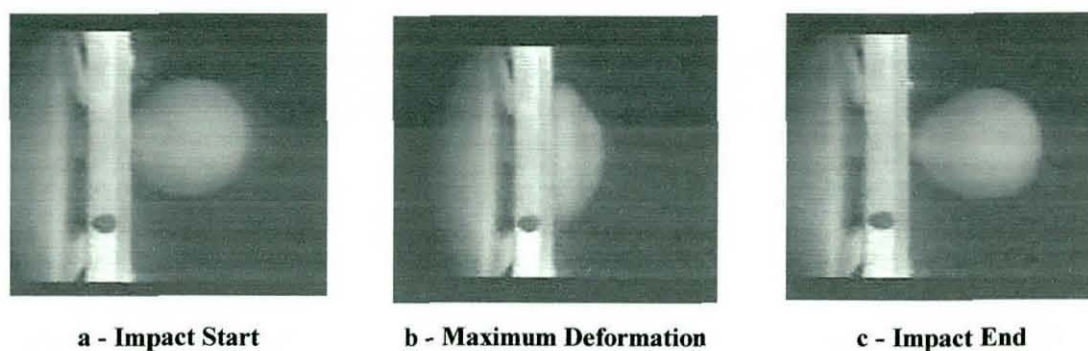
Y – Maximum Tangential Deformation

**Figure 5.5 – Measured Deformation Characteristics.**



---

In order to measure impact duration the frames of initial and final contact must be determined for each impact, as shown in Figure 5.6. The frame number for each is then noted, as well as the frame at the time of maximum compression. Subtraction of the two frame numbers divided by the frame rate gives the impact duration. The time taken from initial impact to maximum compression was also recorded as a percentage of the total contact time.

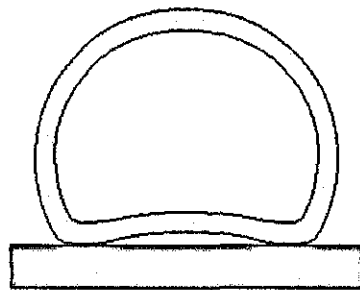


**Figure 5.6 – Points of Interest During Impact.**

---

### 5.3.3 Laser Vibrometry Analysis of Local Deformation

In addition to measuring both normal and tangential gross deformation during impact, it is desirable to know how the ball behaves within the impact footprint, that is, the region of the ball in contact with the impacting surface at any time during impact. Previous work (chapter 1) has described an impact phenomenon whereby at maximum deformation the initial impact point is no longer fully in contact with the impacting surface. It is suggested that bending within the wall of the ball is such that the initial contact point comes off the surface during impact, forming a bubble, as shown in Figure 5.7. By using piezo-electric cells Cross (1998) argues that the resulting force pattern suggests this phenomena, however any movement away from the surface locally by the ball during impact has never been measured. In order to achieve this, it is necessary to use a non-contacting measurement method as the effect is likely to be small and so any invasive measuring technique will significantly alter the characteristics of the deformation in the contact region. The use of laser vibrometry is well suited to this task.



**Figure 5.7 – Inversion of the Contact Region.**

---

In order to maintain a constant set of impact conditions across the tests, the same setup was used as described for the HSV testing. The balls were projected normally onto an aluminium surface using the pneumatic cannon, with the ballistic photocells used to record inbound and rebound velocities. The aluminium plate was constructed to allow optical measurement of the impact zone, with a thin section of Lexan (toughened perspex) sandwiched between two machined plates of aluminium containing a slot, providing a single impact plate with a clear window through which to take measurements. Balls were projected at velocities in the range of 15m/s (35mph) to 25m/s (55mph), which was limited by the useful range of the vibrometer, as discussed overleaf.

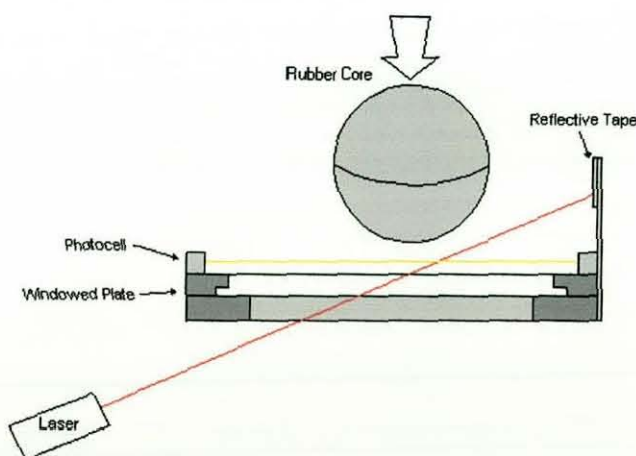
The LDV measuring system is highly sensitive to noise and the accuracy of the resulting data is affected by the strength of the returned signal. It is therefore desirable that the surface under investigation be highly reflective. This is made possible for any surface by the use of self-adhesive reflective tape. However, in order to be sure that the data being captured is generated solely by the movement of the surface of interest and that there is no relative movement between the tape and the surface, it is necessary to ensure good adhesion. For this reason it will be difficult to investigate the deformation of a cloth covered ball using this method as little or no signal could be received from the cloth and application of reflective tape is not practical. However, it was possible to use uncovered rubber cores as the surface was smooth and continuous, providing a good area on which to affix the reflective tape. Because of this, testing was undertaken using cores only, both pressurised and pressureless. As previous work suggests that greater deformation is seen in tests using 'old' balls, both old and new cores were tested. New cores were taken directly from the pressurised can having been stored and pre-compressed as per ITF rules, appendix I. Old cores had been stored at room temperature and atmospheric pressure for 1 week and were also pre-compressed.

The cannon is designed to project balls with nominally zero initial spin ( $< 3$  rpm). However, even a small amount could result in the reflective tape missing the plate window if the covered area is not of sufficient size. Whilst cost and practicality prevent total coverage of the cores it was possible to cover an area of less than half the core surface, allowing a signal to be recorded for most impacts.

---



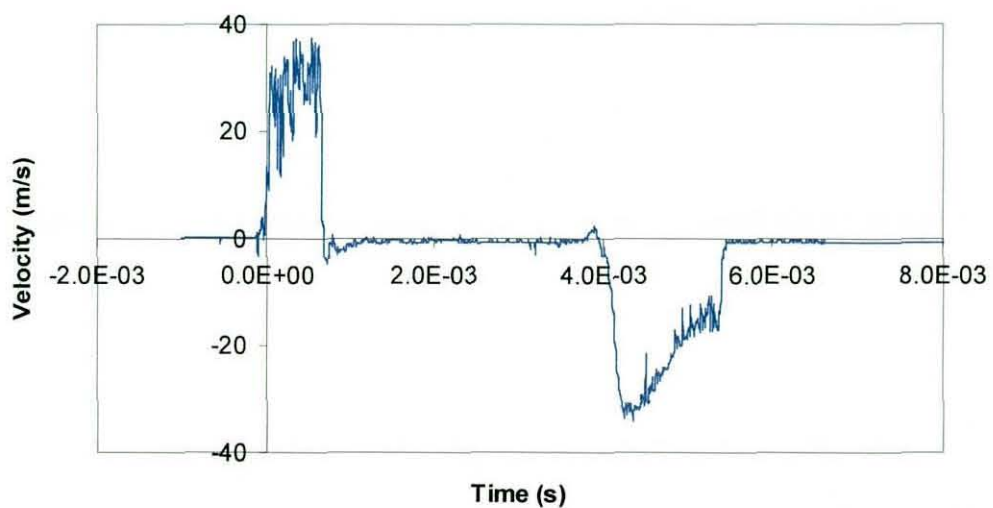
The useful range of the LDV is 20m/s to an accuracy of  $\pm 2\mu\text{m/s}$ , with accelerations up to  $2 \times 10^6 \text{ms}^{-2}$ . This introduces the problem that the measurement limit is lower than the maximum impact velocity used in the analysis. In order to be able to measure impacts at higher velocities, it was necessary to align the laser at an angle to the direction of impact, as shown in Figure 5.8. This allowed the measurement of a component of the impacting velocity which was within the limit of the equipment. Whilst the movement was now no longer in the plane of measurement, careful manipulation of the data would allow meaningful results to be obtained. Unfortunately, as the beam was not initially fixed on any target prior to impact, no signal was generated before or after impact. This resulted in a sudden over-ranging of the equipment as the ball initially broke the beam and the signal was not able to return within range before the start of impact. In order to allow measurements to be taken for the whole impact, it was necessary to allow the beam to focus on some stationary target prior to the ball arriving at the surface. This was accomplished by simply applying reflective tape to a fixed target mounted to the side of the plate. The signal was now more stable before and after impact allowing the resulting velocity data to be resolved. However, it was still unclear as to exactly where the impact was beginning and ending by simply analysing the velocity data. In order to allow these points to be accurately determined, a small photocell was mounted on the impacting surface (Figure 5.8) such that the beam was broken within 1ms of either end of the impact. As both this small photocell and the laser vibrometer were triggered from the main ballistic light gate at the same time, this allowed more accurate interpretation of the vibrometry data.



**Figure 5.8 – Laser Vibrometer in Use at an Angle to the Impact Direction.**

---

A typical velocity signal generated by a normal impact is shown in Figure 5.9. It shows the points where the core first breaks the beam as sudden marked changes in velocity. Initially, the measured velocity, being that of the fixed target, is zero. However it can be seen that the initial signal is non-zero, due to a small amount of noise within the signal. As the data is to be integrated to provide displacement results, then this discrepancy must be accounted for. If not, the integration of a constant offset would result in the true data being superimposed upon a slope of constant gradient. With this offset removed, it is then a case of processing the resulting data through a software package (MATLAB) in order to perform the integration and provide a useful set of through-impact displacement data from the initial impact point.



**Figure 5.9 – Typical Laser Vibrometer Velocity Trace for a Core Impact.**

---

## 5.4 Results

Restitution coefficients for all ball types are shown in Figure 5.10. As COR is specified by the ITF in its standard drop test, it is no surprise that the results for pressurised and pressureless balls are similar, as are the core CORs. Performing paired t-tests on the data for velocities above 18m/s shows no significant difference between core type ( $p=0.820$ ), however the difference between ball type is significant ( $p=0.008$ ). The difference between the values for corresponding cores and balls is significant for pressureless ( $p=0.015$ ) but not for pressurised ( $p=0.944$ ). If we group all values for both balls and for both cores then the difference between these groups is just significant ( $p=0.052$ ), which suggests that COR is reduced due to the addition of a cloth cover. Similarly, by grouping cores and balls as either pressurised or pressureless, we see that the difference due to internal pressurisation is not significant ( $p=0.146$ ). The COR falls with increasing impact velocity in all cases and the relationship appears to be linear.

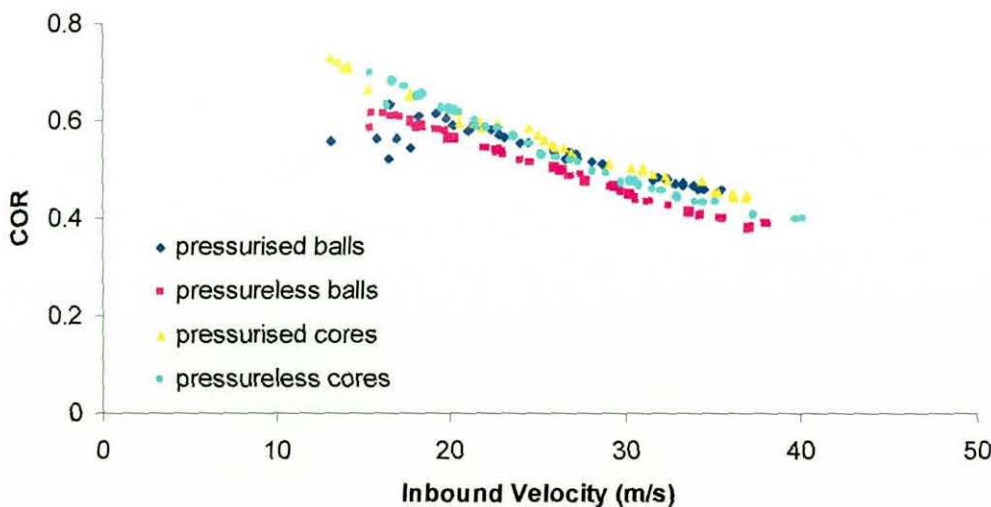


Figure 5.10 – Restitution Coefficients for Both Ball and Core Types.



An examination of impact duration in Figure 5.11 again reveals evidence of how similar the rebound characteristics are for all the ball types. Whilst the data appears more spread, perhaps reflecting the  $\pm 0.11\text{ms}$  measurement accuracy, on analysis the differences are more marked. Impact duration for the cores appears slightly longer than for the balls, and the absence of internal pressurisation would seem to increase impact duration. Again using paired t-tests we see that the difference between the values for balls and cores is highly significant, with a value  $p < 0.001$  in both cases and the average duration being higher for cores than balls. Whilst the differences between the two types of ball ( $p = 0.072$ ) and core ( $p = 0.058$ ) cannot be considered significant, these values indicate a definite trend. If we again group balls and cores depending on internal pressure, then the difference between these two groups is significant ( $p = 0.025$ ), with the average impact duration of pressurised balls and cores being lower. There appears to be a fall in duration with increasing impact velocity in all cases.

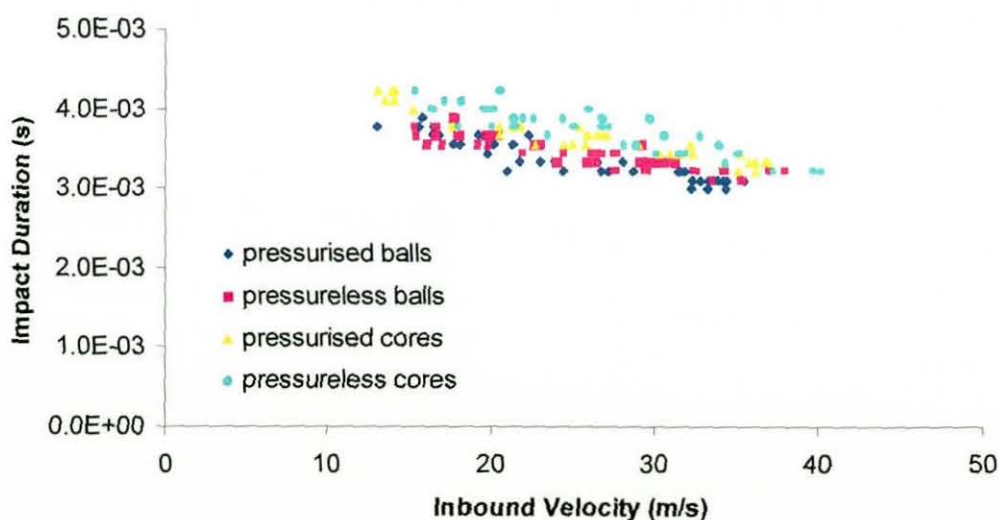


Figure 5.11 – Impact Duration for All Ball and Core Types.

The maximum deformation of the ball normal to the surface, termed the X deformation previously, is shown in Figure 5.12. It is expressed non-dimensionally, thus allowing balls and cores of differing diameters to be compared directly. The value represents the deformed 'diameter' as a percentage of the undeformed value and so illustrates how much the ball is 'squashed', relative to the impact velocity. Again balls and cores of both types display similar characteristics. The balls deform less than the cores relative to their original diameters and internal pressurisation leads to a greater gross deformation for both balls and cores. However it should be remembered that the deformation is a gross measurement and does not take into account local variations which may affect these 'apparent' measurements. These local effects are discussed further in section 5.5. Gross normal deformation is proportional to the incident velocity for all ball types, to a maximum of around 50% at 35m/s.

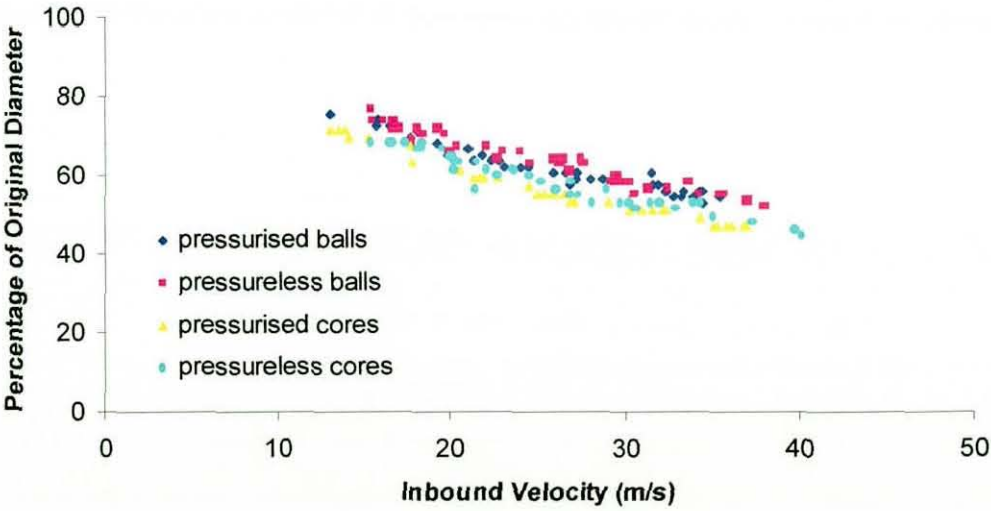
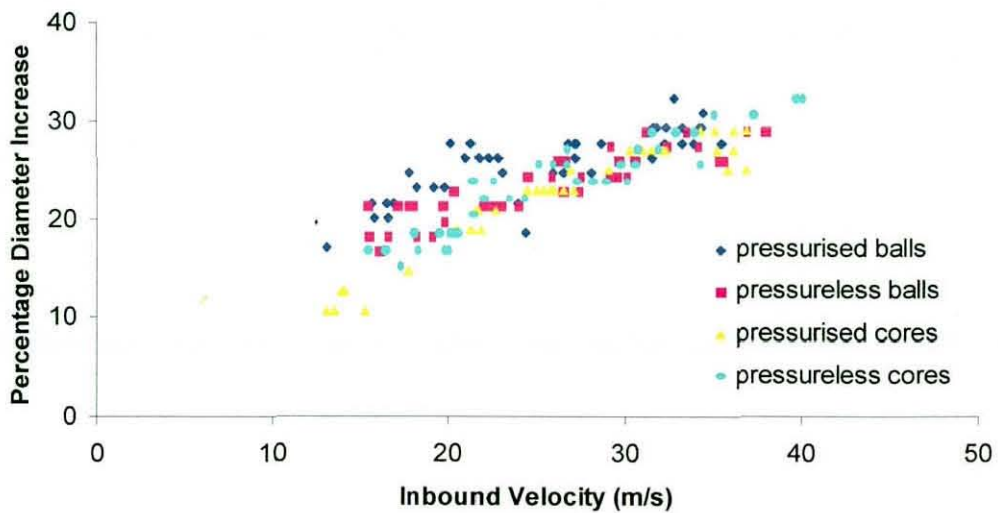


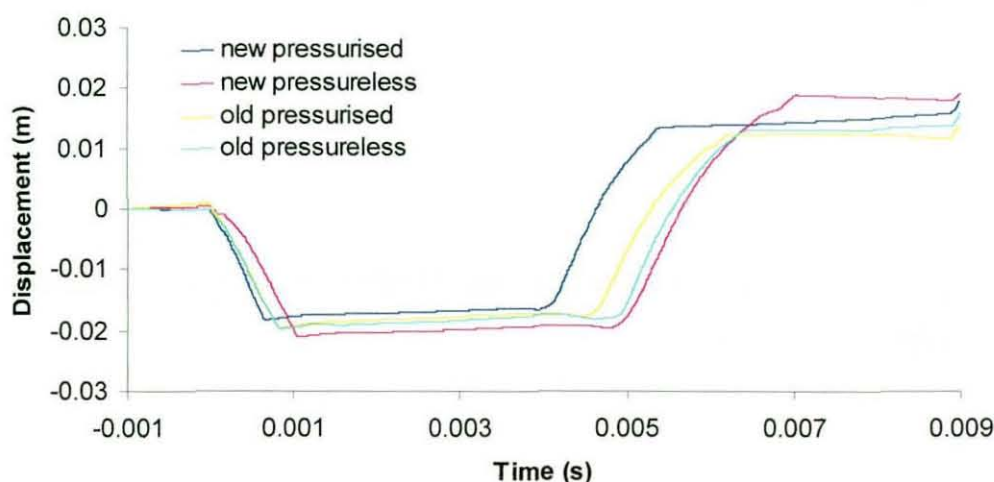
Figure 5.12 – Deformation Percentage Normal to the Impact Surface.

The maximum deformation tangential to the surface, the Y deformation is shown in Figure 5.13. It is again expressed non-dimensionally, as a percentage diameter increase. It is seen that the resulting data is much more spread than any previously shown. Whilst core deformation appears less at the lower impact velocities, results for all types overlap at the higher end of the velocity range. Similarly there is no discernible effect due to internal pressurisation.



**Figure 5.13 – Deformation Percentage Tangential to the Impact Surface.**

The local velocity measured by the laser vibrometer has been integrated to give a local displacement over time and is seen in Figure 5.14. In all core types there appears a characteristic movement away from the point of initial impact, with the magnitude being greater for old cores than for new and for pressureless cores compared to pressurised. Despite allowance made for non-zero velocity data prior to impact, the displacement pattern is still superimposed upon a gradient. All displacements are of the order of a millimetre.



**Figure 5.14 – Local Deformation at the Initial Impact Point from Laser Vibrometry.**



---

## 5.5 Discussion

Decreases in COR over an increasing velocity range is well known and has been seen in much of the previous work concerning balls (see chapter 1). However, little work has been seen on the properties of cores. It is somewhat surprising then that the CORs for cores and balls are similar in value. After all, balls are covered in a layer of cloth of comparable thickness to that of the rubber core and it would be expected that large compression of the 'fluffy' cloth would result in an increased energy loss within the balls. Whilst pressureless balls have a COR significantly lower than any other, the average COR for pressurised balls and cores and pressureless cores is within 1%. It is not immediately apparent why the behaviour of the two ball types should be different when the corresponding cores are so similar. We must examine all characteristics together to develop a clear understanding of the processes which lead to this.

The reduction in COR for the balls at the lowest impact velocities probably highlights the inability of the ball cannon to provide the necessary conditions to test at these low speeds. It is possible that the effective area over which the air pressure acts is more varied for balls than cores due to the nature of the cloth cover. This would introduce increased clearance in the barrel and so result in a more varied initial velocity for a given air pressure. Also if the ball is more free to move within the barrel, a higher level of spin may be imparted than is acceptable and there may be some ball deformation. However, it is most likely that the problem is simply the effect of gravity. At the lower speeds, the impact location of the heavier balls is seen to vary in practice. This would imply that the ball travels further off line upon rebound with the resulting velocity measurement then being the horizontal component of the true velocity. Increased drag on the 'fluffy' balls as opposed to the relatively smooth cores may also be a factor at these low speeds. As the points above 20m/s appear linear and less scattered, it is possible to discard the cloudy low speed results and extrapolate from the remaining data. Knowledge of the lower speed COR specified in the ITF rules also helps this process. It is for this reason that data for inbound velocities below 18m/s were discounted in the statistical tests.

---



---

The COR value specified for the ITF 100 inch drop test can vary between 0.728 and 0.761. It can be seen that the values obtained here are significantly different and velocity dependent. This brings into question the worth of the ITF test specification particularly when dealing with ball materials that are highly strain rate dependent. Furthermore, it is seen that whilst pressurised and pressureless balls behave similarly at low velocities, as indeed they must to meet regulations, there is a significant difference between the two over the range. This difference appears proportional to velocity and it may well be that this is the characteristic that leads to tennis players describing pressureless balls as feeling 'dead' during play.

The impact duration for tennis balls has been measured previously but only at relatively low velocities, comparable to the ITF drop test. It has previously been suggested that the duration remains constant over the velocity range, but these results clearly show that this is not the case, with a fall of 1ms over the range of interest. Contrary to the initial theory of the cloth taking additional energy out of the system, which would be expected to result in a longer impact duration, it is evident that balls actually have significantly lower impact duration (8% lower on average). This would imply that the addition of cloth to the balls increases the stiffness relative to their respective cores.

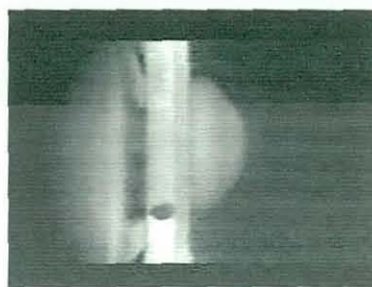
As the dominant mode of deformation during a tennis ball impact is bending, then much of the outer surface will be subject to positive strain during the impact and the cloth layer will be subject to tension within its plane. Being relatively strong in this deformation mode, the cloth acts as a stiffener. This 'composite' shell then displays lower magnitude bending deformation and so results in a lower impact duration. This reduction in impact duration with increase in ball stiffness is evident in other ball impacts. Roberts, Jones et al. (2001) showed that increased ball compression reduced golf ball impact duration.

---

This stiffening effect explains the lower gross deformation magnitudes both normally and tangentially seen for the balls relative to the cores. It is somewhat puzzling that the data spread for the normal deformation measurements appears greater than that for the tangential measurements, considering the lower measurement accuracy previously noted in the normal direction. However, observation of the HSV images reveals the problem to be primarily due to lighting conditions, as the level of illumination required for operation at such high frame rates is considerable. There is significant difficulty in providing sufficient lighting to illuminate all sides of the ball equally and this is not helped by the physical restrictions imposed due to the testing environment of the ball cannon enclosure. Consequently, the upper and lower surfaces of the ball are poorly illuminated and so it is difficult to accurately determine the extremities of the ball from the video image. The cloth cover further complicates the issue and as the ball 'fluffs up' due to impact it is often a matter of experience in determining the location of the physical extent of the ball. The greater spread of data for balls as opposed to cores may be the result of this estimation. For the normal direction, the fluff tends to lie flat and the back of the ball, being at a constant height throughout, is well illuminated. This results in a lower data spread despite the lower measurement accuracy. However, this is not to say that the tangential data should be discounted, for sufficient data points exist for a relationship to be drawn.

From the high-speed video, it is evident that there are two modes of deformation which occur during the impact. Initially the ball (or core) compresses with little bending, with the impacting surface appearing to merely intersect the spherical shell. However this is soon followed by a buckling of the hollow shell at the edge of the contact region, evident as increased bending near to the surface. This bending wave travels around the ball such that it is apparent that at around half of the impact duration the sides of the ball are travelling away from the impact surface, whilst the top of the ball remains stationary.





**a – Pressurised Core**



**b – Pressureless Core**

**Figure 5.15 – Tennis Ball Cores at Maximum Deformation.**

The still images above of the cores at maximum deformation reveal a marked difference in shape between the pressurised and pressureless cores (Figure 5.15a and Figure 5.15b respectively). This is most apparent at the higher impact velocities, 35m/s in the case shown. Whilst the obvious difference between the two core types is the internal pressure, the rubber core material also appears responsible for the dissimilar deformations. In order for pressureless balls to conform to the same ITF specifications as the pressurised balls, the core wall thickness has to be constructed greater, resulting in comparable CORs at the specified impact velocity. However, as ball mass is also specified in the rules then the rubber used to construct pressureless cores must be less dense. In chapter 6 it is shown that this rubber has a higher elastic modulus than that of the corresponding pressurised core and so it would be expected that under comparable loading conditions the pressureless core should exhibit smaller strains. However, the viscoelastic energy loss for the pressureless rubber is much lower than for the pressurised rubber. It is these two factors which combine to produce the greater magnitude bending in the pressureless core.

---

The speed at which stress waves travel through the material, the dilation wave speed  $c_d$ , follows the relationship:

$$c_d \propto \frac{\text{stiffness}}{\text{density}}$$

This means that for the pressureless rubber, which is both stiffer and less dense than its pressurised equivalent, the wave speed will be greater and so bending waves will be able to propagate more freely. Secondly, the lower energy loss within the material will result in the faster travelling bending wave retaining greater amplitude. This higher magnitude bending may propagate around the core at greater speed and with less resistance and it is this which results in the characteristic impact shape of the pressureless core, as seen in Figure 5.15b.

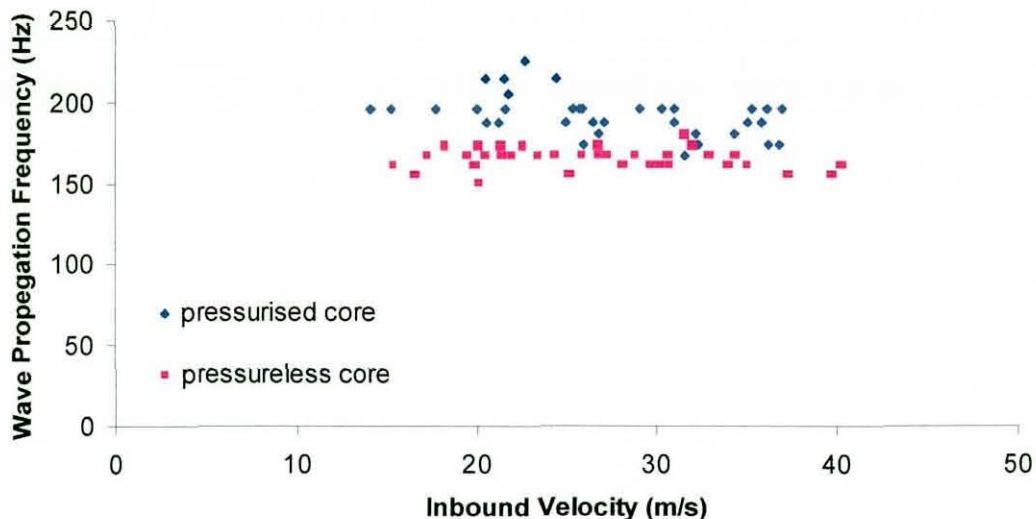
Whilst gross tangential deformation is comparable for the two core types, the inverted 'T' shape of the deformed pressureless core, as seen in Figure 5.15 gives it less apparent normal deformation. However, local strains within this core type at maximum deformation are in fact greater. At the end of impact the spherical shell becomes 'egg shaped' with the pointed end remaining in contact with the surface (Figure 5.6c). Again the reduced stiffness of the pressureless rubber results in a greater deformation at this time which may account for an increase in impact duration in comparison to the pressurised balls and cores. The increased bending magnitude throughout impact also results in greater overall energy loss through hysteresis which is seen as lower values of COR for pressureless balls. Whilst the difference between pressureless and pressurised cores is not significant there appears to be a trend at higher velocities and further testing may reveal a difference. As the increased bending is more evident at greater incident velocities then this would explain the velocity dependence of the difference.



---

The reduced impact duration at higher velocities can be explained by the strain rate dependency of rubber. Higher impact velocities will have the effect of increasing local strain rates within the ball. Rubber is a rate dependant material and at increased strain rates behaves stiffer at the same level of strain. This is discussed in detail in chapter 6. Hence at higher speeds, the ball will behave stiffer despite higher magnitude deformation, which leads to the reduction in impact duration seen here.

Further analysis of the HSV core images reveals the bending wave to remain for a few cycles after the impact ends. It is possible, by recording the frame numbers of maximum apparent bending at the front and back of the cores, to determine the wave frequency. Whilst there is probably similar behaviour for the balls also, the reduced magnitude bending results in the wave being visually undetectable. The first point of note is that there are clearly two waves evident through visual inspection. As the front of the core fully recoils a few frames before the end of impact, which itself is concurrent with full recoil of the rear of the core, then there must be two separate waves. The wave responsible for the forward recoil is of greater magnitude and for the highest speed impacts appears as a point at the front of the core. By contrast the rear wave produces a more rounded egg shape, as previously shown. At the next times of maximum forward and backward bending, the rearward wave is most evident, indicating that the original front wave has now travelled around half the core. The wave speed can be measured as the difference in frames and the resulting frequency for both core types is seen in Figure 5.16. The wave in the pressureless cores has a constant frequency of around 170Hz, whereas in the pressurised cores the frequency is higher, around 195Hz and appears velocity dependant, although that is more probably due to data scatter. From the model results presented in chapter 6 and the explanation above, it seems likely that measurement error here is significant. The data spread for the pressurised core is greater as the bending magnitude is lower and so the wave is more difficult to identify.



**Figure 5.16 - Frequency of the First Forward Bending Wave around Both Core Types.**

It would appear that both waves are a result of the same bending phase during the impact. As this develops less than half way around the ball and also it is seen that the forward wave reaches the front of the ball before the rearward wave reaches the back, then it would follow that the rearward wave must possess a lower frequency. However, due to the large energy loss within the rubber, it is not possible to visually determine when this wave reaches the front of the ball and so its frequency cannot be measured from the HSV. Finally, in the highest speed pressureless core impacts, where deformation magnitude is greatest, a third wave can just be seen at the rear of the ball around half way between the two previously mentioned. Being relatively low amplitude this wave is only visually detectable in a few impacts but it exists none the less. Whilst not seen here, it is expected that another similar wave exists separated by half a cycle. It would appear that the impact excites a natural frequency of the core that sets up a bending mode which if viewed through the cross-section would be a cross shape with four nodes. This would also mean that for any point on the core, measurement of radial deformation or acceleration would yield a signal of around 700Hz – 800Hz, similar to that previously reported by Cross.

---

In contrast to the remainder of this chapter, the measurement of local ball displacement using laser vibrometry is inconclusive. Whilst there appears to be a movement away from the initial point of contact of up to a few millimetres, the whole curve is shifted by an amount greater than this over its range. It is quite possible that there is no movement in the direction of impact and the measured displacement corresponds to local tangential movement of the rubber across the surface, due to initial lateral compression during impact. Even if the measurement point was exactly coincident with the initial impact location, which is in doubt due to the variability of the cannon, any movement of the rubber away from the surface would result in the laser being incident upon a constantly changing point on the ball surface. For this reason, the results from this experiment must be questionable and a more effective measurement method is required.



---

## 5.6 Conclusions

Restitution coefficient and impact duration are both negatively proportional to incident velocity. Gross ball deformation increases proportionally to velocity both normally and tangentially to the direction of impact and the cloth covering, whilst absorbing energy under compression also has the effect of stiffening the core. The resulting energy loss is comparable between balls and cores, however pressureless cores and balls lose more energy during impact due to greater bending of the shell.

The impact excites bending modes within the balls and cores that set up waves which are seen to propagate around the ball at some frequency, being a factor of impact duration. It is evident that, whilst both ball types are designed to meet the same specifications, their behaviour outside this single test condition is markedly different. Laser measurement of the initial impact location failed to confirm any discontinuity in the contact area.

It appears that normal impact rebound characteristics are dependent primarily upon the core characteristics. Whilst the addition of cloth provides some stiffening its effect on the physical characteristics is of secondary importance.

---

## 6 A High Stain Rate Finite Element Rubber Model

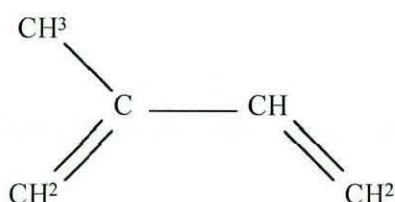
### 6.1 Introduction

#### 6.1.1 The Development of Modern Rubber

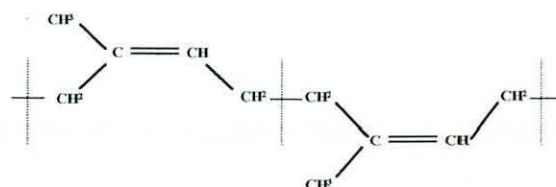
Rubber can be thought of as any material which may be stretched considerably and returns to its approximate original shape on release. However, in this chapter we are concerned only with rubber manufactured using the naturally occurring raw gum elastomer polyisoprene, commonly known as *natural rubber*. The tree *Hevea brasiliensis*, having originated in Brazil and been introduced to Malaysia and Indonesia, current world leaders in the production of raw *natural rubber*, secretes a milky sap which is a mixture of water and polyisoprene, along with various proteins and carbohydrates which are mostly removed. Drying out this sap produces latex, of the form used in medical gloves and condoms with a raw rubber content of around 90%, whilst the sap contains only around 35%. Despite rubber being named for its ability to rub out pencil marks, it was the mechanical properties that were of interest to early scientists. Indeed, the mechanical properties of natural rubber were recognised more than 2000 years ago by the Aztecs and Mayas of South America, using it for shoe soles, coated fabrics and playballs (Ciesielski, 1999).

Rubber used in its 'natural' form exhibited a characteristic which could be an advantage or a problem; it was stiff at low temperatures and sticky in the heat. This remained a problem until the 19<sup>th</sup> century when Charles Goodyear revolutionised the rubber industry by combining the latex with sulphur and white lead and then heating the mixture. This produced a leather-like material with much improved mechanical properties and less temperature dependence. This process, later named vulcanisation after Vulcan, the god of fire, is the basis for the majority of rubber products (including sports balls) that exist today.

All rubbers, both natural and synthetic, are built from hydrocarbon units called monomers. Within each monomer adjacent carbon atoms are linked by either single (saturated) or double (unsaturated) bonds. An isoprene monomer is shown in Figure 6.1a and it can be seen that the double bonds exist at either end. As these bonds are more chemically reactive than single bonds it is possible, using an outside agent, for the carbon atoms on each end of the monomer to link up with corresponding atoms on another. This can start a chain reaction (polymerisation) eventually leading to a superchain called a polymer, which contains thousands of monomers. As the double bonds have become single bonds then the free links created on the middle atoms combine to create a new double bond within the monomer. Figure 6.1b shows the isoprene 'unit' as part of a polymer chain, hence polyisoprene. Natural rubber polymer chains consist of about 3000 to 5000 isoprene units.



**Figure 6.1a – An Isoprene Monomer.**



**Figure 6.1b – An Isoprene Monomer forming part of a Polyisoprene Chain**

So it is seen that raw gum elastomers consist of thousands of separate polymer chains, all coiled up and tangled together like spaghetti but mostly independent of other polymer chains. The material is in a solid state as the size of the polymer chains prevents much molecular movement, but as each chain is separate within the material, it may be better thought of as a very slowly moving (viscous) liquid. The process of vulcanisation works by taking advantage of the unused double bonds in the polymer chains to join them to each other in a process called cross-linking. The improved material properties previously reported are the result of these cross-links making the material more stable. In Goodyear's original process, sulphur was used to create these cross-links and it is still used today in a large number of rubbers. There are many forms of vulcanisation, some not involving sulphur at all, but these are beyond the scope of this work.



---

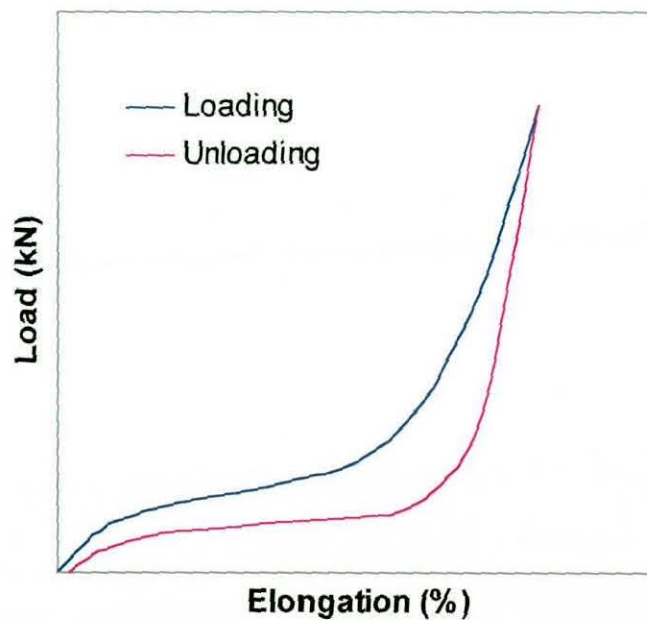
A further advance in rubber production came later in the nineteenth century when John Dunlop invented the first commercially successful pneumatic tyre. It was found that introducing a powder called carbon black into the rubber further improved its mechanical properties. This was the first use of fillers in commercial rubber. Whilst cured raw gum elastomers are strong, vulcanisation has a weakening effect and so fillers are used to reinforce the material. The reinforcement provided is dependant upon the size of the filler particles (smaller particles give better reinforcement) as well as particle shape and surface chemistry. Carbon black, silica, clay and chalk are all popular fillers.

### **6.1.2 Mechanical Properties of Vulcanised Rubber**

A typical plot of load against elongation for rubber in Figure 6.2 shows a marked difference in behaviour to that of metals. Rubber is non-linear; in other words it does not obey Hooke's law and so cannot be given a simple elastic modulus. It may also be elongated to several times its initial length and still recover its original shape. However, during this recovery energy is lost to internal friction and manifested as heat. This recovery loss is termed hysteresis and is characterised by an open loop on the extension/relaxation plot in Figure 6.2, with the energy lost equal to the area within the loop. In natural rubber the energy loss is relatively small compared to synthetic rubbers which, for objects that are subject to repeated deformation during a short time (such as sports balls) is important. Highly filled rubbers also have much larger hysteresis losses. Cyclic loading causes more energy in the form of heat to be stored within the material and as the temperature increases, so the properties of the rubber itself change, as will be shown later. With each cycle the loop becomes smaller and so the energy loss is reduced, due to a stress-softening phenomenon called the 'Mullins' effect. Loading causes some molecular bonds to be broken which results in softer material behaviour, seen as a smaller gradient in the stress/strain curve and a corresponding reduction in the size of the hysteresis loop. With each cycle the number of potentially breakable bonds is less and so the losses reduce until the material reaches a constant state. If the loading is stopped, then over time bonds will re-establish and the material stiffness will increase.

---

Figure 6.2 also shows that after relaxation, the rubber has not returned completely to its original state. This is because rubber is not completely elastic, although if allowed time to rest this residual strain will reduce somewhat. This process is known as stress relaxation and is inherent to rubber. In reality it occurs very rapidly and in order to see it to the effect shown in Figure 6.2 the rubber would have to be loaded and unloaded almost instantly.



**Figure 6.2 – Typical Force against Elongation Plot for Natural Rubber.**

---

Both hysteresis and stress relaxation are viscous effects and so rubber is said to be viscoelastic. It is classically defined as a combination of an elastic solid, obeying Hooke's law and a viscous liquid, described by Newton's law.

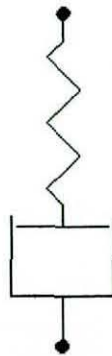
Hooke's law:  $\sigma = E\varepsilon$

where stress  $\sigma$  is equal to strain  $\varepsilon$  multiplied by an elastic modulus  $E$  (a basic spring model)

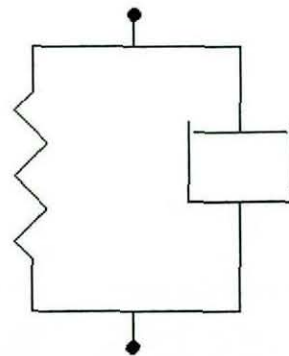
Newton's law:  $\sigma = \eta\dot{\varepsilon}$

where stress is equal to strain rate  $\dot{\varepsilon}$  multiplied by a viscosity modulus  $\eta$  (a basic dashpot model)

It is common to use mass spring damper models to represent the material behaviour. Figure 6.3a shows a Maxwell model, where the systems are in series, whereas Figure 6.3b shows a Voigt model, where the two are in parallel.



**a – Maxwell Model**



**b – Voigt Model**

**Figure 6.3 – Mass Spring Damper Models of Viscoelastic Behaviour.**

Both models may be used to describe rubber behaviour and the deformation history of each subject to a unit load is seen in Figure 6.4 overleaf.



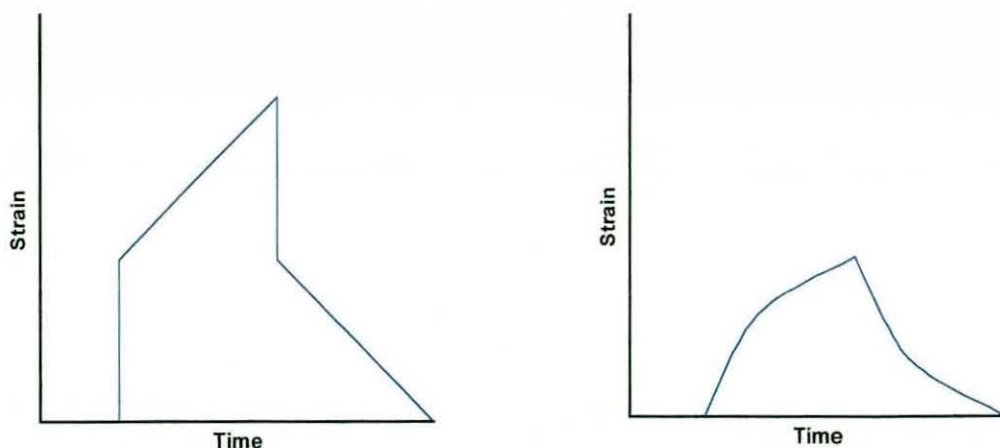


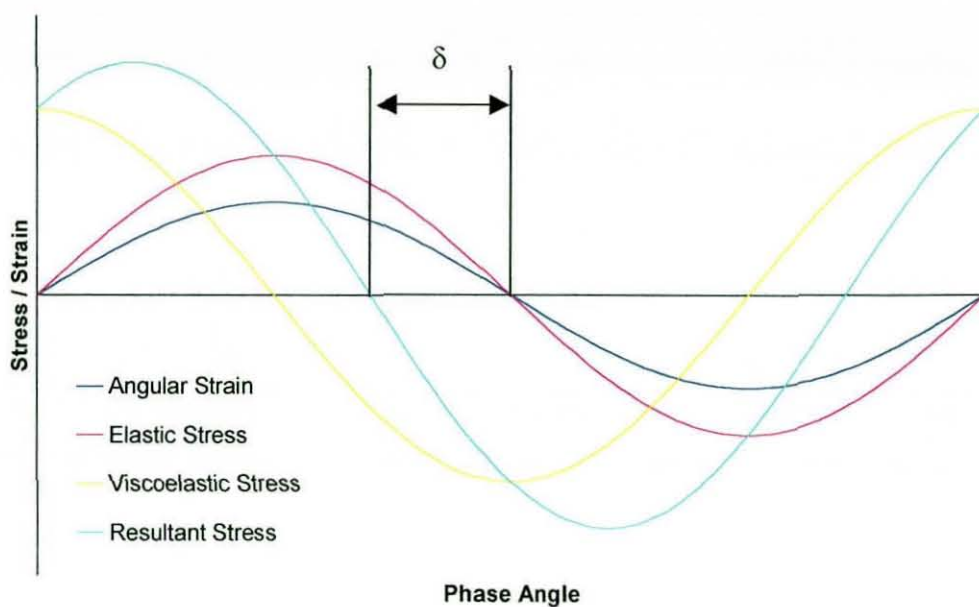
Figure 6.4 - Strain Histories for the Maxwell and Voigt Models.

In both models the viscous strain, and hence stress, lags the dynamic stress. It is common to relate the two values using the formula:

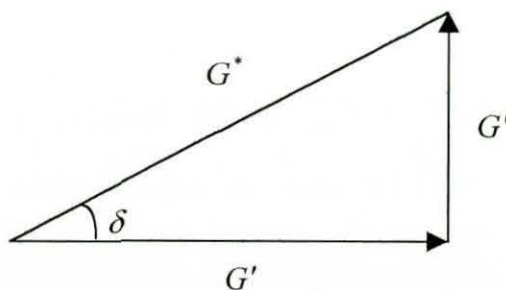
$$G^* = G' + iG''$$

where  $G^*$  is the complex modulus, comprising a real elastic component  $G'$  and an imaginary viscous component  $G''$ . This idea is used in modern standard tests for viscoelastic material properties. The material is loaded through forced vibration and the resulting sinusoidal force is measured by a dynamometer. From this type of test it is possible to show that  $G' \equiv E$ , the elastic modulus and  $G'' \equiv \omega\eta$ , where  $\omega$  is the circular frequency of oscillation and  $\eta$  is the viscosity modulus. A typical plot of angular strain and stress against phase angle  $\omega t$  is shown in Figure 6.5, where it can be seen that the resultant stress  $G^*$  lags the strain by some angle  $\delta$ . The elastic stress is also out of phase with the viscous stress by an angle of  $90^\circ$ . If the two stress moduli are plotted as a vector diagram in Figure 6.6 then it becomes obvious that the ratio of viscous to elastic modulus is equal to the tangent of the loss angle, i.e.  $\tan \delta = G''/G'$ .





**Figure 6.5 – Dynamic Response of a Viscoelastic Material Subject to a Sinusoidal Load.**

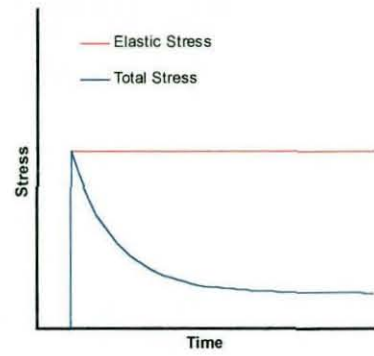
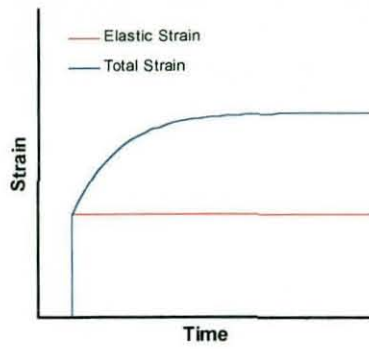
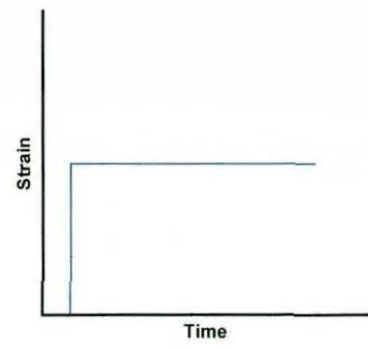
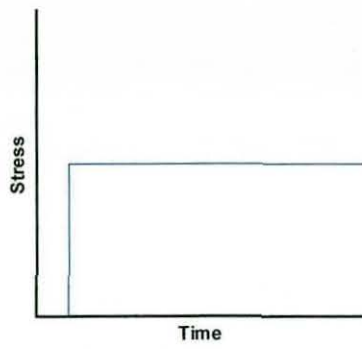


**Figure 6.6 – Vector Representation of Loss Angle.**

All this assumes of course that unfilled natural rubber is being tested. The addition of filler to rubber introduces a large degree of non-linearity above strains of the order of 0.05%. However, unfilled rubber remains linear at much greater strains, over 100%. Ahmadi and Muhr present data for rubbers with increasing carbon black content, showing the non-linearity to be effected mostly at low values of strain (<20%).

---

Another viscoelastic property seen in rubbers is the time dependency of both stress and strain. For a material subject to an instantaneous stress which is then held constant, the corresponding strain will increase over time up to some maximum value as  $t \rightarrow \infty$ , seen in Figure 6.7a. If the stress is subsequently removed then the increased strain is recoverable; this process is commonly known as creep. In a similar process known simply as stress relaxation, a material under a constant strain will exhibit a decay in the corresponding value of stress as  $t \rightarrow \infty$ , as shown in Figure 6.7b. The rate of relaxation in unfilled rubbers is proportional to the instantaneous stress and for materials which behave as viscoelastic fluids, such as unvulcanised rubber, the final value of stress will be zero. However, the timescale of such relaxation can be very long, of the order of months or even years.



**a – Creep in Rubber Subject to a Constant Stress**

**b – Stress Relaxation in Rubber Held at a Constant Strain**

**Figure 6.7 – Time Dependent Rubber Behaviour.**

---

#### 6.1.2.1 Strain Rate Effects

In the above testing, the strain rate is equivalent to the vibration frequency. Ahmadi and Muhr (1997) showed that the values of  $G^*$  and  $\tan \delta$ , even for natural rubber, are affected by changes in temperature and frequency. Figure 6.8 and Figure 6.9 show, in graphical form, the data they present. Whilst temperature dependence is of interest, this effect can be controlled by conducting tests at a specific constant temperature. Of greater importance is the effect of frequency or strain rate on the complex modulus and loss angle. It is seen that both values are increased at greater frequencies, which may be interpreted as the material becoming stiffer and less elastic, i.e. more energy lost during a cycle at higher rates of strain. In both filled and unfilled natural rubbers, the data shows the increase in modulus to be relatively small and at frequencies below 50 Hz, almost linear. The increase in loss tangent is by contrast significant, doubling for unfilled rubber from 50 Hz to 400 Hz, and is non-linear, although the rate of change reduces with increasing frequency.

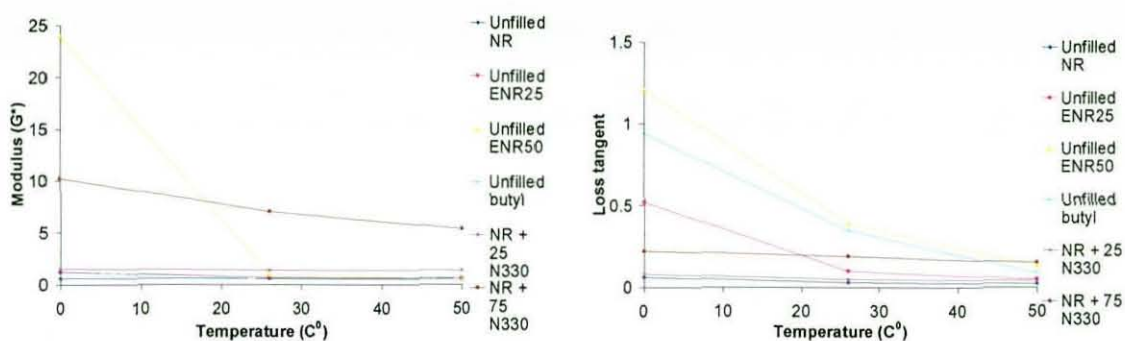


Figure 6.8 – Effect of Temperature on Rubber Properties.

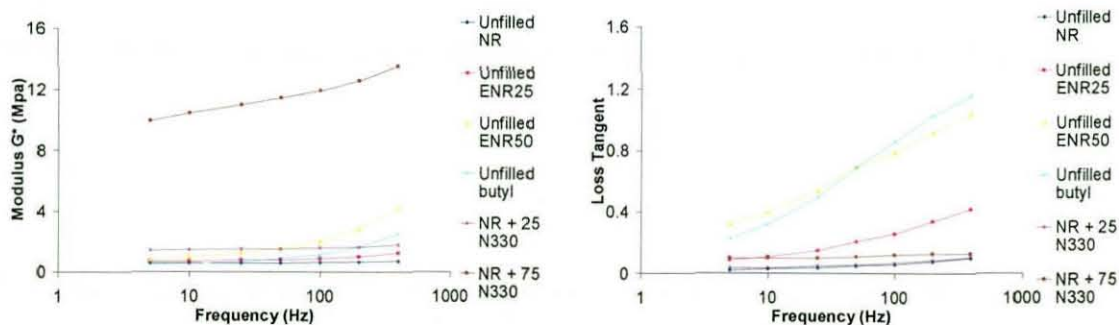


Figure 6.9 – Effect of Frequency on Rubber Properties.



---

### 6.1.3 Developing Constitutive Rubber Models

Rubber constitutive models have been developed using strain energy functions and assume that the material is elastic, isotropic and approximately incompressible. All models are defined in terms of the strain energy density  $U$ , which is the amount of energy stored per unit volume for a specific applied strain. Strain energy potential is defined in terms of strain invariants  $I_1$ ,  $I_2$  and  $J$  which themselves may be defined in terms of principal stretches such that:

$$I_1 = \lambda_1^2 + \lambda_2^2 + \lambda_3^2, \quad I_2 = \lambda_1^2 \lambda_2^2 + \lambda_2^2 \lambda_3^2 + \lambda_3^2 \lambda_1^2, \quad J = \lambda_1 \lambda_2 \lambda_3$$

$$\text{where } \lambda_i = 1 + \varepsilon_i \quad \text{and hence} \quad U = U(I_1, I_2, J)$$

The simplest form proposed by Treloar (1975) is the neo-Hookean, where:

$$U = C_{10}(I_1 - 3)$$

$C_{10}$  is a calibration constant, which may be derived from the elastic modulus. The equation is developed from statistical theory whereby any bond within a polymer chain is free to rotate about the axis of adjoining bonds. The length and configuration of a statistical polymer chain can then be calculated with the distribution of all other chains within the material defined by a Gaussian function. It is then possible to develop a model based on assumptions such as the number of chains per unit volume, the position of cross-links being fixed and the presence of cross-links not affecting chain configuration. The resulting model provides a good first approximation of rubber behaviour.



---

The Mooney-Rivlin form extends this to include a second term:

$$U = C_{10}(I_1 - 3) + C_{01}(I_2 - 3)$$

$C_{01}$  is an additional calibration constant. It is the most general form describing a linear relationship between stress and strain in simple shear and provides a marginally better fit to experimental data. However, as neither model takes account of chain extension being finite, they are only accurate for relatively low strains.

A more general model is the polynomial strain energy function, taking the form:

$$U = \sum_{i+j=1}^N C_{ij} (I_1 - 3)^i (I_2 - 3)^j$$

It can be seen that for an incompressible model with  $N=1$  the equation reduces to the Mooney-Rivlin form and that further, if  $C_{01} = 0$  then we have the neo-Hookean form. With the use of further orders of expansion ( $N \geq 2$ ) then higher levels of strain can also be represented. The Ogden model defines  $U$  based on the principal stretch ratios:

$$U = \sum_{i=1}^N \frac{2\mu_i}{\alpha_i^2} (\lambda_1^{\alpha_i} + \lambda_2^{\alpha_i} + \lambda_3^{\alpha_i} - 3)$$

Here,  $\mu_i$  and  $\alpha_i$  are calibration constants. Again, the Ogden model may be reduced to the Mooney-Rivlin form by setting  $N=1$ ,  $\alpha_1 = 2$  and  $\alpha_2 = -2$  whereas if  $N=1$  and  $\alpha_1 = 1$  then we have the neo-Hookean model once more.

---

### 6.1.3.1 Rubber Models in ABAQUS/Explicit

Within ABAQUS, all of the hyperelastic strain energy functions are defined in terms of deviatoric or revised strain invariants  $\bar{I}_j$  and deviatoric stretches  $\bar{\lambda}_i$ , where  $\bar{\lambda}_i = J^{1/3} \lambda_i$ , in order to differentiate between deviatoric and volumetric effects, which are expressed as separate terms within the equations. ABAQUS/Explicit allows the use of three models, which are the Ogden, Polynomial and Reduced Polynomial strain energy functions. Another model, the Yeoh form, is available but is simply a special case of the reduced polynomial where  $N=3$ . The reduced polynomial itself is a special case of the polynomial form where  $j=0$ . It is seen that setting  $N=1$  gives the neo-Hookean form. The reduced polynomial equation may be used in Abaqus for values of  $N$  from 1 to 6, as can the Ogden model. The polynomial form however can only be used for  $N=1$  or  $N=2$ .

All strain energy equations within Abaqus may be defined in two ways. The coefficients may be specified directly, or else they may be computed by the software from user specified material test data. As all models define elastic behaviour, it is possible to define the coefficients from a knowledge of the value for  $G'$ , however as this value is determined by complex vibration testing then the use of simple static tests is often preferred. The test data may be from one or more of the following: uniaxial tensile or compressive tests, equibiaxial tensile or compressive tests and planar tensile or compressive tests. Some of these are equivalent to one another so not all need to be performed. Uniaxial tension is equivalent to equibiaxial compression, and vice versa, whilst planar tension and compression are also similar. Choice of model is made on the availability of test data. Both the polynomial and Ogden forms require more than one set of test data to provide accurate results for different deformation modes. The reduced polynomial model, having no dependence on  $\bar{I}_2$ , will provide more accurate results for all deformation types if only one set of data is available. Also, use of the polynomial model with  $N=2$  or the Ogden model with  $N \geq 3$  requires experimental data for strains to at least 100% in tension and 50% in compression.

---

---

### 6.1.3.2 Adding Viscoelastic Effects

Whilst all the previously mentioned models are designed to predict rubber deformation and hence can be defined in terms of the elastic modulus  $G'$ , they make no reference to the energy lost during the relaxation phase, or the loss factor  $\tan \delta$ . Hence all models predict perfectly elastic behaviour with no account taken of hysteresis effects. In order to accurately predict the behaviour of a deformation cycle, it is necessary to incorporate some means of energy loss into the model. ABAQUS/Explicit provides two methods by which this may be accomplished.

A viscoelasticity function is available which describes rate-dependant material properties, assuming independent deviatoric (shear) and volumetric behaviours and is similar to those of the hyperelastic functions defined previously. The model is based on the ability of viscoelastic materials to exhibit stress relaxation. Abaqus uses this phenomenon to define a relaxation modulus as a function of the instantaneous stress. The viscoelasticity function then replaces the elastic coefficient within any of the models (i.e.  $C_{ij}$  or  $\mu_i$ ) with a corresponding relaxation coefficient  $C(\tau)$  or  $\mu(\tau)$ . Similarly, the bulk modulus  $D_i$  is replaced with a bulk relaxation modulus  $D(\tau)$ , although this may be eliminated if the material is considered incompressible. Each is defined using a Prony series of the form:

$$C_{jk}(\tau) = C_{jk}^0 \left[ 1 - \sum_{i=1}^n \bar{g}_i^P (1 - e^{-\tau/\tau_i}) \right]$$

$\bar{g}_i^P$  is the dimensionless shear relaxation modulus.

$C_{jk}^0$  is the instantaneous shear coefficient  
( $\equiv C_{ij}$  in the hyperelastic model).

---

The function is expressed in terms of the relaxation time  $\tau$  and is defined within the software either by directly specifying the moduli at each time  $\tau_i$ , or by the input of test data from either a creep test or a stress relaxation test. Both can be related by a simple equation which allows the software to determine appropriate model constants from either form of test data. However, in order for the model to produce accurate results, it is necessary to include data over the time domain of interest. This introduces serious problems for high speed analysis, as the equipment used to perform these standard tests has a response time greater than the time domain of interest.

It is a much simpler process to use the damping option within ABAQUS to define energy loss. This option provides Rayleigh damping specified by two damping factors  $\alpha_R$ , the mass proportional damping term and  $\beta_R$ , the stiffness proportional damping term. Mass proportional damping creates damping forces due to the absolute velocities of the model, being proportional to the mass matrix for each element. It can be visualised as if the model is moving through a viscous ether so that any motion of any point produces a resisting force. Stiffness proportional damping introduces damping stresses  $\sigma_d$  proportional to strain rate. It can be thought of as viscous material damping, creating additional stress proportional to the strain rate, given by the equation:

$$\sigma_d = \beta_R D^{el} \dot{\epsilon}$$

$D^{el}$  is the elastic stiffness in the strain-free state (i.e.  $D^{el} \equiv G'$ ).

The fraction of *critical damping* (being 100% damped) for a particular mode is given by the equation:

$$\xi_i = \frac{\alpha_R}{2\omega_i} + \frac{\beta_R \omega_i}{2}$$

where  $\omega_i$  is the frequency of the mode of interest.

---

However, it must be noted that whilst damping may be desirable to control a particular vibration mode, the chosen damping factor will be applied to all modes equally. It is the amount of damping applied at the highest mode that controls the stable time increment of the analysis and so the change in stable time increment is:

$$\Delta t \leq \frac{2}{\omega_{MAX}} \left( \sqrt{1 + \xi_{MAX}^2} - \xi_{MAX} \right)$$

where  $\omega_{MAX}$  is the frequency in the highest mode.

$$\text{and } \xi_{MAX} = \frac{\beta_R \omega_{MAX}}{2}$$

Where  $\xi_{MAX}$  is the damping in the highest mode.

This assumes that only stiffness proportional damping is used and shows that the decrease in stable time increment is proportional to  $\omega_{MAX}/\omega_i$  in this case. However, using only mass proportional damping gives the maximum damping as:

$$\xi_{MAX} = \frac{\alpha_R}{2\omega_{MAX}}$$

The decrease in stable time increment is now proportional to  $\omega_i/\omega_{MAX}$ . This implies that in general, mass proportional damping should be used for low frequency modes whilst stiffness proportional damping performs best for higher frequency modes.

---

#### 6.1.4 Tennis Ball Core Construction Method

Whilst an individual rubber compound of a ball manufacturer is a closely guarded secret, it is likely to consist of the raw gum elastomer, sulphur, accelerators, filler and possibly other ingredients. It is this compound which when mixed will provide the mechanical properties required for the ball to bounce as specified by the ITF. Once mixed, the compound is extruded into small pellets which are then placed in moulds and cured under pressure. The result is a vulcanised hemispherical shell of rubber which is then adhered to a similar shell under pressure using a different compound rubber as the adhesive. The result is a hollow rubber sphere with an internal pressure that may be greater than or equal to atmospheric depending upon the type of ball being manufactured.

Having previously seen the effect of fillers to reduce elasticity and knowing that a tennis ball core is highly elastic then one must assume that the quantity of fillers used in tennis ball rubber is low and/or is of a type that has little effect on the elastic properties. It can then be assumed that strain amplitude has no effect on elastic or loss moduli so that the two values depend only on frequency.



---

## 6.2 Methodology

Materials tests are available for high strain rate testing of rubbers using methods such as the exploding wire technique, where a cylinder of material is rapidly loaded by a shockwave, generated from an exploding wire passing through its centre (Al-Maliky and Parry, 1996). Unfortunately these tests are highly specialised and so are neither easily accessible nor financially appealing. However, it is possible using the information previously presented to perform simple 'static' tests and extrapolate to data at higher strain rates.

Rubber tensile tests are specified in a number of standards, generally all being identical. The British Standard is BS903 Part A2, with the equivalent American Standard (ASTM) being D412 and the International Standard ISO 37. The test defined by these standards allows specification of tensile strength, elongation at break, stress at a given strain and elongation at a given stress, for any vulcanised (or thermoplastic) rubber. Rubber test pieces may be either dumb-bell shaped or ring shaped, although as stress is non-uniform over the cross section of ring test pieces, these are only suggested for use in automated testing where they may be more easily handled. Within the dumb-bell shape, there are four types specified, although type 3 and 4 are basically miniature test pieces for applications where insufficient material is available for types 1 and 2. Dimensions for all four types are specified in BS903 and are designed to exhibit extension within only the narrow portion such that the resulting stress may be considered uniform throughout the section. The tensile test itself is performed using a tensometer such as the Instron (model 4411). This machine allows measurement of tensile load up to 10kN via a load cell which is mounted between the top jaw and the travelling arm. The arm is driven by a screw thread at a speed of up to 999mm/min, whilst the lower jaw remains fixed. The system is controlled by a computer allowing the specification of a standard test or any reasonable user defined conditions. Load and displacement data is then output to the p.c. at regular intervals over a specified range and with previous knowledge of the test piece geometry, may be manipulated to provide results in terms of stress and strain.

---

---

The resulting stress/strain data is of the form required by Abaqus to define a material using the test data input option and can be read directly from an ASCII text file. As data is restricted to the tensile test only, the reduced polynomial strain energy equation is expected to provide the most accurate modelling solution based on the specified test data. In order to verify this all three material models were generated over the range of possible levels ( $N=1,2,3$ , etc) and the resulting stress-strain curves were compared to the original test data. As previously discussed, the use of only a single set of test data requires careful selection of the material model in order to provide accurate solutions to other modes of deformation. Where experimental data is provided for the tensile test only, it has been shown that the most appropriate material models to use are the reduced polynomial ( $N=2,3$ ), Ogden ( $N=1,2$ ) and polynomial ( $N=1$ ). In order to determine the best model to use for further analysis, data fits will be performed for each of these models over the range of strain described in the experimental data.

Having decided upon the most appropriate material model from the test described above it is then necessary to consider the effect of strain rate. From part 6.1.3 it is seen that the rubber model coefficients are proportional to material stiffness and so it is possible to increase these coefficients thereby raising material stiffness in a manner appropriate to the increased strain rate. To assess the effect of this process on the core model, normal core impacts were simulated using rubber material models of varying stiffness and the results compared to those from chapter 5. It was expected that material stiffness would affect all the characteristics previously discussed; namely COR, impact duration and gross deformation.

Once an appropriate stiffness level had been reached where model data closely matched the experimental results, the effect of material damping could be assessed. As the amount of damping is proportional to the energy lost during impact, it follows that COR would provide a good indication of how much damping is required. Effects on impact duration and deformation would be less marked as these values should be unrelated to the relaxation phase of the deformation cycle.

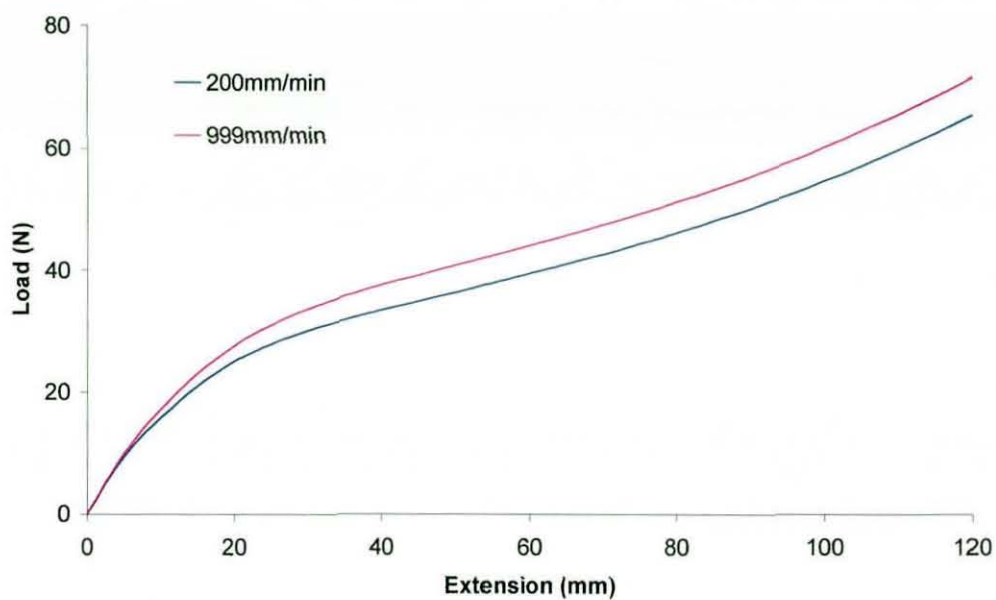
---

## 6.3 Results

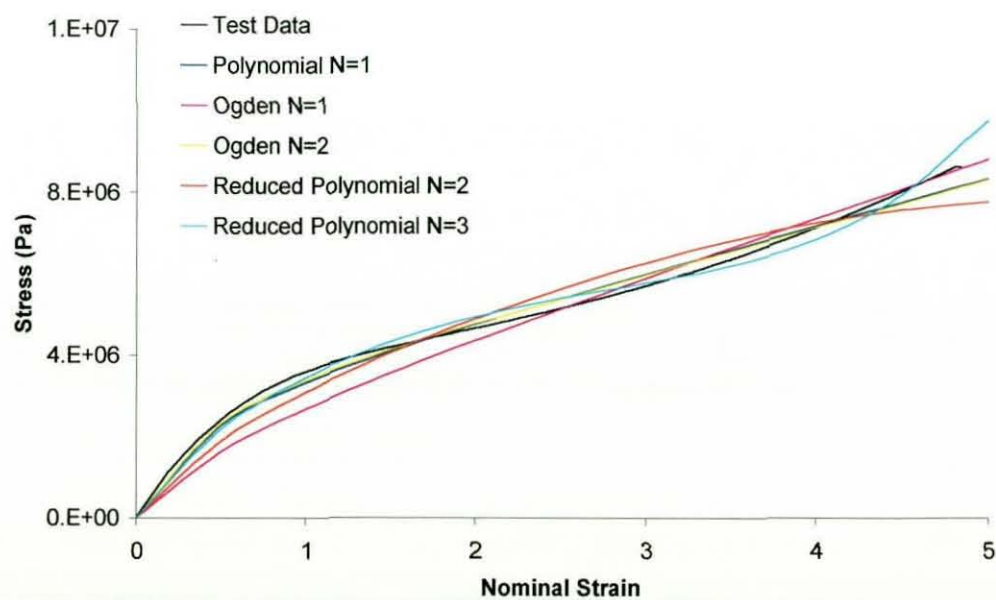
### 6.3.1 Low Strain Rate Tensile Testing and Subsequent Model Development

A standard tensile test of the rubber used in constructing pressurised tennis balls yields results of the form shown in Figure 6.10. The tennis ball compound exhibits the classic characteristic curve seen in rubbers where the initial modulus is high but quickly reduces, before increasing again at the highest strain levels. The two curves represent averaged results over a series of tests at two separate rates of extension, one at 200mm/min being some arbitrarily low value and one at 999mm/min being the maximum speed of the tensile tester. As all samples were cut to the same specimen size then the rate of extension may be equated to the strain rate. It is seen that there is a marked dependence upon strain rate even at these relatively low values. A five-fold increase in strain rate has resulted in an additional load of 6.2N ( $\approx 10\%$ ) required to produce equivalent extension at a level just below failure. It is obvious that strain rate effects will be many orders of magnitude greater during a core impact.

The characteristic curves displayed in Figure 6.10 describe exactly how the material behaves during loading at the specified rates of extension. ABAQUS uses a 'least-squared' data fit to produce material models that best describe the experimental test data. This results in material behaviour being approximated over the range of strain, specified by a series expansion. It is therefore necessary to assess the accuracy of each material model through comparison with the tensile test data. Initially, all models are compared over the full range of test data at 900mm/min, up to a nominal strain of five, with the results seen in Figure 6.11 for each model type considered. It is seen that the accuracy varies considerably from first order approximation in the Ogden  $N=1$  with a maximum error of around 30% at  $\epsilon=1$  to less than 10% error in the polynomial and Ogden  $N=2$  models. Neither reduced polynomial model provides a good fit to the experimental data.



**Figure 6.10 – Averaged Tensile Test Data for Pressurised Tennis Ball Core Rubber Compound at Rates of Extension of 200 and 999mm/min.**



**Figure 6.11 – Comparison of Material Models and Experimental Data to a Nominal Strain of Five.**

---

It is expected that the maximum strain experienced locally during a tennis ball impact will be less than one, probably nearer one half. It is not necessary to predict material behaviour above this level and in reducing the range of strain considered by the material model then the data fit should also improve. Figure 6.12 shows predicted material behaviour for the same constitutive models but is fitted only to the data between strains of zero and one. It is seen that there is a significant improvement in accuracy for all models with a maximum error of 5% at strains of around one half. Whilst the Ogden  $N=1$  and reduced polynomial  $N=2$  models are again the least accurate the difference is now only small. In Figure 6.13 we see material models fitted to the experimental data in the range of strain from zero to one half, where there appears to be little increase in the accuracy of the fit.

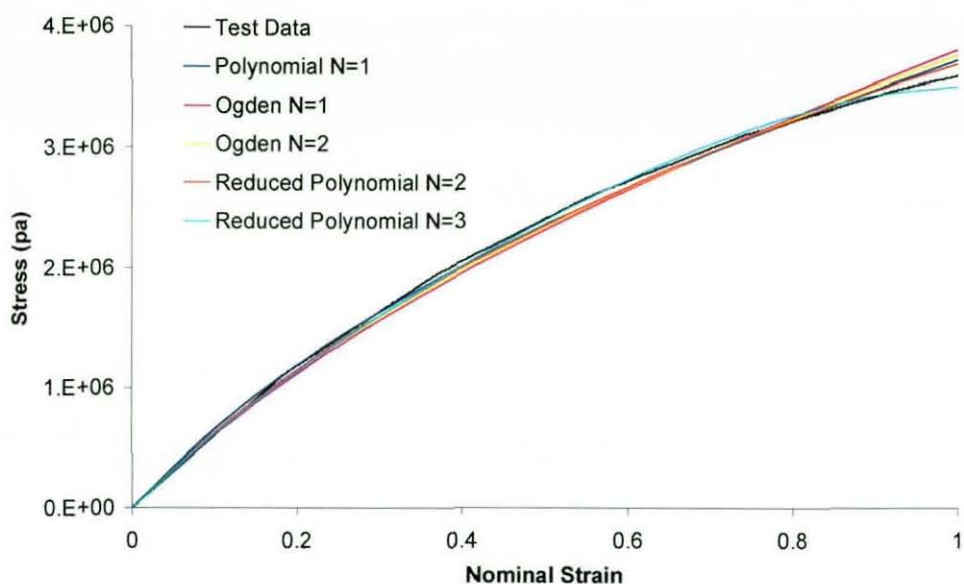


Figure 6.12– Comparison of Material Models up to a Nominal Strain of One.

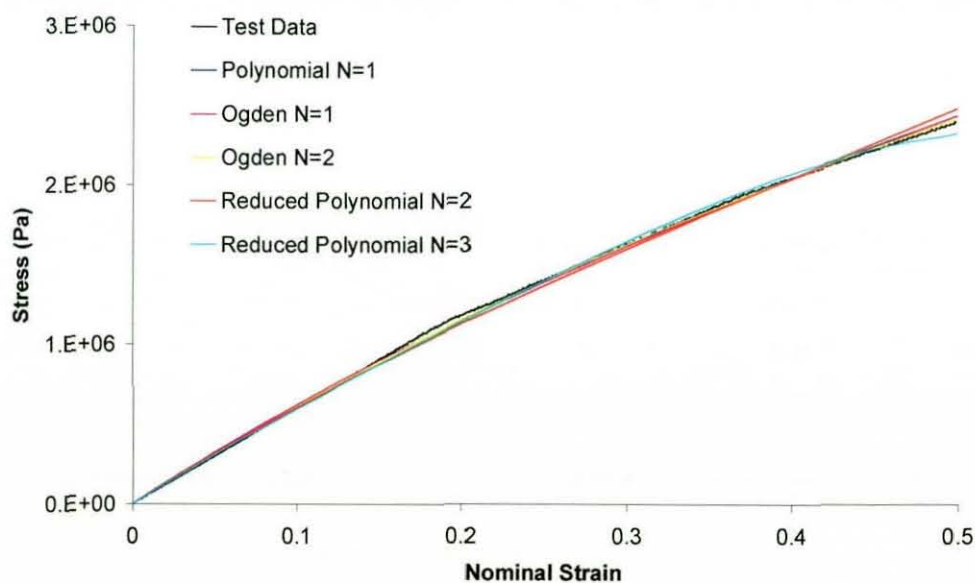


Figure 6.13 - Comparison of Material Models up to a Nominal Strain of One Half.



### 6.3.2 Increasing Strain Rate Within the Model

The material coefficients derived from the low strain rate experimental data have been inserted into the core impact model. The resulting post impact characteristics of COR and impact duration have then been compared to the core normal impact experimental data from chapter 5 for each impact velocity.

It is known that the coefficient  $C_{10}$  may be related to the elastic modulus of the material and hence the material model may be made stiffer by increasing  $C_{10}$ . Figure 6.14 shows the effect of increasing  $C_{10}$  in a two term reduced polynomial expansion on the stress/strain characteristics of the material model and is as would be expected. The effect appears linear such that doubling  $C_{10}$  results in a corresponding increase in stress at a given strain to twice the original value. Also in Figure 6.14 we see that the coefficient  $C_{20}$  which is negative in this case, is only influential on material behaviour above strains of 0.2. A negative decrease in value corresponds to an increase in elastic modulus and so results in a corresponding increase in local gradient of the stress strain curve. Whilst this may allow modification of the higher speed impact models where strains are greater, the effect compared to that for  $C_{10}$  is small.

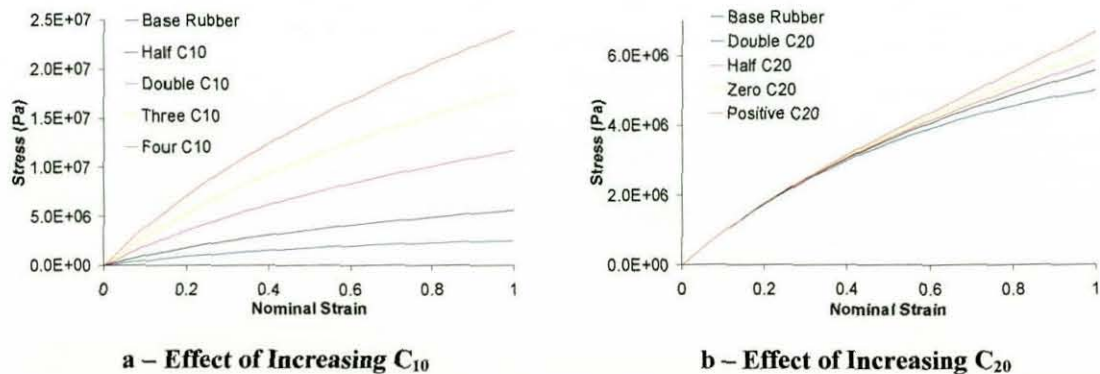


Figure 6.14 – Effect of Increasing Coefficients  $C_{10}$  on Reduced Polynomial Rubber Model.

Normal impact models using increasing values of  $C_{10}$  were run and the resulting characteristics are shown in Figure 6.15 and Figure 6.16. In Figure 6.15 we see that COR is dependent upon material stiffness such that a stiffer model will exhibit greater values of COR. Increasing stiffness also results in a lower impact duration as seen in Figure 6.16. There are also reductions in maximum gross deformation both normal and tangential to the surface, although this effect is not considered at this stage.

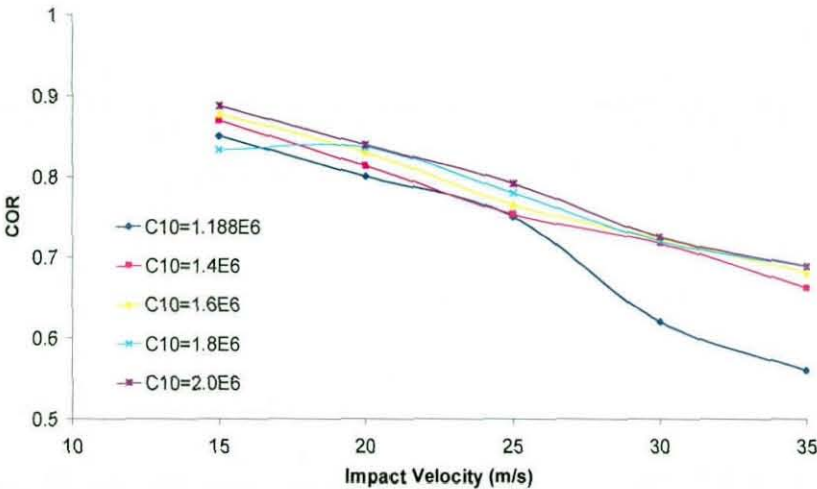


Figure 6.15 – Effect of Increasing Stiffness Coefficient  $C_{10}$  on COR for Impact Model.

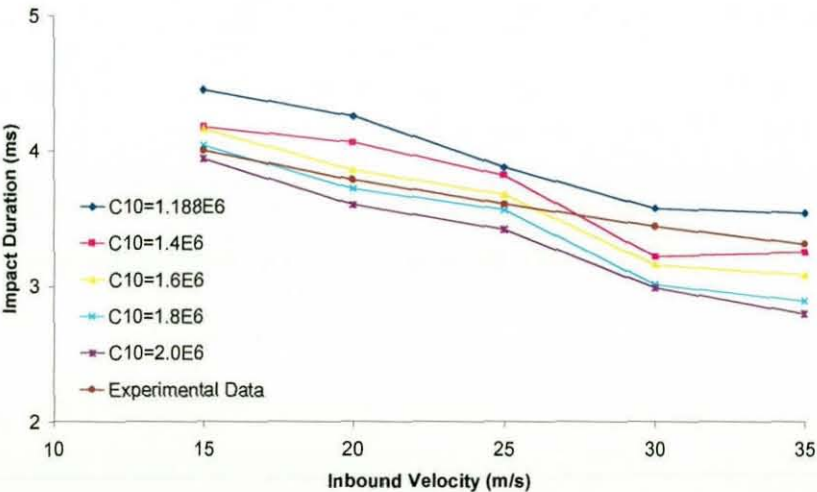


Figure 6.16 – Effect of Increasing Stiffness Coefficient  $C_{10}$  on Impact Duration for Impact Model.

---

### 6.3.3 Material Damping

As previously discussed, strain rate not only affects material stiffness but also energy loss through hysteresis or stress relaxation. Whilst no experimental data was obtained for the hysteresis properties of the tennis ball rubber, the energy loss during impact may be implied from the experimental data in chapter 5. In fact, as COR is the ratio of rebound to incident velocity and velocity itself is a measure of the kinetic energy in the system, then COR essentially equates to the energy lost during impact. By adding increasing levels of damping to the model, the corresponding effects on the impact characteristics are seen in Figure 6.17 and Figure 6.18. As expected, Figure 6.17 shows that the damping coefficient is proportional to a negative function of COR, i.e. increasing damping reduces COR, but the relationship is non-linear. Interestingly in Figure 6.18 we see that there is little effect on impact duration due to damping. Again, there are corresponding reductions in maximum gross deformation with increasing values of damping coefficient, but this is not shown here.

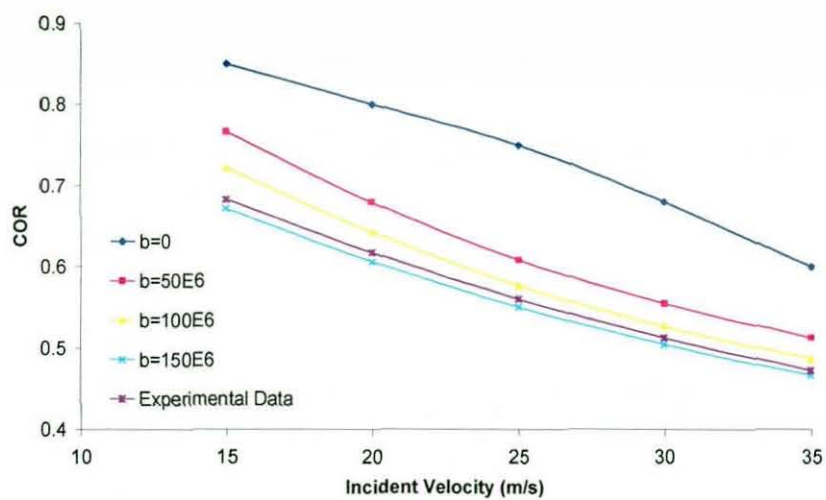


Figure 6.17 – Effect of Increasing Damping Coefficient  $\beta_R$  on COR for Impact Model.

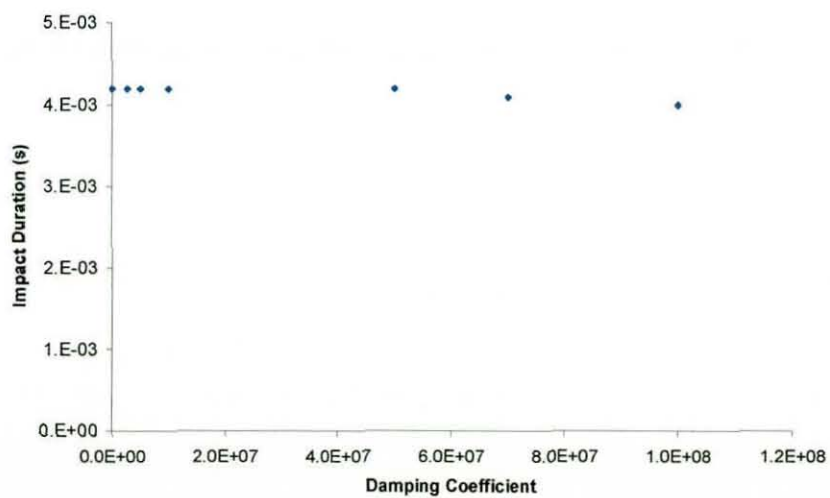


Figure 6.18 – Effect of Increasing Damping Coefficient  $\beta_R$  on Impact Duration for Impact Model at 15m/s.



---

#### 6.3.4 Developing the Finished Pressurised Core Model

The effects of strain rate, implied through changes in material stiffness (elastic modulus) and damping factor (loss modulus), upon the impact characteristics of the core model have been shown. By using these results it is possible to tune the material parameters to reproduce impact behaviour seen experimentally. As impact duration may be considered independent of damping coefficient, then it is possible to change the material model coefficient  $C_{10}$  until the difference between predicted model impact results and the experimental data is acceptably small. Then the COR may be altered by increasing damping coefficient until a similar agreement is seen. Maximum gross deformation values may be used as a check that the material behaviour is predicting accurate impact characteristics.

Through an iterative process, values of  $C_{10}=1.75E6$  And  $C_{20}=-3.9E4$  are arrived at, with a corresponding damping coefficient of  $\beta_R=137E6$ . The resulting impact characteristics are seen in Figure 6.19 to Figure 6.22. Good agreement is seen in all cases, as would be expected.

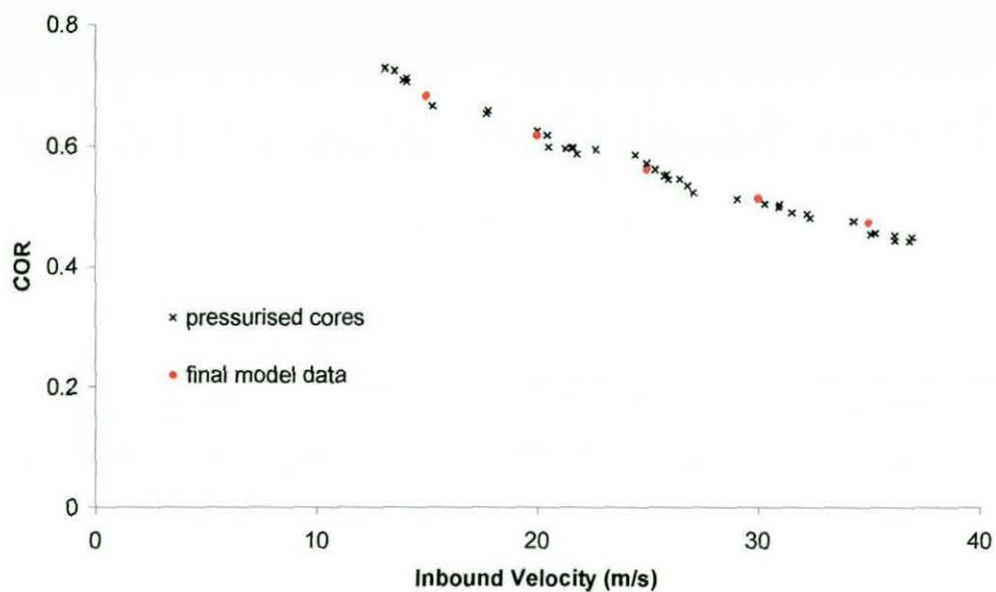


Figure 6.19 – Comparison of Final Pressurised Core Model with Experimental COR Values.

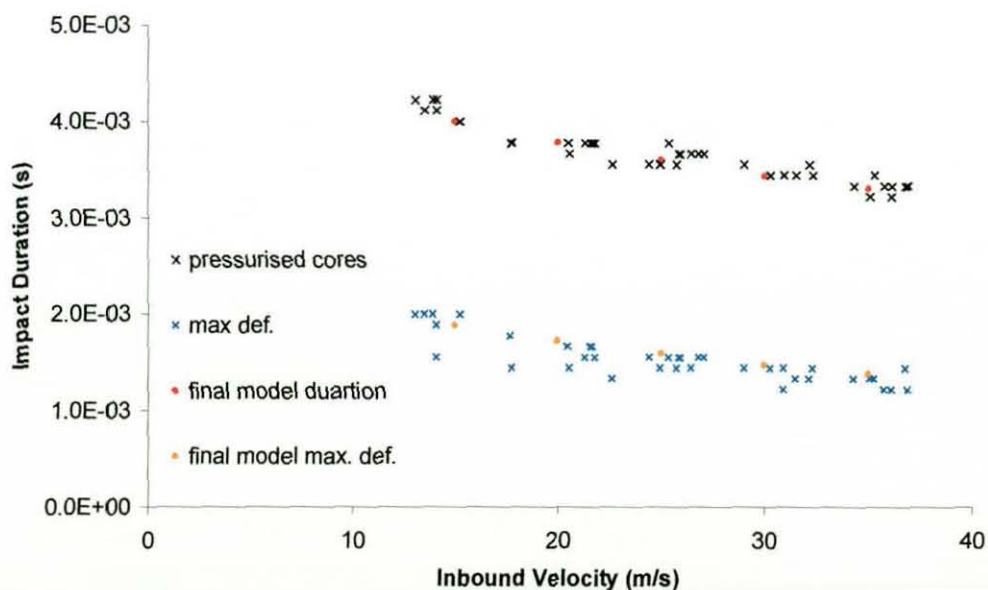


Figure 6.20 – Comparison of Final Pressurised Core Model with Experimental Impact Duration.



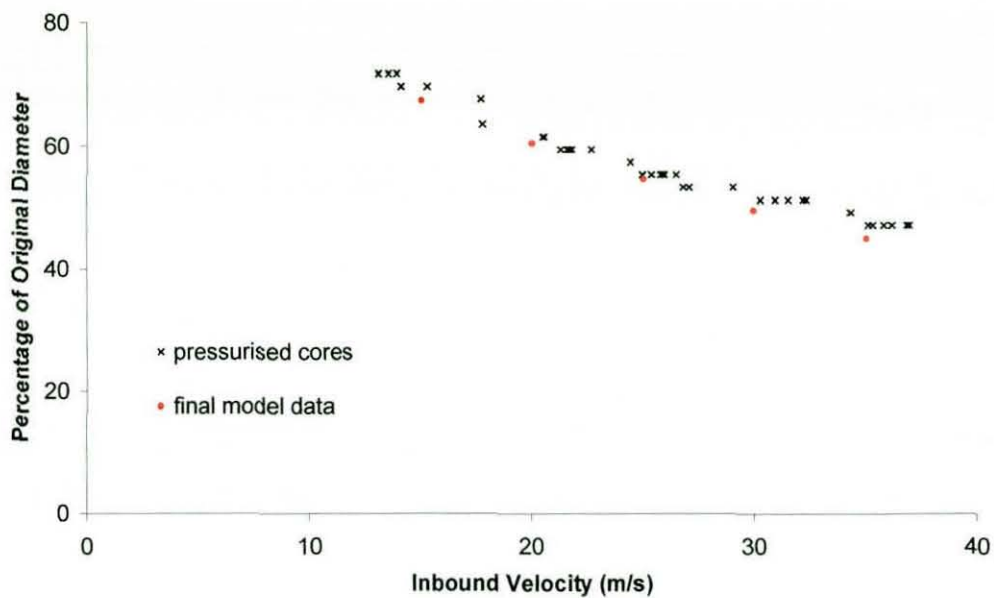


Figure 6.21 – Comparison of Final Pressurised Core Model with Experimental Gross Normal Deformation Values.

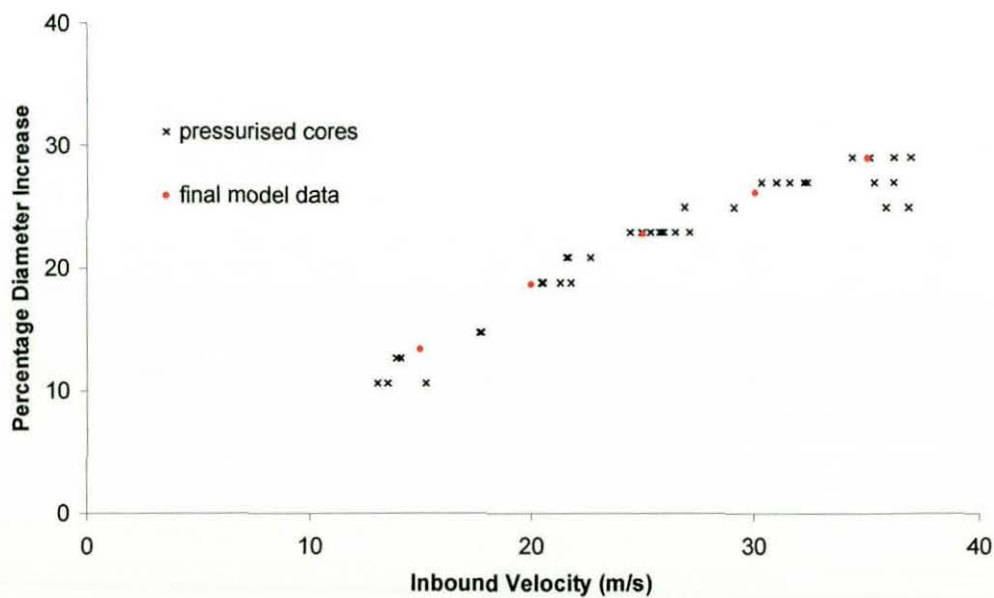


Figure 6.22 – Comparison of Final Pressurised Core Model with Experimental Gross Tangential Deformation Values.

---

### 6.3.5 Developing the Finished Pressureless Core Model

Through a similar process, a pressureless core rubber material model may be developed. The only difference between the two is that the pressureless core is thicker as the lack of internal pressurisation requires the rubber to provide all of the rebound energy. As the cores must be of equal weight then the corresponding density is less. The final coefficients for the pressureless rubber model are  $C_{10}=1.8E6$ ,  $C_{20}=-3.6E4$  and  $\beta_R=80E6$ . Using this material description, the pressureless core model behaves as shown in Figure 6.23 to Figure 6.26. Again, the expected agreement between all the characteristics is seen.

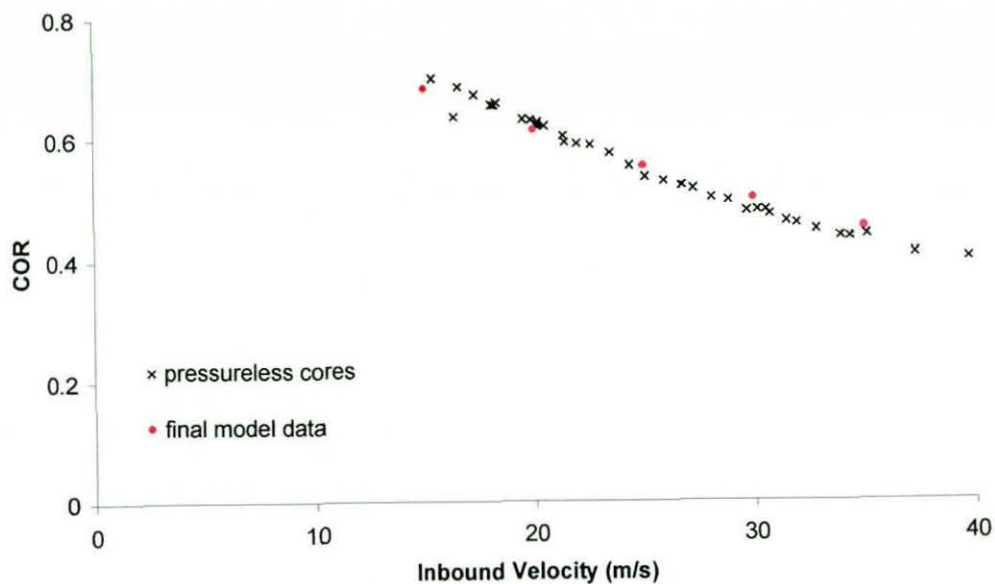


Figure 6.23 – Comparison of Final Pressureless Core Model with Experimental COR Values.

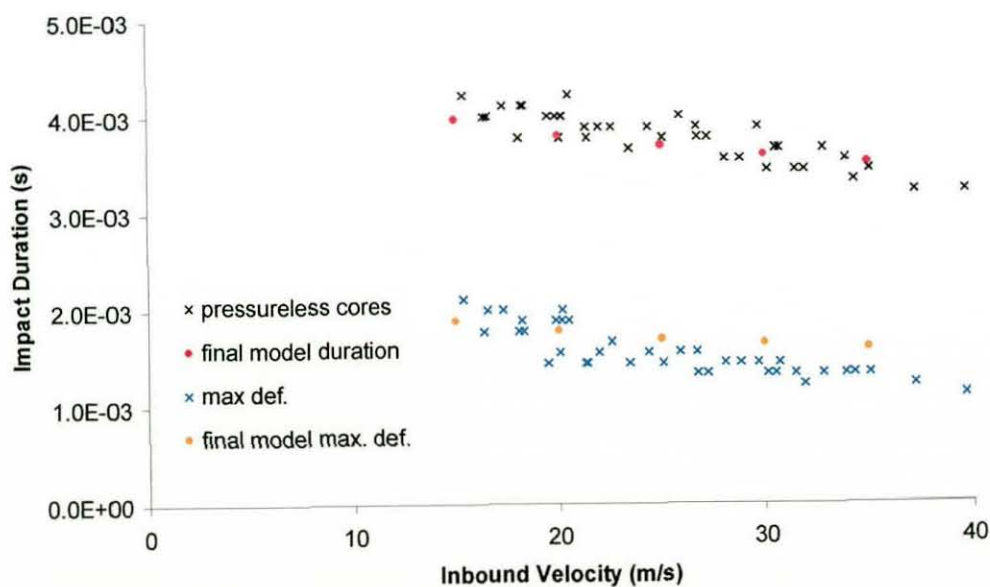
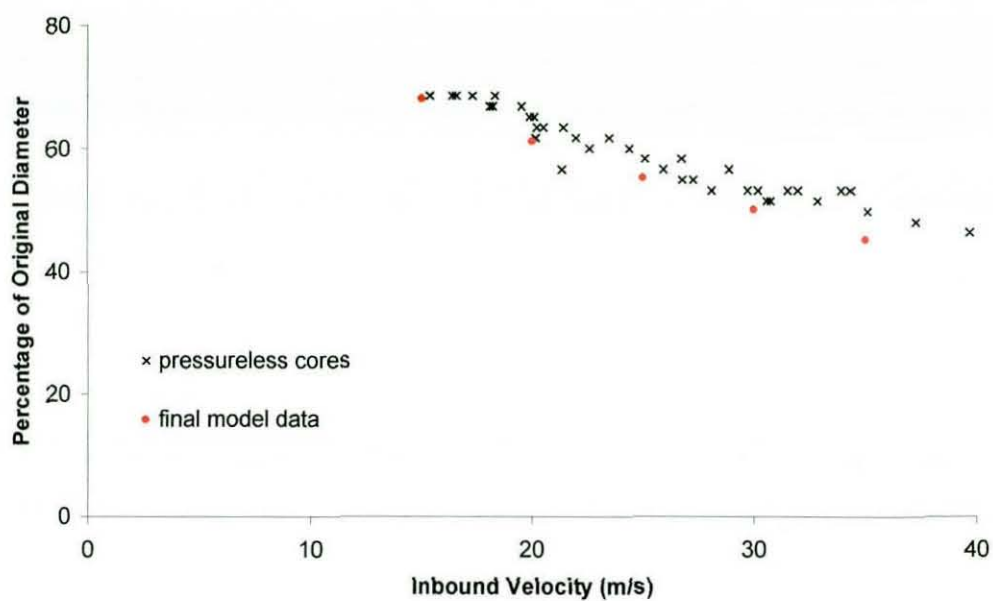
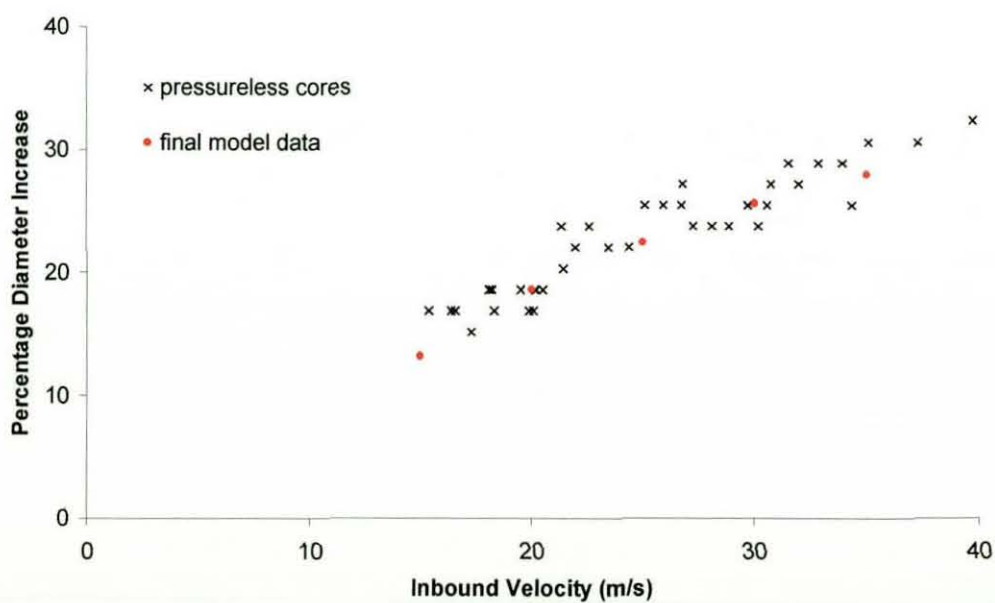


Figure 6.24 – Comparison of Final Pressureless Core Model with Experimental Impact Duration.



**Figure 6.25 – Comparison of Final Pressureless Core Model with Experimental Gross Normal Deformation Values.**



**Figure 6.26 – Comparison of Final Pressureless Core Model with Experimental Gross Tangential Deformation Values.**

---

## 6.4 Discussion

### 6.4.1 Low Rate Tensile Testing and Subsequent Model Development

It was seen in Figure 6.11 that the models considered, which were generated using the ABAQUS materials module were of limited accuracy over the range of strain from zero to five. However, even the initial soft models used during the mesh geometry assessment exhibited strains limited to less than one. Within this limited range, it is seen that all models are of acceptable accuracy and so this is not a limiting factor in choice of material model. Knowing this, the model is then selected on criteria outlined in section 6.1.3 which results in the reduced polynomial model being considered the most appropriate for this application. Whilst the model of order  $N=3$  will by its nature provide a closer fit to the data than that for  $N=2$ , the increase in accuracy in this case is minimal. A more complicated material model will increase computation cost and is also less stable at higher levels of strain. For these reasons the second order reduced polynomial model is chosen as the most desirable.

If the low strain rate tensile test data is used as input for the Abaqus material model then two models are generated with coefficients  $C_{10}$  of  $1.112E6$  and  $1.187E6$  for rates of  $200\text{mm/min}$  and  $999\text{mm/min}$  respectively. The values of coefficients  $C_{20}$  are less than a few percent by comparison and are shown in Figure 6.14 only to affect stress at strains above 0.2. This effect is secondary and so the contribution of  $C_{20}$  can be neglected in the following discussion. As was previously stated, the sum of the coefficients in the reduced polynomial model is equal to half the elastic shear modulus. The data from experiments by Ahmadi and Muhr (1997) presented in part 6.1.2.1 show a clear relationship between the elastic shear modulus and strain rate, or frequency of oscillation in this case and it is fair to assume that the tennis ball rubber will similarly follow this trend. Figure 6.27 shows the low strain rate model coefficients plotted against strain rate on the same axes as the frequency data with a logarithmic trend line through the points. The frequency data appears linear at lower rates on the logarithmic scale and increases at



a greater rate at higher frequencies. Using this knowledge it is possible to suggest a value for  $C_{10}$  representative of the high strain rate characteristics from the low rate model values. At the strain rate in question, around 250/second, the coefficient  $C_{10}$  should be around 1.7E6. Although the trend line is only fitted to two data points and so accuracy is questionable, comparison to the frequency data of Ahmadi and Muhr would suggest that the model data is of a similar form and may be accepted. A comparison of the suggested coefficient with the final value will determine the accuracy of this method as a predictive tool.

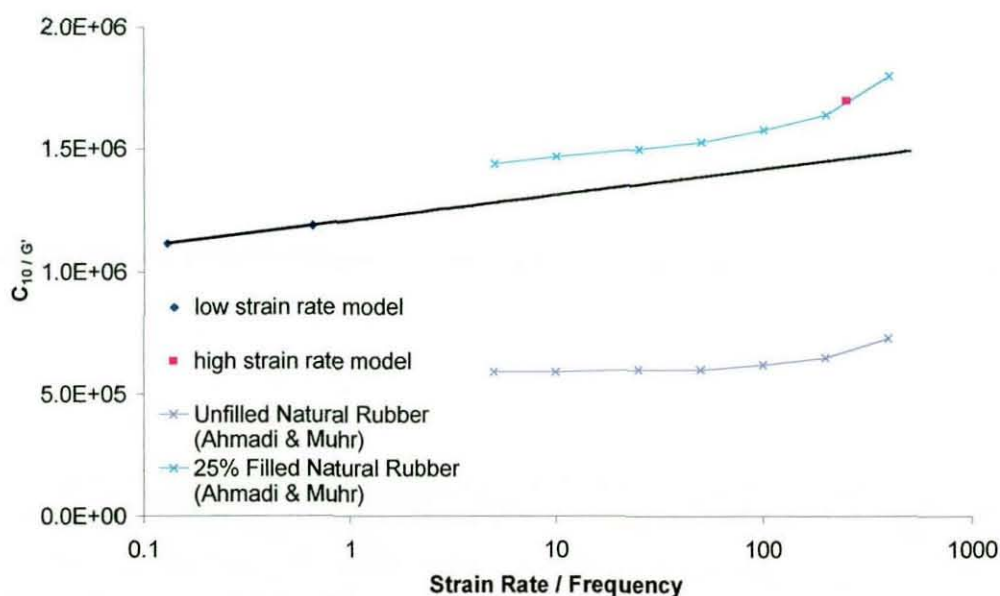


Figure 6.27 – Derivation of High Strain Rate Model Stiffness Coefficient from Low Rate Values.



---

### 6.4.2 Increased Strain Rate in the Model and Comparison to Experimental Data

Using the material model developed from the low rate tensile test data gives a core model which is considered much too soft. From Figure 6.15 and Figure 6.16 we see that the maximum deformations are too large and the impact duration is too long and yet the COR is too high. It would be expected intuitively, and from research in other ball sports, that a 'soft' ball would have a lower COR than a 'hard' ball. However it must be remembered that the model at this stage takes no account of energy loss due to hysteresis and so the material stiffness will have little bearing on the true value of COR. There will be an effect on the duration of impact and running normal impact models with increasing values of  $C_{10}$  shows this, as seen in Figure 6.16. Lack of damping in the model results in deformation due to vibration modes, especially at higher velocities making determination of the true duration difficult. This is seen here in the non-linearity of predicted impact duration for all stiffness values, in contrast to the linearity seen in the results in chapter 5. However, we can see that duration values taken from the experimental data fall between those predicted by values of  $C_{10}=1.6E6$  and  $C_{10}=1.8E6$  at the lower velocities. This would suggest a value around  $C_{10}=1.7E6$ , which is in agreement with that suggested previously from the low strain rate data. In fact, in order to best fit the experimental data, a value of  $C_{10}=1.75E6$  was found to be most suitable.

### 6.4.3 Material Damping

Determination of a value for damping factor in this case is simply iterative and was accomplished by running normal impact models with increasing levels of damping. The effect on COR was of most interest as this is the characteristic which reflects system energy loss. From Figure 6.17 we see that a value of  $100E6 < \beta_R < 150E6$  is required and unlike the impact duration data in Figure 6.16 this is satisfied at all velocities. This is because unlike impact duration, determination of the rebound velocity from the model is more straightforward and so the result is likely to be more accurate. We see that the drop

---

---

in COR with increasing damping is non-linear as would be expected, with increases at higher damping values resulting in correspondingly smaller falls in COR. Remembering that increased damping is equivalent to increasing the strain rate and COR is a measure of energy loss, then looking back at the loss angle data of Ahmadi and Muhr (Figure 6.9) we see that the forms are similar. In order to achieve impact duration comparable to that from the experimental data, then it was seen that a value of  $\beta_R = 137E6$  provided the best solution.

#### **6.4.4 The Finished Core Models**

Having derived values of stiffness coefficient and damping factor, it is simply a matter of using these within the model. The resulting normal impact characteristics are seen in Figure 6.19 to Figure 6.22. As COR and impact duration were used to 'tune' the material model then these results are accurate, as would be expected. The predicted deformations are similarly accurate and, as these characteristics are a result of the material behaviour, then the model is acceptable.

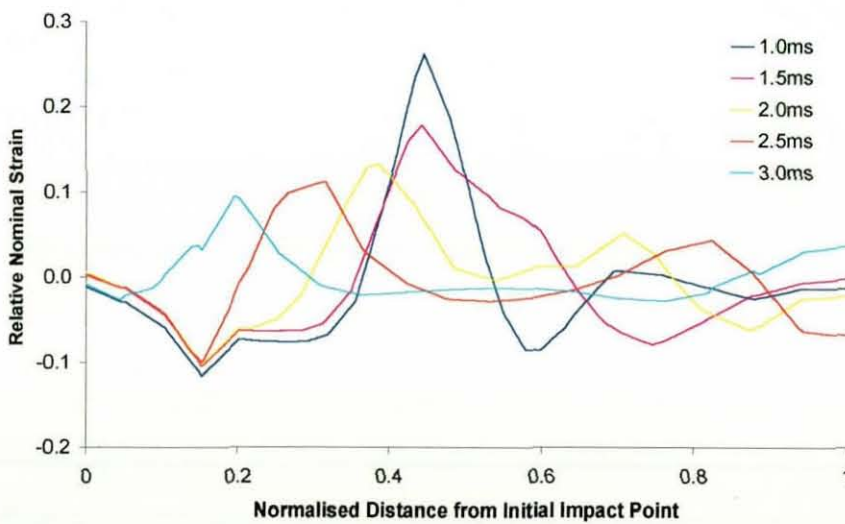
For the pressureless model, a similar process yields results seen in Figure 6.23 to Figure 6.26. Again COR and impact duration have been used to tune the material characteristics and again are accurate as would be expected. The gross maximum deformations are similarly accurate indicating that the material model used provides a good representation of the core characteristics.

---

### 6.4.5 Bending Waves

As was shown in chapter 5 bending waves excited by the impact are a major contributor to the ball characteristics. These may be seen for a pressureless core and the corresponding model in Figure 6.29 overleaf. For both core types the frequency of the primary wave was calculated and may be used to further verify the models. Conversely, if the models are seen to be accurate, they may provide an insight into the processes which lead to the development of these waves.

A path may be defined for the core model from the initial impact point, around the outer surface of the core to a point diametrically opposite. The path is then a semicircle connecting the bottom and top nodes of the core. A similar path may also be defined for the inner surface of the core and as the model is generated in spherical space then the primary strains in the second co-ordinate direction  $\varepsilon_{22}$  are strains along these defined paths. If each path length is defined nominally from zero at the initial impact node to one at the opposite node then some nominal distance along each path will correspond to points along the same radius. The difference in strain between the two paths then yields results for the bending around the core.


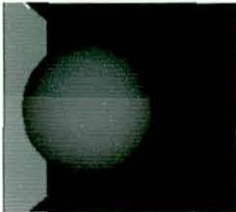

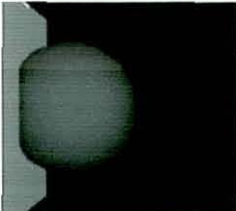
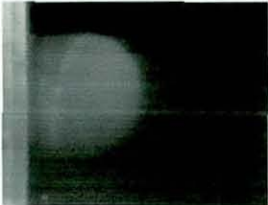
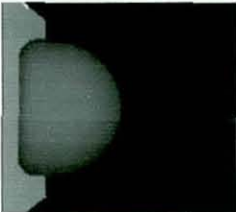

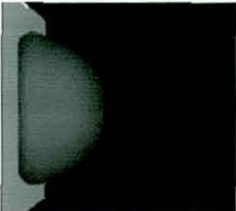

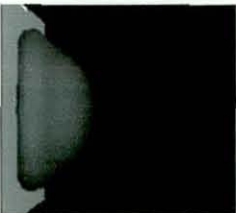






**Figure 6.28 – Bending Wave Propagation for a 35m/s Pressurised Core Impact.**

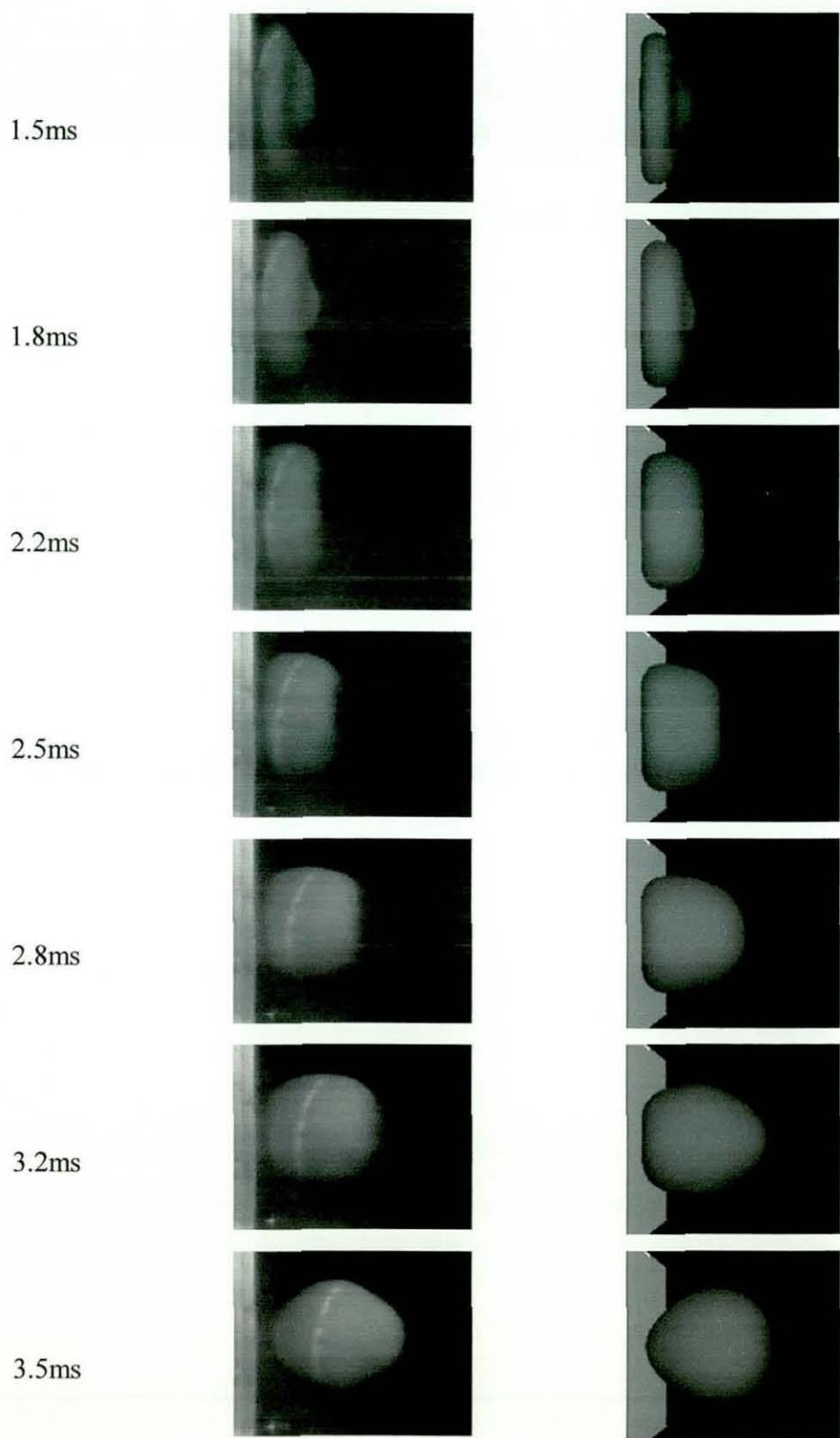
---



---

Time from Contact	High Speed Video	Model
0ms		
0.25ms		
0.5ms		
0.75ms		
1.0ms		
14.25ms		
1.5ms		

---



**Figure 6.29 – Deformation History of a Pressureless Core and the Corresponding Model.**

---

Figure 6.28 shows how the bending waves develop in a pressurised core at 35m/s impact velocity. It is seen that in proximity to the initial impact node, bending is actually negative, as the initially curved shell is flattened against the rigid surface. Further around the shell at about 80 degrees, the location of maximum bending is found, occurring at around 1ms. Ahead of this is another region of negative bending and further still the core is relatively unaffected by the impact at this time. As the ball rebounds, accompanied by a drop in bending magnitude, it is clear that two waves develop. One continues around the core whilst the other returns towards the surface. By identifying these two peaks over time the wave speeds can be calculated. The resulting frequencies are 170Hz for the forward wave and 125Hz for the rearward wave. This confirms what was seen in the HSV in chapter 5 that the forward wave travels faster than the rearward. Similar analysis of the pressureless core model reveals similar forward and rearward waves at 190Hz and 85Hz respectively. Again we see a considerable drop in frequency for the rearward wave. This is consistent with the increased impact duration for the pressureless cores and this evidence, along with the HSV, would suggest that it is the rearward deformation wave that is responsible for the rebound of the ball and hence impact duration. As the two waves move further apart (Figure 6.28) the development of a small intermediate wave may be seen. This wave also divides and travels in both directions around the core. This would seem to confirm the intermediate wave seen in the highest speed pressureless core impacts in chapter 5.

The differing frequencies seen here for both core types are opposite to those seen in chapter 5 in that the pressureless core model predicts a higher wave speed than that of the pressurised core. The dilation wave speeds of the respective materials would seem to confirm the model results, with both bending wave speeds being a quarter of the dilation wave speed. The HSV results are more likely to be inaccurate due to measurement error. Whilst the frequencies measured from HSV analysis and those predicted by the core models were not entirely in agreement, they were of the same order and allowing for error the differences are acceptable. This allows us to use the model as a predictor to investigate the process by which bending occurs. In Figure 6.30 we see the bending in a pressurised core model over the first millisecond. It is clear that the flattening of the area in contact with the surface initially dominates the deformation.



---

As the contact area increases then the angle between the surface and the neighbouring shell becomes greater and so the bending magnitude increases. It appears that the bending wave simply travels around the shell, increasing in magnitude during this time. However, from examination of Figure 6.31 it is clear that a change occurs between 0.08ms and 0.12ms with a local reduction in negative strain that appears to be the initiation of the bending wave. This buckling will result in a drop in apparent stiffness as the primary deformation mode changes from compression to bending. This phenomenon has been reported previously (Cross, 1998) and is seen as a change in slope of the normal impact forces in chapter 8.

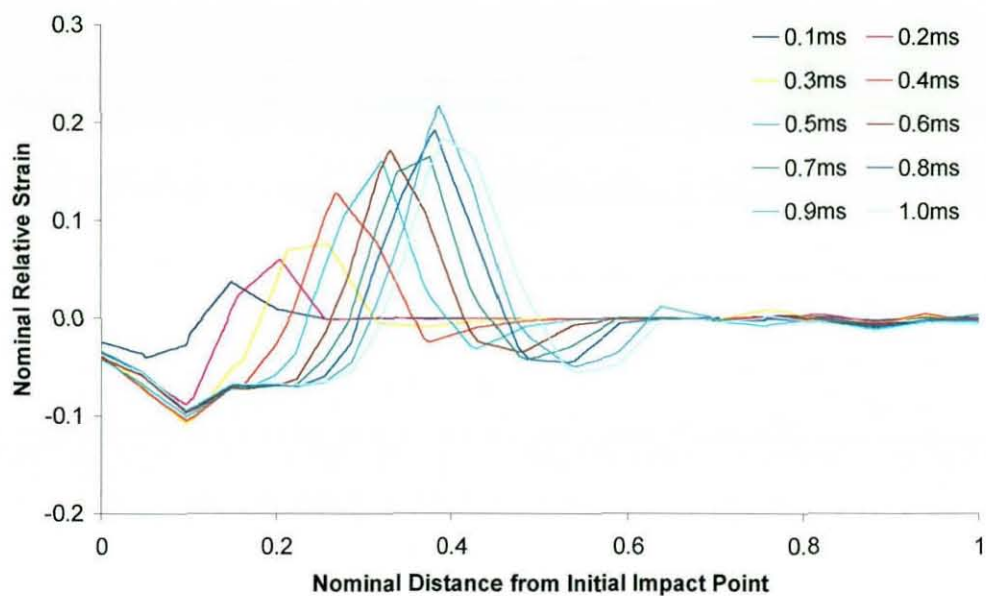


Figure 6.30 - Initial Bending Phase of the Pressurised Core Model at 35m/s.

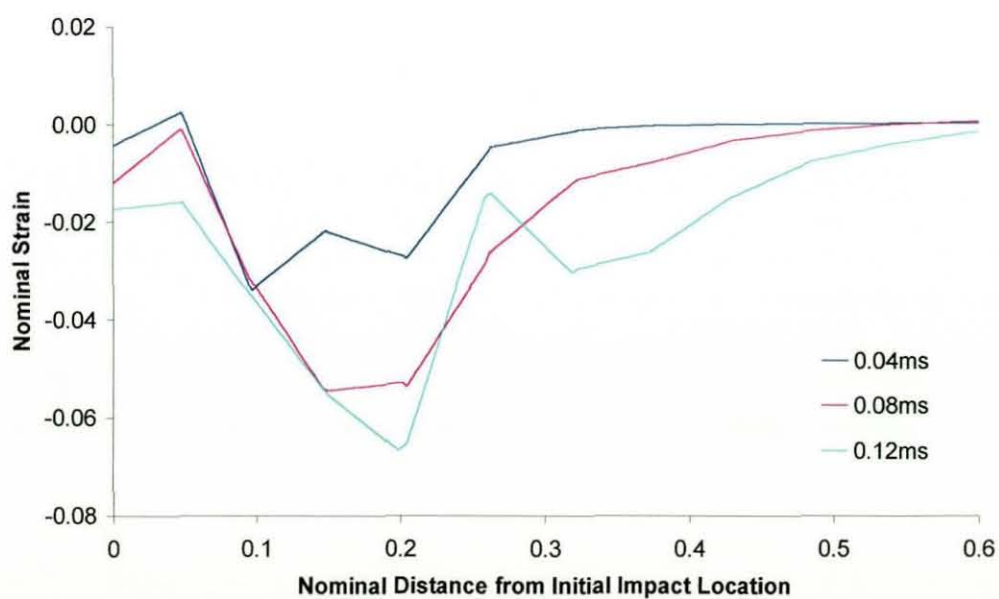


Figure 6.31 – Strain in the Outside Surface Only of the Rubber Core During Initial Bending.

---

## 6.5 Conclusions

Previous knowledge of the characteristics of natural rubber at various strain rates allows high rate material properties to be derived from low rate test data. This process is verified by modelling impacts over a range of material stiffness coefficients. The effect of increasing strain rate may be accounted for by increasing both the material stiffness coefficient and more significantly the damping factor. Provided nominal strains are relatively low ( $<1$ ) then a reduced polynomial equation of order  $N=2$  is sufficient to model material behaviour. Tensile test data provides sufficient information to derive a model accurate in all deformation modes. By considering impact duration and COR separately the effects of stiffness and damping may be seen to be independent. This allows the material model to be tuned to the experimental data. The results may then be verified by the deformation values. The model also predicts the formation and subsequent propagation of bending waves within the core.

---

## 7 Dynamic Measurement of Friction

### 7.1 Introduction

Having used the simplified case of the normal impact to verify the core model, it was necessary to consider the possibility of spin generation during impact. Whilst ultimately it is desirable to include pre- and post-impact spin about all three Cartesian axes, simplification of the impact conditions is needed in order to develop the model further. For this case, oblique impacts will be considered with initially zero spin and in such a manner that post impact spin is limited about one axis only.

Spin is generated when an object is subject to a tangential force, that being one whose line of action does not pass through the centre of mass of the object in question. In order for a tangential force to be applied during an impact, there must be interaction between the contacting surfaces of the objects. The science of interacting surfaces in relative motion is known as tribology, from the Greek word *tribos*, meaning rubbing. However, the processes involved are more commonly known as *friction* and *wear*. In this chapter we shall only be concerned with the generation of friction forces, although the two are intrinsically linked.

A friction force may be defined as the resistance encountered by one body moving across the surface of another. Amontons' basic laws of friction state that the friction force is proportional to the normal load between the two surfaces and is independent of the apparent area of contact or the sliding velocity. Whilst these laws were developed in the late 17<sup>th</sup> century, they are surprisingly reliable in a large number of cases. Whilst the first law may seem a fair assumption, the second, that friction force is unaffected by area of contact, was not so readily accepted at the time. In order to explain how this law may hold, it is necessary to observe what is occurring on an atomic level.



Any surface can be considered rough on an atomic scale. Even with modern production methods in machining, metals such as steel will exhibit roughness of the order of  $10^{-8}\text{m}$ . In comparison to an atomic diameter measured in Angstroms, where  $1\text{\AA}$  is equivalent to  $10^{-10}\text{m}$ , this roughness is of the order of  $10^2$  atoms. It is apparent then that surfaces appearing smooth to the eye are in fact composed of large numbers of troughs and peaks, or *asperities*.

Solids are composed of millions of atoms and although the atomic structure may vary considerably between different types of material, each solid exists due to the attraction forces between individual molecules; the molecular bonds. These attraction forces decrease with increasing separation, as shown in Figure 7.1, and for distances greater than  $10\text{\AA}$  are very weak. There also exists a repulsive force between atoms, which acts at a separation of up to  $3\text{\AA}$ . The resulting atomic force against separation is also given in Figure 7.1 and indicates a neutral separation at which the net force on the atom is zero. This also implies that in order to deform a solid, it is necessary to do work against these molecular bonds. For small strains, molecular separation will be within the limit of the attractive forces and so the solid will return to its original shape, this is the process of elastic deformation. Should the deformation be large enough, molecular separation will exceed the limit of the attractive forces and so bonds will be broken. Molecules will form new bonds with their new nearest neighbours and when the loading is removed, permanent deformation will be visible. This is plastic deformation. These intermolecular forces are very important in the understanding of friction.

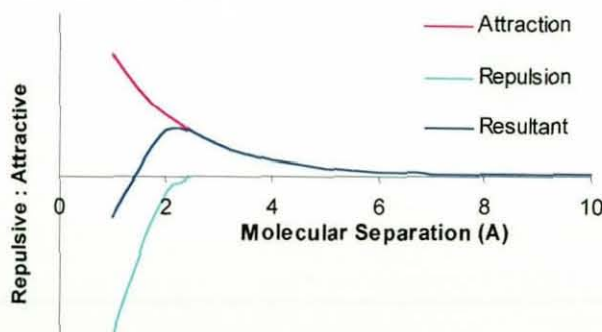


Figure 7.1 – Molecular Forces and the Effect of Separation.

---

When two surfaces are placed in contact, the initial load is taken by only a few corresponding asperities. The true area of contact is considerably less than the apparent area, and so the pressure at these points is very large. In metals, this load is always large enough to cause plastic deformation. Asperities deform, thereby increasing the true area of contact, until equilibrium is reached between the applied load and the contact area. Further increasing the load will cause a corresponding increase in contact area through greater plastic deformation of the contact surfaces. Tabor and Bowden (1973) state that, for two centimetre squares of mild steel in contact under a load of 100kg, the true area of contact is  $1/100 \text{ cm}^2$ . It can be seen that by increasing the apparent area of contact, the number of contacting asperities will be greater, but each will carry a smaller proportion of the load. This will lead to less plastic deformation and so the true area of contact remains unchanged. The true area is then proportional to the load and independent of the size of the bodies. This is similar to the first two of Amontons laws and so it would appear that the true area of contact is closely related to the friction force.

The Bowden and Tabor model for sliding friction, in its simplest form, states that friction arises from two sources, adhesion and deformation. Whilst these two processes cannot strictly be treated as independent, the model provides a good means of understanding the processes involved.

It is seen, most strongly in very clean and highly ductile materials, that adhesion occurs between the two materials in contact, as molecules within each solid are attracted towards each other. This has been shown experimentally for a number of materials under ultra-high vacuum where bonds can become very strong. The two materials must be physically pulled apart and in doing so, molecules of one material are transferred to the surface of the other. Under normal circumstances, most surfaces are not clean enough to exhibit significant adhesion, due to the build up of oxides and adsorbed films. However, more important is that the elastic strains surrounding the plastically deformed asperities generate enough stress during unloading to break the asperity junctions. This is why adhesion is not usually observed between surfaces that are loaded and unloaded normally. However, when the surfaces slide over each other, the normal load still exists and so it is the tangential load which must now shear the asperity junctions. The friction

---



---

force due to adhesion is then dependent upon the shear strength of the asperity junctions, which is itself dependent upon the materials in contact. This also explains why lubrication is so effective in lowering friction.

The second process of deformation, also known as ploughing, is easily observed in many cases where one solid is harder than the other. The asperities of the harder solid press into the surface of the softer solid under normal loading such that under tangential load, material is 'ploughed out' of the softer solid. The friction force necessary to achieve this is proportional to the hardness and shear strength of the material and the geometry of the asperities. It is also possible that ploughing will produce wear particles which will in turn create further deformation and hence increase friction further.

When considering polymers, friction no longer obeys Amontons' simple laws. Deformation during loading is elastic and asperities flow easily, such that the true and apparent areas of contact are similar. The coefficient of friction varies greatly with normal load and sliding speed, but it is still possible to describe the origin of friction force in terms of deformation and adhesion.

It is possible to isolate the deformation by considering rolling contact, where there is no adhesion. In the case of a polymeric object, such as a sphere, rolling across a more rigid surface, the polymer will deform elastically. The front of the object will compress under the normal loading and the rear of the object will unload elastically as it leaves the surface and return to its original shape. If the material were truly elastic then there would be no energy loss and thus no friction force. However, as the material is viscoelastic, energy is lost through hysteresis and dissipated as heat. Also, rolling contact usually contains some degree of slip and so there is some component of sliding friction. It has already been shown that adhesion is related to the true contact area. As polymers deform viscoelastically, then the contact area is proportional to the normal load raised to some power  $n$ , where  $n$  is usually somewhere between 0.75 and 0.8 for most polymers and 0.66 for natural rubber. For this reason COF is proportional to normal load and in most engineering applications where contact occurs at a large number of asperities, the relationship is nearly linear.

---

---

In textiles, friction is complicated further by the characteristics of the material. In woven fabrics, fibres pass over and under each other forming distinct ridges within the surface. In addition, any surface finish applied to the fabric such as *raising* will further increase surface roughness. Upon initial contact, a raised surface will have a very low true area of contact as the raised fibres support the load. However, the resultant pressure causes a rapid flattening of the individual fibres and the fabric surface then behaves much more like that of a non-raised material. Under further compression, the material will behave much like a polymer with asperities deforming elastically and creating a large true area of contact. Once sliding is initiated, the raised fibres may align themselves with the direction of motion, which should have the effect of decreasing the COF. However, if the fibres themselves have directional properties, such as wool, then the COF may in fact increase. Experiments have shown (Ajayi and Elder, 1994) that COF is proportional to compression for fabrics and is highly dependent upon apparent contact area and sliding velocity.

In all cases, the force necessary to initiate sliding is greater than or equal to the force needed to maintain sliding. In other words, the coefficient of static friction is greater than or equal to the coefficient of dynamic, or kinetic friction. Static friction is somewhat time dependant as adhesion can be either reduced due to surface contamination or increased due to creep within asperities or further interfacial bonding. In initiating sliding, the tangential force rises until it reaches the maximum static value. Once relative motion begins, the force necessary to maintain this motion is often much lower and so the sliding object will accelerate. If the object is being driven by a constant velocity load then the applied force will be reduced until at some time it falls to zero and the object will come to rest. This is the basis of the stick-slip phenomenon commonly observed when the static COF is much greater than the dynamic COF.

---

### 7.1.1 Variables

From the discussion on the origins of friction, it is clear that in order to accurately develop a model for the COF of tennis ball cloth during impact, measurements of normal and tangential force need to be made during impact. Also, it is desirable to know the effect that the cloth is having on the post impact characteristics of the ball. For this reason measurements of post-impact spin for all impacts are required to investigate any relationship between the tangentially applied load and the resulting spin generated.



---

## 7.2 Equipment

### 7.2.1 Sensicam

Spin measurement was made using the Sensicam system and a bespoke software digitising system *Flightpath*. This system consists of a Sensicam digital camera controlled by p.c. software via a fibre optic link to a high powered long duration flash and image processing software capable of resolving spin.

The Sensiflash comprises a power unit consisting of a number of high-powered capacitors, which supplies a flash unit and is able to provide around 10ms of high intensity light with little decay over that time. Thereafter decay is more rapid and the resulting light is of little use for image capture. The power unit allows the overall light intensity to be adjusted and may be triggered either manually or by an external trigger. The flash unit consists of a main flash bulb as well as a lower power bulb which can be switched on manually for longer periods to allow system set-up.

The monochrome digital camera is fan cooled and is operated with an electronic shutter that can be triggered at up to ten intervals by the controlling software. The camera is connected via a fibre optic link to an image-processing card, one of two built into the p.c. system.

The significant component of the system is the controlling software. A typical control screen is shown in Figure 7.2 which is made up of a number of windows. The main image window shows either the current output from the camera for setting up the system, or it shows the last image captured to memory. The camera control window allows accurate use of the electronic camera shutter, since it defines the delay between each shutter incident and a corresponding exposure time, for up to ten incidents. All times are set in microseconds up to a maximum of 1000 $\mu$ s, or one millisecond, allowing events of up to 9ms duration to be captured. Each image captured is overlaid onto a

single frame, containing all images from that shutter sequence. This displays the event as a visual time history allowing all images to be considered at once. However, if the event of interest is such that objects travel only a short distance between consecutive exposures then the corresponding images will overlap, making discrete measurement difficult. It is often more desirable to capture fewer images separated by greater intervals of time so that they are distinguishable. This is accomplished by setting exposure times for the intermediate shutters to zero. A captured image is saved as a .bmp file and may be manipulated prior to saving using the colour control window. This allows adjustment of light intensity over the image, either via a linear or logarithmic relationship.

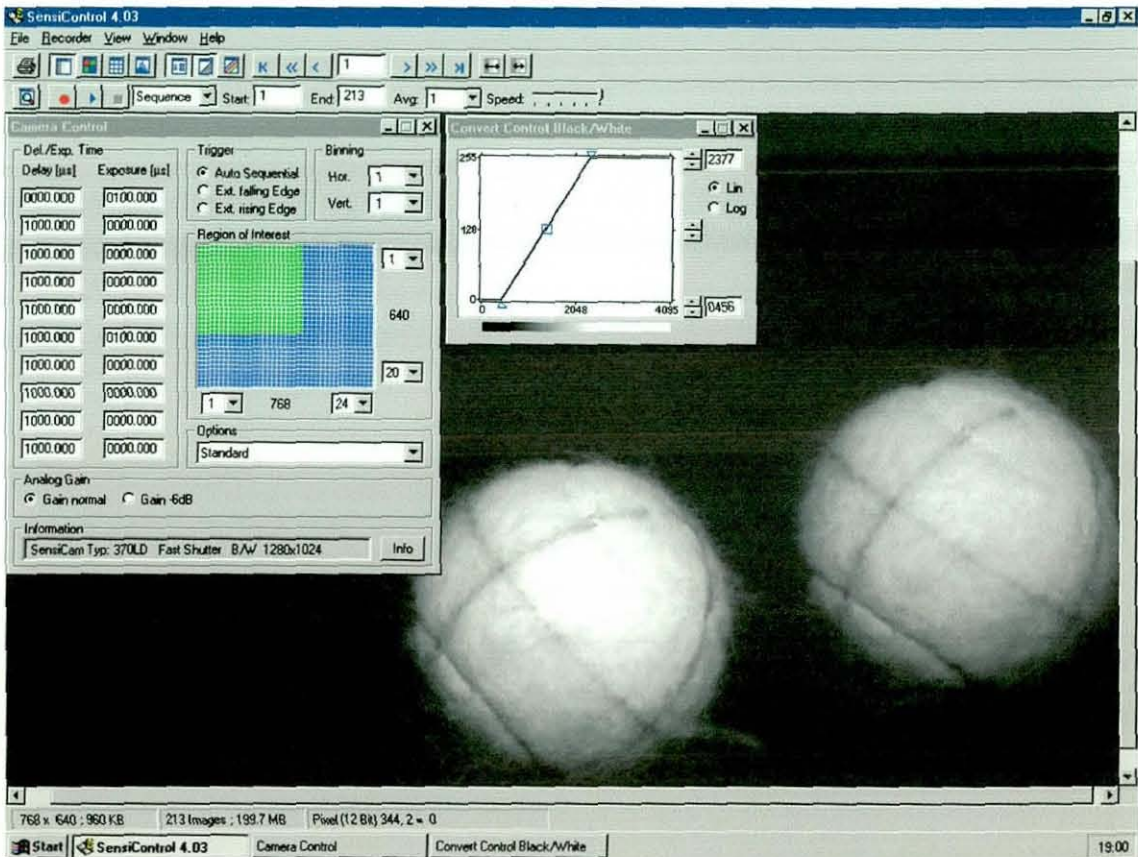


Figure 7.2 – Screenshot from the ‘Sensicam’ Controller Software.



---

The shutter sequence is triggered externally and in order to coordinate its timing with that of the flash system, an external signal generator is used. The signal generator itself is also triggered externally allowing up to eight distinct pulses to be controlled independently, with timing based on the external trigger. For use with the Sensicam system, two pulses are used with the first triggering the flash unit and second triggering the shutter timing. By altering the delay to the first pulse from the external trigger, it is possible to ensure that the event of interest is within the viewable area. The delay between the first and second pulse is used to account for the rise time of the Sensiflash power supply, ensuring the light is at full intensity before any images are recorded.

The final part of the spin measurement system is the image analysis software. The *Flightpath* software package is purpose written to enable spin to be determined from the analysis of two or more images of a ball captured by strobe photography. Using mouse picks, each image is digitised such that a circular outline is drawn round the ball, capturing its position in space. By initially digitising a calibration grid and specifying the shutter timing, the distance and time between images is then known. Also, it is possible to determine the two dimensional rotation of the ball in the plane of view by constructing a line from the ball centre to a fixed point on the edge of the ball, for each image. This is most readily accomplished by drawing circumferential lines in the three Cartesian planes around the ball prior to image capture, as seen in Figure 7.2. These lines can then be used as a guide whilst digitising the image, providing a more accurate means of determining spin. The system also provides values of ball velocity and launch angle.



---

### 7.2.2 Load Cell

In order to make measurements of impact forces, a Kistler Type 9067 tri-axial load cell was used. The load cell consists of three layers of piezo-electric crystals which, when loaded produce a small charge proportional to the change in loading. Careful arrangement of these layers allows independent measurement of the three Cartesian components of load with nominally zero cross-talk. The crystal layers are enclosed within a solid casing, shown in Figure 7.3, such that load is measured by the two annular faces. It is quite apparent how the instrument measures compressive forces however, to measure tensile and tangential forces it is necessary to mount the load cell in a pre-loaded system. It is clamped between two 15mm thick aluminium plates via a pre-loading bolt which passes through the centre of the cell. The compressive (z-component) output is used to determine the pre-load applied, up to the manufacturer's specification of 20kN. As piezo-electric crystals generate a charge due to the rate of change, a constant load does not produce any signal and the charge already generated is quickly lost. The load cell is then in a state of equilibrium until a time when further load is applied. The pre-load is sufficient that tangential forces are measured through the contact friction between the aluminium plates and the faces of the cell. Tensile forces are really an unloading of the crystals, however as the cell is initially in a state of zero charge, this change in loading state produces a corresponding charge.

The charge output is small, in the order of microvolts, so in order for the signal to be useful it must be amplified. A Bruel and Kjaer 4-channel charge amplifier was used for this task. The load cell is calibrated by the manufacturers and is supplied with the appropriate calibration information. This is then used to set the correct output from the charge amplifier. The x, y and z component signals are fed into separate channels of the amplifier which converts the charge in microvolts into a usable output in the order of volts. The calibration values are used to convert the input into the relevant number of Newtons force electronically. The output is then chosen as a value of volts per Newton such that it is as near to ten volts as is possible, this being the maximum output of the amplifier and so ensures maximum data resolution and hence increased accuracy.

---

To be able to view and manipulate the charge amplifier output, it is transferred to a LeCroy 9304C oscilloscope. This instrument is menu driven and allows data to be displayed in a number of forms, mathematically manipulated and stored for later use. Storage is to either internal memory, floppy disk or direct to a p.c. via a parallel port connection, which also allows remote control of the unit via p.c. based software.

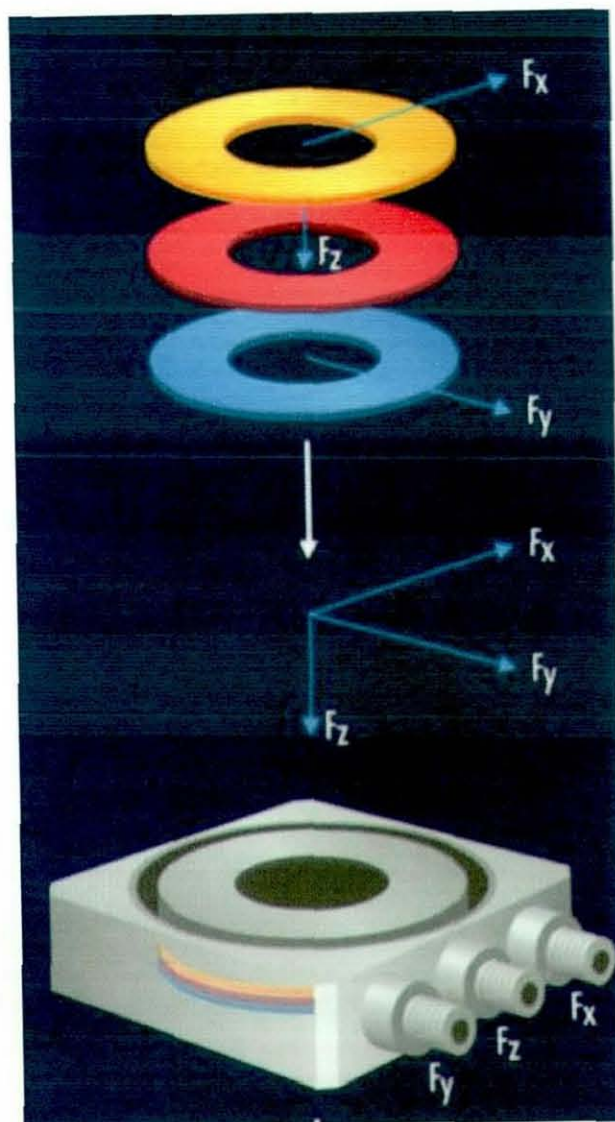


Figure 7.3 – Layered Crystal Construction of the Load Cell (Kistler, 2000).

---

### 7.3 Experimental Procedure

Pressurised tennis balls were projected by the pneumatic ball cannon towards the force plate, which was mounted in the cannon enclosure. As it is only intended to investigate the effect of the cloth cover, differences between pressurised and pressureless balls are of little interest, so for this reason only pressurised balls were used. The light gates allowed inbound velocity to be measured and also provided a trigger signal for the Sensicam system. The angle of the force plate was increased at intervals of 10 degrees from the normal impact case, 0 degrees, up to 50 degrees (where the angle stated is that between the incident velocity vector and the plate normal). The range of angles was limited by the physical extent of the impacting surface of the load cell. Balls were projected with velocities in the range from 15m/s to 35m/s for each angle, with twelve impacts recorded for each velocity, giving 420 impacts in total.

During impact the load cell provided real time loading information in directions both normal and tangential to the front plate. The Sensicam system was used to capture post-impact images of the ball in order to determine the resulting rebound velocity, angle and spin rate. These results were determined by analysis of each image within the *Flightpath* software package.



---

## 7.4 Results

### 7.4.1 Post Impact Characteristics

#### 7.4.1.1 Velocity and Restitution Coefficient

Initially, the post impact characteristics are presented, before a more detailed discussion of the impact forces themselves is made and relationships are drawn.

Considering first absolute velocities, Figure 7.4 shows the relationship between inbound velocity and COR. We see that as has been previously seen, COR decreases in a linear manner with increasing inbound velocity with the gradient being lower as inbound angle increases. It is interesting to note that the data for all angles appears coincident around 25m/s inbound velocity.

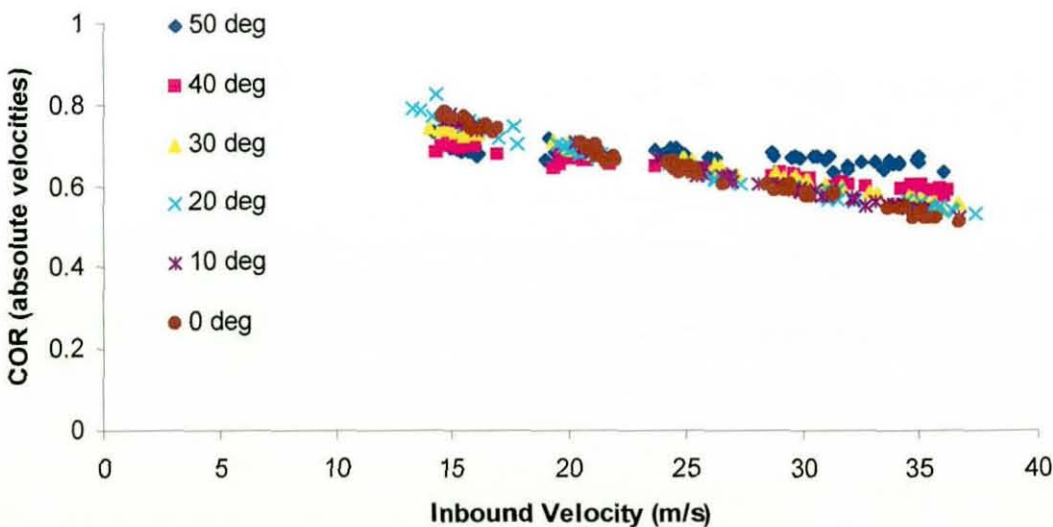


Figure 7.4 – Absolute Inbound Velocity against COR for Impacts at Varying Inbound Angle.

---

---

If the inbound and rebound velocities are considered in their component forms then the corresponding relationships between component inbound velocity and COR are seen in Figure 7.5 and Figure 7.6.

Figure 7.5 shows components of velocity normal to the impact surface and it is immediately apparent a correlation exists. The data for all inbound angles can be described by a single curve, being a straight line relationship of gradient  $-0.0117$  with a y-axis intercept value of  $0.9407$ . Only the data for the lowest velocities at  $50$  degrees inbound angle do not fit this trend.

It is both obvious and interesting from Figure 7.6 that such a relationship does not exist tangential to the surface. Here the data is much more scattered, which indicates the variability associated with the tangential interaction between tennis balls and surfaces. There appears to be a linear relationship between incident velocity and COR but it is angle dependant and a distinct difference exists between the data for  $50$  degree inbound angles and that for lower angles. Also, it is apparent that at small values of inbound angle, where the tangential component will be similarly low, the variation in COR is large, as would be expected for a quantity calculated as a ratio of small numbers.



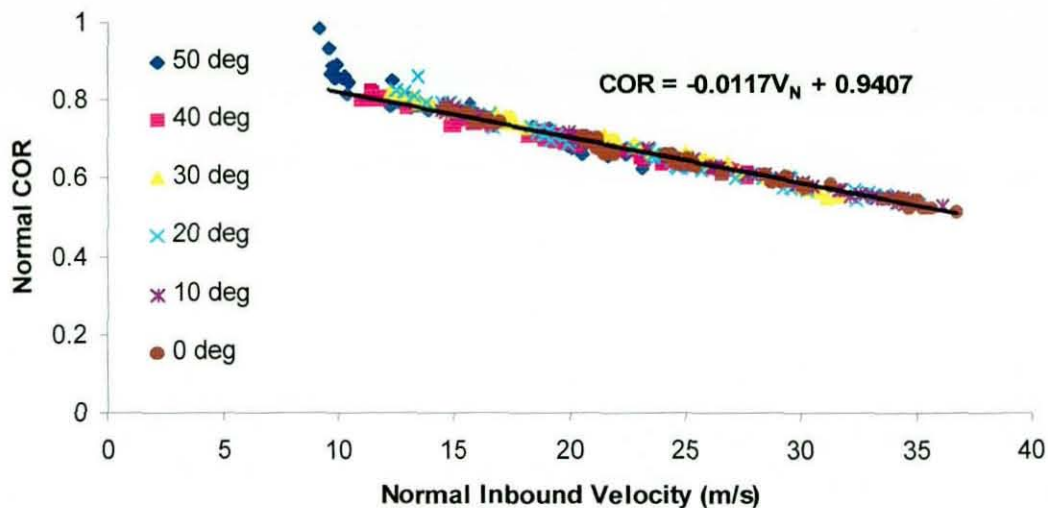


Figure 7.5 – Normal Components of Velocity and COR for Impacts at Varying Inbound Angle.

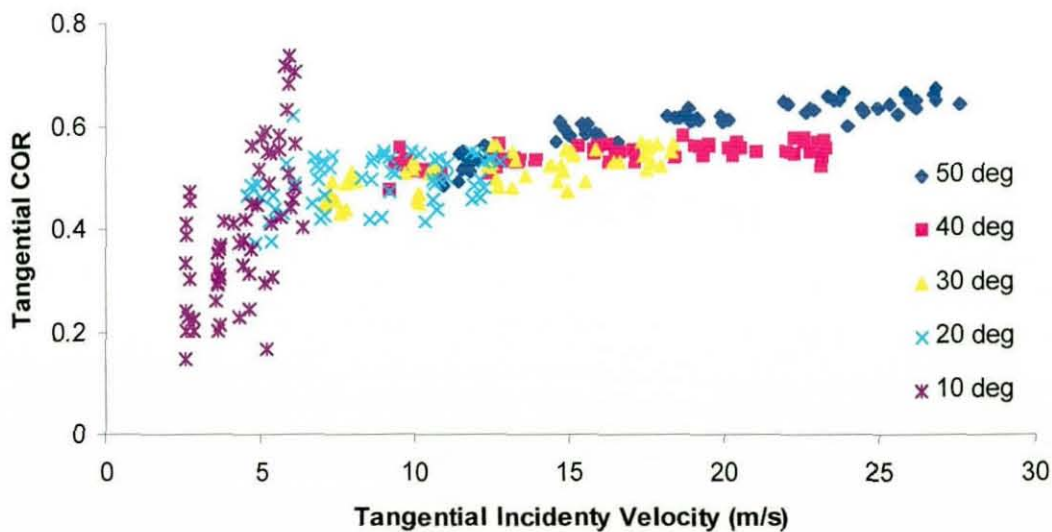


Figure 7.6 – Tangential Components of Velocity and COR for Impacts at Varying Inbound Angle.

#### 7.4.1.2 Rebound Angle

Rebound angle, measured as the angle between the absolute rebound velocity vector and the plate normal, is a reflection of the relationship between normal and tangential components of rebound velocity. In Figure 7.7 we see that the variation of inbound velocity with rebound angle is linear for each inbound angle with the gradient increasing as does the angle. If this data is processed further to allow consideration of inbound tangential velocities at constant values of normal velocity, then the effect on outbound angle is seen in Figure 7.8. The relationship between tangential inbound velocity and outbound angle at a constant normal velocity is linear in all cases, as might be expected. If trend lines are fitted to the data then all pass within  $\pm 2$  degrees of the origin.

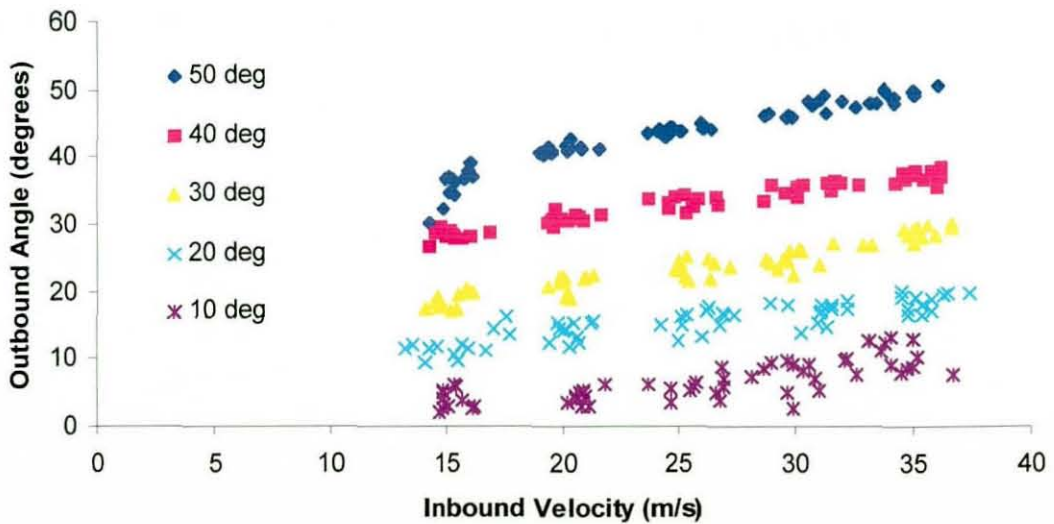


Figure 7.7 – Rebound Angle for Oblique Impacts at Varying Inbound Velocity and Angle.

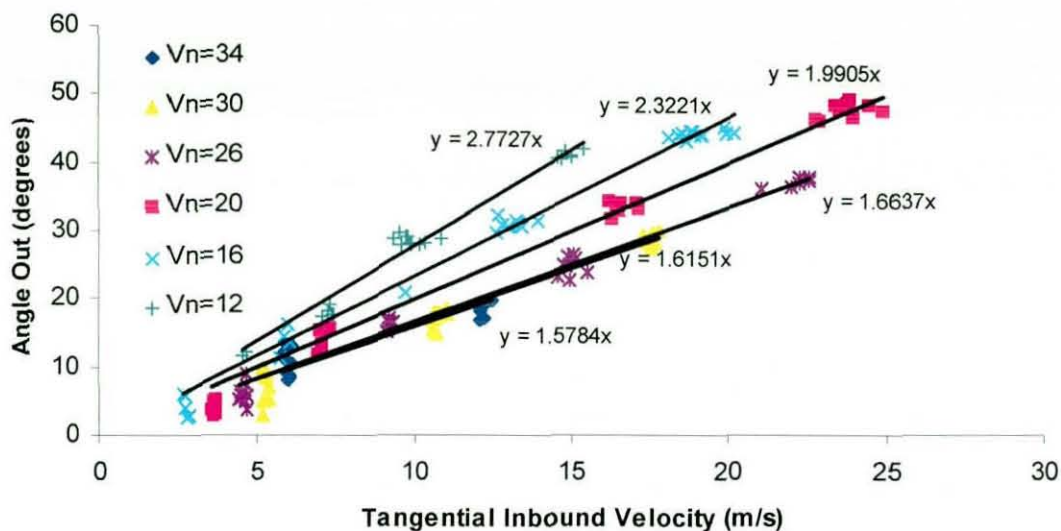


Figure 7.8 - Tangential Inbound Velocity against Rebound Angle at Constant Values of Normal Inbound Velocity.

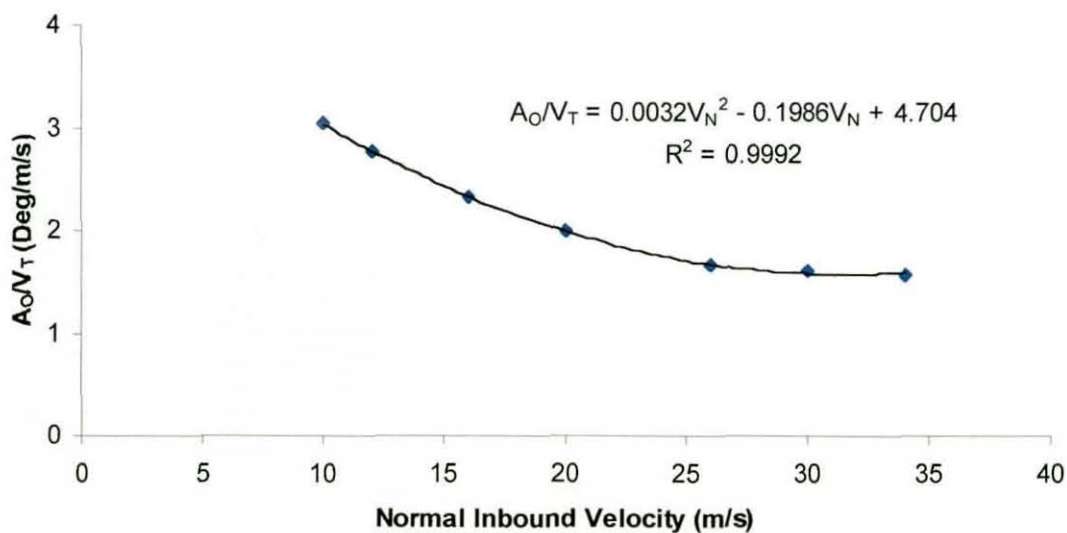


Figure 7.9 - Variation of the Relationship between Tangential Velocity and Outbound Angle with Increasing Values of Normal Velocity.

---

If we take the gradient of each trend line, then we can see there is a relationship between  $\frac{dA_o}{dV_T}$  and  $V_N$  of the form shown in Figure 7.9. This clearly shows that the increase in outbound angle due to tangential velocity is reduced as normal velocity increases, with the reduction appearing to decay with further increases in normal velocity. It is possible to fit a second order polynomial to the data to an accuracy of  $R^2=0.9992$ , providing a useful equation to the relationship between inbound velocity components and outbound angle.

It is obvious that the rebound angle is intrinsically linked to the inbound value, with larger incident angles producing greater outbound angles. In order to directly compare results over the range, it is necessary to define a function that may be applied equally in all cases. Such a function is the *angle ratio*, being simply the division of the outbound angle by the incident angle. Results are then presented in a normalised form where the value represents the percentage angle increase. It has been shown that the tangential component of inbound velocity is of primary importance and so these two values are compared in Figure 7.10. Initially it would seem that the results are somewhat dependent upon incident angle at the lower velocities, but at higher velocities this relationship appears to diminish. It is noted that the data scatter is much greater at lower velocities but again this is simply a characteristic of the function at small values. As these low tangential velocities correspond to small angles of incidence, then censoring the data for the lower angles may provide more clear trends. It is also desirable to eliminate the variation in normal velocity by considering the data at constant values. This data is presented in Figure 7.11 and appears to show a clearer relationship between tangential velocity and angle ratio. More importantly there appears to be little dependence upon the inbound angle. Again it is clear that at lower velocities the data becomes more scattered. By eliminating the variable data at all values below  $V_T=9\text{m/s}$  it is possible to fit a function of the form  $A_R = 0.3401V_T^{0.3231}$  to the data.

---



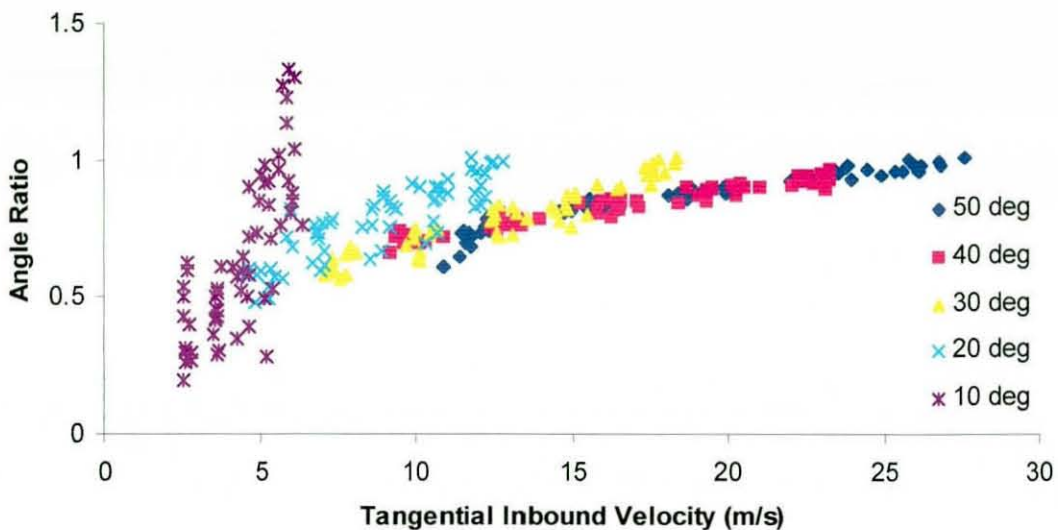


Figure 7.10 – Tangential Inbound Velocity against Angle Ratio at Varying Inbound Angle.

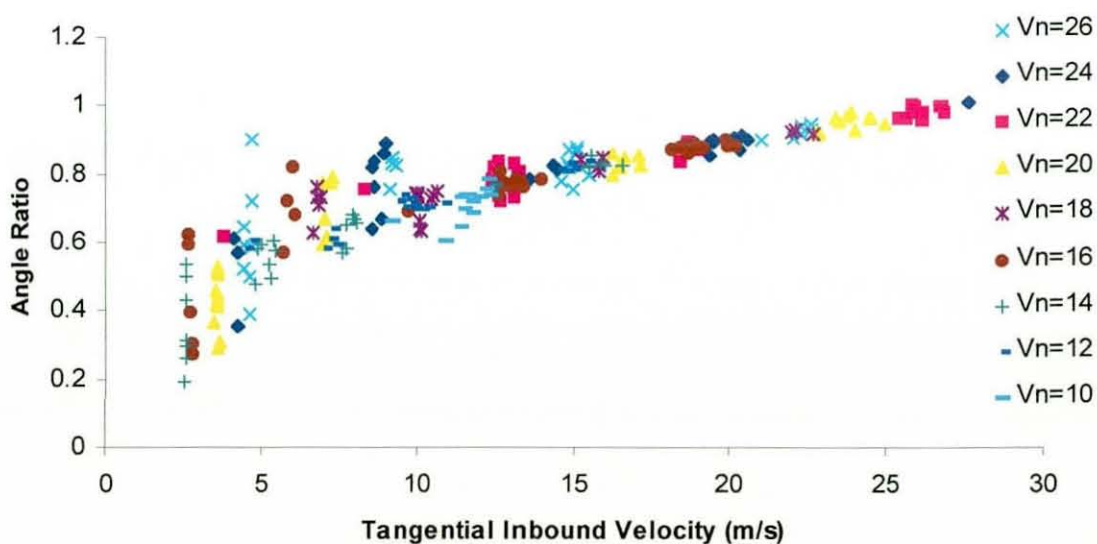


Figure 7.11 - Inbound Tangential Velocity against Angle Ratio at Constant Values of Normal Incident Velocity.



---

#### 7.4.1.3 Spin

As previously stated, spin generation is a direct result of the friction force. We have also seen that tangential COR is an indicator of the energy loss parallel to the surface and so it would follow that spin should be dependent upon the tangential velocity. In Figure 7.12 it is clear that, like rebound angle, spin is related to inbound velocity and incident angle. Intuitively one would expect spin and rebound angle to be related so this result is of no surprise. In examining the effect of the tangential velocity component, in Figure 7.13, there appears a clear positive relationship between the two. Unlike the data concerning rebound angle, here the scatter is more pronounced at higher values of the dependant variable. Again this is not unexpected as previous work on tennis ball impacts has shown there to be considerable variation between individual impacts and if the variation here is as a percentage of the average spin then it would be greatest at the highest value. Tangential velocity is considered at constant values of normal velocity in Figure 7.14. Here we see a linear relationship for all values of normal velocity, with spin increasing as normal velocity falls, at a constant tangential velocity.

Having seen similar effects on spin and rebound angle from incident velocity, then one would expect the two to be related. Comparing the two variables in Figure 7.15 we see that this is the case. With rebound angle being reliant upon incidence angle then each set of data occupies a different area of the chart. Spin appears linearly proportional to rebound angle in each case, with the difference in spin between consecutive angles reducing with each angle increase. Again a distinction may be made between the data for lower incident angles and that for the 50 degree impacts.

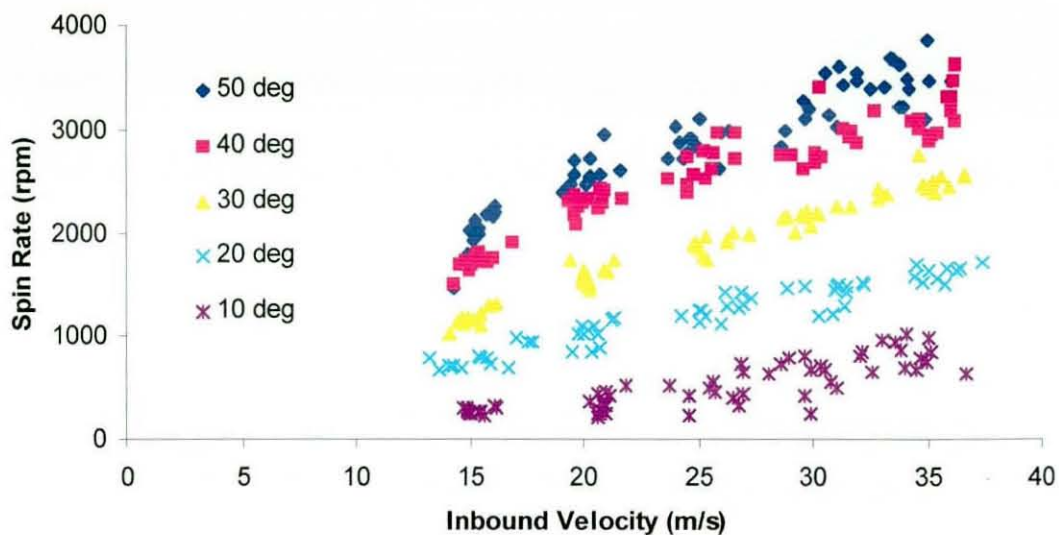


Figure 7.12 – Absolute Incident Velocity against Spin at for Impacts at Varying Inbound Angle.

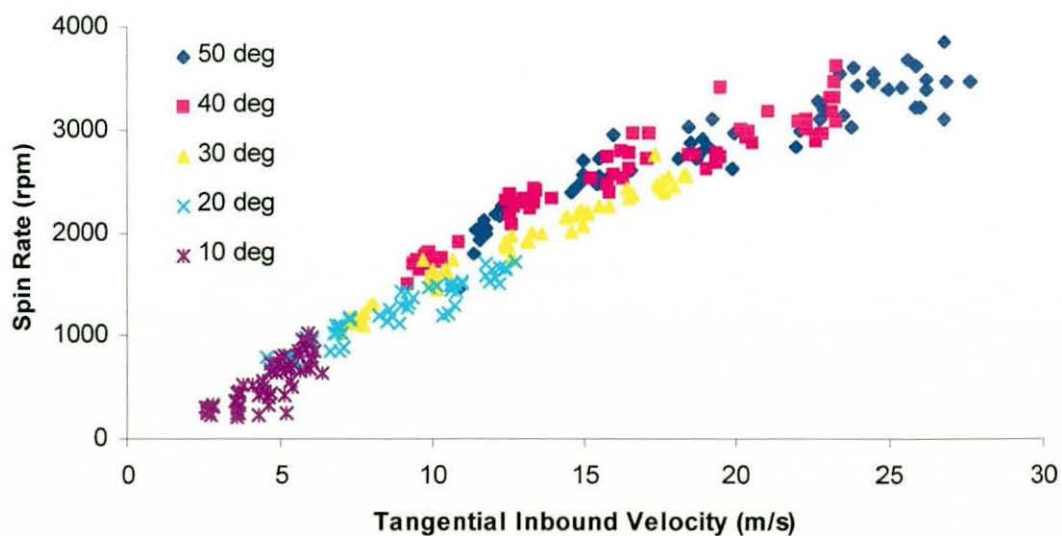


Figure 7.13 – The Effect of Tangential Inbound Velocity on Spin Generation in Oblique Impacts.

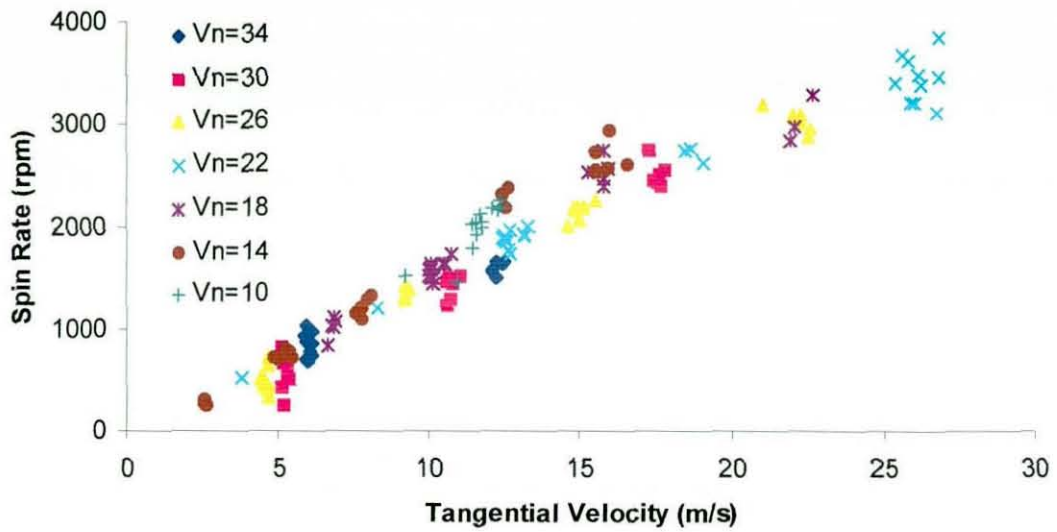


Figure 7.14 – Effect of Tangential Velocity on Spin at Constant Values of Normal Inbound Velocity.

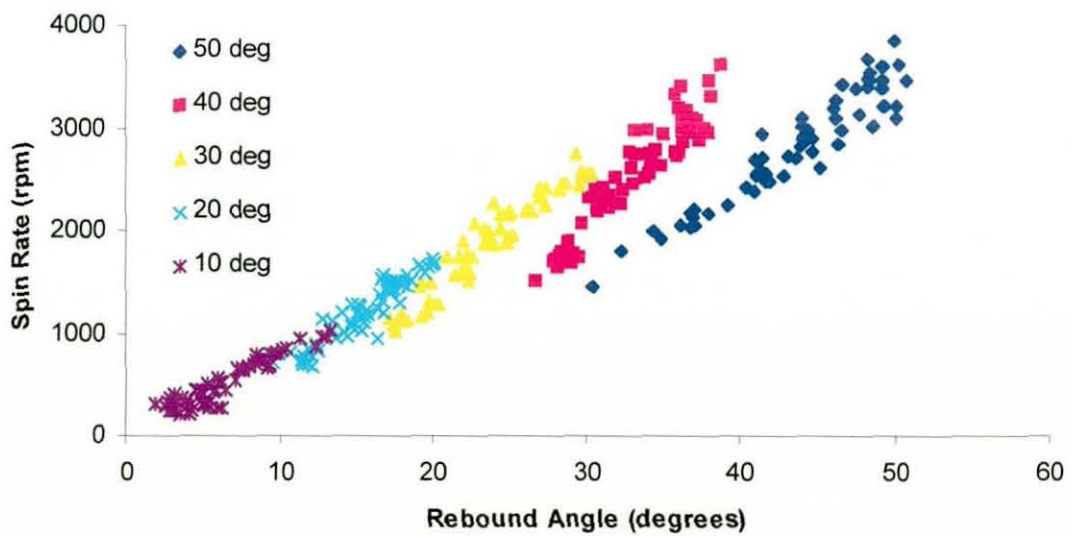


Figure 7.15 – The Relationship Between Rebound Angle and Spin for Oblique Impacts with Varying Inbound Velocity and Angle.

---

### 7.4.2 Impact Forces

From the results it is apparent that the post impact characteristics vary according to inbound velocity components, specifically tangential velocity. A better understanding is gained by examining the forces reacted both normally and tangentially by the surface during impact.

#### 7.4.2.1 Forces Normal to the Impact Direction

If we first consider forces reacted normal to the surface, then it would be sensible to consider initially those present during normal impacts, that is with zero component of tangential velocity. Such forces are seen in Figure 7.16 and on inspection it is immediately apparent that a difference exists between the loading cycle for a 'lower' speed impact (15m/s) and that of a 'higher' speed impact (35m/s). The lower speed impact force approximates a half sine wave, with a steady rise and fall and a peak load at approximately half duration. In contrast the higher speed impact is characterised by an initial sharp rise in load which then plateaus before falling to reveal a second peak. Through examination of the forces at intermediate velocities it is apparent that this second peak corresponds to the peak observed in the low speed trace and that the initial large force appears with increasing magnitude as the velocity increases. This force profile is repeated for all incident angles.

It is clear from Figure 7.16 that there is some overshoot in the signal following the end of impact. This is due to movement of the mounting frame within the cannon enclosure, as previously discussed in section 5.3. However, it was seen that both the magnitude and frequency of the post impact oscillation had little effect on the results.



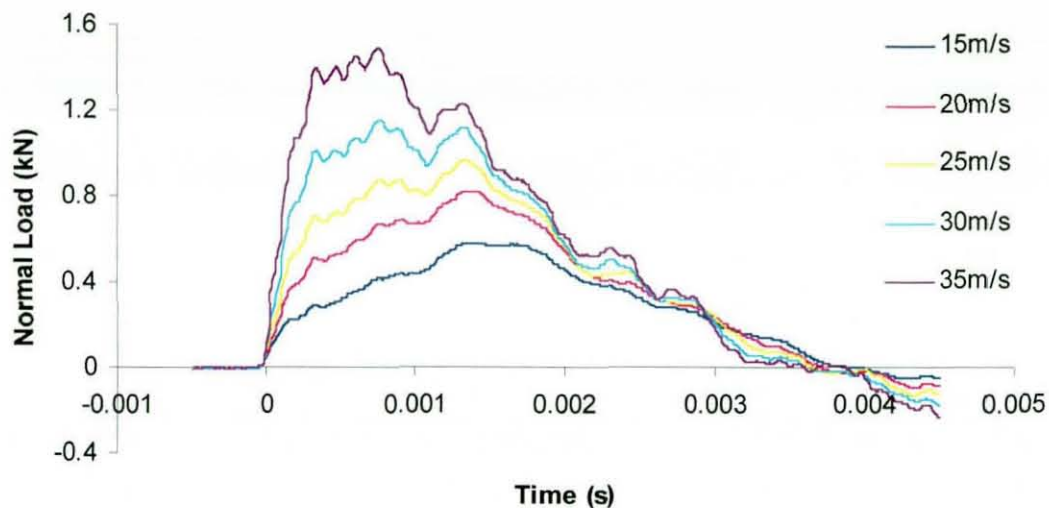


Figure 7.16 – Force Traces for Normal Impact (zero degrees incidence) at Increasing Velocities.

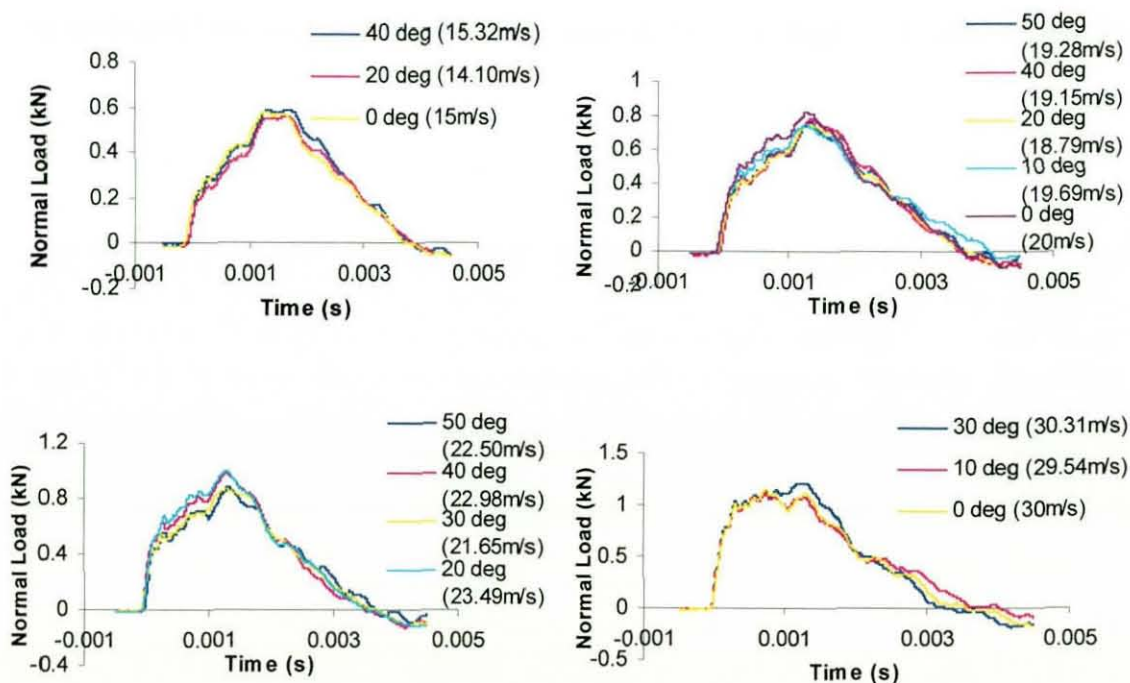


Figure 7.17 - Normal Force Comparison at Varying Inbound Angle with Comparable Normal Impact Velocities

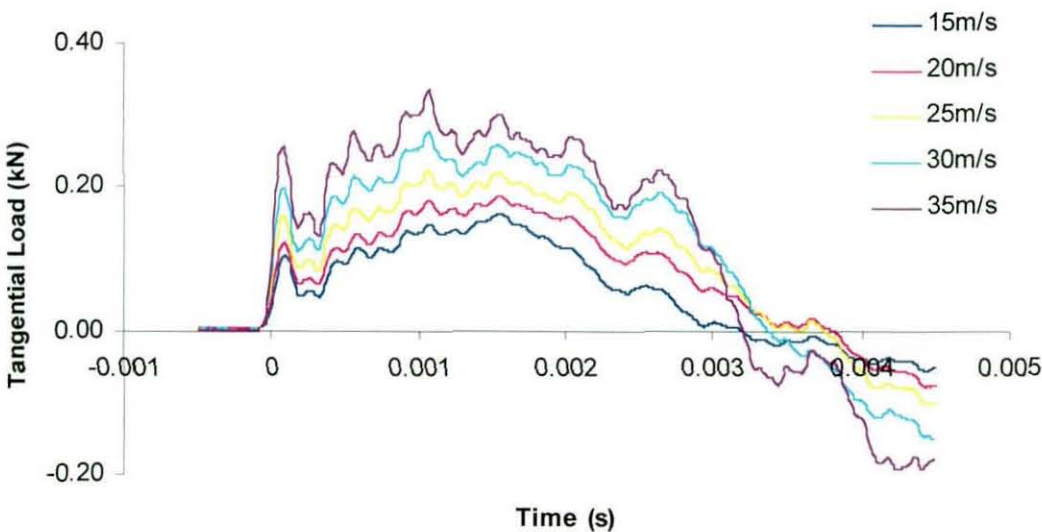


---

It is seen (Figure 7.5) that the COR normal to the surface may be described by a single line, being independent of inbound angle and hence tangential velocity. As COR is an indicator of energy loss during the impact, then it would be expected that normal loads during impact would be similar for all inbound angles providing the velocity component perpendicular to the surface was constant. Figure 7.17 compares force traces taken from impacts at different incident angles but with similar normal inbound velocities of around 15m/s, 19m/s, 22m/s and 30m/s respectively. In each case it can be seen that the force profiles are remarkably similar and most differences in magnitude may be explained by the slight variation in velocity between the angles.

### 7.4.2.2 Forces Tangential to the Impact Direction

Comparison of tangential impact force at a constant inbound angle in Figure 7.18 again shows a marked difference in profile over the velocity range. All traces rise to a peak at around half duration, with the faster impacts having a greater peak force and shorter duration. It is interesting that the tangential force profile displays an initial peak seen in the first 0.2ms and this was evident for all angles and velocities.



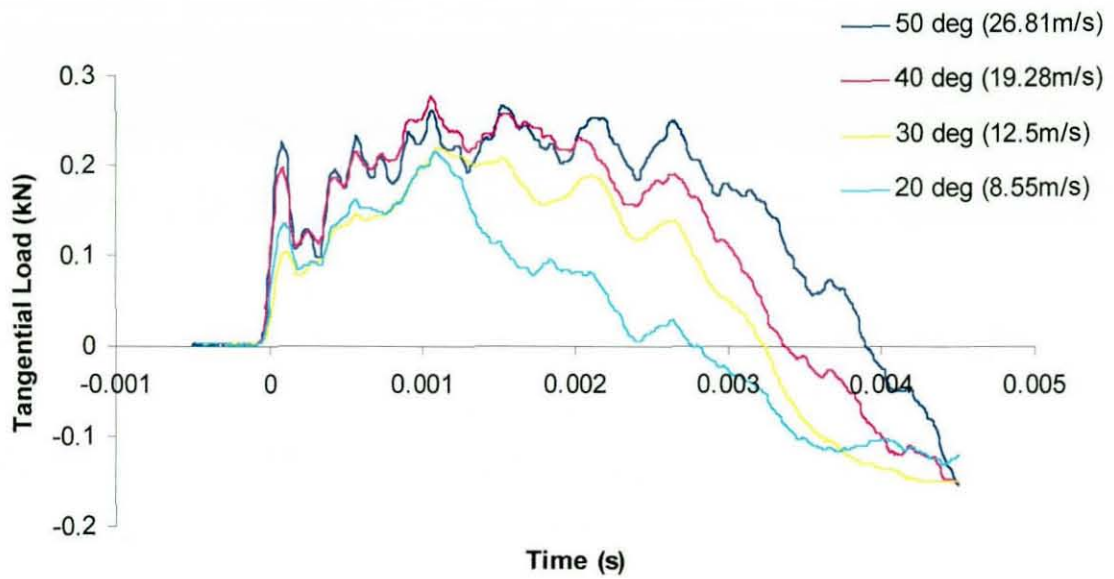
**Figure 7.18 - Tangential Forces for a 40 Degree Impact at Increasing Values of Absolute Velocity.**

It is known that even at a low sliding velocity the friction force for a fabric is not directly proportional to the normal load (section 7.1). If this were the case then having seen the dependency of normal impact forces on their velocity components, comparison of friction forces at constant normal velocity should show similar results. Figure 7.19 confirms that this is not the case. Whilst all normal velocities are constant, the tangential velocity components (shown in brackets in the legend) must obviously increase with inbound angle and the resulting force profile appears dependent upon this. To further

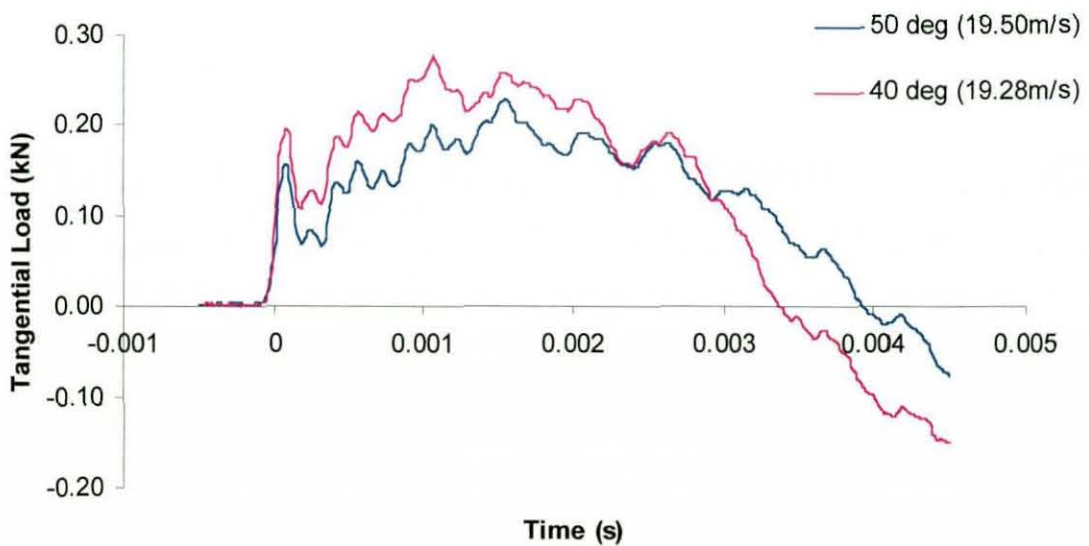
---

complicate matters it appears that there is a similarity in behaviour as the profiles rise to peak force, but a marked difference as the force decreases.

If there is a dependence upon tangential velocity then comparison of friction force at a constant value may provide further evidence. Whilst these tests provide limited cases of constant tangential velocities, Figure 7.20 shows results for 40 and 50 degree impacts with velocity components around 19m/s. Here we see a similar profile for both angles with the 40 degree impact subject to increased loading due to the corresponding higher normal force. As the balls rebound, the 40 degree impact force falls more sharply due to the lower impact duration. From this and other comparisons of tangential forces, it appears that there is indeed a relationship between the friction force and component velocity.



**Figure 7.19 - Tangential Force Comparison at Around 22m/s Normal Impact Velocity for Varying Incident Angles.**



**Figure 7.20 - Tangential Force Comparison for Impacts at Around 19m/s Tangential Velocity.**



---

## 7.5 Discussion

### 7.5.1 Velocity and Restitution Coefficient

Whilst oblique impacts may be best described in terms of their absolute velocities, these values are of little use in their analysis. It has been shown that the normal and tangential components are independent of each other and so the variation of absolute COR with inbound velocity is merely an indication of the combined effect of both components. That the data for all angles appears coincident around 25m/s merely indicates that in this particular case, combined energy losses due to each component are equal. It is through the separate consideration of component velocities that better insight is gained.

It is seen that normal COR is independent of inbound angle and hence tangential velocity, with all data fitting the same straight line, even that for normal impacts. Although the ball rotates during contact and hence changes its orientation relative to the surface, this has no effect on the normal COR. As a result, the energy loss due to material properties and post-impact vibrations must be entirely due to the normal component of the impact in all cases. This is confirmed in Figure 7.17 where it is seen that comparable normal velocities result in similar force profiles. Previous work (chapter 1) has shown that the energy loss during impact may be calculated from the difference between the compressive and restitutive impulse, given by the respective areas under the force profiles either side of the peak load. As all profiles are of a similar form then it follows that normal COR should be the same at all angles. Using this method, further analysis of the force profiles in Figure 7.16 reveals the reason for COR decrease with increasing impact speed. As normal velocity is increased then the compressive impulse rises, showing a more convex path in the force profile. The restitutive impulse, whilst having the same peak force, displays a convex path and so the difference between the two is greater. Figure 7.17 also show stiffer behaviour of the ball during the first 0.2ms corresponding to the compressive deformation phase as discussed in chapter 5.



---

Tangential COR is proportional to the energy loss due to the applied friction force and as all other energy losses appear due to the normal component then tangential losses must only be due to friction. Earlier in the chapter it was shown that the friction force is proportional to the normal load, contact area and sliding velocity and so the relationship between tangential COR and incident velocity is complex. That the ball may slide and roll during impact further complicates the friction force. As friction force is dependent upon normal load then the normal and tangential components of impact may not be completely separated. However, the key to analysing oblique impacts is the knowledge that normal properties only depend upon incident velocity and so analysis of tangential components at constant normal values allows the effects of normal load and sliding velocity to be assessed separately. It is reasonable to assume that comparable values of normal load must result in similar ball deformations and so contact area and normal load may be considered together, as a contact pressure.

With the knowledge that tangential COR is dependent upon the friction force alone then it is of no surprise that the variation in COR is so great. Tennis ball cloth exhibits directional properties due to a number of factors, as discussed in chapter 8 and this is further complicated by the orientation of the cloth pieces on the ball itself. It is also not possible, using the experimental setup, to either control or monitor ball orientation prior to impact. This results in relative motion during impact between the cloth and rigid surface which may be aligned to the direction of either fibre type within the cloth, or to some intermediate position. Resulting friction and shear forces will then be within a range due to the directional properties and hence tangential COR will be variable even for a constant inbound tangential velocity. The rubber seam may also be within the contact region during impact, further complicating the situation.

---

### 7.5.2 Rebound Angle

Having seen that normal COR is only dependent upon inbound velocity but tangential COR is affected by incidence angle also, it would be expected that rebound angle would similarly be dependent upon inbound angle and velocity and this is seen in Figure 7.7. Data spread seen here is again a result of the variability of tangential velocity. From examination of Figure 7.8 we begin to understand the mechanisms by which the tangential velocity is controlled. At constant values of normal velocity, and hence similar normal load profiles, the rebound angle is proportional to tangential velocity, and hence inbound angle. This implies that on isolating normal load then the friction force is approximately linearly proportional to tangential velocity and hence sliding velocity. Furthermore, from Figure 7.9 we see that as normal velocity is increased then the increase in rebound angle with tangential velocity is reduced, implying a greater friction force.

The angle ratio appears a more convenient method of displaying the angle changes than absolute values as the inbound angle does not have such a great effect on the results. Instead it allows the percentage change in angle to be displayed which is more indicative of the energy loss. However, this is only fully appreciated if the data is displayed at constant values of normal velocity. From Figure 7.11 it can be seen that a clear relationship exists between tangential velocity and angle ratio, or more generally friction, above initial velocities of 10m/s. At lower velocities the data is much more scattered and this would seem to indicate a transition from sliding to rolling is occurring. The tangential inbound velocity will become the initial sliding velocity of the cloth cover over the impact surface. As the friction force increases then this sliding velocity will diminish, with some of the energy transferred from linear to rotational motion.

Analysis of the tangential force profiles in Figure 7.18 reveal that with increasing absolute velocity and hence normal load then the restitutive friction force falls to zero more sharply. Similarly in Figure 7.19, a lower tangential velocity at constant normal value results in the tangential force falling more rapidly. Both these effects are a result of

---

---

an increased friction coefficient causing faster retardation of the relative linear motion. Clearly at the lowest velocities, relative motion of the contact surfaces would rapidly decelerate resulting in the transition from sliding to rolling. Also, as the ball will be at some random orientation then this effect will occur at different times during the impact in each case. As transition occurs at different times in each case then the impulse method used to determine the normal COR does not hold.

The tangential force profiles also display an initial peak load that appears coincident with the initial stiffness shown in the normal force profiles. As the load sharply falls following the transition, it would appear that the shape or size of the contact area or its pressure distribution must change as a result.

### 7.5.3 Spin

Spin is the direct result of the friction force and as such must be dependent upon exactly the same factors. Clearly, increasing either or both velocity components will have the effect of enhancing ball spin as has already been discussed. Of significant interest is the fact that, whilst tangential COR increases with its component velocity, implying a smaller loss due to friction, the spin shows a similar increase. Examining the force profiles of Figure 7.19, it is clear that the tangential load falls to zero before the end of impact in all cases. This would imply that the ball always rolls off the surface. If this is true then the sliding velocity must be reduced to zero and so for higher incident velocities would require a greater force, as has already been shown. However whilst the ball is sliding no energy is lost tangentially due to the deformation of the ball. Once the ball begins to roll then its forward part must compress whilst its rearward section recovers its shape. As the material is deformed then energy is lost through hysteresis effects as discussed earlier in the chapter and this is entirely due to its tangential motion. Thus the COR at lower velocities, where the ball begins to roll much earlier during impact, will be less than at higher speeds. This process of energy loss through hysteresis in rolling is discussed further in chapter 8.

---

## 7.6 Conclusions

The experimental programme concerned with evaluation of impact forces and subsequent analysis has enabled several facts to be established:

In oblique impacts, the ball behaviour in the normal direction is independent of any tangential motion. Force profiles and CORs are the same at all inbound angles.

The tangential ball behaviour is entirely due to the friction force. As this is itself dependent upon normal load and sliding velocity then these factors effect the tangential behaviour.

Force profiles suggest that the ball rolls off the surface in all cases and that the time during impact that transition between sliding and rolling occurs increases with initial sliding velocity.

---

## **8 Mechanical Properties of Fabrics**

### **8.1 Introduction**

#### **8.1.1 Fabric Construction**

The cloth cover of a tennis ball is a woven fabric. As with all weaves it consists of a warp, being the fibres aligned along the length of the original piece, and the weft, being the crossing fibres which are woven into the warp to form the finished cloth. There are many possible methods of weaving cloth depending upon the likely application and these are differentiated by the number of warp fibres passed over or under by the weft fibre in each row and the variation of this pattern from row to row.

The most basic weave is that where weft fibres pass alternately over and under each warp fibre in turn, with this pattern being alternated for each row. This is called a plain weave and produces a strong cloth where the surface characteristics are a mix of the materials used for each fibre. If different materials are used for warp and weft, then the fabric will be orthotropic, having different mechanical properties in each direction.

Tennis ball cloth is of a more complicated construction. It is a 'sateen' weave, which as the name may suggest is the opposite of a 'satin' weave. It is constructed by passing the weft over a number of consecutive warp fibres at a time before passing under only one or two. This pattern is repeated throughout the row and is staggered through consecutive rows. This method has the effect of creating a large proportion of the surface of the fabric from the weft material, around 80% for tennis cloth, resulting in surface properties being greatly dependent upon the material used in the weft fibres. In tennis cloth, this is a mix of natural and synthetic wool. Viewing natural wool under a microscope reveals its surface to be serrated, much like human hair. This means that when the individual fibres are spun into a thread, they grip each other and help to lock the structure of the



---

thread into place. The man made fibre content is used mainly to reduce cost, as natural wool is an expensive resource. The synthetic fibres are crimped along their length to mimic natural wool, however as they are extruded then the natural surface roughness cannot be reproduced. It is mainly the wool content that provides structure to the threads. The warp fibres are made up of cotton strands, twisted together to form a yarn which provides structure and strength to the fabric.

Once the weaving process is complete, the material surface is then raised. This is a mechanical scouring of the fabric surface creating the 'fluffy' nature of the finished cloth. It has the effect of pulling apart some of the spun weft threads such that individual wool fibres stand out from the surface. This significantly alters the mechanical properties of the original fabric, especially surface friction and compression in the thickness plane. The fabric is dyed after this stage.

---

### 8.1.2 Mechanical Properties

Fabric behaves much like rubber under tension. It is elastic up to relatively high strains of the order of 25%. As fibres are woven, then they will be deformed laterally where they pass over and under cross-fibres (Realf, 1994). When initially subject to tension, the kinks in the loaded fibres straighten out and so large apparent strains are recorded for relatively small stresses. Once the fibres become straight then the load is taken by the fibre itself and the fabric behaves much stiffer.

As fabrics were historically analysed by feel or touch, so the analysis of fabric mechanical properties has come to be known as 'hand evaluation'. Fabric hand is characterised by expressions such as 'stiff' and 'soft', but is often governed by an individual's own subjective opinion and language, making standardisation of analysis difficult. In order to overcome this problem, a standard set of material properties tests for fabrics was developed in order that a numerical value could be placed on fabric hand. These tests were developed by Suetō Kawabata and this standardisation of hand evaluation bears his name (Kawabata (1980)). The Kawabata tests comprise a series of mechanical property tests for tension, compression, bending and shearing. These are complemented by tests for the physical properties of weight, thickness, surface roughness and associated friction. Results from these tests are used to derive a hand value from a set of conversion charts or tables.

Unfortunately, these tests are aimed at providing useful data for the textile industry and the results are of limited value in an engineering context. During the tests loads and hence strains are small and it is not possible to accurately extrapolate test data at greater loads. Instead, it is necessary to look towards engineering materials tests to provide useful data. A standard tensile test provides a full load history for a sample of fabric strained up to its elastic limit. This data is much more useful for developing a FE model, which requires discrete stress/strain data over the range of interest. Kawabata test results merely state a maximum value of strain at a specified maximum load and the linearity of the strain response over this range. In order to produce useful data from these results, it

---

would be necessary to derive an equation for a suggested curve that would give the linearity quoted and sample points from this curve. The resulting data would be questionable at best. Results from tests such as the bending test, which give values of load necessary to produce bending in the sample of a specified curvature, are of no use. Whilst the physical properties tests are of use, the derived coefficient of friction is dependant upon factors such as slider material and speed of travel. The equipment used is not representative of the case of a bouncing tennis ball and so separate tests are suggested to derive a coefficient of friction within chapter 7.

### 8.1.3 Dumbells

In order to appreciate the effects of the cloth on impact it is also worth briefly describing the method of constructing the actual tennis ball covering. Large sheets of cloth are first coated on the back with a rubber-based adhesive. The characteristic dumbell shapes are cut from the cloth on the bias, that is at 45 degrees to both warp and weft orientation and adhesive is then applied to the cut edge of each dumbell. Two of these pieces are applied to each rubber core under pressure so that the adhesive begins to bond. Any gaps between the cut edges are closed before the balls are cured, so that the adhesive forms the seam around the ball. Cutting the cloth on the bias ensures that the dumbells do not become overly distorted once applied to the cores and also, the effects of the directional properties of the cloth on play are somewhat reduced.

---

## 8.2 Material Testing

### 8.2.1 Equipment

In order to develop a material model for the cloth within Abaqus, it is necessary to determine the stress/strain characteristics of the fabric under tension and compression. This was achieved using a Lloyd Instruments tensometer. The machine comprises a loading arm controlled by a motor driven screw thread. On the arm is mounted a load cell with a maximum capacity of 1kN. Onto this was attached a set of clamps which are designed for testing highly deformable materials such as fabrics. As the clamp has an off-centre pivot, the clamp tightens under increasing load. Another similar clamp was mounted on the base of the machine. The tensometer is controlled by a manufacturer supplied software package 'Nexigen'. This allows the user to select from a number of standard tests such as pull to break, load cycle, pull to limit, or to create user defined tests. It is possible to control pre-loads and strain rate, to a maximum of 999mm/min, as well as set loading and deflection limits. For the compression test, again using the tensometer, a set of connected platens are used which move together as the ends are pulled apart. This allows samples to be compressed whilst still using the machine in tension as it is designed.

Data is saved to the p.c. in tabulated form as a .txt file. The software allows the user to specify the number of data points recorded to the file and allows saving of load, extension, and time data. The saved data can then be manipulated in a spreadsheet package such as Excel.

---

### 8.2.2 Experimental Procedure

Whilst it has already been shown in previous chapters that the strain rate during a tennis impact is considerably greater than is achievable in a standard tensile test, the data obtained can be used confidently as a starting point for the model. In order to assess the effect of material orientation on the tensile characteristics, ten test samples were cut across each of the warp and weft directions from the cloth. Each sample was in turn subjected to a constant strain rate of 900mm/min until it failed.

For the compression test, a maximum load of 900N was specified to protect the load cell from over-ranging and the strain rate was reduced to 200mm/min in order to prevent overshoot. As the compression was applied perpendicular to the fibres, material orientation had little effect on the results. However, as the fabric thickness is around 4.5mm, it would be difficult to subject a single sample to load using the setup described. For this reason a stack of ten samples was used to allow greater deformation. However, as strain is non-dimensional then the results would still be valid. Whilst there will be interactions between the sample layers which introduce errors into the results, these should be small in comparison to the overall stresses involved.

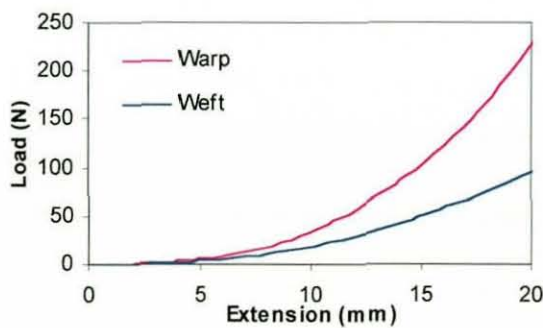


---

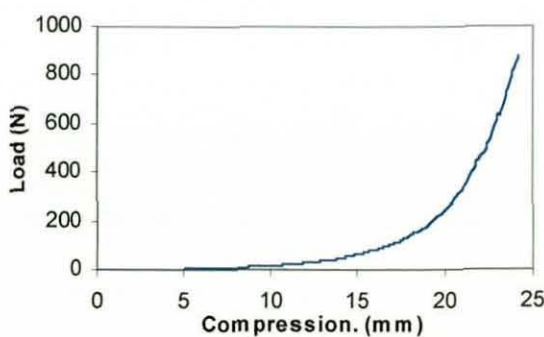
### 8.2.3 Experimental Results

Figure 8.1 and Figure 8.2 show respectively tensile and compressive stress against strain data, averaged over the twelve samples. Whilst samples were pulled to break in each case, only the region of elastic deformation is considered here. From Figure 8.1 it is clear that the cloth behaves like a polymer under tension, with its stiffness increasing in proportion to the applied strain. Also, it is evident that the cloth is over twice as stiff in the warp direction as it is in the weft. Furthermore, whilst the variation in strains recorded for samples in the weft direction was only a few percent, in the warp direction strain varied by over 30%.

The through thickness compressive behaviour seen in Figure 8.2 is markedly different, with very large deformation during the initial phase before the cloth stiffens considerably at higher strains. This behaviour is more characteristic of a foam, where the cells buckle initially under small loads, whilst at higher loads the cell walls are compressed against each other resulting in a much higher stiffness. Whilst it is clearly not a foam, this analogy may be useful in developing a finite element material model. Variations of only a few percent were seen over the range of samples for compression.



**Figure 8.1– Average Tensile Load vs Extension  
For Tennis Ball Cloth.**



**Figure 8.2 – Average Compressive Load vs  
Extension For Tennis Ball Cloth.**

---

## **8.3 Developing the Cloth Material Model Through Normal Impact Analysis**

### **8.3.1 Directional Material Properties**

It is clear that tennis ball cloth behaves markedly different in each of its constituent directions, yet the transfer of this directionality into the finite element environment is problematic. The cloth exhibits large strains and it has already been shown in chapter 6 that ABAQUS lacks the provision of an orthotropic material model that can provide such deformations. Clearly there must be some compromise between geometric accuracy and material properties. As large strains are required then a directional material is not possible. If this is to be the case then another problem arises, which set of material data should be used to represent the cloth within the model.

### **8.3.2 Appropriate Test Data**

Whilst it is desirable to develop a model which predicts both tensile and compressive deformation accurately, the difference in behaviour of the cloth for each of these means that it is not possible. From visual inspection of Figure 8.1 and Figure 8.2, it is seen that compressive deformation is much greater than tensile for comparable loading and so compression would be expected to dominate the material deformation. It has already been suggested that cloth behaviour is foam-like under compression, with large deformations through the thickness resulting in negligible deformation perpendicular to the direction of load application. Foams are composed of polyhedral cells and this determines their material behaviour. Under tension foams behave much like rubbers, the cell walls become aligned under small to moderate loads, and as the load is increased further so the cell material itself is stressed resulting in stiffer behaviour.

Foams are more commonly loaded under compression and in this situation their behaviour is very different. Initially the material may be stiff as the cell walls bend, but it rapidly becomes less rigid as the cells buckle elastically and very large strains may occur during this phase. Finally, densification occurs as cells crush against each other, resulting in a very stiff material behaviour. Whilst tennis ball cloth does not have a foamlike construction, its behaviour is somewhat similar. The initial stiffness of the cloth under compression does not really exist, although an analogy could be drawn to the longitudinal compression of individual fibres as the load is first applied. However, this would occur over such a short period that it would be indeterminate. The large strain increase at relatively small loads is shown by cloth and is initially due to the raised fibres being compressed, then subsequent deformation of the woven structure itself. Finally, as the load increases further, the fibres themselves become diametrically compressed, similar to the densification of foams, resulting in a high material stiffness. Clearly the two behaviours are similar.

Foam-like materials may be modelled within ABAQUS using the 'Hyperfoam' material model. This energy function is similar in form to that of the Ogden hyperelastic model from chapter 6, except that here the volumetric behaviour is related to the Poisson's ratio for the material. Thus the strain energy equation becomes:

$$U = \sum_{i=1}^N \frac{2\mu_i}{\alpha_i^2} \left[ \hat{\lambda}_1^{\alpha_i} + \hat{\lambda}_2^{\alpha_i} + \hat{\lambda}_3^{\alpha_i} - 3 + \frac{1}{\beta_i} (J_{el}^{-\alpha_i \beta_i} - 1) \right]$$

**Equation 8.1**

where  $\beta_i = \frac{\nu_i}{1-2\nu_i}$  and  $J_{el} = \hat{\lambda}_1 \hat{\lambda}_2 \hat{\lambda}_3$



As has been discussed, the compressive and tensile behaviours of foam are very different and this is also true of the hyperfoam model. For this reason it is not possible to model both compressive and tensile properties using a single function. Furthermore, if we attempt to fit a hyperfoam model to either set of test data, it is clear that predicted behaviour is only good for the type of loading considered. Figure 8.3 shows both sets of test data plotted as a single curve, with material models fitted using either the compressive or tensile data only. Both models appear to predict very low stiffness for deformation in the opposite sense to that considered. Whilst we have seen in chapter 5 that the addition of a cloth layer stiffens the ball, it is also clear that the compression mode dominates cloth deformation during impact and so it is this data that must be used to derive the material model.

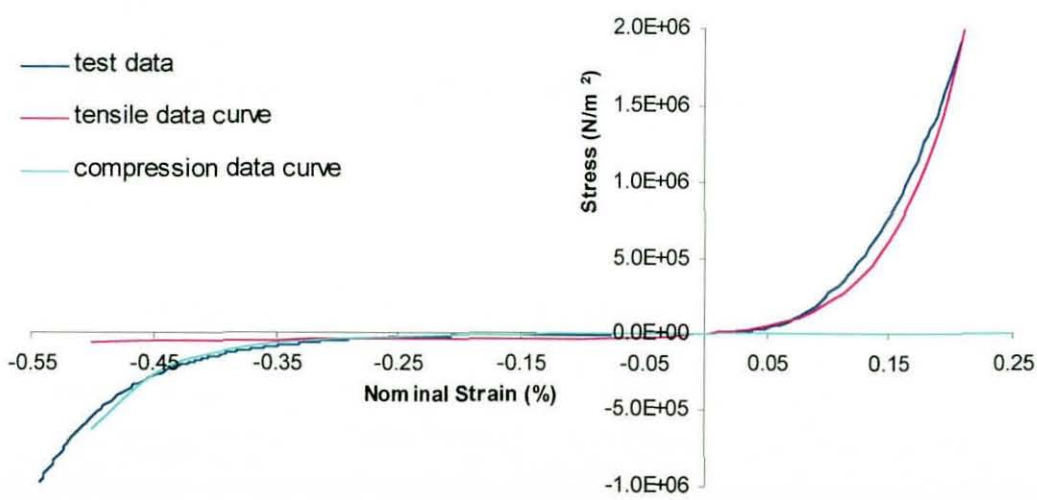


Figure 8.3 – 2<sup>nd</sup> Order Hyperfoam Models fitted to Cloth Test Data

---

### 8.3.3 Developing the Hyperfoam Material Model

Having seen that the cloth is best defined from compression test data and the Hyperfoam material model, it is necessary to determine the order of expansion  $N$  for the strain energy equation. The transition in the cloth from low to high stiffness appears rapid and so it would be expected that a high order function is necessary to represent the behaviour accurately. Figure 8.4 reveals this is not the case and that a value of  $N=1$  is sufficient to provide a good first order approximation to the test data. Thus values of  $\mu_i$ ,  $\alpha_i$  and  $\beta_i$  are required for  $i=1$  only.

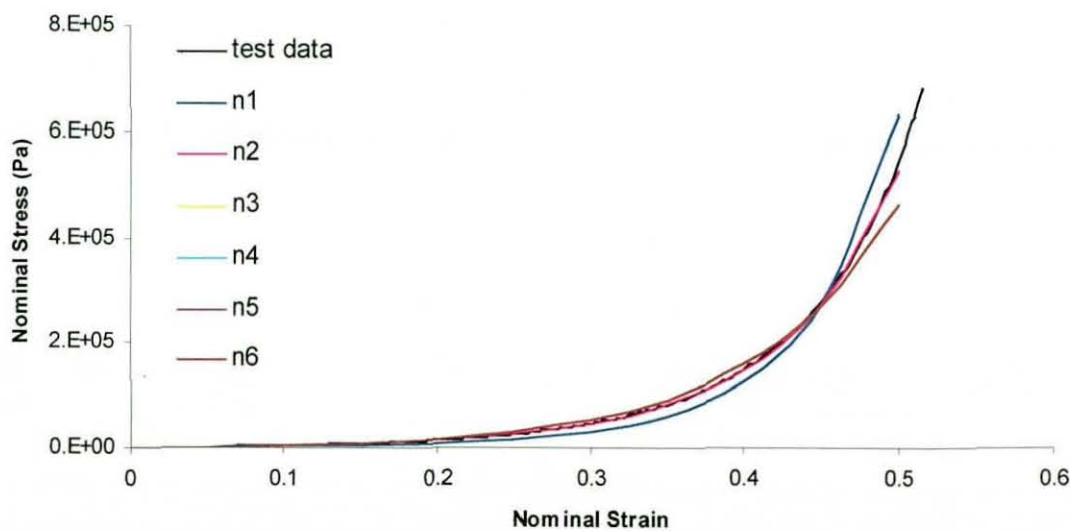


Figure 8.4 - Effect of Expansion Order on Cloth Compression Model.



---

Consideration of compressibility allows further simplification of the model. It has been stated that through thickness compression of the cloth as considered here is primarily due to the flattening of raised fibres. Only at high stresses is the woven structure affected by the load and the resulting strain increase is low. Thus it is likely that out of plane strains due to the compression are minimal and hence the effective Poisson's ratio will be nominally zero. If we consider Equation 8.1, then for  $\nu_i = 0$  we seen that  $\beta_i = 0$  also. Through substitution of a Taylor series expansion it can be shown (H.K.S.inc, 1998) that the strain energy equation reduces to:

$$U = \sum_{i=1}^N \frac{2\mu_i}{\alpha_i^2} [\hat{\lambda}_1^{\alpha_i} + \hat{\lambda}_2^{\alpha_i} + \hat{\lambda}_3^{\alpha_i} - 3 - \alpha_i \ln J_{el}]$$

**Equation 8.2**

Thus, whilst the material model is isotropic in nature it is possible, through specification of a zero valued Poisson's ratio, to allow independent uniaxial deformation.

---

#### 8.3.4 Strain Rate Effects

It is known that the individual fibres and yarns behave viscoelastically under quasi-static loading. Furthermore, work on the dynamic properties of fibres by Smith, Blansford et al. (1960), Petterson and Stewart (1960) and Vinson and Zukas (1975) although mostly concerned with the characteristics of textile body armour has shown that strain rate dependency is similar to that of polymers. Whilst much of the work subjected fibres to transverse impacts, the fibres deformed into a V shape and the primary mode of deformation was extension. Work on high-speed compression is less evident but it is expected that the results would be similar. Lyons (1963) states that the behaviour of woven fabrics is similar to that of the constituent fibres, although their complex structure means that direct comparisons are not possible. However, it is reasonable to assume that an increase in modulus proportional to strain rate holds for fabrics as it does for rubber. From this assumption then a high strain-rate material model may be developed in a similar manner to that of chapter 6.

Within the Hyperfoam strain energy function, the coefficient  $\mu_i$  controls material stiffness and is analogous to the elastic modulus. Whilst little data exists on the relationship between strain-rate and elastic modulus for any woven fabric, regardless of material and weave type, it is possible to artificially increase the coefficient  $\mu_i$  and assess the effect on ball model rebound characteristics. In a similar manner to the rubber model development, it is then possible to tune the material parameters to replicate the experimental data. From the compression test data, an initial value of  $\mu_1 = 5.5E3$  is derived. This was increased in a manner similar to that for the rubber model and ball impact model results compared to the experimental data. A similar method was adopted for the determination of a damping coefficient to represent the time-dependent energy loss due to the cloth. Results are shown in section 8.5.

---

## 8.4 Developing the Cloth Friction Model Through Oblique Impact Analysis

### 8.4.1 Experimental Determination of COR

#### 8.4.1.1 Dynamic Friction

The previous chapter presented results for oblique impact characteristics of cloth covered balls and highlighted the dependency of the friction force upon normal load and sliding velocity. However, in order to be able to transfer that information to a F.E. model, the relationship between these variables must be determined. The dependence of the friction force on the normal load is commonly defined by a coefficient of friction, being a simple ratio of the two values. Chapter 7 discussed how this coefficient is a constant at low sliding velocities for metals, but varies for fabrics over a range of normal loads and sliding velocities. If we plot normal load against friction force for a sample impact (Figure 8.5) we see that the relationship here is equally complex. There is an oscillatory component to the trace which is most likely a result of the fabric geometry.

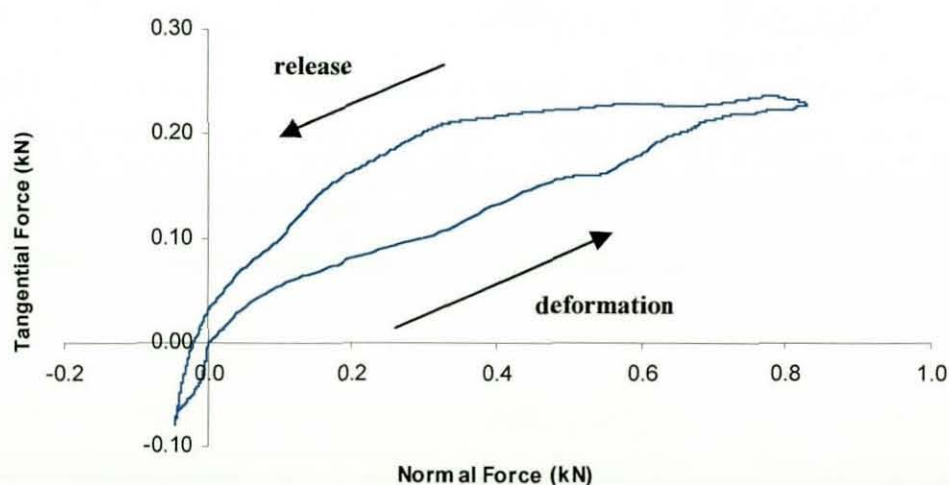


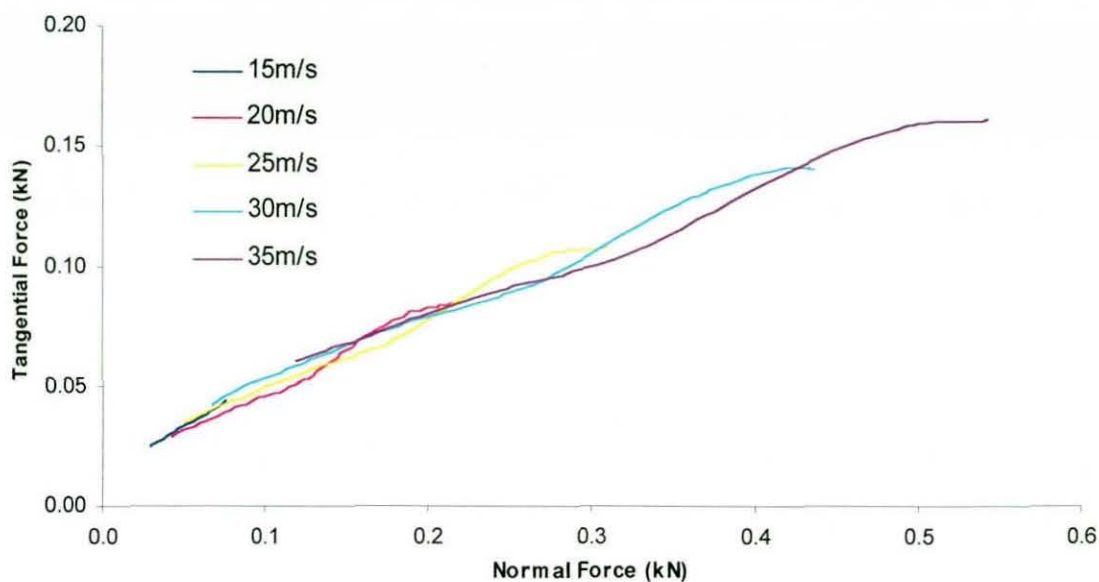
Figure 8.5 – Friction Force vs Normal Load for 50 Degree Impact at 25m/s.



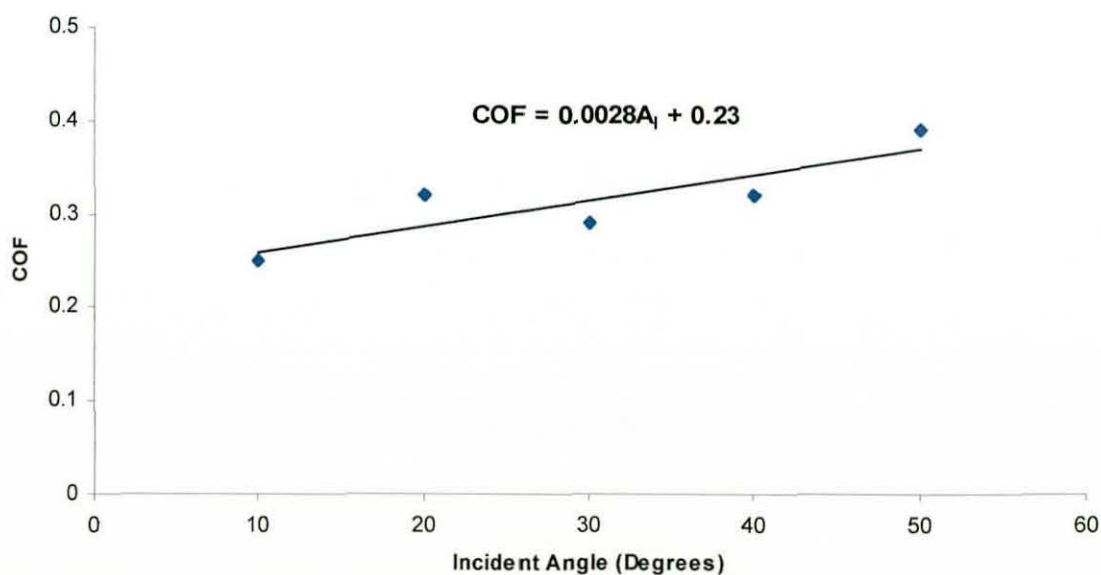
---

Hosseini Ravandi, Toriumi et al. (1994) have shown that the dynamic friction behaviour of fabrics is characterised by a stick-slip motion which is due to the fabric structure; such characteristics as yarn density and spacing. The vibration characteristics of the impacting surface and its supporting structure may also be superimposed upon the force data. However, it is possible during the compression phase, after the initial period of high stiffness, to fit a straight line to the data, which would seem to indicate a constant kinetic COF. If the data for all incident velocities at one incident angle are plotted for the compression phase only on the same chart (Figure 8.6), then it becomes clear that all data may be approximated by the same trend line. This would suggest that the kinetic COF for any one incident angle is independent of the initial velocity, and for any ratio of (initial) sliding velocity to normal load, i.e. the incident angle, is a constant.

Having fitted trend lines to each data set, the values of kinetic COF for each angle are shown in Figure 8.7. Whilst there is some data scatter, it is possible to determine a relationship between incident angle and kinetic COF and this may be used to develop the F.E. friction model. This is clearly a simple approach, but it provides a good means of characterising the relationship within the modelling environment, as will be shown.



**Figure 8.6 – Friction Force vs Normal Load for 50 Degree Impacts at all Incident Velocities during the compression phase only.**



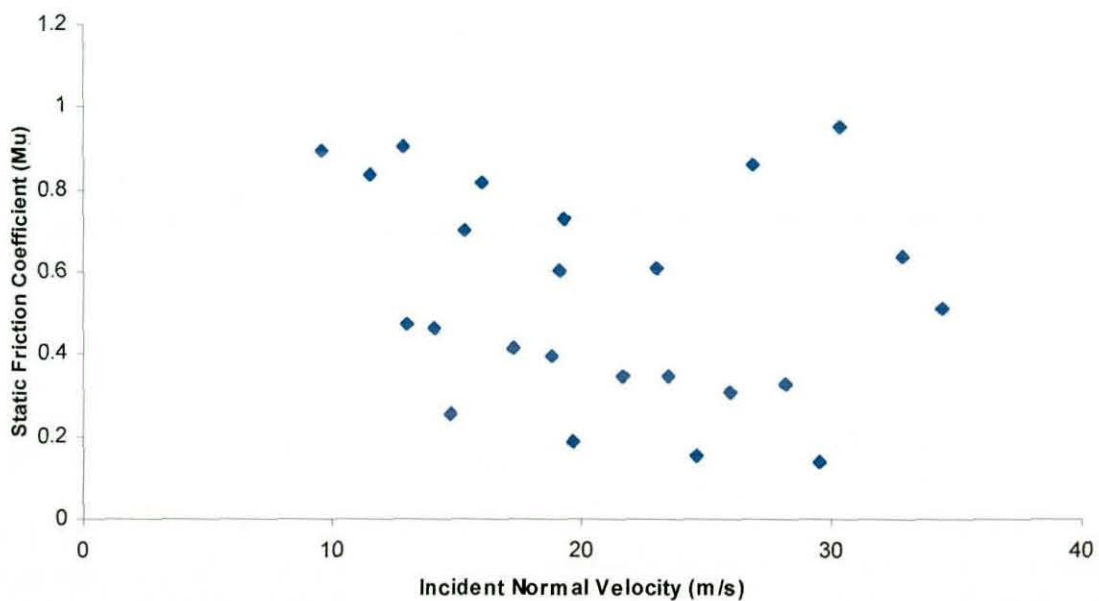
**Figure 8.7 – Relationship between Kinetic Friction Coefficient and Incident Angle.**



---

#### 8.4.1.2 Static Friction

The static friction coefficient must be greater than its respective kinetic value, as discussed in chapter 7. Assuming the ball rolls during some of the impact in nearly every case, then sliding velocity will be zero at that time and static friction occurs. It is then possible to determine the static COF from the region of maximum gradient during the rebound phase of each impact force plot, shown in Figure 8.8. As would be expected, no relationship is apparent between the initial normal velocity component and static COF, such that a single value may be selected to represent the static COF in all cases. From the data, an average value of 0.54 is found and this will be used in the initial model.



**Figure 8.8 – Static Friction Coefficient against Normal Incident Velocity.**

---

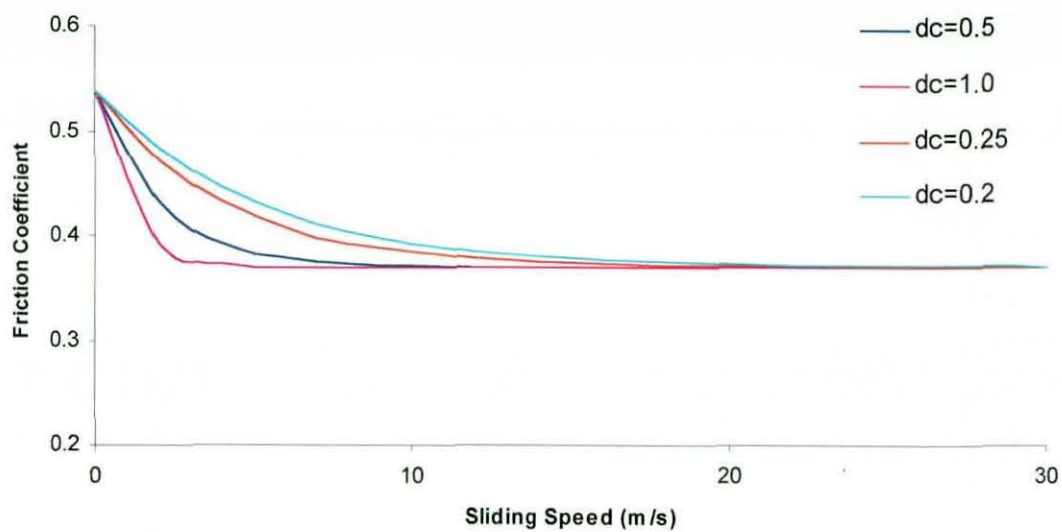
#### 8.4.2 Friction Models in ABAQUS

Abaqus provides a number of options for specifying tangential contact interaction, all based on the Coulomb friction model. The most basic of these requires only a single value of friction coefficient to be specified, which then relates the normal and tangential contact forces at all times. In an expansion of this, the COF may be defined at multiple values of dependant variable such as slip rate, contact pressure and temperature. Ideally this method would be used to create a detailed friction model with dependencies upon sliding velocity and normal load as previously discussed. However, as the exact relationship is not known at discrete values, definition by this method is not possible using the data available.

It is possible to use the previously presented relationship between inbound angle and kinetic COF as well as the single static COF to develop a friction model which is angle dependent. ABAQUS provides a model whereby the value of COF at any slip rate  $\gamma_{eq}$  is defined by static and kinetic coefficients and an exponential decay between them, using the equation:

$$\mu = \mu_k + (\mu_s - \mu_k)e^{-d_c \gamma_{eq}} \quad \text{where } d_c \text{ is the exponential decay constant.}$$

An example of the model is shown in Figure 8.9 for 50 degree impacts, where the effect of decay coefficient can be seen. It is not possible to determine the nature of transition from static to dynamic values from the impact force data. However, comparison of the F.E. impact model results using this friction model to the oblique impact data will allow a suitable value to be chosen. Using the relationship between inbound angle and kinetic COF, such a model may be defined easily for any inbound angle, where the static COF and decay parameter are constant.



**Figure 8.9 – COF model for 50 Degree Impact Showing Effect of Decay Constant.**

---

## 8.5 Results

### 8.5.1 Normal Impacts

Having shown that a cloth material model may be developed in a similar manner to that of the rubber, then the resulting normal impact model should be verified using the same method also. Figure 8.10 shows the normal impact model predicted CORs for the cloth covered ball against the experimental data, whilst in Figure 8.11, the impact duration is shown for the same case. Clearly, as the experimental results were used to tune the material parameters, good agreement would be expected. Values of  $\mu_1 = 1.9E6$ ,  $\alpha_1 = 23.44$  and  $\beta_R = 6E7$  were determined to provide the best approximation to experimental results.

Close approximation is seen in Figure 8.12 for the maximum deformation normal to the surface, which would appear to indicate that the cloth material model is accurate. However, Figure 8.13 shows a difference of around 25% between the experimental and predicted tangential deformation. As the predicted deformation is more accurate in one direction than the other, this would suggest that it is the characteristic bending wave that is not being accurately modelled in this case. It was noted in chapter 5 that its reduced magnitude in the cloth covered balls prevents determination of the wave characteristics from high speed video. As a result, the current cloth model must be used for the oblique impact analysis in the knowledge that some inaccuracy may result.

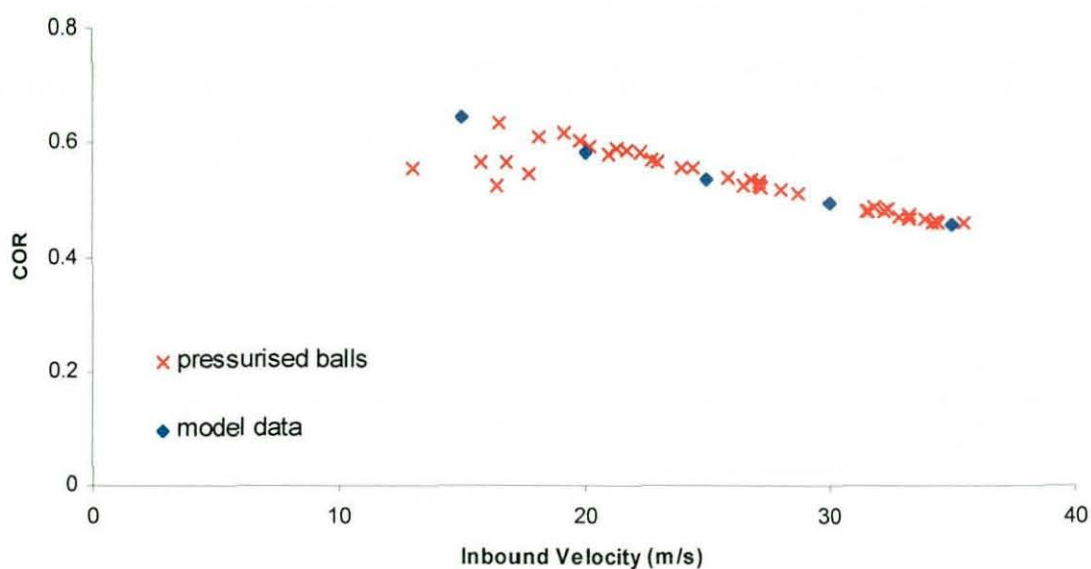


Figure 8.10 – Pressurised Ball Model COR Compared to Experimental Data.

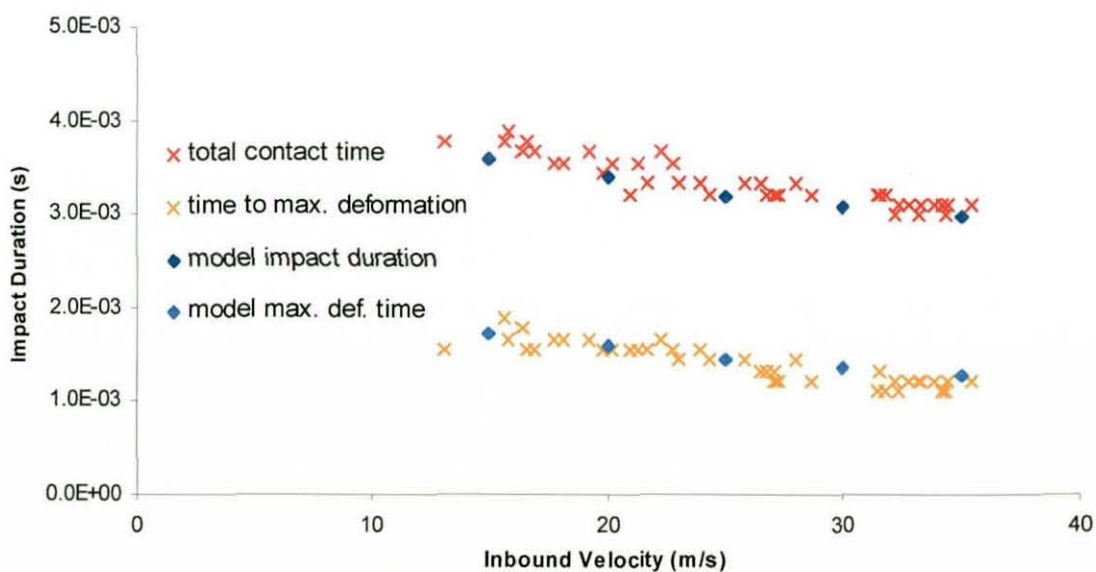


Figure 8.11 – Impact Duration for the Pressurised Ball Model Compared to Experimental Data.



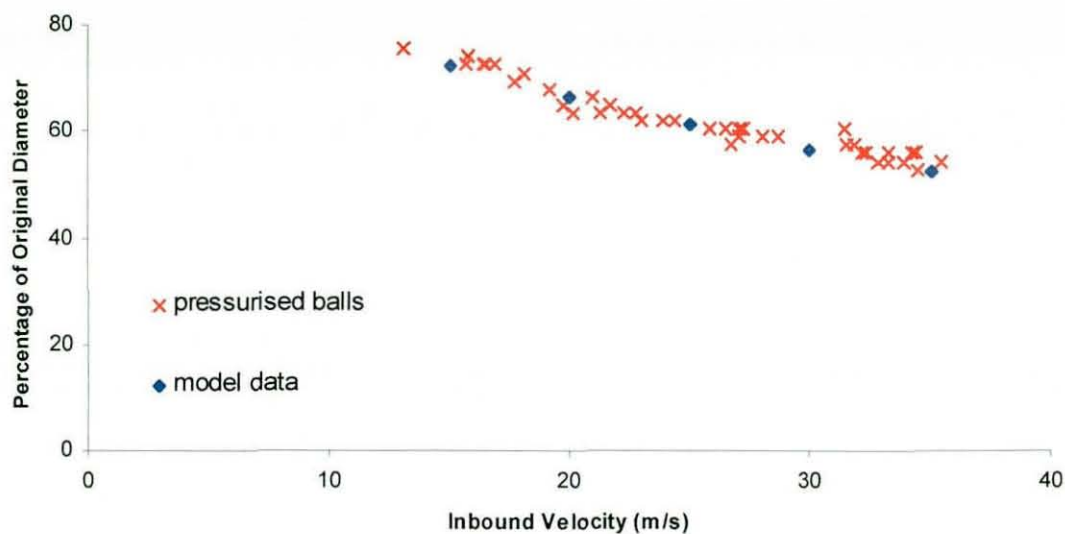


Figure 8.12 – Gross Deformation Normal to the Impact Surface and F.E. Predicted Results.

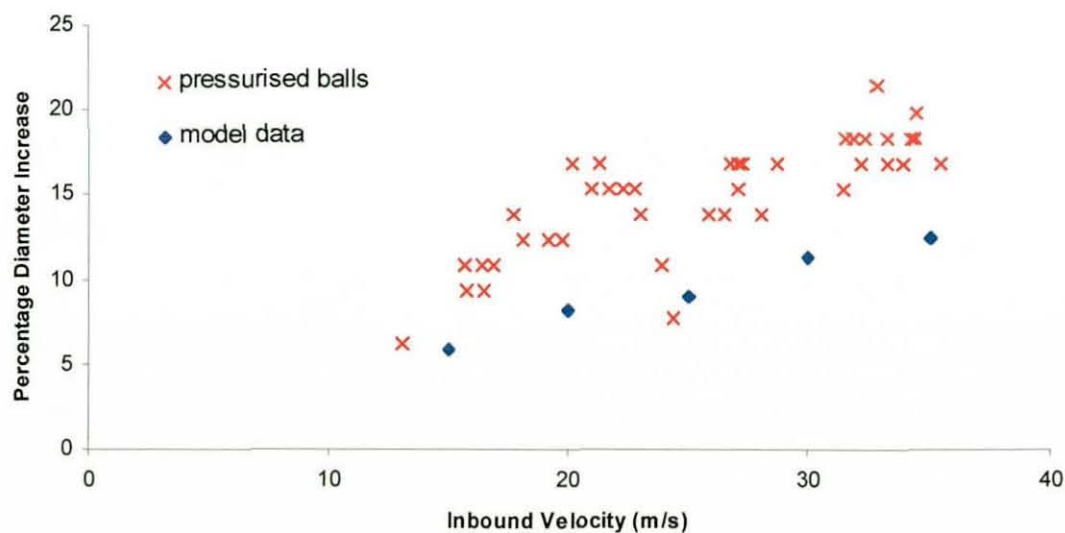


Figure 8.13 - Gross Deformation Tangential to the Impact Surface and F.E. Predicted Results.

---

### 8.5.2 Oblique Impacts

Applying the friction model developed previously to the F.E. ball model, results for post-impact component velocities and spin rate were generated and compared to experimental data. The initial model run at the intermediate velocity of 25m/s for all angles revealed a difference between predicted and experimental values for tangential velocity and spin. As seen in Figure 8.14, the tangential component of predicted rebound velocity was too low in all cases, especially for smaller angles, implying that the COF is too high. It is not surprising that the initial COF values do not provide good correlation, as they were derived from scattered and noisy data. By adjusting the dynamic COF for each angle, it is possible to provide a better fit to the data and the improved values are shown in Figure 8.15, against the original data. The relationship between COF and angle is similar with a slightly increased gradient and lower constant in the equation. In order to improve the lower angle impacts the static COF was also reduced, with a value of 0.39 proving the most suitable over the range of conditions. Again, this is a marked reduction from the initial suggested value, but is well within the range of the data from which it was derived and agrees well with several individual values from the experimental data (Figure 8.8). Using the improved friction models, oblique impact over the full range of impact velocities and angles were modelled and the results compared to experimental data.

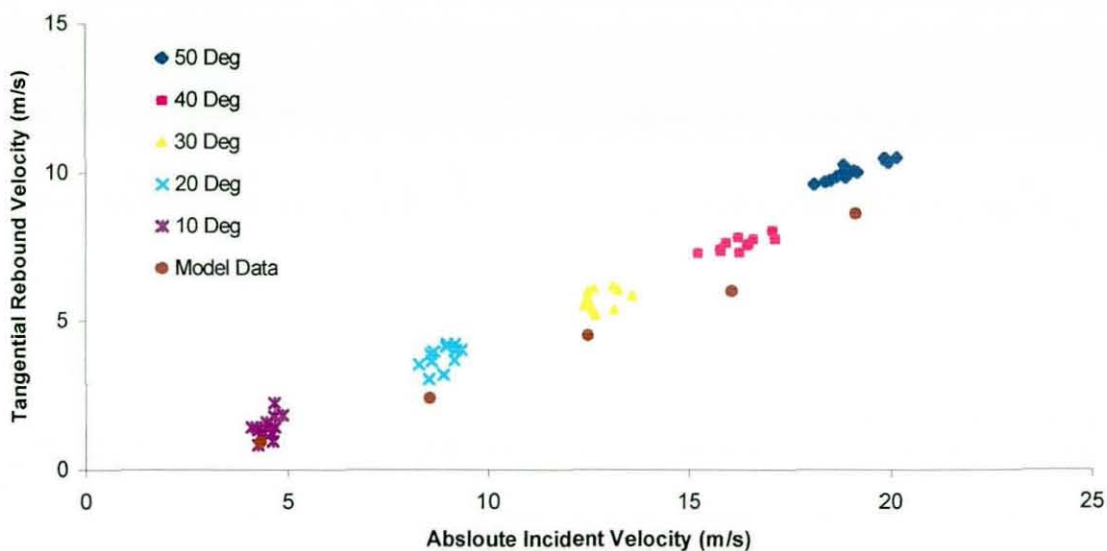


Figure 8.14 – Original F.E. Predictions of Tangential Rebound Velocity.

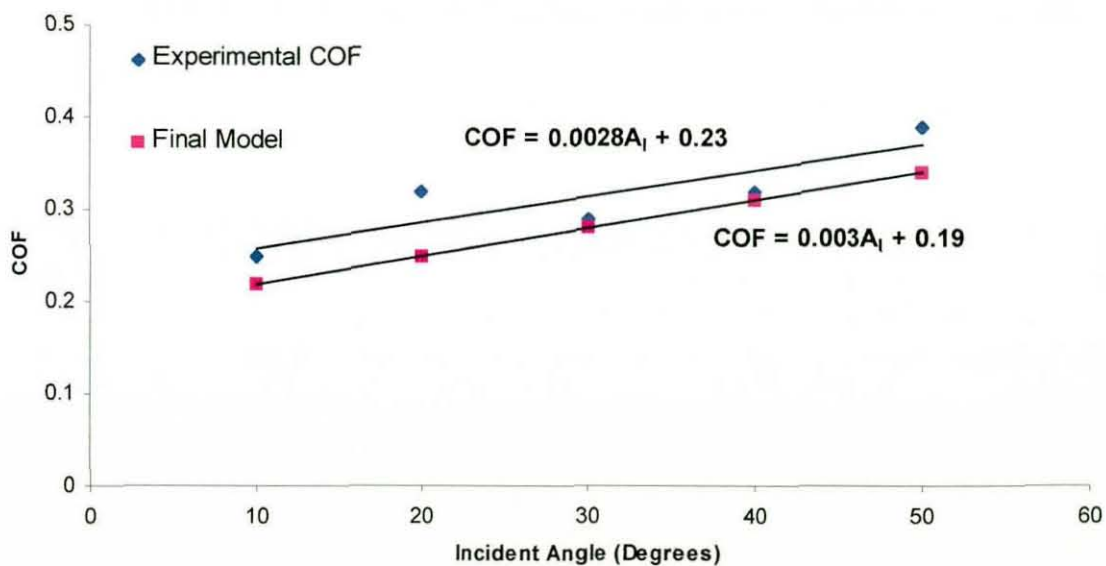


Figure 8.15 – Improved Kinetic Friction Model Displayed against the Original Values.

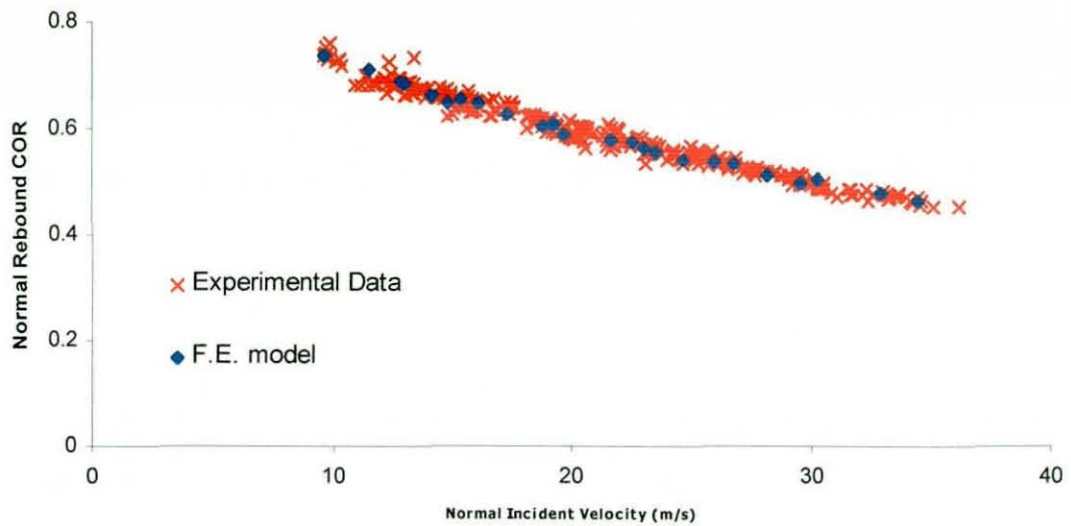
---

Figure 8.16 compares predicted normal COR to the experimental data and agreement is good. This would be expected as the material model was developed from normal impact data and we have seen in chapter 7 that the normal component of rebound velocity is independent of incident angle. The COR should therefore be independent of the COF and normal properties would be expected to agree regardless of friction values.

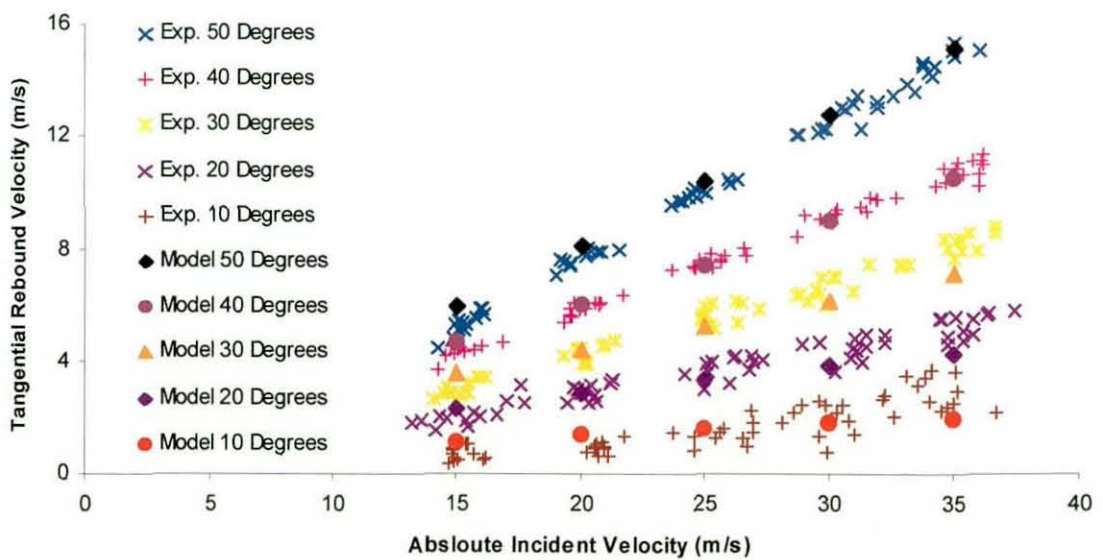
Figure 8.17 displays the predicted outbound tangential velocity as a function of absolute incident velocity and inbound angle. Good agreement is seen over the full range of velocity and for all angles, especially at the higher incident angles. Lower incident velocities are less well represented by the model, with predicted outbound tangential velocities being higher than the experimental values. There is a maximum difference in each case of 0.5m/s at 15m/s incident velocity. For higher incident velocities, the lower angled model impacts predict rebound velocities that are lower than their experimental equivalent, with a maximum difference of around 1m/s at 35m/s incident velocity for 10, 20 and 30m/s impacts.

Post-impact spin rates for the models are shown in Figure 8.18 against the experimental data. Once more, the model results provide good approximation to the experimental values, with comparable accuracy at all angles. At high values of incident velocity the model provides a good data fit in all cases, with the predicted behaviour being within the range of experimental values in all but one case, that of the 30 degree impact. At low incident velocity, the model predicts a spin-rate that is above the average experimental value for each angle by around 200rpm.



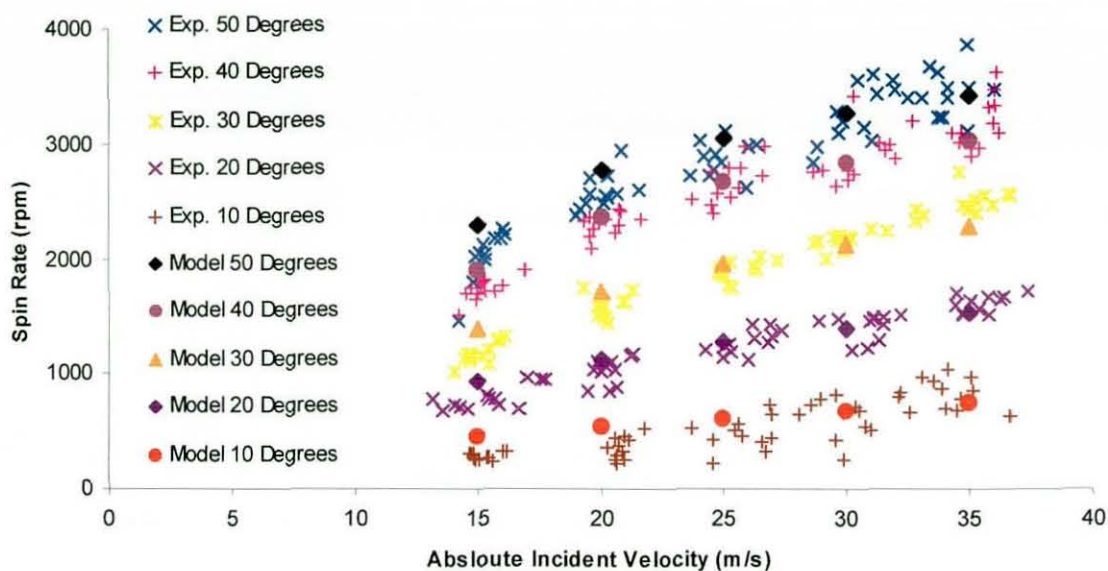


**Figure 8.16 – Normal Coefficient of Restitution for Oblique Impacts at Varying Normal Incident Velocities.**



**Figure 8.17 – Tangential Rebound Velocity Component for Various Inbound Angles and Velocities: Experimental Results against Predicted Behaviour.**





**Figure 8.18 – Post-Impact Spin Rate for Various Inbound Angles and Velocities: Experimental Results against Predicted Behaviour.**

---

## 8.6 Discussion

The lack of published data on the behaviour of woven fabrics makes the development of a high-strain rate model difficult and material parameters such as stiffness and damping must be initially estimated based on the behaviour of similar materials. Hence the F.E. model is produced by tuning the material coefficients to fit experimental data. This reduces the parameters by which the model may then be verified in the same way as it did for the rubber, in fact more so as the bending waves were unable to be identified for the cloth covered ball. Whilst the gross normal deformation predicted by the model was a good fit to the experimental data, the results for tangential deformation were not, which suggests that the ball model does not accurately capture the bending during impact. If this is the case then a reduction in the magnitude of such waves would suggest that not enough energy is being transferred to the bending mode through impact. This excess energy must be accounted for to produce accurate normal COR values and it is probably consumed within the damping coefficient. It will also be shown that this underestimation of the bending mode affects the tangential properties of the impact.

It was seen that the method used to determine the coefficients of static and dynamic friction is limited and the initial values had to be modified to provide a more accurate representation. The resulting model behaviour closely matches the experimental data for oblique impacts over the range of pre-impact conditions investigated, with a particularly good fit seen at high angles and velocities. It was seen from the force traces in chapter 7 that a greater proportion of the contact occurred in sliding for these conditions and so it appears that the rolling behaviour is less accurately predicted by the model. This is confirmed if we look at the sliding velocity from the model at different incident angles. If we consider the initial impact node, then providing it remains within the contact region during impact it is possible to equate its tangential velocity to the slip rate. The highest spin achieved is around 3000rpm for a 50 degree impact at 35m/s, which must be developed throughout the impact, giving an average spin of around 1500rpm over the four millisecond impact duration. This assumes linear spin generation, which is a reasonable approximation for this calculation. This would result in an angular rotation of

---



---

36 degrees in this extreme case which may just remove the initial impact node from the contact region. Figure 8.19 shows the tangential velocity of the initial impact node for angles of  $10^\circ$ ,  $30^\circ$  and  $50^\circ$  at an incident velocity of 25m/s and several interesting phases of impact are observed. Initially it appears that the contact region is rapidly decelerated, with sliding velocity reaching zero for the 15m/s impact as the surfaces stick. This occurs during only the first few microseconds, as the small area of contact simply compresses under load and was also evident in the force profiles of chapter 7 where the initial tangential load reaches a peak within the first 0.2ms of impact and the resulting COF appears higher. It has already been suggested that this corresponds to the initial stiff ball behaviour, prior to wall buckling. As the impact progresses, the sliding velocity falls almost linearly for around a millisecond before a sharp reduction brings the initial contact node to rest. This would appear to signify the transition from sliding to rolling, where both friction modes operate within the contact region. Just prior to the end of contact the velocity of the initial impact point actually goes negative, with sliding occurring locally against the direction of whole body motion. This phenomenon is due to localised energy gradients and is discussed later during the consideration of spin. Clearly there is some action that triggers the transition from sliding to rolling, although the cause is not apparent from Figure 8.19. What is clear is that the percentage of the impact that occurs in rolling is proportional to the incident angle, with higher angles having less rolling throughout. It is interesting that the time during impact that rolling begins is similar for the  $10^\circ$  and  $30^\circ$  impacts. However, the negative sliding phase that accompanies the end of contact begins earlier in the  $30^\circ$  impact and so impact duration and hence overall rolling percentage are reduced.

Figure 8.20 shows the relationship between incident velocity and slip rate for modelled  $30^\circ$  impacts. Here we see that rolling actually begins earlier for higher initial velocities, however the negative slip phase and end of impact also occur first. The result is a reduced overall rolling percentage for the higher incident velocities. This confirms the relationship between incident angle, initial velocity and rolling percentage and so the argument that it is the lower predicted energy loss during rolling that accounts for the higher rebound velocities from the model would seem reasonable.

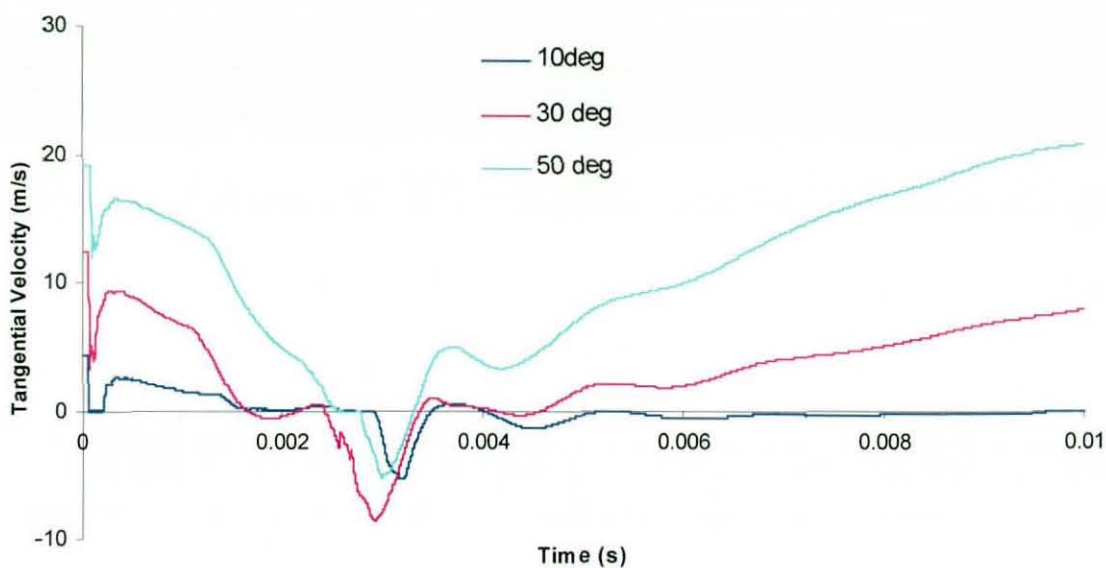


Figure 8.19 – Tangential Velocity of Initial Impact Node for 25m/s Impacts at  $10^{\circ}$ ,  $30^{\circ}$  and  $50^{\circ}$  Angles of Incidence.

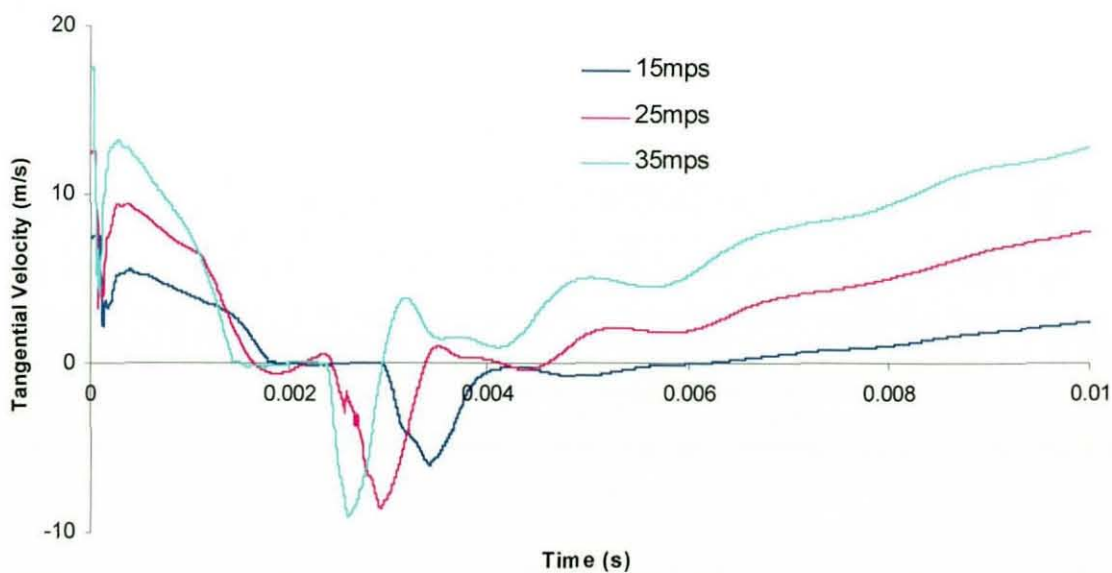


Figure 8.20 – Tangential Velocity of Initial Impact Node for 30 Degree Oblique Impacts at Varying Incident Velocity.



---

Having observed how the ball slides and rolls during impact, it is desirable to attempt to follow the development of 'spin' during the contact phase. Classically, spin is defined as the rate of angular rotation of some point on the surface of an object about its centre of rotation. For a rigid body where all points on the surface are fixed relative to one another throughout time then this definition is quite convenient. However, in the case of a tennis ball, which is highly deformable, then this relationship no longer holds. In a state of maximum compression, a tennis ball may be likened more to a belt passing over a pulley at either end. Clearly for a rigid belt then every point on its surface would possess the same tangential velocity. At either end where the belt passes over the pulley wheels then any surface element may be said to have an angular velocity proportional to the radius of the pulley. However, in between the pulleys the belt travels in a straight line, possessing only linear velocity and so here the 'spin' would be zero. Whilst we may attempt to define a centre of rotation and calculate a spin value based on some average radius, this is further complicated when we consider that the belt is not in fact rigid, but surface elements may move relative to one another, resulting in in-plane strains. The pulleys may also translate and also increase or decrease in radius and so any 'centre of rotation' would be an approximation at best. However what may be of use is knowledge of the local surface velocity values, which are an indicator of the energy possessed by each element and it is this idea that will be used to attempt to explain the phenomenon of spin.

If surface velocities are to be considered then local surface orientations must first be defined. Whilst velocity values are nodal data, each node is simply a point in space and has no direction, rather the local surface orientation must be calculated from the surface normals of neighbouring elements, having the point of interest at a vertex. The component velocities for each point are then transposed into a coordinate framework unique to the local surface orientation. Resulting 'normal' and 'tangential' velocity components are then those either away from the surface at ninety degrees or in the surface plane. If tangential velocities for all points of impact are given as positive in the direction of final rotation, then the final values of tangential velocity will be equal to the surface velocity calculated from the rigid body angular rotation value.



---

Figure 8.21 shows the tangential 'surface' velocity for points around the ball as previously defined in chapter 3, relative to the whole ball velocity, calculated from component values for a 10 degree impact at 25m/s. It is clear that the velocity of the 'bottom' point of the ball corresponds to the sliding velocity data presented in Figure 8.19. As the bottom of the ball initially sticks then the relative velocity of that point must equal the whole ball velocity, as is clearly seen. Once this point is released and sliding commences, its relative velocity falls to almost zero indicating that the material recovers and rejoins whole ball motion. However at the same time, the 'front' and 'back' of the ball begin to move relative to the absolute motion. This would suggest that the friction force experienced during the initial stick transfers energy which travels around the ball in a wave, taking twice as long to reach the 'top' of the ball as the 'front' and 'back'. As the time taken to travel around half of the ball is less than 0.5ms then it would appear to be translated at the dilation wave speed of the material as a compressive or tensile wave, rather than in the slower bending wave already identified. It is the 'top' of the ball that appears to accelerate most rapidly, reaching a peak surface velocity before either the 'front' or 'back', probably due to the 'top' of the ball being least constrained. It is also evident that the 'front' of the ball reaches a peak surface velocity before the 'back' which would indicate that the energy from the friction force is transferred more rapidly through tension than compression. Having reached a peak velocity, all three points show a subsequent drop in surface velocity to a common final value. This may again be due to energy losses during the rolling phase.

It is the consideration of the 'bottom' point of the ball in comparison to the whole ball velocity that yields the most interesting result. Having fallen to a value of nearly zero surface velocity, the 'bottom' point on the ball surface accelerates to reach a constant surface velocity, at which point the sliding velocity is zero and there is 'stiction' and the ball rolls. Interestingly we see that during rolling the corresponding whole ball tangential velocity is equal to the surface velocity of the 'bottom' point which is analogous to the solid body case where the ball rotates instantaneously about the centre of its contact area. The surface velocity of the 'bottom' point is also much lower throughout impact than the other three points, which would suggest that the unconstrained portion of the ball attempts to 'roll' with a greater velocity than the surface friction will allow, which

---

---

should result in greater compressive stress at the front of the ball and tensile stress at the back of the ball. Also, as the ball rolls then the compressed front region of the ball will enter the contact zone, where it will stick to the surface and so retain its compression throughout contact.

During rolling there is a reduction in the 'bottom' surface velocity which would suggest a small sliding phase, before the surfaces stick once more. Most prominent in the behaviour of the 'bottom' point is the large peak in relative velocity just prior to the end of contact. This is a highly localised phenomenon and appears to be due to out of balance stresses within the contact zone which have been held in place by the sticking of the surfaces. As the normal loading is released then the shear forces within the contact zone will be greater than the shear strength of the adhered asperities and so the surfaces will slip. It appears that it is during this sudden release of energy that the material within the contact zone accelerates to attain a surface velocity equal to that of the rest of the ball. As the 'bottom' point slips during this time then the ball is not accelerated by the sudden increase in local surface velocity, resulting in an outbound tangential ball velocity that is lower than would be expected from the rigid body 'spin'. It appears that the energy released during this final slip is dissipated in a 'rotational' vibration mode, seen as oscillations of the local surface velocities after impact. Figure 8.22 and Figure 8.23 show a similar pattern of events for 30 and 50 degree impact at 25m/s. Whilst results for the 10 and 30 degree impacts appear similar, for the 50 degree impact the profiles differ, with the surface and absolute tangential velocities being similar in value. This is due to the lower normal deformation at higher angles such that rotation about the 'bottom' is at a distance similar to the undeformed radius. The accompanying sudden slip of the 'bottom' point is also less marked as a result and it is possible that this is a limiting factor in spin generation.

Figure 8.24 shows the average surface velocity value calculated from the four points of interest against the sliding velocity of the 'bottom' point. It is clear that by giving equal weighting to the 'bottom' surface velocity its effect upon the average value is marked. However the resulting motion is of interest. It appears that the ball develops all its relative surface velocity, what we may equate to rigid body spin, within the first



---

millisecond of impact, whilst the ball is still sliding. This value then appears constant throughout impact and beyond, with only a small period of sudden increase due to the slip of the 'bottom' point. As the average surface velocity subsequently returns to its previous value then this would further indicate that the energy released during this sudden slip is lost within the ball. The fact that the average surface velocity appears to rise to a maximum level at which it remains throughout would suggest that no surface energy is lost through rolling and the associated hysteresis cycle. However, this cannot be the case and it appears that energy losses do occur locally, seen in the variation of surface velocity around the ball.

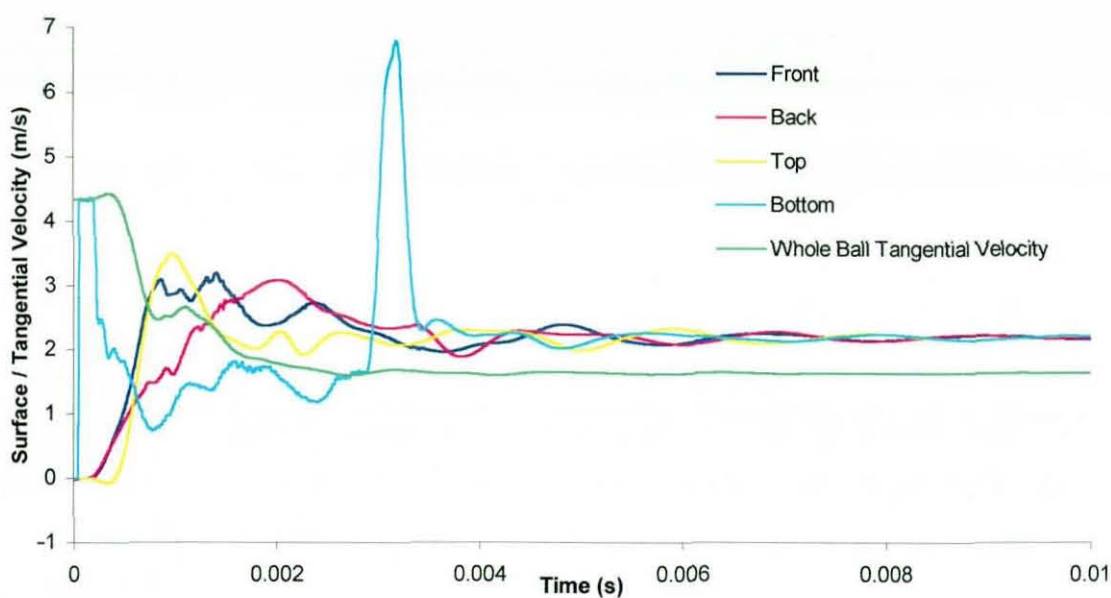


Figure 8.21 – Surface Velocity of Points Around the Ball for a 10 Degree Impact at 25m/s.

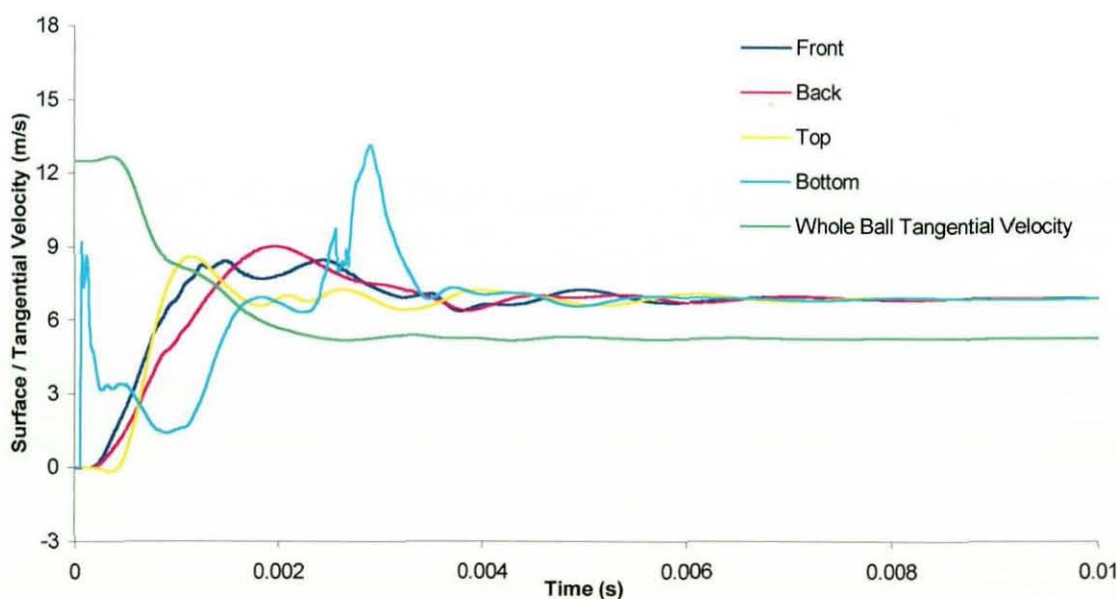


Figure 8.22 – Surface Velocity of Points Around the Ball for a 30 Degree Impact at 25m/s.

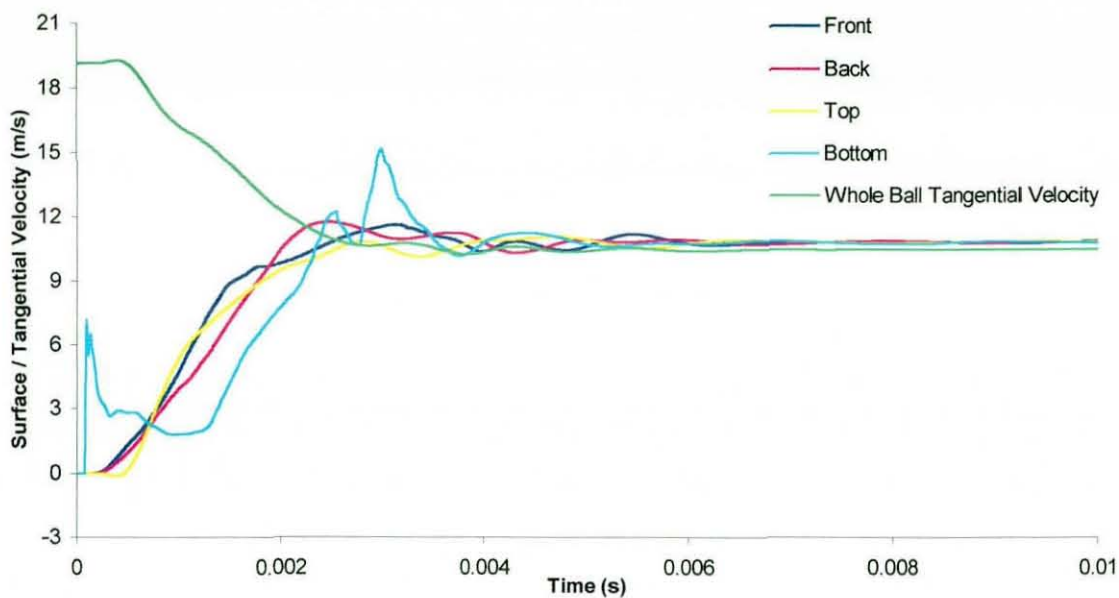


Figure 8.23 – Surface Velocity of Points Around the Ball for a 50 Degree Impact at 25m/s.

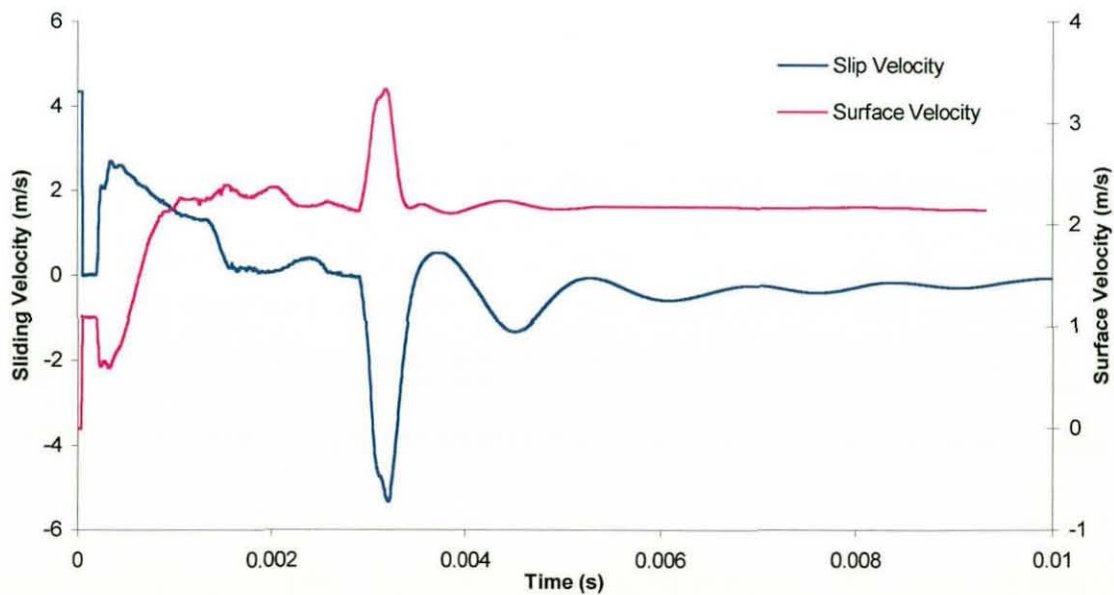


Figure 8.24 – Sliding Velocity and Average Surface Velocity for a 10° Impact at 25m/s.



---

## 8.7 Conclusions

Whilst there is clearly some discrepancy between experimental data and predicted model behaviour, the F.E. ball model does provide a good first order approximation in all cases and the fit is much better in some instances. This suggests that the basic cloth material model behaves correctly under the conditions experienced during an oblique surface impact, but that further development is required to fully capture the important bending behaviour of the ball.

In order to consider spin during oblique impacts of highly deformable objects, it is shown that 'spin rates' defined using standard rigid body mechanics no longer hold. A more general method is introduced whereby the local surface velocities are calculated and used to indicate the energy possessed by the 'rotational' mode during impact. From this it is seen that surface velocity is generated early during impact, before sliding finishes and during the rolling phase the whole ball may be said to instantaneously rotate about the centre of contact. As impact ends, the contact surface rapidly slips such that post impact tangential velocity is not equal to the final surface velocity.

---

## 9 Final Conclusions

It has been shown that a finite element hollow sports ball model accurately predicts rebound characteristics for known incident conditions. Furthermore, the model has also been used to explain these rebound characteristics in terms of the physical behaviour of the ball during impact.

The geometry used to define the ball affects the rebound characteristics and ball meshes display directional properties related to their underlying geometries. Element choice may also have a significant effect upon the impact characteristics. These effects are minimised by using a high density icosahedral mesh with two element layers.

Defining the model in spherical space allows simple manipulation ball diameter and layer thickness, whilst retaining the same mesh geometry. Pressurisation is also simplified by using this coordinate system.

Characteristics normal to the impact surface are proportional to incident velocity. These characteristics appear primarily dependent upon the core properties, with the addition of a cloth cover stiffening the balls. The impact excites bending modes within the ball and distinct waves are seen to propagate around the shell.

The model shows that the strain rate dependency of rubber has the greatest influence on core rebound characteristics. It is possible to extrapolate low strain rate tensile behaviour to higher strain rates through published data and the resulting core model accurately predicts impact behaviour over a range of impact velocities. Whilst restitution appears related to both material stiffness and damping, impact duration is dependent upon stiffness only. The development and subsequent propagation of the observed bending waves is also predicted by the model, with these waves appearing to develop as the shell buckles at the edge of the contact zone, around 200 $\mu$ s after impact commences.

---

In oblique impacts, normal components of velocity and force are independent of incident angle and hence any tangential component, giving similar results to those for normal impacts.

Tangential characteristics are governed by the interaction between the ball and impacting surface. The friction force is dependent upon the normal force and sliding velocity.

The compressibility of cloth is best defined as a foam model, however this limits the accuracy of predicted tensile behaviour. As a result the bending behaviour is not as accurately predicted as impact duration and restitution. It is possible to define a friction model as a function of incidence angle that provides accurate prediction of impact behaviour over a range of conditions.

In attempting to define 'spin' generation during impact, it is seen that the classical rigid body approach no longer holds for a highly deformable object. A surface velocity approach is suggested as an alternative method and shows the 'spin' to develop during the first millisecond of impact, during the sliding phase. The ball subsequently rolls as an instantaneous rotation about the centre of contact. As impact ends, it is seen that the small remaining contact region slips such that the final surface velocity is greater than the whole body tangential velocity. The sudden local energy increase is propagated around the ball as a surface wave and has little effect on the spin rate.

---

## 10 Recommendations for Further Work

In developing the spherical model geometry, it was assumed that the ball is isotropic and so behaves the same regardless of orientation. In reality the rubber tennis ball core is constructed from two separate hemispheres that are bonded by a rubber based adhesive. It is suggested that the effect this construction has upon the ball deformation and rebound characteristics be investigated. Impact testing of the core at controlled orientations would reveal any directional effects due to the location of the join, whilst materials tests on the bonded seam itself would determine its localised effect on the material properties. As for the cloth layer, it is suggested that a refined outer geometry be developed which would replicate the dumbbell shape of the cloth pieces, with a corresponding seam modelled as a thin line of rubber brick elements. With regards to a generic ball model, it is suggested that a method be developed whereby 'panel' geometry may be generated automatically from a set of user defined parameters. This would allow studies to be made into the effect of panel geometry on ball characteristics, which is an ongoing problem not only in tennis but also in sports such as soccer.

The effect of the adhesive used to bond the cloth to the rubber core may also be assessed through peel tests and a more accurate definition for this interface may be included within the model to replace the current solution. The cloth material model is also in need of refinement to more accurately predict bending waves within the covered ball. In order to eliminate the poor tensile performance of the hyperfoam model, a layer of shell elements could be included between the solid element layers of the rubber and cloth to represent the woven base of the material. The tensile properties of the cloth may then be applied to this layer which would have the desired effect of stiffening the ball, whilst the solid element layers would entirely capture the compressive behaviour and provide friction. This would be analogous to the actual properties of the cloth. The tensile shell would ideally be capable of applying anisotropic material properties, whilst the solid compressive layer would more accurately represent the frictional properties.

---

In order to improve the friction model it is suggested that component force measurement be carried out at constant values of sliding velocity and normal load. A friction map may be generated capable of predicting the dynamic COF for any combination of load and velocity. Furthermore, the possibility of using other materials and methods to cover the tennis ball should be investigated, such as an assessment of one piece coverings.

Having developed a more accurate ball model, a set of complementary playing surfaces should then be developed to assess the interaction between the two. The surfaces would likely have a layered structure to reflect their construction methods, with suitable material properties to predict deformation behaviour and energy loss. The ITF has a set of standard tests to determine surface properties and these may be used initially, although may not provide suitable results for finite element model development. Other impact 'surfaces' such as racket string beds should also be developed to allow further contribution to current ball impact knowledge.

It is suggested that the model be used to predict the impact characteristics of 'prototype' balls, whereby ball parameters such as radius, wall thickness and material stiffness are varied, to determine possible future ball products for the tennis industry. Using parameters and properties derived from other hollow sports balls, models should be developed for standard balls in each sport and assessed against experimental data. Similar parametric studies should be performed in order to assess the possibility of developing novel ball products for all sports.

The possibility of using the finite element ball impact model as part of a trajectory simulator should also be assessed. Aerodynamic properties could be defined within the model itself which, coupled with a dynamic racket or string bed model would allow the prediction of ball behaviour during an entire event.



---

## 11 Bibliography

- ABC (1993). Bowling Ball Specifications, American Bowling Congress: 48.
- Achenbach, E. (1972). "Experiments on the flow past spheres at very high Reynolds number." Journal of Fluid Mechanics **54**: 565-575.
- Ahmadi, H. R. and A. H. Muhr Measurement and Application of Dynamic Stress-Strain Properties of Rubber. UK, Tun Abdul Razak Research Centre: 8.
- Ajayi, J. O. and H. M. Elder (1994). "Fabric Technology: Fabric friction and wear study Comparative Studies of Yarn and Fabric Friction." Textile monthly **12**(21).
- Al-Maliky, N. S. and D. J. Parry (1996). "A freely Expanding Ring Technique for Measuring the Tensile Properties of Polymers." Meas. Sci. Technol. **7**: 746-752.
- Anderson, D. J. A., M.D. (1982). The Science of Tennis, Racquet Press Inc.
- Andrews, J. G. (1983). "A Mechanical Analysis of a Special Class of Rebound Phenomena." Medicine and Science in Sports and Exercise **15**(3): 256-266.
- Armstrong, C. W., T. A. Levendusky, et al. (1987). Influence of Inflation Pressure and Ball Wetness on the impact Characteristics of Two Types of Soccer Balls. First World Congress of Science and Football, Liverpool, United Kingdom.
- Baran, N. M. (1988). Finite Element Analysis on Microcomputers, McGraw-Hill.
- Bernstein, A. D. (1977). "Listening to the Coefficient of Restitution." Am. J. Phys. **45**(1): 41-44.
- Brancazio, P. J. (1981). "Physics of Basketball." Am. J. Phys. **49**(4): 356-365.
- Bridge, N. J. (1998). "The Way Balls Bounce." Phys. Educ. **33**(3): 174-181.
- Bridge, N. J. (1998). "The Way Balls Really Bounce." Phys. Educ. **33**(4): 236-241.
- Brody, H. (1984). "That's how the ball bounces." The Physics Teacher **22**: 494-497.
- Brody, H. (1990). "The Tennis Ball Bounce Test." The Physics Teacher **28**: 407-409.
- BSI (1995). Specifications for Cricket Balls, British Standards Institution: 14.
- CAEC (1989). Championship Ball Specification, Croquet Association Equipment Committee: 1.
- Caffi, M. and F. Casolo (1993). Ball dynamic characteristics: a fundamental factor in racket optimization. World Congress of Science and Racket Sports (1st), United Kingdom.
-

- 
- Carter, J. M. (1992). Medieval Games : Sports and Recreations in Feudal Society, Greenwood Press.
- Casolo, F. (1997). Moments of Coefficient of Restitution for Tennis Balls on Various Surfaces. Milan, D.S.T.M. - Politecnico di Milano.
- Casolo, F., A. Vallatta, et al. (1997). Measurement of the Dynamic Properties of Tennis Balls. Milan, D.S.T.M. - Politecnico di Milano.
- Chou, P. C., D. Liang, et al. (1994). Contact Forces, Coefficient of Restitution and Spin Rate of Golf Ball Impact. World Scientific Congress of Golf (2nd), St. Andrews, Scotland.
- Ciesielski, A. (1999). An Introduction to Rubber Technology, Rapra Technology Limited.
- Crisco, J. J., S. P. Hendee, et al. (1997). "The Influence of Baseball Modulus and Mass on Head and Chest Impacts: A Theoretical Study." Medicine and Science in Sports and Exercise 29(1): 26-36.
- Cross, R. (1998). "The bounce of a Ball." Pending Submission: 18.
- Cross, R. (2000). "The Coefficient of Restitution for Collisions of Happy Balls, Unhappy Balls, and Tennis Balls." Am. J. Phys. 68(11): 1025-1031.
- Daish, C. B. (1972). Physics of ball games, London English Universities Press.
- Decker, W. (1992). Sports and Games of Ancient Egypt, Yale University Press.
- Dowell, I. J., S. R. Snowden, et al. (1991). "A Comparison of Force of Impact Compression Area and Velocity of selected Balls." Journal of Human Movement Studies 20(6): 279-289.
- Dowell, L. J. and G. Krebs (1991). "A formula for Comparison of Selected Sport Ball Compressibility." British Journal of Sports Medicine 25(1): 34-37.
- Dowell, L. J., F. Smith, et al. (1987). "The Effect of Angle of Incidence on Rebound Deviation of a Tennis Ball." Journal of Human Movement Studies 13(2): 69-73.
- DSI (1988). The History of the Golf Ball, Dunlop Slazenger International.
- Duery, A. (1994). "The Impact of the Table Tennis Ball on the Racket." International Journal of Table Tennis Science 2: 1-13.
- Dunlop, J. J., C. J. Milner, et al. (1992). "Sports Surface-Ball Interactions: Laboratory Measurement Techniques." Journal of Sports Turf Research Institute 68: 114-123.
-

- 
- FIBA (1998). Official Basketball Rules, International Basketball Federation: 98.
- FIFA (2001). Laws of the Game, International Football Federation.
- FIVB (2001). Official Volleyball Rules, International Volleyball Federation.
- Gillmeister, H. (1997). Tennis - A Cultural History. London, Leicester University Press.
- Gobush, W. (1990). Impact Force Measurements on Golf Balls. World Scientific Congress of Golf (1st), St. Andrews, Scotland.
- Goodwill, S. R. (1997). Dynamic Comparison of Tennis Ball Impacts on an Artificial Surface. Mechanical Engineering. Sheffield, University of Sheffield: 49.
- Groppel, J. L. (1992). High Tech Tennis, Human Kinetics Pub. (Europe) Ltd.
- Gugan, D. (2000). "Inelastic Collision and the Hertz Theory of Impact." Am. J. Phys. 68(10): 920-924.
- H.K.S.inc (1998). Rubber Elasticity with Abaqus.
- Haake, S. (1995). The Mechanics of Golf Ball Impacts. British Society for Strain Measurement.
- Haake, S. (1999). Modelling and Analysis of Oversized Balls. Sheffield, University of Sheffield: 16.
- Haake, S. and S. Goodwill (1998). Tennis Ball Impacts on Synthetic Turf, Sheffield University: 7.
- Harris, H. A. (1972). Sport in Greece and Rome. London, The Camelot Press Ltd.
- Hendee, S. P., R. M. Greenwald, et al. (1998). "Static and Dynamic Properties of Various Baseballs." J. App. Biomech. 14(4): 390-400.
- Hertz, H. (1882). "Uber die Beruhrung fester elastischer Korper (On the contact of elastic solids)." J. Reine Angew. Math. 92: 156-171.
- Hocknell, A., R. Jones, et al. (1996). "Experimental Analysis of Impacts with Large Elastic Deformation: I. Linear Motion." Meas. Sci. Technol. 7: 1247-1254.
- Hocknell, A., R. Jones, et al. (1998). Computational and Experimental Analysis of the Golf Impact. Third World Scientific Congress of Golf, St. Andrews, Scotland.
- Hope, A., L. J. Dowell, et al. (1988). "A comparison of the effect of angle of incidence of slow, and fast incidence velocities on velocity deviation of a ball." Journal of human movement studies 15: 299-305.
-

- 
- Hosseini Ravandi, S. A., K. Toriumi, et al. (1994). "Spectral Analysis of the Stick-Slip Motion of Dynamic Friction in the Fabric Surface." Textile research journal 64(4): 224.
- IBAF (1999). Official Baseball Rules, International Baseball Federation.
- IFNA (2001). Rules of Netball, International Federation of Netball Associates.
- IRB (2001). Laws of the Game, International Rugby Board.
- ITF (1998). An Initial ITF Study on Performance Standards for Tennis Court Surfaces, International Tennis Federation.
- ITF (2000). Rules of Tennis, International Tennis Federation: 33.
- ITTF (1994). The Ball - Technical Leaflet T3, International Table Tennis Federation.
- ITTF (2001). The Laws of Table Tennis, International Table Tennis Federation.
- Johnson, S. H. and B. B. Lieberman (1994). An Analytical Model for Ball-Barrier Impacts Part 2: A Model for Oblique Impact. World Scientific Congress of Golf (2nd), St. Andrews, Scotland.
- Johnson, W., S. R. Reid, et al. (1973). The Impact, Rebound and Flight of a Well Inflated Pellicle as Exemplified in Association Football. Manchester Association of Engineers.
- Kawabata, S. (1980). The Standardization and Analysis of Hand Evaluation. Osaka, Japan, The Textile Machinery Society of Japan: 93.
- Kistler Cutting Force Measurements. Innovative Precision for Optimizing Productivity. Winterthur, Switzerland, Kistler Instruments Ltd.
- Leigh, D. C. L., W-Y. (1992). "Dynamics of the Interaction Between Ball, Strings, and Racket in Tennis." International Journal of Sport Biomechanics 8: 181-206.
- Levendusky, T. A., C. W. Armstrong, et al. (1987). Impact Characteristics of Two Types of Soccer Balls. First World Congress of Science and Football, Liverpool, United Kingdom.
- Lieberman, B. B. and S. H. Johnson (1994). An Analytical Model for Ball-Barrier Impact Part 1: Models for Normal Impact. World Scientific Congress of Golf (2nd), St. Andrews, Scotland.
- Lyons, W. J. (1963). Impact Phenomena in Textiles. Cambridge, Massachusetts, M.I.T. Press.
-

- 
- Maw, N., J. R. Barber, et al. (1976). "Oblique Impact of Elastic Spheres." Wear 38(1): 101-114.
- MCC (2000). The Laws of Cricket, Marylebone Cricket Club.
- Metha, R. D. (1985). "Aerodynamics of Sports Balls." Annual Review of Fluid Mechanics 17: 151-189.
- Metha, R. D. (2001). "Aerodynamics of a Tennis Ball." Sports Engineering 4(4): 177-189.
- Morgan, R. (1995). Tennis - The Development of the European Ball Game. Oxford, Ronaldson Publications.
- NASA (1997). Tennis Sport Science, NASA: Learning Technologies Project Cislunar Aerospace. 1997-2001.
- Newton, I. (1687). Mathematical Principles of Natural Philosophy and his System of the World.
- Pauchard, L. and S. Rica (1998). "Contact and Compression of Elastic Spherical Shells: the Physics of a 'Ping-Pong' Ball." Philosophical Magazine B 78(2): 225-233.
- Petterson, D. R. and G. M. Stewart (1960). "Dynamics of Body Armor Materials Under High Speed Impact, Part II. Stress-Strain Curves and Strain-Position Distributions." Textile Research Journal 30(6): 422-431.
- Rayleigh, L. (1877). "On the Irregular Flight of a Tennis Ball." Messenger of Mathematics 11: 14-17.
- Realff, M. L. (1994). "Identifying Local Deformation Phenomena During Woven Fabric Uniaxial Tensile Loading." Textile research journal 64(3): 135-141.
- Roberts, J. R., R. Jones, et al. (2001). "Measurement of Contact Time in Short Duration Sports Ball Impacts: an Experimental Method and Correlation with the Perception of Elite Golfers." Sports Engineering 4(4): 191-203.
- Ronchi, C., R. Iacono, et al. (1996). "The 'Cubed Sphere': A New Method for the Solution of Partial Differential Equations in Spherical Geometry." Journal of Computational Physics 124: 93-114.
- Rose, P. (1999). Ball / Surface Impacts. London, International Tennis Federation: 13.
- Sahr, K. and D. White (1998). "Discrete Global Grid Systems." Computing Science and Statistics 30.
-



- 
- Smith, J. C., J. M. Blansford, et al. (1960). "Stress-Strain Relationships in Yarns Subject to Rapid Impact Loading." Textile Research Journal 30(10): 752-760.
- Smith, J. F. (1990). The effect of angle, velocity, and rotation of incidence on the deviation of rebounding tennis balls. College of Human Performance. Oregon, University of Oregon.
- Snowden, S. R., L. J. Dowell, et al. (1989). "Velocity, Compression Area, and Stopping Distance Compared for Balls used in Physical Education." Journal of Human Movement Studies 17(1): 23-32.
- Stensgaard, I. and E. Laegsgaard (2001). "Listening to the Coefficient of Restitution - Revisited." Am. J. Phys. 69(3): 301-305.
- Stepanek, A. (1988). "The aerodynamics of tennis balls - The topspin lob." American Journal of Physics 56: 138-142.
- Stronge, W. J. (2000). Impact Mechanics. Cambridge, Cambridge University Press.
- Tabor, D. and F. P. Bowden (1973). Friction. London, Heinemann Educational Books Ltd.
- Thomson, J. J. (1910). "The Dynamics of a Golf Ball." Nature 85(2147): 2151-2157.
- Titely, U. A. and R. McWhirter (1970). Centenary History of the Rugby Football Union. London, Redwood Press Ltd.
- Treloar, L. R. G. (1975). The Physics of Rubber Elasticity. Oxford, Clarendon Press.
- Ujihashi, S. (1994). Measurement of Dynamic Characteristics of Golf Balls and Identification of their Mechanical Models. World Scientific Congress of Golf (2nd), St. Andrews, Scotland.
- Viney, N. (1978). An Illustrated History of Ball Games. London, William Heinemann Ltd.
- Vinson, J. R. and J. A. Zukas (1975). "On the Ballistic Impact of Textile Body Armor." Journal of Applied Mechanics: 263-268.
- Witters, J. and D. Duymelinck (1986). "Rolling and sliding resistive forces on balls moving on a flat surface." American Journal of Physics 54(1): 80-83.
- WSF (2001). Rules of World Singles Squash, World Squash Federation.
-

